Chimpanzee Research Today Page 30

2 April 2010 | $10

Science

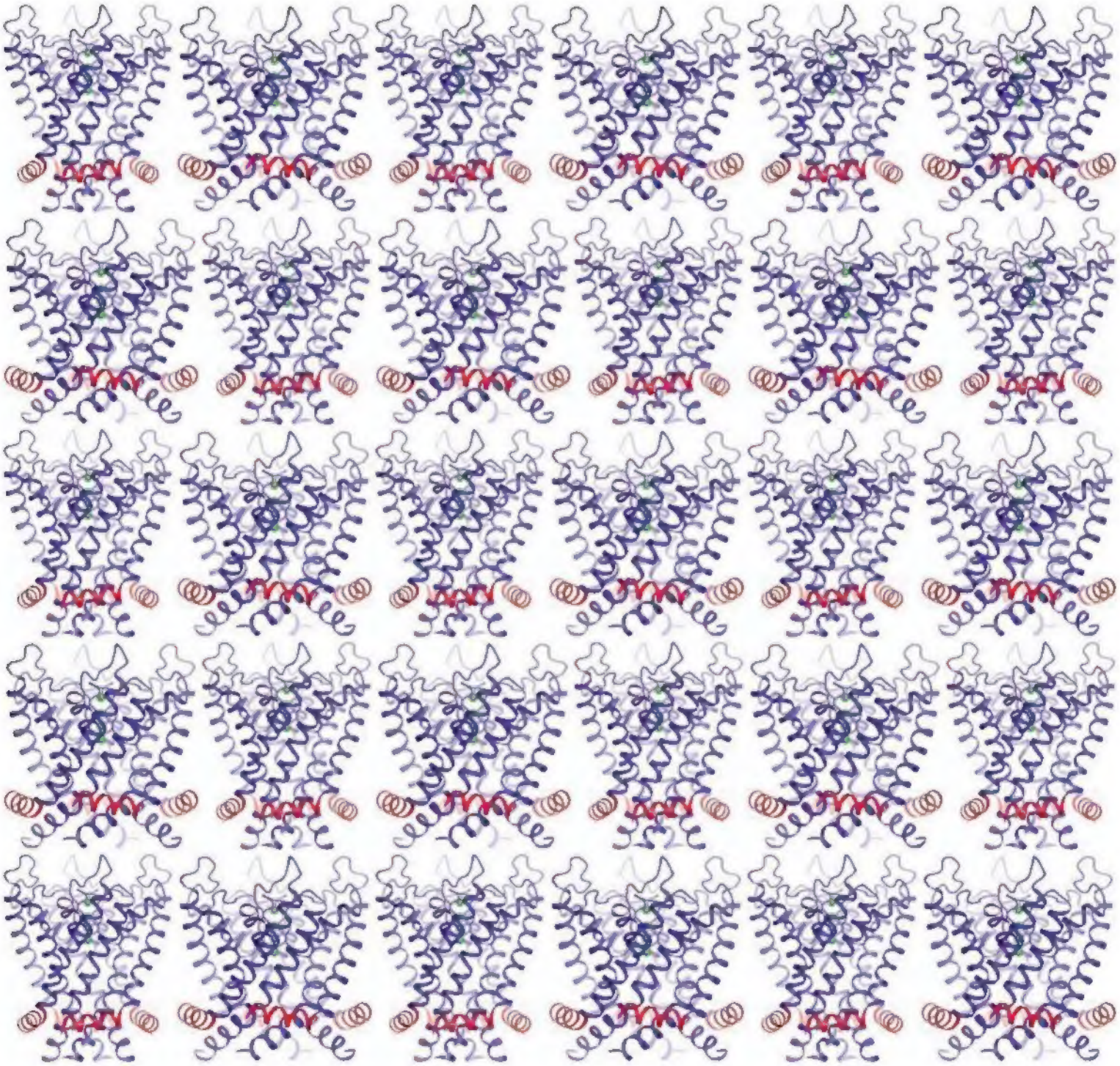

AAAS


SIGMA
Life Science
Where bio begins™


SIGMA
Life Science
Where bio begins™

It becomes you.

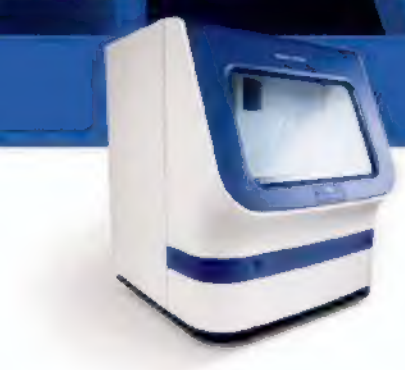

Introducing the 3500 Series Genetic Analyzer.

Get ready to make an amazing discovery: the new 8-capillary and 24-capillary 3500 Series Genetic Analyzers take DNA analysis to an entirely new level of performance. A level where your daily workflow seems like a natural extension of your own intuition. Where precise, quality-assured data inspires greater confidence. And where a new consumables design and intuitive software interface keep you current and in control.

Take a closer look, and you'll find the new 3500 and 3500xL Genetic Analyzers are like second nature. Which is our first priority when it's your data.

Discover the 3500 System at **www.appliedbiosystems.com/3500Series**

Easy-to-Use Consumables

Control at Your Fingertips

Quality-Assured Data

applied biosystems
part of life technologies

GE Healthcare
Life Sciences

GE02-10 First published January 2010.

Drop. Measure. Done.

NanoVue™ Plus: intelligent performance across all spectrophotometer applications

It's all the convenience you want in a spectrophotometer, packaged in a portable, ergonomic device. NanoVue Plus features a new hydrophobic, gold-colored sample plate coating that delivers outstanding results for sub-microliter amounts of proteins and nucleic acids. It operates without a PC and does not require time-consuming third-party path length recalibration.

NanoVue Plus enables easy protocol selection using advanced software that includes intuitive drop-down lists for the full range of CyDye™ fluorescent dyes, as well as lists for common fluors. Results can exported using a USB cable or Bluetooth™ connections for print via computer (PVC) or stored using the new SD card option. An integrated printer is also available.

- Swift, accurate analysis of 0.5 µl samples of nucleic acids and proteins
- Practical drop and measure mechanism
- Outstanding sample recovery
- Reliable and reproducible measurements
- Automatic self-calibration on start up
- Path length recalibration kit available as accessory

Experience the NanoVue Plus first hand.
Register for a trial at:

www.gelifesciences.com/tryNanoVuePlus

| AKTA | Amersham | Biacore | IN Cell Analysis | Whatman | GE Service |

imagination at work

EDITORIAL

NEWS OF THE WEEK

NEWS FOCUS

LETTERS

BOOKS *ET AL.*

POLICY FORUM

PERSPECTIVES

CONTENTS continued >>

page 30

page 48

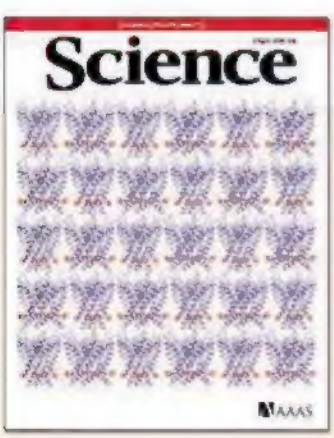

COVER

An array of alternating open and closed potassium channel pores. A Research Article on page 67 describes a mechanism by which cell membrane voltage, through the action of protein voltage sensors, controls ion channel opening and closing to produce electrical impulses in the nervous system.

Credit: Xiao Tao, Rockefeller University

DEPARTMENTS

Choose QIAGEN for detection

Detection platforms, assays, and analysis software by QIAGEN

Use QIAGEN® solutions from sample to result, and benefit from sensitive and reliable detection systems:

- **Quantitative, real-time PCR detection**
- **Automated analysis of DNA fragments and RNA**
- **Pyrosequencing® sequence-based DNA detection and quantification**
- **Optimized, ready-to-use assays and reagents**

Making improvements in life possible — www.qiagen.com

QIAGEN®

Sample & Assay Technologies

RESEARCH ARTICLES

REPORTS

CONTENTS continued >>

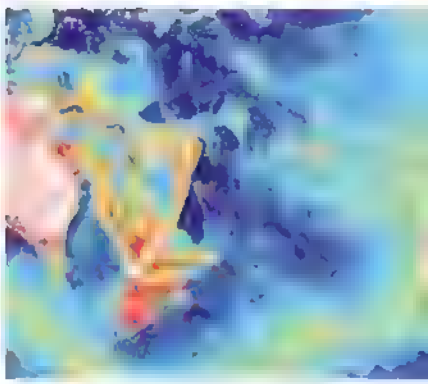

pages 54 & 83

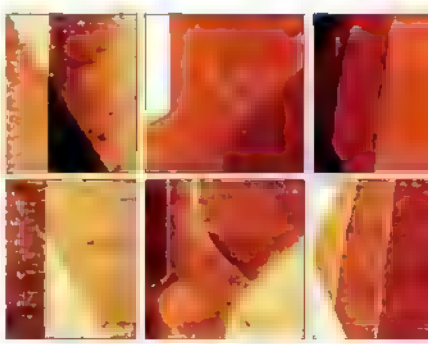

pages 52 & 76

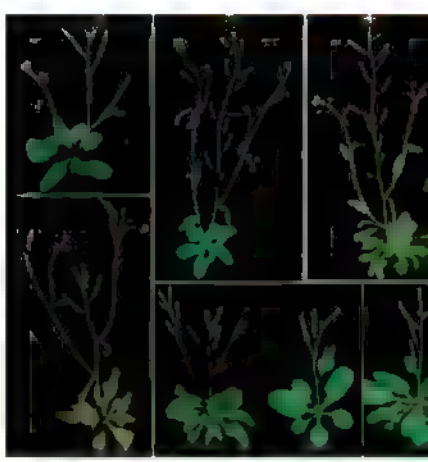

page 85

"The fastest separations and the gold standard method.

That's **electroforward** thinking."

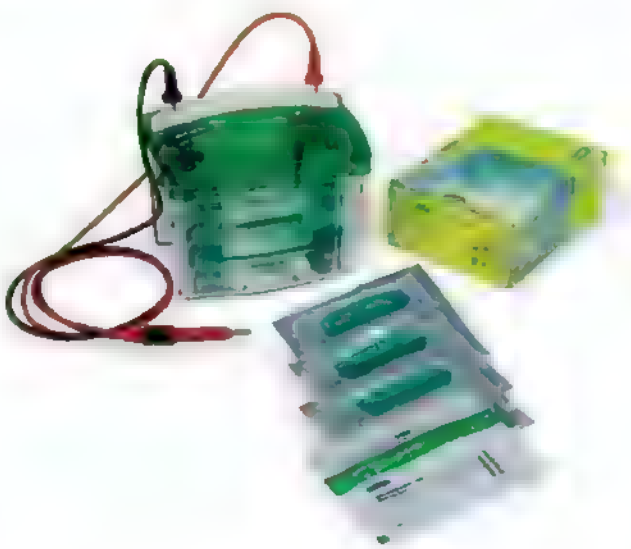

Next-generation precast gels. No special buffers required.

Introducing long shelf life Mini-PROTEAN™ TGX (**T**ris-**G**lycine e**X**tended) Gels from Bio-Rad. The innovative TGX formulation delivers consistent, near separation without the need for expensive, specialized buffers.

Get results faster with:

- Run times as short as 15 minutes
- Transfer in as little as 15 minutes
- New bottom-opening cassette design for faster setup and less handling for downstream applications

Get with us at **www.miniprotean.com.**

Research. Together.

To find your local sales office, visit **www.bio-rad.com/contact/** In the U.S. call toll free at 1 800 4BIORAD (1 800 424 6723)

Visit us at www.bio-rad.com

BIO-RAD

SCIENCEONLINE

SCIENCEXPRESS
www.sciencexpress.org

Fermi Gamma-Ray Imaging of a Radio Galaxy
The Fermi-LAT Collaboration

Gamma rays from a radio galaxy are relic cosmic microwave background radiation that underwent inverse Compton scattering
10.1126/science.1184656

Onset of Convective Rainfall During Gradual Late Miocene Rise of the Central Andes
C. J. Poulsen et al.

Increased precipitation, rather than rapid uplift, drove isotopic changes in soil carbonates of the Andes in the late Miocene
10.1126/science.1185078

Systematic Analysis of Human Protein Complexes Identifies Chromosome Segregation Proteins
J. R. A. Hutchins et al.

A strategy designed to decipher the function of proteins identified in RNA interference screens reveals new insights into mitosis
10.1126/science.1181348

SCIENCENOW
www.sciencenow.org
Highlights From Our Daily News Coverage

Murder or an Accident? The Brain Knows

Researchers finger region of the brain that helps us evaluate the intentions of others

Toward Liquid-Cooled Computers

Superwicking technique improves cooling efficiency of silicon chips

Engineers Create First Motion-Powered Nanodevice

Devices could power new generation of tiny electronics.

SCIENCESIGNALING
www.sciencesignaling.org
The Signal Transduction Knowledge Environment

RESEARCH ARTICLE: Differential Redox Regulation of ORAI Ion Channels—A Mechanism to Tune Cellular Calcium Signaling
I. Bogeski et al.

Redox sensitivity of T cells decreases through ORAI Ca^{2+} channel subunit switching during T cell differentiation

RESEARCH ARTICLE: New Roles for the LKB1-NUAK Pathway in Controlling Myosin Phosphatase Complexes and Cell Adhesion
A. Zagorska et al.

PODCAST
D. R. Alessi and A. M. VanHook

The tumor suppressor LKB1 not only keeps cell proliferation in check but also modulates cell adhesion

PERSPECTIVE: GPCR Dimers Fall Apart
N. A. Lambert

Oligomers of G protein–coupled receptors may be less stable than previously suspected

REVIEW: The Role of the Kinases RIP1 and RIP3 in TNF-Induced Necrosis
P. Vandenabeele et al.

Programmed necrosis in response to TNF requires the activity of two serine-threonine kinases

SCIENCECAREERS
www.sciencecareers.org/career_magazine
Free Career Resources for Scientists

SPECIAL FEATURE: TECHNOLOGIES ASSISTING SCIENTISTS AND ENGINEERS

Assistive Technologies Enable Discovery
S. Carpenter

Like a microscope, assistive technologies allow scientists and engineers to extend their capabilities.

Profiles in Technological Adaptation
S. Carpenter

With assists from technology, these scientists and engineers are getting their work done

Taken for Granted: Trying to Account for Tastes
B. L. Benderly

Research finds that scientists' career preferences are far wider than stereotypes suggest.

SCIENCETRANSLATIONALMEDICINE
www.sciencetranslationalmedicine.org
Integrating Medicine and Science

PERSPECTIVE: Toward an Oligonucleotide Therapy for Duchenne Muscular Dystrophy—A Complex Development Challenge
M. J. A. Wood

By correcting the reading frame in mutant DMD genes, antisense oligonucleotides can restore the production of missing dystrophin protein

COMMENTARY: Complexity in Common Diseases—Big Biology for All
J. R. Lamb and N. Gibson

Discovery of diagnostic tools and treatments for common human diseases requires integrating research in academic and industrial institutions.

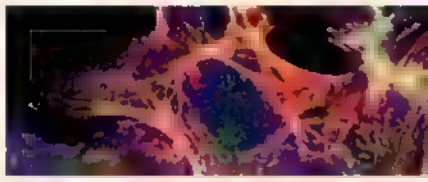

CREDIT: ANNA ZAGÓRSKA AND ALAN R. PRESCOTT/UNIVERSITY OF DUNDEE

SCIENCESIGNALING
Controlling cell adhesion

RESEARCH ARTICLE: Plasmacytoid Dendritic Cells Delineate Immunogenicity of Influenza Vaccine Subtypes
S. Koyama et al.

Rare, circulating dendritic cells differentially shape the immunogenicity mechanisms for protection against H1N1 influenza

RESEARCH ARTICLE: Microfluidic Isolation and Molecular Characterization of Circulating Tumor Cells from Patients with Localized and Metastatic Prostate Cancer
S. Stott et al.

Automated imaging of prostate-specific cancer cells from the blood provides a measure of circulating tumor cell half-life after tumor resection.

SCIENCEPODCAST
www.sciencemag.org/multimedia/podcast
Free Weekly Show

Download the 2 April *Science* Podcast to hear about insights from chimpanzee research, how cytomegalovirus evades the immune system, sinking sea floors, and more.

SCIENCEINSIDER
news.sciencemag.org/scienceinsider
Science Policy News and Analysis

SCIENCE (ISSN 0036-8075) is published weekly on Friday, except the last week in December, by the American Association for the Advancement of Science, 1200 New York Avenue, NW, Washington, DC 20005. Periodicals Mail postage (publication No. 484460) paid at Washington, DC, and additional mailing offices.

Domestic individual membership and subscription (51 issues): $146 ($74 allocated to subscription). Domestic institutional subscription (51 issues): $910; Foreign postage extra: Mexico, Caribbean (surface mail) $55, other countries (air assist delivery) $85. First class, airmail, student, and emeritus rates on request. Canadian rates with GST available upon request, GST #1254 88122 Publications Mail Agreement Number 1069624. **Printed in the U.S.A.**

Change of address: Allow 4 weeks, giving old and new addresses and 8-digit account number. **Postmaster:** Send change of address to AAAS, P.O. Box 96178, Washington, DC 20090–6178. **Single-copy sales:** $10.00 current issue, $15.00 back issue prepaid includes surface postage; bulk rates on request. **Authorization to photocopy** material for internal or personal use under circumstances not falling within the fair use provisions of the Copyright Act is granted by AAAS to libraries and other users registered with the Copyright Clearance Center (CCC) Transactional Reporting Service, provided that $20.00 per article is paid directly to CCC, 222 Rosewood Drive, Danvers, MA 01923. The identification code for *Science* is 0036-8075. *Science* is indexed in the *Reader's Guide to Periodical Literature* and in several specialized indexes.

AAAS
ADVANCING SCIENCE, SERVING SOCIETY

UNPARALLELED CONFIDENCE

PCR Reagents

There are already enough variables in PCR, don't let polymerase performance be one of them. Choose from one of the largest selections of polymerases for PCR applications from the leader in enzyme technology and bring unparalleled confidence to your experiments.

Not all PCR polymerases are created equal

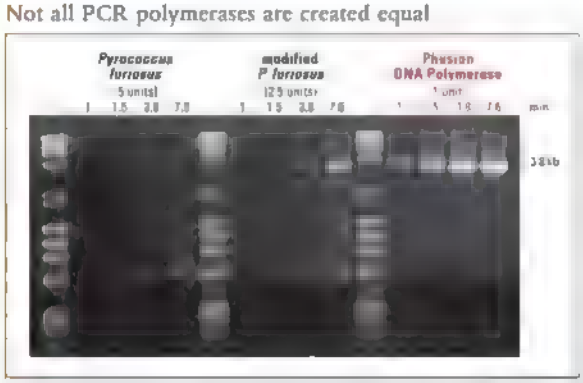

Amplification of a 3.8 kb fragment from human beta globin gene clearly illustrates the extreme speed and robustness offered by using Phusion DNA Polymerase.

Phusion is a registered trademark of Finnzymes Oy

NEB has the polymerase for your application:

- **Routine**
- **Hot start**
- **Fast**
- **High-fidelity**
- **Long or difficult templates**
- **High throughput**
- **Extraction-free PCR**
- **Master Mixes**

Visit confidentPCR.com to learn more, and to find PCR-related special offers.

CELEBRATING 35 YEARS

NEW ENGLAND BioLabs® Inc.

enabling technologies in the life sciences

DNA AMPLIFICATION & PCR | PROTEIN EXPRESSION | GENE EXPRESSION ANALYSIS

www.neb.com

<< Tailor-Made Tumor

The biotrophic smut pathogen *Ustilago maydis* specifically infects the important crop plant, maize. The pathogen elicits large tumors on all aerial maize organs by redirecting primordia into a tumor pathway, and maize developmental mutants can disrupt tumor progression. **Skibbe *et al.*** (p. 89) examined gene expression in parallel in both the host plant and the smut pathogen and found that organ-specific gene expression patterns were required in both for tumor formation. Thus, fungal pathogens may exert distinct effects on different organs and tissues in plants, perhaps explaining the diverse pathologies that can be produced in diseased plants.

On the Origins of Magnetism

The magnetic fields in galaxies and galaxy clusters are thought to result from the amplification of weak primordial magnetic fields, which, according to one class of theories, should exist in the voids between galaxies and galaxy clusters. **Neronov and Vovk** (p. 73) present evidence for the existence of intergalactic magnetic fields and derive a lower limit for their strength, based on an analysis of data from the Fermi Large Area Telescope. The results place constraints on magnetogenesis models and suggest that magnetic fields originated in the early universe before galaxy formation took place.

Cytomegalovirus Immune Evasion Strategy

Cytomegalovirus (CMV) infects a large percentage of the world's population. Most of those infected are asymptomatic; however, CMV is a substantial public health concern for immunocompromised individuals and neonates. CMV is unusual in that it can superinfect: it re-infects hosts who are already infected with the virus, even in the presence of a strong, specific immune response. **Hansen *et al.*** (p. 102; see the Perspective by **Hengel and Koszinowski**) now find that in rhesus macaques, a good model for human CMV superinfection, CMV establishes superinfections by evading the immune response mediated by $CD8^+$ T cells. A series of viral mutants deficient in expression of the US2-11 glycoproteins, which regulate antigen presentation to $CD8^+$ T cells, revealed that, although able to establish the initial infection, these viral mutants were unable to superinfect. Depletion of $CD8^+$ T cells from the monkeys allowed infection by the mutant viruses. These results highlight the difficulties in developing an effective protective vaccine against CMV itself, but suggest that CMV-based vectors may be useful in other vaccine efforts such as those against HIV.

Thin Friction

The rubbing motion between two surfaces is always hindered by friction, which is caused by continuous contacting and attraction between the surfaces. These interactions may only occur over a distance of a few nanometers, but what happens when the interacting materials are only that thick? **Lee *et al.*** (p. 76; see the Perspective by **Müser and Shakhvorostov**) explored the frictional properties of a silicon tip in contact with four atomically thin quasi–two dimensional materials with different electrical properties. For all the materials, the friction was seen to increase as the thickness of the film decreased, both for flakes supported by substrates and for regions placed above holes that formed freely suspended membranes. Placing graphene on mica, to which it strongly adheres, suppressed this trend. For these thin, weakly adhered films, out-of-plane buckling is likely to dominate the frictional response, which leads to this universal behavior.

Oceans Before the Dawn

Although the fossil record shows a clear explosion of animal diversity in the oceans at the beginning of the Cambrian period (~542 million years ago), the evolutionary pressures driving this increase in diversity remain unclear. The likely scenario involves drastic changes in the distribution of oxygen in ocean basins, but global glaciations and poor preservation of rocks from this time often prevent a clear picture of global ecology before the dawn of animal life. **Li *et al.*** (p. 80, published online 11 February; see the Perspective by **Narbonne**) characterized the geochemical makeup of sedimentary rocks from south China that indicate alternating layers of sulfide- and iron-rich (i.e., sulfate-limited) anoxic waters in the several million years leading up to the Cambrian. These conditions may have set the stage for an eventual increase in productivity of photosynthetic life that oxygenated the oceans and allowed for rapid animal evolution.

Forming Antimatter Nuclei

Atomic nuclei are everywhere and form all the matter visible to us in the universe. Their counterparts, however—antinuclei or antimatter—are relatively shy about making an appearance. **Chen *et al.*** (p. 58 published online 4 March; see the Perspective by **Cohen**) used the Relativistic Heavy-Ion Collider to coax them into existence by colliding high-energy beams of gold ions head-on. Within the debris from the collisions, evidence was found in the decay paths and particle tracks that suggested the formation of nuclei from antimatter. The ability to form these exotic particles in abundance should help to probe fundamental aspects of nuclear physics, astrophysics, and cosmology.

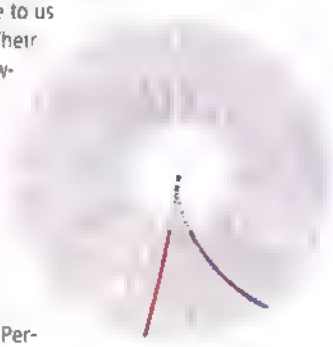

Continued on page 15

CREDITS: (TOP TO BOTTOM) VIRGINIA WALBOT AND DAVID S. SKIBBE; CHEN *ET AL.*

abcam®

We do proteins too!

Over 8,200 proteins and peptides available, with 150 new products added every month. All our products are supported by industry leading datasheets providing detailed application and technical data, just one click away!

Stay up-to-date on the latest developments with our human cytokines expressed in barley.

- Serum- and endotoxin-free
- Eukaryotic glycosylation and folding
- Biologically active

For more information visit **www.abcam.com/proteins**

The barley expression system provides unique features including proficient protein machinery, long-term protein protection and storage

Abcam Inc.
1 Kendall Square, Ste 341
Cambridge, MA 02139-1517
USA

Tel: 1-617-225-2272
Toll free: 1-888-77-ABCAM
Toll free Fax: 1-866-739-9884

Continued from page 13

The Size of the Father

Evolutionary biologists have recently discovered an intriguing phenomenon: High-fitness males often sire low-fitness daughters. The emerging consensus is that this sexual conflict overwhelms the benefits of mate choice for "good genes," thus challenging a central tenet of evolutionary theory. **Cox and Calsbeek** (p. 92, published online 4 March) provide a counterpoint by showing that female brown anole lizards can obtain genetic benefits by biasing offspring sex to produce disproportionately more sons with high-fitness (large) sires. The advantage of this sex-ratio bias was confirmed by tracking the fitness of sons and daughters in their natural environment, illustrating the importance of sexual conflict in the wild. Thus, because maximal fitness payoffs can be achieved by shifting offspring production from daughters to sons as sire size increases, mate choice can overcome antagonistic fitness effects.

Histone Inheritance

Chromatin, the packaging material for eukaryotic genomes, is a potential repository for epigenetic information. The core structure of chromatin is the nucleosome, which consists of an octamer of histone proteins, two dimers each of histones H2A and H2B, and histones 3 and 4. Histones 3 and 4, in particular, carry a series of covalent modifications presumed to be passed on through cell division. Using mass spectrometry of tagged and isotope labeled histones, **Xu *et al.*** (p. 94; see the Perspective by **Ray-Gallet and Almouzni**) followed the inheritance of the histones themselves through mitosis. The H2A-H2B dimers were inherited randomly through cell division, correlating with their lack of major covalent marks. In comparison, replication-deposited H3.1-H4 dimers did not separate through cell division, implying that H3 and H4 histone modifications might be maintained by copying from neighboring preexisting histones. Intriguingly, up to one-quarter of the nonreplication-deposited H3.3-H4 dimers, which mark active chromatin, did split during cell division.

Sperm Production-Line Maintenance

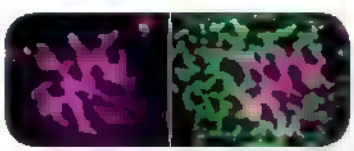

The average man makes upwards of 1500 sperm per heartbeat. Such a feat requires a robust stem cell system. Using mice, **Nakagawa *et al.*** (p. 62, published online 18 March) shed light on some of the properties of the murine germline stem cell system that contribute to its robustness. During steady-state spermatogenesis, the majority of the stem cell population lies within a subset of cells called type A spermatogonia. However, during regeneration (for example, during recovery of the stem cell pool after drug exposure) the system in essence hijacks early-differentiating cells back into the stem cell compartment. Lineage analysis and live-imaging also suggests that during sperm production there is more than one path from a stem cell to differentiation.

Open Sesame

The proteosome plays a key role in cellular homeostasis through catalyzing protein degradation. It is a barrel-shaped nanomachine whose activity is regulated through gating substrate entry. **Religa *et al.*** (p. 98) now show that N-terminal gating residues in the proteasome interconvert on a second's time-scale between conformations that place them either outside or inside the proteasomal antechamber. An increase in the number of termini occupying the "in" state decreased rates of hydrolysis. Furthermore, proteasome activators known to increase the proteolysis rate lead to an increase in the number of termini in the "out" state.

Precise and Efficient Cortical Communication

How do thalamic neurons reliably transmit information to the cerebral cortex, despite making few synaptic connections onto their target neurons? Correlated input spikes from the thalamus have been reported, but the number of synchronous inputs and their precision and reliability is unclear. **Wang *et al.*** (p. 106) analyzed a unique data set of simultaneous thalamic and cortical recordings in vivo and compared them with simulations of a model cortical neuron. Using the recorded spike trains as inputs to the model, and constraining the model by the measured output spike trains, allowed strong predictions of the degree of convergence of synchronous inputs from the lateral geniculate nucleus. Synchrony, rather than the strength or frequency of synaptic inputs, was key to signaling, and the data suggest that there may be a region of optimal synchronous coding.

CREDIT: NAKAGAWA ET AL.

Forget DNA purification

Choose Direct PCR

Take the direct route from sample to results

Finnzymes' Direct PCR approach saves you time and cost by allowing amplification of DNA directly from the source material. No DNA purification is needed. Direct PCR is suitable for various kinds of sample materials such as plant and animal tissues, blood, and FFPE tissue samples.

Direct PCR is based on Finnzymes' unique PCR enzymes, Phusion® High-Fidelity and Phire® Hot Start DNA Polymerases. These polymerases are exceptionally tolerant of many PCR inhibitors. To achieve the shortest possible protocols, combine the Direct PCR approach with Finnzymes' Piko® Thermal Cyclers and UTW® reaction vessels.

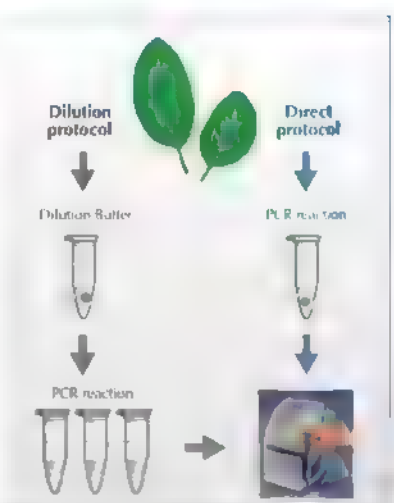

NEW!

Optimized kits available:

Phire® Plant Direct PCR Kit
for plant material

Phire® Animal Tissue Direct PCR Kit
for various animal tissues

Phusion® Blood Direct PCR Kit
for blood

See the latest results, application notes and product updates at www.finnzymes.com/directpcr

FINNZYMES
Part of Thermo Fisher Scientific

Empowering Young Scientists

T. Brück is head of the Department of International Economics at the German Institute for Economic Research (DIW Berlin), professor of Development Economics at Humboldt-University of Berlin, and Chair of the Board of Die Junge Akademie. E-mail: tbrueck@diw.de

C. Beaudry is an associate professor of Innovation Economics at the École Polytechnique de Montréal, in Canada, a member of the Center for Interuniversity Research on Science and Technology, and a researcher at the Center for Interuniversity Research and Analysis of Organizations. E-mail: catherine.beaudry@polymtl.ca

H. Hilgenkamp is a professor in Physics at the University of Twente, Enschede, and at Leiden University in the Netherlands and a member of the Young Academy of the Netherlands. E-mail: h.hilgenkamp@utwente.nl

N. Karoonuthaisiri is head of the Microarray Laboratory at the National Center for Genetic Engineering and Biotechnology, Thailand, and founding co-chair of the GYA. E-mail: nitsara.kar@biotec.or.th

H. Salah-Eldin Mohamed is an associate professor of Molecular Biology at the Institute of Endemic Diseases, University of Khartoum, Sudan, and a member of the Sudanese Academy of Young Scientists. E-mail: hibasalah@iend.org

G. A. Weiss is a professor in the Departments of Chemistry, Molecular Biology, and Biochemistry at the University of California, Irvine, and founding co-chair of the GYA. E-mail: gweiss@uci.edu

THE VANCOUVER OLYMPICS REVEAL STARK DIFFERENCES BETWEEN THE WORLDS OF SPORTS and science. In both, young people from around the world try to surpass all previous accomplishments in pursuit of world records or scientific discoveries. Selected entirely on merit, athletes receive honor just for participating in the games, spurring the next generation of young people in each nation to excel. And as star athletes age, they often support their sport in other ways, serving as advocates, mentors, or coaches. In contrast, in too many nations, the selection and promotion processes in science involve considerations other than merit. Senior scientists receive most of the resources available for scientific research, and young scientists rarely receive societal recognition for their work. This situation is growing worse as life expectancies and retirement ages increase, along with the average age for attaining scientific independence.* Perhaps as one consequence, science is typically not a top career choice. How many exceptional scientists around the world thereby go unrecognized, their talents allowed to wither away untapped? In an attempt to reverse such trends, a nascent "young national academies" movement has begun across the globe, and a new international group has recently been established to promote this cause.

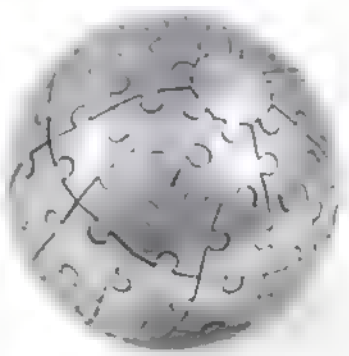

A world that increasingly faces global challenges such as climate change, resource exploitation, and public health disparities must mobilize all of its talents, regardless of age, gender, or country of residence. In the interests of scientific and resource sustainability, such a world also should encourage the views and approaches of its best young scientists, who often tackle research problems in less conventional ways than do their older, more established peers.

More than 100 young scientists from 40 countries have now created an organization called the Global Young Academy (GYA) (www.globalyoungacademy.org), with the encouragement and support of senior scientists through the InterAcademy Panel for International Issues (IAP).** The GYA will unite talented young scientists from around the world: those around the age of 35 who are nominated by senior scientists in their own nations as likely future leaders. Membership, capped at 200, will be highly competitive, involving international peer review of nominations from national academies and similar organizations. Membership is temporary (4 years), to prevent the organization from becoming an "old academy."

This effort is modeled on the formation of national young academies, only a few of which have been established so far. Die Junge Akademie was the first, founded in Germany 10 years ago by the Berlin-Brandenburg Academy of Sciences and Humanities and the Leopoldina. Similar academies have been established in the Netherlands by the Royal Netherlands Academy of Arts and Sciences and in Sudan by the Sudan Academy of Sciences. They encourage and empower their members to engage in interdisciplinary research, communicate science to society, and provide advice on national science policies, especially those affecting young scientists. The GYA will help establish national young academies and provide a forum for young scientists in countries without such organizations.

Support for the GYA concept by the IAP and the World Economic Forum began in 2008 and led to the first planning meeting in February 2010 in Berlin, Germany. The GYA emphasizes bringing together young scientists from developed and developing countries to expand research capacity and exchange best practices in science policy and education. This effort aspires to advance communications between science and society and to build on the global spirit of the Olympics through productive and friendly international interactions.

–Tilman Brück, Catherine Beaudry, Hans Hilgenkamp, Nitsara Karoonuthaisiri, Hiba Salah-Eldin Mohamed, Gregory A. Weiss

10.1126/science.1185745

*C. Holden, *Science* **319**, 391 (2008). **The authors are founding members of the GYA.

The role of duplicate genes in evolution remains contentious—whereas some have argued that they provide the raw material for evolutionary novelties on which selection acts, others have suggested that only less essential genes are maintained after they are duplicated. In flowering plants, the *FLOWERING LOCUS T* (*FT*) gene is an important determinant of fitness through its control of the time of flowering. Blackman *et al.* identified four *FT* genes in the sunflower that appear to have arisen via genus-specific duplications. Although the coding regions of all of these genes were conserved, their expression patterns differed, one of these replicates is not expressed and thus is probably nonfunctional. Transgenic *Arabidopsis ft* mutants expressing the wild sunflower genes showed accelerated flowering. However, an allele found in all domesticated sunflowers extended the time to flowering, suggesting that it may be a negative regulator. This allele shows signatures of selection consistent with domestication and provides an example of how the duplication of genes controlling development can bring about phenotypic change during domestication, and maybe during evolution generally. — LMZ

Curr. Biol. **20**, 10.1016/j.cub.2010.01.059 (2010).

APPLIED PHYSICS

Ghost Hunting

The usual method of viewing an object involves photons bouncing directly off the object and then making their way to your eye (or perhaps a photodetector), where an image is formed and stored. Ghost imaging, in contrast, builds an image with photons that have never interacted with the object. Two correlated beams of light are used, one of which interrogates the object while the other heads straight to the detector. If the beams are entangled, a perfect image can be obtained. For stealth imaging, however, thermal (that is, incoherent) light would be preferred—the object would then experience no sign of being under surveillance. With thermal light, an image is assembled by correlating the intensities of signal and reference photons at a pixelated detector and by then subtracting a background. Thus far, however, images so obtained have been rather blurry. Chan *et al.* present a theoretical treatment directed toward understanding which factors are most critical in improving the clarity of such images. They find that analysis of normalized high-order correlations offers comparable improvements to coupling low-order correlation analysis with background subtraction. — ISO

Opt. Express **18**, 5562 (2010).

Tight Squeeze

One of the first things students learn in a chemistry course is the octet rule: Atoms of the light elements are capable of sharing at most eight electrons, which limits them to four bonding partners (at two electrons to a bond). Of course, rules are made to be broken, as students soon realize when they are confronted with the stability of PF_5 and SF_6. And then there are the metals, such as iron and chromium, that routinely form six-coordinate compounds by using their partially vacant *d* orbitals. Notable exceptions in this realm involve coordination by seven guests, but it all depends on how big the guests are; smaller ones such as hydrogen can crowd together more effectively.

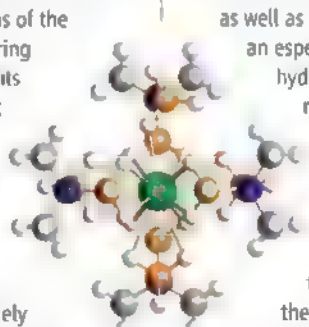

This brings us to tetrakis(*N*,*N*-dimethylaminodiboranato)thorium. Among the heaviest metals, thorium boasts a comparatively large radius, and Daly *et al.* have managed to squeeze 15 different hydrogen atoms around it, tethering the central metal to eight boron centers in the periphery. The authors characterized the compound by neutron as well as x-ray diffraction (the former being an especially sensitive technique for hydrogen detection), and their theoretical simulations suggest that, were it not for crystal packing effects, yet another hydrogen would coordinate. Heating this crowded compound induces some chemical rearrangements, the net effect of which is to bring the coordination number down to the rather less shocking value of 14. — JSY

Angew. Chem. Int. Ed. **49**, 10.1002/anie.200905797 (2010).

CREDITS (TOP TO BOTTOM): PHOTOS.COM; DALY ET AL., ANGEW. CHEM. INT. ED. **49**, 10.1002/ANIE.200905797 (2010)

NEUROSCIENCE

Insurance Against Deprivation

Individuals suffering a stroke show various degrees of neurological dysfunction due to brain tissue that has been deprived of oxygen. Strategies to minimize damage from this common problem are needed, and this has focused the attention of investigators on a process whereby the resistance of neurons to ischemia (or loss of blood flow) is increased if cells have been exposed previously to a mild bout of ischemia insufficient to cause permanent damage. Stapels *et al.* conducted a systematic search for proteins that showed increased abundance in such resistant neurons and identified SCMH1, a mouse homolog of a *Drosophila* polycomb group protein. SCMH1 can modify histones and is thought to function by repressing transcription. In a mouse neuroblastoma cell line, depletion of SCMH1 diminished the induction of tolerance to ischemia, and overexpression of SCMH1 promoted tolerance even in the absence of a conditioning ischemic event. SCMH1 associates with the promoters of two potassium ion–channel genes, and inhibiting the transcription of these genes was sufficient to produce tolerance to subsequent ischemia. — LBR

Sci. Sig. **3**, ra15 (2010)

MATERIALS SCIENCE

The Power of Annealing

Combine a conducting polymer with a small molecular acid and you get high conductivity but poor processability. A polymeric acid improves processability, but the conductivity plummets. Yoo *et al.* show that you can have the best of both worlds by using a polymeric acid as the dopant and then performing a post-processing solvent annealing step that substantially improves the conductivity. Polyaniline becomes conductive through proton doping with poly(2-acrylamido-2-methly-1-propanesulfonic) acid. Exposure to dichloroacetic acid (DCA) decreases film roughness by allowing the colloidal particles that form during polymerization to blend, leading to chain conformations with improved charge transport. A somewhat different effect occurs in poly(ethylene dioxythiophene) films doped with poly(styrene sulfonic) acid (PSS). Treatment with DCA increases conductivity as well as surface roughness. The authors attribute this result to disruption by DCA of the insulating surface layer of PSS that forms during spin casting. The DCA-treated films were tested in organic thin-film transistors, solar cells, and light-emitting diodes. In all cases, the treated films showed much better characteristics than the untreated ones. Although the properties did not match those of devices made with indium tin oxide (the current benchmark material), the annealed films could be considered as practical alternatives to a range of metals and metal oxides, especially if cost is a concern. — MSL

Proc. Natl. Acad. Sci. U.S.A. **107**, 10.1073/pnas.0913879107 (2010).

BIOCHEMISTRY

Pain Relief

The endogenous alkaloids of the opium poppy, such as morphine and codeine, have been used as analgesics for several millennia. These compounds and their precursors, especially thebaine, have also been used as the starting material for making semisynthetic opioids, with the aim of creating a less dangerous yet still potent drug. The focal differences are situated at positions C3 and C6: thebaine contains two O-methyl groups, codeine has undergone 6-O-demethylation, and morphine has been denuded of both O-methyl groups. Hagel and Facchini have identified the enzymes responsible for these reactions, thebaine 6-O demethylase (T6ODM) and codeine O-demethylase (CODM), by differential transcript screening against a poppy varietal that is deficient in both morphine and codeine. Both enzymes are members of the α-ketoglutarate/Fe(II)–dependent dioxygenase family, and the mechanism probably involves the insertion of an oxygen into a C-H bond of the methyl group and then elimination of a molecule of formaldehyde. — GJC

Nat. Chem. Biol. **6**, 273 (2010)

EVOLUTION

Structured Differently

Selection may amplify or promote sex-specific differences within a species, and many morphological and behavioral changes have been correlated with differences between the sexes within a species. Li and Merila investigated genome-based sex bias in wild Siberian jays and identified a significant amount of genomic differentiation between males and females. They found that on average, females were more heterozygous than males; that the Z sex chromosome showed greater selection than the autosomes; and that linkage disequilibrium differed between the sexes, with males showing lower levels than females. These data suggest that females and males experience different selective forces, which may either be due to or drive life history traits, such as sex-specific dispersal. — LMZ

BMC Evol. Biol. **10**, 10.1186/1471-2148-10-66 (2010)

CREDIT: ISTOCKPHOTO.COM

www.sciencemag.org

Science

1200 New York Avenue, NW
Washington, DC 20005
Editorial: 202-326-6550, FAX 202-289-7562
News: 202-326-6581, FAX 202-371-9227

Bateman House, 82-88 Hills Road
Cambridge, UK CB2 1LQ
+44 (0) 1223 326500, FAX +44 (0) 1223 326501

SUBSCRIPTION SERVICES For change of address, missing issues, new orders and renewals, and payment questions: 866-434-AAAS (2227) or 202-326-6417, FAX 202-842-1065. Mailing addresses: AAAS, P.O. Box 96178, Washington, DC 20090-6178 or AAAS Member Services, 1200 New York Avenue, NW, Washington, DC 20005

INSTITUTIONAL SITE LICENSES please call 202-326-6755 for any questions or information

REPRINTS: Author inquiries 800-635-7181
Commercial inquiries 803-359-4578

PERMISSIONS 202-326-7074, FAX 202-682-0816

MEMBER BENEFITS AAAS/Barnes&Noble.com bookstore www.aaas.org/bn; AAAS Online Store www.apisource.com/aaas/ code MKB6; AAAS Travels: Betchart Expeditions 800-252-4910, Apple Store: www.apple.com/eppstore/aaas, Bank of America MasterCard 1-800-833-6262 priority code FAA3YU, Cold Spring Harbor Laboratory Press Publications www.cshlpress.com/affiliates/aaas.htm, GEICO Auto Insurance: www.geico.com/landingpage/go51.htm?logo=17624, Hertz 800-654-2200 CDP#343457, Office Depot: https://bsd.officedepot.com/portal_login.do: Seabury & Smith Life Insurance 800-424-9883, Subaru VIP Program 202-326-6417, VIP Moving Services www.vipmayflower.com/domestic/index.html, Other Benefits: AAAS Member Services 202-326-6417 or www.aaasmember.org

science_editors@aaas.org	(for general editorial queries)
science_letters@aaas.org	(for queries about letters)
science_reviews@aaas.org	(for returning manuscript reviews)
science_bookrevs@aaas.org	(for book review queries)

Published by the American Association for the Advancement of Science (AAAS), *Science* serves its readers as a forum for the presentation and discussion of important issues related to the advancement of science, including the presentation of minority or conflicting points of view, rather than by publishing only material on which a consensus has been reached. Accordingly, all articles published in *Science*—including editorials, news and comment, and book reviews—are signed and reflect the individual views of the authors and not official points of view adopted by AAAS or the institutions with which the authors are affiliated.

AAAS was founded in 1848 and incorporated in 1874. Its mission is to advance science, engineering, and innovation throughout the world for the benefit of all people. The goals of the association are to: enhance communication among scientists, engineers, and the public; promote and defend the integrity of science and its use; strengthen support for the science and technology enterprise; provide a voice for science on societal issues; promote the responsible use of science in public policy; strengthen and diversify the science and technology workforce; foster education in science and technology for everyone; increase public engagement with science and technology; and advance international cooperation in science.

INFORMATION FOR AUTHORS
See pages 352 and 353 of the 15 January 2010 issue or access www.sciencemag.org/about/authors

EDITOR-IN-CHIEF **Bruce Alberts**
EXECUTIVE EDITOR **Monica M. Bradford** NEWS EDITOR **Colin Norman**
MANAGING EDITOR, RESEARCH JOURNALS **Katrina L. Kelner**
DEPUTY EDITORS **R. Brooks Hanson, Barbara R. Jasny, Andrew M. Sugden**

EDITORIAL SENIOR EDITORS/COMMENTARY Lisa D. Chong, Brad Wible; SENIOR EDITORS Gilbert J. Chin, Pamela J. Hines, Paula A. Kiberstis (Boston), Marc S. Lavine (Toronto), Beverly A. Purnell, L. Bryan Ray, Guy Riddihough, H. Jesse Smith, Phillip D. Szuromi (Tennessee), Valda Vinson, Jake S. Yeston; ASSOCIATE EDITORS Kristen L. Mueller, Jelena Stajic, Nicholas S. Wigginton, Laura M. Zahn; RESEARCH ASSOCIATE Alexis Wynne Mogul; ONLINE EDITOR Stewart Wills; ASSOCIATE ONLINE EDITORS Robert Frederick, Tara S. Marathe; WEB CONTENT DEVELOPER Martyn Green, Andrew Whitesell; BOOK REVIEW EDITOR Sherman J. Suter; ASSOCIATE LETTERS EDITOR Jennifer Sills; EDITORIAL MANAGER Cara Tate; SENIOR COPY EDITORS Jeffrey E. Cook, Cynthia Howe, Harry Jach, Barbara P. Ordway, Trista Wagoner; COPY EDITORS Chris Filbatreau, Lauren Kmec; EDITORIAL COORDINATORS Carolyn Kyle, Beverly Shields; PUBLICATIONS ASSISTANTS Ramatoulaye Diop, Joi S. Granger, Jeffrey Hearn, Lisa Johnson, Scott Miller, Jerry Richardson, Jennifer A. Seibert, Brian White, Anita Wynn; EDITORIAL ASSISTANTS Emily Guise, Michael Hicks, Patricia M. Moore, Miriam Weinberg; EXECUTIVE ASSISTANTS Alison Crawford, Sylvia S. Kihara; ADMINISTRATIVE SUPPORT Maryrose Madrid; EDITORIAL FELLOW Melissa R. McCartney

NEWS DEPUTY NEWS EDITORS Robert Coontz, Eliot Marshall, Jeffrey Mervis, Leslie Roberts; CONTRIBUTING EDITORS Elizabeth Culotta, Polly Shulman; NEWS WRITERS Yudhijit Bhattacharjee, Adrian Cho, Jennifer Couzin, David Grimm, Constance Holden, Jocelyn Kaiser, Richard A. Kerr, Eli Kintisch, Greg Miller, Elizabeth Pennisi, Robert F. Service (Pacific NW), Erik Stokstad, Jue Wang; INTERN Lauren Schenkman; CONTRIBUTING CORRESPONDENTS Jon Cohen (San Diego, CA), Daniel Ferber, Ann Gibbons, Sam Kean, Robert Koenig, Andrew Lawler, Mitch Leslie, Charles C. Mann, Virginia Morell, Gary Taubes; COPY EDITORS Linda B. Felaco, Melvin Gatling, Melissa Ramondi; ADMINISTRATIVE SUPPORT Scherraine Mack; BUREAUS San Diego, CA: 760-942-3252, FAX 760-942-4979; Pacific Northwest: 503-963-1940

PRODUCTION DIRECTOR James Landry; SENIOR MANAGER Wendy K. Shank; ASSISTANT MANAGER Rebecca Doshi; SENIOR SPECIALISTS Steve Forrester, Chris Redwood; SPECIALIST Anthony Rosen; PREFLIGHT DIRECTOR David M. Tompkins; MANAGER Marcus Spiegler; SPECIALIST Jason Hillman

ART DIRECTOR Yael Kats; ASSOCIATE ART DIRECTOR Laura Creveling; SENIOR ILLUSTRATORS Chris Bickel, Katharine Sutliff; ILLUSTRATOR Yana Greenman; SENIOR ART ASSOCIATES Holly Bishop, Preston Huey, Nayomi Kevitiyagala; ART ASSOCIATES Kay Engman, Matthew Twombly; PHOTO EDITOR Leslie Blizard

SCIENCE INTERNATIONAL

EUROPE (science@science-int.co.uk) EDITORIAL: INTERNATIONAL MANAGING EDITOR Andrew M. Sugden; SENIOR EDITOR/COMMENTARY Julia Fahrenkamp-Uppenbrink; SENIOR EDITORS Caroline Ash, Stella M. Hurtley, Ian S. Osborne, Peter Stern; ASSOCIATE EDITOR Maria Cruz; LOCUM EDITOR Helen Pickersgill; EDITORIAL SUPPORT Deborah Dennison, Rachel Roberts, Alice Whatley; ADMINISTRATIVE SUPPORT John Cannell, Janet Clements, Louise Hartwell; NEWS: EUROPE NEWS EDITOR John Travis; DEPUTY NEWS EDITOR Daniel Clery; CONTRIBUTING CORRESPONDENTS Michael Balter (Paris), John Bohannon (Vienna), Martin Enserink (Amsterdam and Paris), Gretchen Vogel (Berlin); INTERN Tim Wogan

LATIN AMERICA CONTRIBUTING CORRESPONDENT Antonio Regalado

ASIA Japan Office: Asca Corporation, Tomoko Furusawa, Rustic Bldg. 7F, 77 Tenjin-cho, Shinjuku-ku, Tokyo 162-0808, Japan; +81 3 6802 4616, FAX +81 3 6802 4615, inquiry@sciencemag.jp; ASIA NEWS EDITOR Richard Stone (Beijing: rstone@aaas.org); CONTRIBUTING CORRESPONDENTS Dennis Normile (Japan: +81 (0) 3 3391 0630, FAX +81 (0) 3 5936 3531, dnormile@gol.com); Hao Xin (China: +86 (0) 10 6307 4439 or 6307 3676, FAX +86 (0) 10 6307 4358, cindyhao@gmail.com); Pallava Bagla (South Asia: +91 (0) 11 2271 2896, pbagla@vsnl.com)

EXECUTIVE PUBLISHER **Alan I. Leshner**
PUBLISHER **Beth Rosner**

FULFILLMENT SYSTEMS AND OPERATIONS (membership@aaas.org), DIRECTOR Waylon Butler; CUSTOMER SERVICE SUPERVISOR Pat Butler; SPECIALISTS Latoya Casteel, LaVonda Crawford, Vicki Linton, April Marshall; DATA ENTRY SUPERVISOR Cynthia Johnson; SPECIALISTS Shirlene Ha..., Tamika Hill, William Jones

BUSINESS OPERATIONS AND ADMINISTRATION DIRECTOR Deborah Rivera-Wienhold; BUSINESS SYSTEMS AND FINANCIAL ANALYSIS DIRECTOR Randy Yi; MANAGER, BUSINESS ANALYSIS Eric Knott; MANAGER, BUSINESS OPERATIONS Jessica Tierney; FINANCIAL ANALYSTS Prith Pamnani, Celeste Troxler; RIGHTS AND PERMISSIONS ADMINISTRATOR Emilie David; ASSOCIATE Elizabeth Sandler; MARKETING DIRECTOR Ian King; MARKETING MANAGERS Allison Pritchard, Alison Chandler, Julianne Wielga; MARKETING ASSOCIATES Aimee Aponte, Mary Ellen Crowley, Wendy Wise; SENIOR MARKETING EXECUTIVE Jennifer Reeves; DIRECTOR, SITE LICENSING Tom Ryan; DIRECTOR, CORPORATE RELATIONS Eileen Bernadette Moran; PUBLISHER RELATIONS, ORESOURCES SPECIALIST Kiki Forsythe; SENIOR PUBLISHER RELATIONS SPECIALIST Catherine Holland; PUBLISHER RELATIONS, EAST COAST Philip Smith; PUBLISHER RELATIONS, WEST COAST Philip Tsoulakidis; FULFILLMENT SUPERVISOR Iqua Edim; FULFILLMENT COORDINATOR Carrie MacDonald; MARKETING MANAGER Christina Schiechl; ELECTRONIC MEDIA: MANAGER Elizabeth Harman; PROJECT MANAGER Trista Snyder; ASSISTANT MANAGER Lisa Stanford; SENIOR PRODUCTION SPECIALISTS Ryan Atkins, Christopher Coleman; COMPUTER SPECIALIST Walter Jones; PRODUCTION SPECIALISTS Nichele Johnston, Kimberly Oster; DIRECTOR, WEB AND NEW MEDIA Will Collins

ADVERTISING DIRECTOR, WORLDWIDE AD SALES Bill Moran
COMMERCIAL EDITOR Sean Sanders: 202 326-6430
PROJECT DIRECTOR, OUTREACH Brianna Blaser

PRODUCT (science_advertising@aaas.org) MIDWEST Rick Bongiovanni: 330 405-7080, FAX 330-405 7081, EAST COAST/U. CANADA Laurie Faraday: 508 747 9395 FAX 617 507 8189 WEST COAST/W. CANADA Lynne Stickrod: 415-931 9782 FAX 415-520-6940; UK/EUROPE/ASIA Roger Goncalves: TEL/FAX +41 41 43 243 1358; JAPAN ASCA Corporation: Nanako Ide +81 (0) 3 6802 4616, FAX +81 (0) 3 6802 4615, ads@sciencemag.jp; SENIOR TRAFFIC ASSOCIATE Deiandra Simms

WORLDWIDE ASSOCIATE DIRECTOR OF SCIENCE CAREERS Tracy Holmes: +44 (0) 1223 326525, FAX +44 (0) 1223 326532

CLASSIFIED (advertise@sciencecareers.org); U.S.: SALES MANAGER Daryl Anderson: 202 326-6543, MIDWEST Tina Burks: 202 326-6577; EAST COAST 202 326-6543; WEST/SOUTH CENTRAL Nicholas Hintibidze: 202-326-6533, SALES COORDINATORS Rohan Edmonson, Shirley Young, SALES Susanne Kharraz, Dan Pennington, Alex Palmer, SALES ASSISTANT Lisa Patterson; JAPAN ASCA Corporation, Jie Chin +81 (0) 3 6802 4616, FAX +81 (0) 3 6802 4615, careerads@sciencemag.jp; ADVERTISING SUPPORT MANAGER Karen Foote: 202 326-6740 ADVERTISING PRODUCTION OPERATIONS MANAGER Deborah Tompkins; SENIOR PRODUCTION SPECIALIST/GRAPHIC DESIGNER Amy Hardcastle, SENIOR PRODUCTION SPECIALIST Robert Buck; SENIOR TRAFFIC ASSOCIATE Christine Hall

AAAS BOARD OF DIRECTORS RETIRING PRESIDENT, CHAIR Peter C. Agre; PRESIDENT Alice Huang; PRESIDENT-ELECT Nina Fedoroff; TREASURER David E. Shaw; CHIEF EXECUTIVE OFFICER Alan I. Leshner; BOARD Linda P. B. Katehi, Nancy Knowlton, Stephen Mayo, Cherry A. Murray, Julia M. Phillips, David D. Sabatini, Thomas A. Woolsey

AAAS
ADVANCING SCIENCE, SERVING SOCIETY

Russian Launches Baikal Petition

A Russian scientist at Iowa State University has started a petition to save Siberia's Lake Baikal. Evolutionary biologist Dennis Lavrov says he felt "an obligation to speak about it," after Prime Minister Vladimir Putin in January overturned a 2001 ban on disposing of toxic waste in the lake Russia calls the "Sacred Sea."

The change allows the Baikalsk Pulp and Paper Mill, which closed in 2008 after 42 years when it couldn't comply with the ban, once more to dump its waste, including cancer-causing dioxins, into the largest, deepest, and oldest freshwater lake in the world.

The online petition to President Dmitry Medvedev is intended "to show that international scientists recognize the danger of the mill … [and] emphasize the importance of Lake Baikal to the whole world rather than just to Russia," says Lavrov. The lake is "truly a globally unique resource," says Steve Kallick, project director of the Pew Environment Group's International Boreal Conservation Campaign in Seattle, Washington, because of its relative isolation, diverse ecosystem, and well-studied fossil record.

Lavrov says for scientists in his homeland, "being in Russia limits their ability to speak openly about the issue." An environmental group that has campaigned to keep waste out of Lake Baikal reported that it was raided in February by Russian police. As of last week, the petition (http://www.ipetitions.com/petition/baikal/) had 476 signatures from scientists and graduate students, including about 20 (some of them "anonymous") from individuals in Russia

MEN FOR MARS

If six men are crammed into a space capsule for 520 days, will they go crazy? Candidates are now competing to help answer that question.

There's no crewed voyage to Mars in the offing, but the joint Russian-European Mars500 project is on track for a simulated year-and-a-half roundtrip to, and a 3-week field trip on, the Red Planet. Six men will enter a capsule this summer at the Russian Institute for Biomedical Problems (IBMP) in Moscow. Nine candidates are currently training in Russia. The final crew, to be announced in May, will comprise three Russians, two Europeans, and either a Chinese or another Russian.

Relaxation in isolation.

Astronauts who venture beyond the protection of Earth's magnetic field must dive behind protective shields periodically to avoid deadly blasts of radiation from solar flares. Otherwise, the daily routine is similar to life aboard a ship: 8 hours each of work, recreation, and sleep. Work includes medical tests, growing vegetables in the greenhouse, and mandatory exercise. Recreation includes the use of an onboard sauna. Unlike Russian cosmonauts, the crew won't be allowed cocktails.

Six men have already successfully endured a 105-day version of the experiment last year. There was only one problem: European-style freeze-dried fare "did not match the Russian taste for food, which at the end led to some weight loss in some of the Russian crew members," says project manager Jennifer Ngo-Anh.

Toning Down the Warming Alarm

The ripple effect of "Climategate" has caught up with London's Science Museum, which is planning a neutral tone for its £4 million climate exhibit to open in November.

Last year, in the run-up to the Copenhagen Climate Summit, the museum had an exhibit called "Prove It! All the evidence you need to believe in climate change."

Now, the museum is soft-pedaling the "change" part. "The focus has shifted to climate science as public trust in science has declined,"

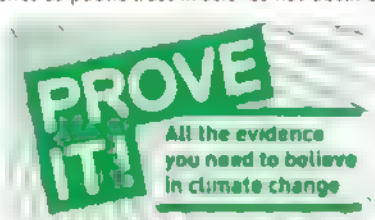

says museum spokesperson Kerry Law, who acknowledges that the "Prove It!" exhibit "did provoke a strong reaction from climate change deniers."

So the museum will present just climate facts in its new climate science gallery and not jump to any alarming conclusions. "It's our job to supply an enjoyable, informative experience," says museum Director Chris Rapley, a climate scientist who has spoken on the potential dangers of global warming. "We're a museum for everybody; … people don't like being told what to think."

Yamanaka Honored Once Again

Last year, it was the Lasker Award. This year, Shinya Yamanaka has collared the $250,000 March of Dimes Prize for his development of induced pluripotent stem (iPS) cells. Yamanaka, 47, currently divides his time between Kyoto University in Japan and the J. David Gladstone Institutes at the University of California, San Francisco. Rapidly evolving iPS cell technology not only potentially eliminates the need to destroy human embryos for stem cells; it also has, in effect, democratized the field by making it possible for any cell biologist to work with pluripotent human stem cells. The prize will be awarded at a ceremony in Vancouver, Canada, on 3 May.

CREDITS (TOP TO BOTTOM): SOURCE: IBMP; SOURCE: SCIENCE MUSEUM/LONDON. CENTER FOR IPS CELL RESEARCH AND APPLICATION (CIRA)/KYOTO UNIVERSITY

Commerce swamps conservation 26

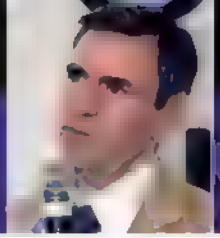

Q&A with head of new climate service 29

CLIMATE STUDIES

'Asilomar 2' Takes Small Steps Toward Rules for Geoengineering

PACIFIC GROVE, CALIFORNIA—Meeting in 1975 at a leafy retreat center here by the sea, molecular biologists grappled with how to unlock the secrets of recombinant DNA without creating infectious, runaway bioagents. Their successful deliberations laid the groundwork for a regulatory framework that allowed research—and ultimately the biotech industry—to flourish.

Last week, nearly 200 experts in geosciences and other scientific and policy disciplines met here to confront a new kind of risky research: large-scale geoengineering projects aimed at countering the buildup of greenhouse gases in the atmosphere. And although the climate scientists may have accomplished less in a week than did their biologist forebears, they did make progress. The conference organizers declared that geoengineering research is "indispensable" but said that it should be done with "humility." Governments and the public should work together to decide what schemes are "viable, appropriate, and ethical," the statement added. Cuts in greenhouse emissions should be a priority, it said, mirroring statements by the American Geophysical Union and the U.K. Royal Society.

Most conferees believe the possibility of climate tipping points has placed geoengineering on the global agenda. And so last week's meeting—The Asilomar International Conference on Climate Intervention Technologies, or Asilomar 2, as it was dubbed—was driven both by fears of climate catastrophes and the potentially dangerous steps that scientists or politicians might take to avert them. It was "a meeting … we all wished was not necessary," conference organizer Margaret Leinen of the Climate Response Fund in Alexandria, Virginia, told the participants.

Leinen's organization was formed last year to fund geoengineering research projects, which fall into two broad categories. The first involves efforts to block the sun's rays, using techniques such as spraying aerosols in the upper atmosphere or brightening clouds with sea salt. The second approach aims to remove carbon from the atmosphere by means of schemes such as growing algae blooms in the ocean. The conference even coined separate phrases for the two activities: "Climate intervention" describes the sun-blocking methods, and "carbon remediation" covers the CO_2-sucking methods.

Two ways to geoengineer. High-altitude planes (*above*) might help study "climate intervention" techniques whereas CO_2-suckers (*right*) involve "carbon remediation."

As the fund began to hit up potential donors, however, several said that the nascent field needed a set of ethical ground rules before practitioners developed research plans. As a result, the goals of last week's meeting were both specific and ambitious: Set up voluntary guidelines for a host of geoengineering methods that had never been deployed on a large scale, or in some cases in any setting outside the lab.

Sobered by such broad societal responsibilities, participants spent a good deal of time discussing research ethics and the geopolitical implications of geoengineering. "I'd expected hubris but didn't find it. No one seemed anxious to get on with geoengineering," said Paul Craig of the Sierra Club. Indeed, Princeton University energy expert Robert Socolow struck a cautionary note by presenting various "nightmares" for his audience to consider, from a rogue state using geoengineering before it was understood to having "all the [world's] climate scientists working on geoengineering."

Although the effects of geoengineering studies might be felt across broad swaths of the planet, they also necessarily affect individuals. Several speakers cited approvingly the approach taken by biomedical researchers: the need for informed consent, a balancing of the benefits and risks to humans, and the appropriate selection of research "subjects."

But that model breaks down at some point because the risks involved in geoengineering are so different from those in medical research. Individual patients may die if a drug trial goes bad. Geoengineering experiments, in contrast, could have wide-ranging and highly uncertain environmental effects, noted earth scientist Jane Long of Lawrence Livermore National Laboratory in California.

That broader scope fed fears of restrictive regulations. And participants worried that those rules could be triggered even by very tiny interventions, such as a much-discussed project off the Scottish coast to spread small

CREDITS (TOP TO BOTTOM): NASA PHOTO/CARLA THOMAS; CARBON ENGINEERING

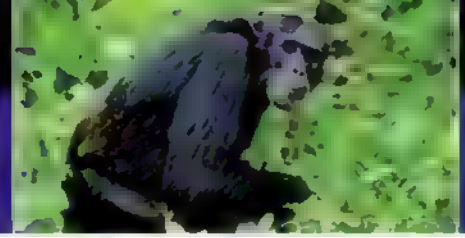

quantities of sea salt into the air and study their cloud-whitening effects.

The meeting also featured five breakout groups that focused on drafting research guidelines for the various kinds of approaches. What level of involvement by governments is appropriate? What role should the military or private companies play? A breakout group devoted to the idea of blocking sunlight, for example, struggled over whether for-profit companies should be barred from the enterprise to ensure maximum "transparency."

Given all the conferees were asked to take on, it's not surprising that many loose ends remained as they headed home. (The 14-hour days drew few complaints—"I had no one ask that we meet less and go walk on the beach," marveled scientific organizing committee chair Michael MacCracken of the Climate Institute, which co-sponsored the meeting.) The final statement was approved by the 13-member organizing committee, for example, although MacCracken hopes to gather signatures from all of the participants over the next few weeks. In addition, the breakout groups are still massaging suggestions on voluntary guidelines for specific geoengineering approaches.

Reflecting the feeling that the meeting was only a start, some participants dubbed it "Asilomar 2.1" as a sign that more meetings would be needed. But everyone seemed optimistic that the answers would eventually provide a solid foundation for the fledgling—if frightening—field. "Asilomar 3 will be in another 30 years, for the next discipline," predicted Socolow

–ELI KINTISCH

ECOLOGY

Madagascar's Forests Get a Reprieve—But for How Long?

Conservation biologists are cautiously celebrating a victory in the effort to pull Madagascar's unique biota back from the brink of extinction. Last week, after months of pressure from scientists, conservation groups, and foreign diplomats, Madagascar's military rulers announced a ban on the logging and exportation of rosewood, a commodity from a threatened ecosystem. Logging of rosewood was banned before but resumed after a military coup toppled Madagascar's science-friendly government a year ago and relaxed controls (*Science*, 27 March 2009, p. 1654). By decree on 24 March, the military government reversed its decision of 6 months earlier.

The government decree has cheered ecologists who have heard only bad news from Madagascar for the past year. "We made it," says Lucienne Wilmé, editor of *Madagascar Conservation & Development*. But now, she says, the challenge is to ensure that the rosewood ban is enforced.

Madagascar has 43 species of rosewood trees—all but one of which exist nowhere else—and thousands of endemic plant and animal species that depend on them. One such species is the silky sifaka, a lemur. It is one of the rarest mammals on Earth, found only in Madagascar's northeastern rosewood forests, where loggers are encroaching.

Conservation in Madagascar has never been easy, says Brian Fisher, an entomologist at the California Academy of Sciences and director of the Madagascar Biodiversity Center in Madagascar's capital, Antananarivo. Inhabitants of the California-sized island are among the poorest in the world. They have stripped more than 90% of the forests for agriculture and charcoal. Since the coup, most foreign aid to the country has been frozen and eco-tourism has plummeted, worsening poverty.

In the months after the regime's relaxation of restrictions on the hardwood trade in September 2009, researchers watched helplessly as Madagascar's forest reserves were plundered. "First come the loggers," says Fisher. After the loggers cut down trees, "the next victims are the lemurs, as [loggers] set up lemur traps to feed themselves and to sell locally for cash."

If it stopped there, says Fisher, "these forests might recover." But what comes next is far more destructive: The vegetation is cleared to the ground, and "the door is now open for settlers." In the middle of the northeastern Ambatovaky Reserve, a government official "has built his home out of rosewood and moved in 60 cattle," says Fisher. "If the land grab continues another year, there will be nothing left of what was once the most beautiful, species-rich lowland forest in Madagascar."

"The northeast is a precious area, and it is being hit very hard right now," says Anne Yoder, director of the Duke Lemur Center in Durham, North Carolina, but it's not the only place. Data gathered by Meredith Barrett, Yoder's Ph.D. student at Duke University, reveals that other rosewood forests across the country are in danger. Rosewood is particularly sensitive, says Barrett, ▶

Tree tragedy. One year after a bloody military coup in Madagascar, logging of endangered rosewood forests in formerly protected areas is rampant.

CREDIT: COURTESY OF STUART PIMM

- Manual dispensing

- Electronic dispensing

- Positive displacement tips

30 years of experience

Performing for excellence

Serial dispensing at its best: Multipette®/Repeater®

The Eppendorf Multipette/Repeater handheld dispensing system offers an outstanding range of benefits:

Together with Combitips plus®, both the electronic and manual hand dispenser, offers automatic tip recognition combined with an automatic volume calculation.
The positive displacement system ensures high-precision dispensing for all kinds of liquids including volatile and viscous solutions. 9 different sizes of tips offer a volume-range from 1 µL – 50 mL.

Easy volume setting
- Multipette/Repeater plus: 1 µL – 10 mL
- stream/Xstream: 1 µL – 50 mL

Up to 100 dispensing steps without stopping
- Multipette/Repeater plus:
  20 different adjustable volumes per tip
- stream/Xstream:
  1,000 different adjustable volumes per tip

For more information visit **www.eppendorf.com/mpplus**
or **www.eppendorf.com/mpxstream**

eppendorf
In touch with life

Your local distributor www.eppendorf.com/worldwide **Application Support** E-mail: support@eppendorf.com
Eppendorf AG Hamburg Germany Tel. +49 40 538 01-0 Eppendorf North America, Inc. USA Tel. +1 800 645 3050 menu option 2

because "it is slow-growing and also grows at a very low density." Populations of rosewood could go extinct locally in a matter of "months or years," she says. To be more exact she needs more data.

But studying Madagascar's forests has become dangerous. Fisher says visitors are sometimes threatened by organized criminal loggers. During his recent survey of the northeastern forests, he says, "we had to monitor our food for possible poisoning." He found only a single unpaid ranger "confronting the lemur trappers and loggers. . . . His life is continually threatened."

Will the new rosewood logging ban reverse the damage? "Given this government's track record, I would be surprised if they actually enforce the decree," says Yoder. She says it is likely "a PR move" to placate international aid donors. Rosewood exportation remains temptingly lucrative. Edelin Calixte Randriamiandrisoa, a former army officer who is now Madagascar's Minister for the Environment, declined to comment. Still, the ban is undeniably "good news," says Yoder. "The government is obviously beginning to feel the international heat." But she says the international community needs to move quickly.

"The next and best step" is to protect all of Madagascar's rosewood trees as threatened species under Appendix III of the International Convention on International Trade in Endangered Species of Wild Fauna and Flora (CITES). Nine of Madagascar's rosewood species are already listed as endangered. But once the trees are reduced to logs, "identifying specific species is next to impossible" without a DNA test, says Erik Patel, a lemur biologist at Cornell University. So all of Madagascar's rosewood trees would need equal protection, he says.

Madagascar could call for protection of its rosewood unilaterally under Appendix III of CITES. If it doesn't, the next chance to propose global protection of rosewood will be at the 2011 meeting of the CITES Plants Committee in Geneva, Switzerland. But if the 2 years go by without enforcing the logging ban, says Barrett, "then the outlook does not appear good." **–JOHN BOHANNON**

ScienceNOW

From *Science*'s Online Daily News Site

Could Tiny Bubbles Cool the Planet?

In an effort to curb global warming, scientists have proposed everything from launching sunlight-blocking dust into the stratosphere to boosting the amount of carbon-sucking algae in the oceans. Now, a Harvard University physicist has come up with a new way to cool parts of the planet: pump vast swarms of tiny bubbles into the sea to increase its reflectivity and lower water temperatures. http://bit.ly/microbubbles

Murder or an Accident? The Brain Knows

If a stranger steps on your foot, you'd probably shrug your shoulders and assure him that no harm has been done. But if that stranger instead takes a swing with his fist, most people are unlikely to be so forgiving. Researchers now believe they've demonstrated which part of the brain gauges another person's motives, a find that could lead to a greater understanding of Asperger syndrome and other autism spectrum disorders. http://bit.ly/moraljudgement

Toward Liquid-Cooled Computers

Tired of the dust bunnies sucked into your computer's air-intake grill? Experts say a new technique called superwicking could provide a better way to cool computer hardware and could help remove one of the biggest barriers to a new generation of high-powered microprocessors. And in the meantime, it could prove a boon to tiny fluid-based sensors. http://bit.ly/coolcomputers

First Motion-Powered Nanodevices

Someday soon, simply walking with your iPod in your pocket could keep it charged, and the lub-dub of your heart could power a portable blood-pressure sensor. These innovations might be based on flat, paper clip–sized "nanogenerators," unveiled in a new study, that pump out the same voltage as a AA battery when they are squeezed, bent, or shaken. http://bit.ly/nanodevices

Read the full postings, comments, and more on **news.sciencemag.org/sciencenow.**

ScienceInsider

From the *Science* Policy Blog

The most controversial patents in biotechnology—covering **breast cancer genes *BRCA1* and *BRCA2***—were declared invalid this week by a U.S. district court. http://bit.ly/diZOey

Cold Spring Harbor Laboratory has sued its law firm, claiming that the patent application it submitted for discoveries in RNA interference contains "extensive portions" of material from another scientist's patent application. http://bit.ly/c67Wf7

Britain's Labour government provided **additional support to universities** for training science and engineering majors and backed construction of a London biomedical center in a new budget that largely marks time before the country's general election later this spring. http://bit.ly/aDBApl

U.S. Energy Secretary Steven Chu has steamed to the rescue of one of his flagship research programs less than a week after a congressional spending panel reiterated its confusion over the **large, multiyear energy hubs** in the department's 2011 budget. http://bit.ly/a7cd4p

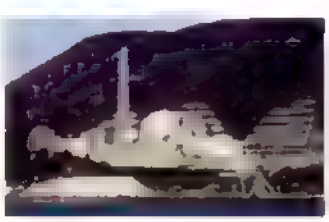

A thumbs-up this spring by the host prefecture would allow Japan's **Monju experimental fast-breeder reactor** to resume operations after a 14-year delay. http://bit.ly/ci954m

Britain's new "Principles for the Treatment of Independent Scientific Advice" have stirred controversy by suggesting that **scientific advisers be required to "maintain the trust"** of politicians. http://bit.ly/bbmoiA

For the full postings and more, go to **news.sciencemag.org/scienceinsider.**

CREDITS (TOP TO BOTTOM): HEMERA/THINKSTOCK; JAPAN ATOMIC ENERGY COMMISSION

Market forces. Japan prevented a trade ban in Atlantic bluefin tuna, which is sliced up for sushi.

CONSERVATION BIOLOGY

Trade Trumps Science for Marine Species at International Meeting

It was all about the money, not the science. So say environmentalists and conservation biologists reeling from a remarkable number of setbacks for wildlife conservation at a major international meeting that wrapped up last week in Doha, Qatar. There were a few victories for land animals—most notably, elephants (see sidebar)—but not so for marine species, which were the focus of most high-stakes proposals at the Convention on International Trade in Endangered Species of Wild Fauna and Flora (CITES). "It's been a complete disaster for the oceans," says Elizabeth Griffin of the advocacy group Oceana in Washington, D.C. The reason: Despite evidence for serious population declines, countries that profit from international trade in these species lobbied hard to keep it unfettered.

Set up by international treaty in 1975, CITES has banned the commercial trade of nearly 900 species, such as gorillas and rhinoceroses. But marine conservation advocates faced a tough challenge in adding several marine species to the list. They suffered one defeat after another. Proposals by the United States and Palau to regulate trade of three species of hammerhead sharks and the oceanic whitetip shark were narrowly rejected. "This decision is a major loss for marine conservation," said Tom Strickland, head of the U.S. delegation, in a statement. As many as 73 million sharks are killed annually for their fins, according to a 2006 global study in *Ecology Letters*, and some populations have declined by up to 99%. A proposal to regulate two other species of shark, spiny dogfish and scalloped sharks, was also a non-starter. The only shark proposal that was accepted, to regulate the less valuable porbeagle, was overturned on the final day.

The highest stakes battle was for Atlantic bluefin tuna, whose populations have dropped by 85% since the mid-1970s. This species makes up just a fraction of the overall tuna trade, but it is the most highly prized for its fatty taste. Most of the global catch is imported for sushi or sashimi in Japan. A single 200-kilogram fish can sell for more than $100,000 at auction. Several scientific panels, including CITES's own, have concluded that a trade ban is warranted.

But Japan lobbied hard to defeat the proposal by Monaco. On 18 March, the proposal didn't even get a majority of votes, let alone the two-thirds required for a ban. "It was a big surprise how badly it failed," says Ellen Pikitch of the Institute for Ocean Conservation Science at Stony Brook University in New York state. The Japanese delegation didn't dispute that the species is in trouble but maintained that conservation is better handled by an international fisheries-management organization, the International Commission for the Conservation of Atlantic Tunas (ICCAT). Skeptics point out that illegal fishing continues, and ICCAT in the past has not cut fishing quotas as much as its scientific advisers have recommended for recovery of the population, although last November quotas were set at the upper end of the range.

If there is a bright side for tuna from the convention, say several advocates, it's that all the media attention could force ICCAT member countries to finally agree to cut fishing quotas much more sharply. "The strategy has to be hold their feet to the fire," says Susan Lieberman, deputy director of international policy for the Pew Environment Group in Washington, D.C. ICCAT

Ivory Ban Upheld

One of the biggest successes of the Convention on International Trade in Endangered Species of Wild Fauna and Flora (CITES) was the 1989 trade ban on ivory from African elephants, which quickly reduced poaching. Some countries have occasionally asked for permission to sell stockpiles of ivory collected from dead elephants, but many scientists object to these sales because analyses suggest that it encourages poaching (*Science*, 12 March, p. 1331).

Last November, Tanzania and Zambia proposed selling elephant ivory. A majority of CITES delegates at last week's meeting in Doha rejected both proposals. "It was a relief," says conservation biologist Samuel Wasser of the University of Washington, Seattle. At a side event before the vote, Wasser and other scientists presented new data about seizures of illegal ivory and questioned whether elephant populations were as healthy as Tanzania and Zambia claimed.

–E.S.

CREDIT: AFP PHOTO/JIJI PRESS/NEWSCOM

Chair Fabio Hazin told CITES delegates he expects that efforts to help bluefin recover would be strengthened when ICCAT meets in November.

Japan, for its part, vowed to work harder. Masanori Miyahara, who led the Japanese delegation, told Agence France-Presse last week that his country has "made the commitment to ensure the recovery of the stock with specific measures and restrictions." Although some advocates remain skeptical, Carlos Drews of the World Wildlife Fund International is among those taking Japanese officials at their word. "I'm starting to believe that they will get the ball rolling."

Still, Drews says he and his colleagues have learned a lesson from Japan's efforts. Start early, lobby hard, have a simple message. Even though economics and politics trumped conservation in Qatar, advocates say that their key weapon remains the data about the species' status. "You have to keep pushing the science," says Lieberman, "or you'll lose one species after the next."

–ERIK STOKSTAD

OTHER CITES DECISIONS

- ✓ Regulate trade of five tree frogs
- ✓ Regulate trade of a Bolivian beetle B
- ✓ Regulate trade of seven Madagascan plants
- X Regulate trade of 31 red and pink corals
- X Ban trade of polar bears
- X Ban trade of ornate spiny-tailed lizard

Tradeoffs. Proposals for less economically valuable species, such as tree frogs, fared better.

PHYSICS

Thought Experiment Torpedoes Variable-Speed-of-Light Theories

Physicists' best chance of spotting an effect of "quantum gravity"—the melding of quantum mechanics and Einstein's theory of gravity—may have evaporated. According to some quantum-gravity theories, the speed of light may change very slightly with the light's wavelength, and experimenters are searching for the effect in radiation from distant stellar explosions. Those searches may be in vain, however. If light's speed varied in this way, then untenable paradoxes would arise, one theorist argues. The speed variations must be at least 23 orders of magnitude smaller than experimental limits set last year, she says.

"It's incredibly hard to find an observable effect of quantum gravity, so I'm a little bit sorry about the result," says Sabine Hossenfelder of the Nordic Institute for Theoretical Physics in Stockholm. Some theorists say that subtle quantum-mechanical effects may avert the paradox, however.

The debate centers on a decade-old idea known as DSR—for "doubly special relativity" or "deformed special relativity." DSR attempts to reconcile Einstein's theory of special relativity—which says the speed of light is the same for all observers, even if they're moving relative to one another—with the possibility that the speed of light also depends on its wavelength. Such a dependence had been suggested by theories of "noncommutative geometry" and emerges from some theories of "loop quantum gravity" (*Science*, 8 November 2002, p. 1166).

Experimenters have already started looking for speed variations in light from cosmic firecrackers called gamma-ray bursts. Last year, NASA's orbiting Fermi Gamma-ray Space Telescope spotted a burst 10 billion light-years away and found no significant difference in speed between the low- and high-energy photons from it. From their results, Fermi researchers put a limit on the maximum delay experienced by the most energetic photon of 0.859 seconds, as they reported in November in *Nature*. That's roughly the size of the effect one might expect to see from DSR.

However, any delay must be far smaller, Hossenfelder argues in a paper in press at *Physical Review Letters*. She considers the following scenario: A high-energy photon from a gamma-ray burst arrives in the lab at the same time as a lower-energy electron from a source across the street. The photon collides with the electron and ricochets into a particle detector, which triggers a bomb set up by a self-destructive scientist. Boom!

Hossenfelder then considers how this scenario would appear to an astronaut gliding over the lab in a spacecraft headed toward the gamma-ray burst. To the astronaut, the photon's wavelength appears slightly shorter because of the Doppler shift. As a result, according to DSR, the photon travels more slowly and arrives at the lab after the electron has come and gone, and the bomb is never triggered. So the scientist in the lab and the astronaut in the spacecraft cannot agree on whether the bomb goes off, a paradox that undermines our sense of a unified reality. Hossenfelder contends that the paradox rules out any theory in which light's speed varies in simple proportion to its energy.

Developers of DSR aren't ready to concede the point, however. Hossenfelder assumes too simply that spacetime is like a smooth paper on which objects' paths cross at well-defined points, says Giovanni Amelino-Camelia, a theorist at the University of Rome La Sapienza. But on the smallest scales, spacetime should be a roiling "quantum foam" in which position and time lose precise meaning, he says. "In quantum spacetime, you don't have points," he says. Lee Smolin of the Perimeter Institute for Theoretical Physics in Waterloo, Canada, agrees that the effects of quantum spacetime may resolve the paradox and says he's studying the matter.

For their part, researchers with the Fermi satellite will continue to look for an effect, says Sylvain Guiriec, an astrophysicist at NASA's Marshall Space Flight Center in Huntsville, Alabama. "It's definitely ongoing work for the Fermi collaboration," he says. However, the chances of seeing a signal seem much smaller now.

–ADRIAN CHO

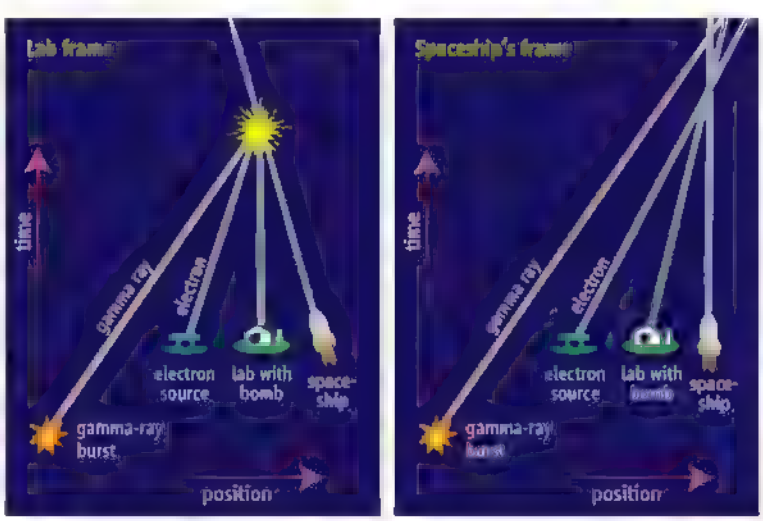

Hit or miss. If light's speed varies with its wavelength, then a scientist in the lab (*left*) and an astronaut passing in a spaceship will not agree whether a photon and an electron reach the lab at the same instant to trigger an explosion.

CREDIT: ADAPTED FROM SABINE HOSSENFELDER, PHYS. REV. LETTERS

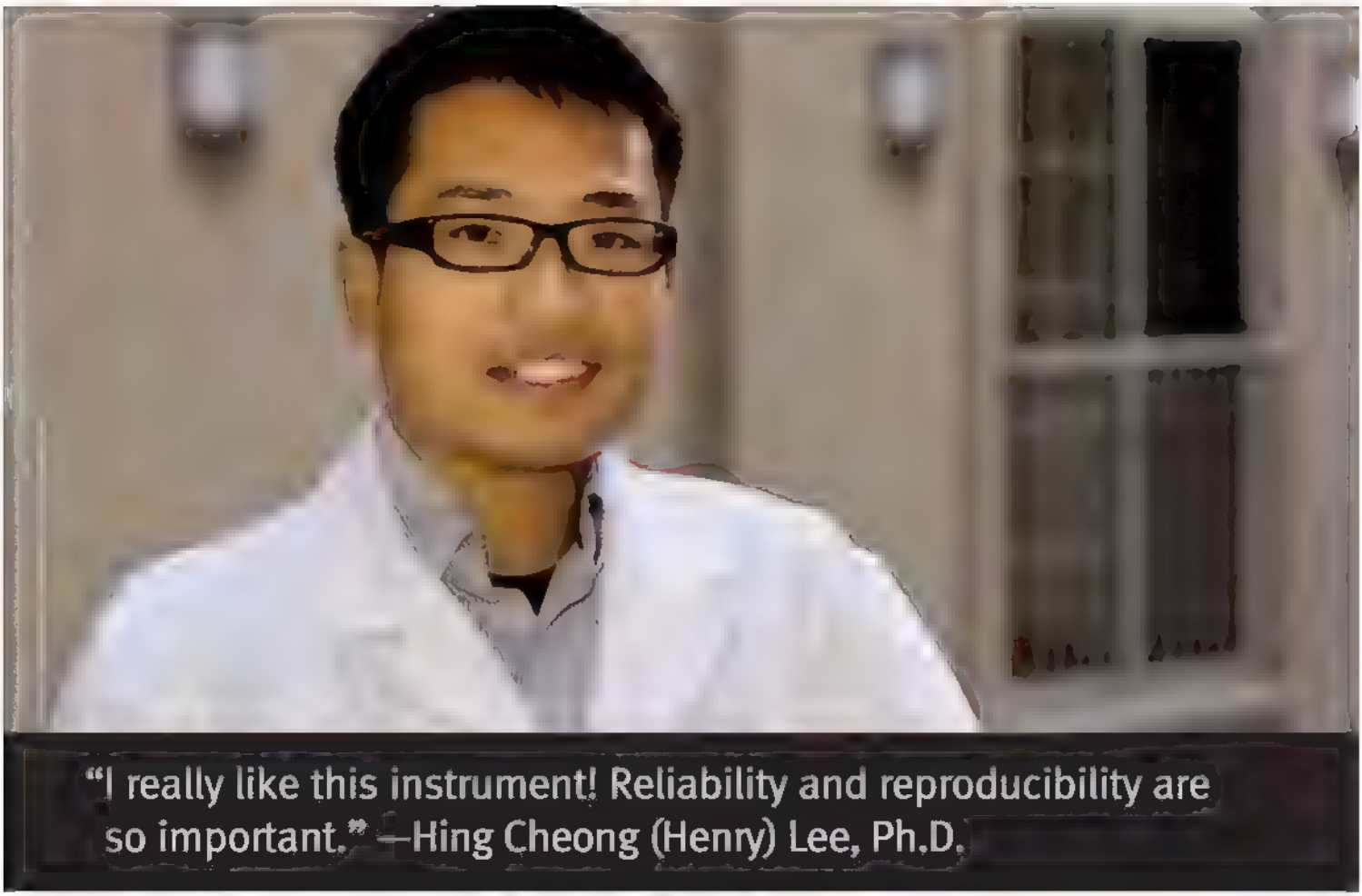

Emotional reactions to instrumentation from scientists are rare. Yet with Thermo Scientific NanoDrop Spectrophotometers, they are becoming commonplace. That's because scientists who own a NanoDrop™ are passionate about its simplicity. These instruments reduce analysis time and minimize sample waste with fast, easy and accurate micro-volume nucleic acid and protein sample quantitation. Just ask Dr. Lee:

"With NanoDrop I use less sample. Reproducibility of results is much higher—and I get them in a few seconds. The previous machine I used to measure DNA took much longer, and the results weren't nearly as reliable. NanoDrop is much faster. It is small, quick and convenient."

"NanoDrop is quick and gives you reproducible results every time."

Try any NanoDrop instrument for free:* www.thermo.com/nanodrop

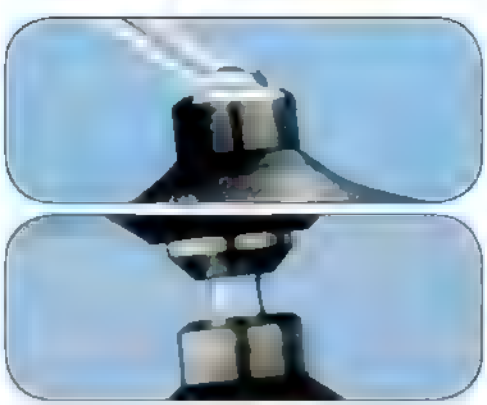

Thermo Scientific NanoDrop UV-Vis Spectrophotometers offer easy, reliable micro-volume analysis, with sample size as low as 0.5 µl and measurement time of less than 5 seconds—no dilutions.

Moving science forward

Thermo SCIENTIFIC

Part of Thermo Fisher Scientific

NEWSMAKER INTERVIEW

NOAA's Tom Karl Takes On Task of Serving Up Climate to the Public

The public conversation about climate could use some help. Hacked e-mails, charges of manipulation and suppression of the data, and plunging public trust in climate scientists are hindering the dialogue.

Last month, the U.S. National Oceanic and Atmospheric Administration (NOAA) announced a step that could help repair climate science's image by doing for climate what the National Weather Service (NWS)—a NOAA organization—has done for weather over the past 140 years. The vehicle is the new NOAA Climate Service (NCS). Like NWS, it will issue forecasts of changing atmospheric conditions for use by the government, business, and the public. But the forecasts will be for larger U.S. regions and longer time scales. In addition, it will predict the impacts of climate change.

The climate service is the product of a reorganization involving three data centers, two research laboratories, and a climate observing network. No new funding is involved. Climatologist Thomas Karl, currently director of NOAA's National Climatic Data Center in Asheville, North Carolina, is its interim director.

Karl has worked at the climate center the world's largest climate archive—since 1980, and led it since 1998. That job has put him in the thick of assessing and disseminating information on climate science. "He's about as straight-up a scientist as I know [and] extremely open-minded," says paleoclimatologist Michael Mann of Pennsylvania State University, University Park. In the 1990s, Mann notes, "Tom's work was often cited by climate skeptics in support of their arguments. As observations increasingly pointed to the reality of climate change, he lost favor with the skeptics."

Karl spoke with *Science* on 18 March. Here is an edited version of his comments.

–RICHARD A. KERR

CREDIT: NOAA

Speaking of climate. Thomas Karl is interim head of the new NOAA Climate Service.

Q: What kind of services will NCS provide?

T.K.: There's a clear history [at NOAA] of strong engagement with the science of climate change and variability. We want to build on that science to provide information about how climate is likely to evolve, as best supported by the science. We'll be trying to understand what users need to make decisions. For example, we've got a lot of information on global sea-level issues. But people are asking, what about my town on the coast? This climate service can take this global information—on models, storms, currents, tides, bathymetry, extreme precipitation events—and make it relevant down to beachside.

Q: Even the Nobel Prize–winning Intergovernmental Panel on Climate Change has stumbled when conveying climate information to decision-makers. How will NCS avoid such pitfalls?

T.K.: There are some principles and guidelines we're going to use. One is transparency. As has been our practice, all the raw data, all the observations, the algorithms, and the peer-reviewed papers that we use to generate products are going to be accessible online. In addition, it will be important for the NCS to communicate in a more effective way than has been done in the past.

Q: Will NCS be able to respond to ongoing climate change and variability as quickly as NWS?

T.K.: People are trying to see how ongoing climate and weather extremes relate to longer term changes in climate. Such events offer opportunities for teaching. The NCS can say whether or not the events are consistent with how climate may change in the future. Sometimes we may be able to say which specific events have contributions from humans; sometimes we won't.

Q: Climate prediction on the global scale is tough enough. How will NCS manage it on the even more challenging regional scale?

T.K.: There are a couple of thrusts, and they have to go together. Models are critical, but there are important pieces often left out of the models: land use changes, ocean circulation, sea ice, biogeochemistry, land ecology. All these pieces have been worked on but not yet put together in an Earth system model; we're trying to make climate models more physically realistic. But no matter how good the models get, we have to understand the uncertainties coming from the models and tailor that information to the regional level.

Q: AccuWeather and The Weather Channel translate and repackage NWS products for the public. Do you expect private entities to enter the climate arena, too?

T.K.: There's so much that needs to be done in the climate arena, there's no conceivable way the federal sector will be able to address all of it. Working with the corporate world, we'll develop guidelines to make sure that [the private sector] can provide the appropriate value added, the information needed for people to act: how to use the data, the forecasts, the projections. If someone can do it on a for-profit basis just as well or better, that's a sign we don't have to.

Q: What's needed to achieve a fully functioning National Climate Service?

T.K.: That discussion is still going on with the [President's] Office of Science and Technology Policy and all [13] of the U.S. Global Change Research Program agencies and departments. Interagency agreements will continue to be an important tool. Discussions we've been having on how to deliver information to the next National Climate Assessment—that is, working on a common product—is really an important tool to better coordination.

In the Shadow of Jane Goodall

Fifty years after Goodall arrived in Gombe, the environment has changed dramatically for both our closest relatives and the scientists who study them

AFTER COMPLETING A MASTER'S DEGREE on banded mongooses in 1999, behavioral ecologist Emily Otali decided to stay at Makerere University in Kampala to pursue a Ph.D. She won a fellowship, which stipulated that she had to study the impact of forest destruction on blue monkeys. "I didn't like it," remembered Otali during a reporter's May 2008 visit to Uganda. The blue monkeys in question were not habituated to humans, so she thought she would get at best sketchy data from her 18 months of fieldwork; she preferred to continue her work on mongooses. She repeatedly complained about this to a documentary producer she was then working with on what would become the National Geographic video *Mongoose Murders*. One day when they were in the field at Queen Elizabeth National Park, he happened to spot Richard Wrangham, a primatologist at Harvard University who co-directs a research project on habituated chimpanzees in Uganda's Kibale National Park. "He dragged me to Professor Wrangham," Otali recalled.

Wrangham had been on the committee that selected Otali for the fellowship, and he recognized her name. Otali, who has a habit of cutting to the point, asked him why he and the other committee members forced her to study blue monkeys. Wrangham had an idea: Why didn't she come to Kibale for a day and see if chimpanzees interested her more? "Is there anything left to study in chimps?" replied Otali, who is a native of Uganda but had never seen chimps in the wild. "I hear Jane Goodall has been doing this all her life."

Wrangham, who began his own career working with Goodall in Gombe in 1970, at first just stared at her. "There's so much to do in chimps," he said

Otali remained skeptical. "I thought nothing was going to take my heart away from mongooses," she said.

Nevertheless, she made the trip to Kibale, and it was, by her account, a boring day of "chimping." She observed just one infant, Ipassa, and her mother, and none of the other 50 chimps that live together in that part of the park. But one small incident had an indelible impact on her: She locked eyes with Ipassa. "Of course you're told not to make eye contact with chimps, but I stole that moment," she says. "It changed everything. I wanted to know more about these creatures that were so like me."

Otali went on to earn her Ph.D. at Kibale, studying the social dynamics of that chimp

Online
sciencemag.org
Podcast interview with author Jon Cohen

CREDIT: MALCOLM UNTON

community. She was the first woman in Africa to earn a doctorate studying our closest relatives. Wrangham later appointed her to be the field manager of their Kibale study

The new breed

Otali is one of dozens of a new crop of chimpanzee investigators *Science* met during the past 3 years in Africa, Europe, the United States, and Japan. They come from a variety of academic backgrounds and are pursuing diverse questions in both wild and captive chimps. But most share a powerful bond with their research subjects—sometimes too strong—and a conviction that studying our closest relatives provides unique insights into human evolution. "It's amazing staying with these animals and trying to understand what they think," says Paco Bertolani, a Ph.D. candidate at the University of Cambridge in the United Kingdom who is doing research in Kibale (p. 32). "You can see that 5 million years ago, we were similar to this creature. We'll never be able to enter their minds, but new experiments and observations can reveal aspects about them that have yet to be discovered."

Much has changed since Jane Goodall first visited what was then called Tanganyika to observe the Gombe chimpanzees. When Goodall took to the field in July 1960, no one had ever followed a group of chimpanzees in the wild and carefully documented the interactions of individuals, their diets, and their range. Goodall and the handful of contemporary researchers who soon began working in the wild created a discipline from whole cloth, making one head-twisting discovery after the next. Goodall changed the popular view of our closest relative through magazine articles, documentaries, and popular books like *In the Shadow of Man*. Similarly, studies of captive chimpanzees began to flourish in the 1960s, with primate centers receiving substantial government support and several academics even keeping animals on campuses and in their homes.

But, as Wrangham intimated, those pioneering studies just scratched the surface. Countless questions, of increasing complexity, remain about chimps—and how they compare to us. "The subtlety of the questions we're able to ask has increased, and there's a great deal of subtlety still left unexplored," says Jim Moore, an anthropologist at the University of California, San Diego, who also cut his teeth working at Gombe and now has many students helping him study savanna chimpanzees in Ugalla, Tanzania.

As Goodall showed, wild chimps use tools, but researchers continue to discover

CREDITS (TOP TO BOTTOM): M. TWOMBLY/SCIENCE, © MICHAEL NEUGEBAUER/JANE GOODALL INSTITUTE, MALCOLM JINTON, COURTESY YETS-JRO MATSUZAWA, MORGAN/SANZ GOUALOUGO TRIANGLE APE PROJECT STEPHANIE BOGART MALCOLM LINTON

Chimps Read Lips

ATLANTA—In 1862, French neurologist Duchenne de Boulogne published *The Mechanism of Human Facial Expression*, which linked specific facial muscles to emotional states such as aggression, surprise, and lasciviousness. More than 150 years later, comparative psychologist Lisa Parr of Yerkes National Primate Research Center is trying to make the same connections to the puckered lips, raised eyebrows, and grins of chimpanzees. "It's just been a really ignored area," Parr says.

Whereas psychologists who study chimpanzees argue endlessly over whether they can understand the intentions and desires of others—the so-called theory of mind—Parr says that debate is too arcane for her tastes. Facial recognition, in contrast, is elemental. "We're starting at the bottom and working up," Parr says. In the process, she has helped to develop an elaborate system that objectively classifies expressions and the muscles that are involved.

Parr is part of a consortium that has created a chimp Facial Action Coding System, which builds on work done in humans in the 1970s. After studying facial muscles dissected from dead chimpanzees, Parr and her colleagues electrically stimulated the muscles in anesthetized live chimps, defining nearly two dozen "action units." Other studies use a joystick-controlled computer to see how chimps interpret different expressions. They are shown three photos of chimps and asked to match the two that have the same facial expression. She's also scanning the brains of living chimps to see how the neural-processing networks compare with those in humans, looking for clues to how human communication evolved; her results suggest that chimps use the same regions of the brain to process faces as humans do—and these regions differ dramatically from the ones used by monkeys. –J.C.

Look here, chump. Facial expressions speak volumes about emotional states.

Map quest. Paco Bertolani has used satellite [illegible] about Uganda's Kibale National Park.

CREDITS (TOP TO BOTTOM): MALCOLM LINTON; PHOTOS.COM (2); ISTOCKPHOTO.COM. PHOTOS.COM; ISTOCKPHOTO.COM. PHOTOS.COM

Makoku at 0°30′N 30°24′E: Chimping Via GPS

KIBALE NATIONAL PARK, UGANDA—With the help of satellites, a handheld GPS device, and his laptop, Paco Bertolani has put together a map that redefines the art of charting chimpanzee life in the wild. As part of his Ph.D. dissertation for the University of Cambridge in the United Kingdom, Bertolani is analyzing the routes chimpanzee use in different habitats. His goal is a better understanding of how chimps orient themselves and save energy. Nearly every day from October 2007 to June 2009, Bertolani followed a different male in the habituated chimp community here, starting in the early morning and ending at nesting time at dusk.

During an outing one day in May 2008, he noted the location of the chimp-of-the-day, Makoku, every 10 meters with the GPS device, and he also mapped the fruiting trees that attract many in the community, tracking how movements change with the availability of different foods. He then overlaid these data on satellite images of the terrain, creating something of a Google Map of the popular pathways, dining spots, and places to sleep. "The GPS in the forest historically has never worked," said Bertolani, noting that new and improved receivers on the ground can finally receive signals from satellites through the thick forest canopy. "So it's never been possible before now to do such a detailed study of ranging." –J.C.

surprising new variations on that theme. More intensive comparisons of different wild sites are documenting a bevy of unique "cultures," from nut-cracking to grooming techniques, in different communities. Researchers have moved beyond teaching apes to communicate (p. 38) to refined studies of vocalizations in both wild and captive chimps (p. 36), an area that has received scant attention. Long-term data amassed in the field and at primate centers and zoos are filling in gaps in information about life span, social structure, reproduction, and disease. Carefully constructed lab experiments are uncovering new insights about cooperation, empathy, and teaching. Comparative work is also taking place with bonobos, the chimp cousin that is equidistant from humans on the family tree.

Today, researchers operate in a different landscape, both in terms of where and how chimps are studied. They have many advantages. For one, several sites have habituated wild communities, which means a student can go to the field and immediately start a research project. New technologies have had an even broader impact, enabling researchers in both wild and captive settings to explore questions they could not have probed 50 years ago. The chimp genome is now available, and more routine DNA sequencing has exposed occult infections like the chimp AIDS virus, SIVcpz, and complex familial relations. Experiments with captive apes using touch-screen computers reveal new dimensions in their cognitive capacities. Global imaging systems help primatologists precisely chart animal movements and habitat. Magnetic resonance imaging scans of captive chimps are clarifying how their brains differ from ours (p. 40).

Just as technology has broadened the research possibilities, lines that once separated groups have blurred. Although some young researchers complain that their mentors are still territorial with each other and their animals—"They're behaving more

and more like chimpanzees," one graduate student groused—several study sites have pooled data. A growing number of investigators have studied both captive and wild chimps. Scientists who oppose invasive biomedical research with chimps now do laboratory examinations of noninvasively acquired blood, hair, feces, and urine. "In the coming decades, we need the interdisciplinary approach to get to know chimpanzees better," says Tetsuro Matsuzawa, who heads the Primate Research Institute of Kyoto University in Inuyama, Japan (p. 41) and also runs a field study in Bossou, Guinea. "You should pay attention to both laboratory and field research. If you're interested in genetics of great apes, you should go to Africa to see the reality."

Nowhere embodies the cross-disciplinary approach more than the Max Planck Institute for Evolutionary Anthropology in Leipzig, Germany, which opened in 1997 and hired topnotch researchers in genetics, psychology, primatology, and paleontology who study chimpanzees and bonobos in the wild and in captivity (*Science*, 17 August 2001, p. 1246). "Our main argument—and why this institute exists—is if you want to understand human uniqueness, you have to understand our closest relatives," says Christophe Boesch, who heads the primatology department and has conducted studies of wild chimpanzees for 3 decades.

In 2001, Max Planck opened the Wolfgang Köhler Primate Research Center at the Leipzig Zoo, the only facility in the world where investigators can study chimps, bonobos, gorillas, and orangutans. "This is a place where if you have an idea, the next day you go test it," says psychologist Josep Call, the center's director. "It's really unbelievable."

Opportunity knocks

As new technologies and intersecting disciplines expand the study of chimpanzees and bonobos, researchers are also grappling with a daunting constraint: These endangered species are dwindling in numbers, both in captivity and in the wild. Funding to study them is also fickle.

The captive population available to scientists for the past 15 years has steadily declined because of concerns in several countries about the ethics and value of sometimes harmful biomedical studies; many former "research chimps" have been "retired" to sanctuaries that forbid their use in any scientific studies, including noninvasive ones (*Science*, 26 January 2007, p. 450). The U.S. National Institutes of Health (NIH), which since 1960 has been

A Matter of Life and Limb

KIBALE NATIONAL PARK, UGANDA—The chimpanzees here are not threatened by poachers for bushmeat. But they face another peril: Many become entangled in snares set in the forest for other animals such as duikers. Typically made from sticks and the wire used on motorbike brakes, the snares lie on the forest floor and cinch on limbs when an animal steps inside them. Chimps often tighten the wire in a frantic attempt to remove it, cutting off the blood supply to their limbs. Sometimes the limbs rot off and then heal; sometimes the animal dies from infection.

Up to one-third of the chimps at Kibale have become entangled in snares, and Max, a 12-year-old male, is one of the most tragic. After losing one leg to a snare, he became caught again and lost his remaining leg. "It's really, really heartbreaking," says Emily Otali, the field manager for the Kibale Chimpanzee Project. "When Max lost his first leg, he was a sport about it," Otali says, explaining that he limped on his good leg, and the stump quickly healed. "Then he lost his other leg, and he had to use his former stump, and he bruised it and it was bleeding, and the new one was bleeding," she said. "He sat on the tree whimpering." Max now crawls about on his two stumps and still climbs trees. "He's not a happy chimp, but he's alive," Otali says.

Trap tragedy. Kibale's Otali (*bottom*) has a snare-removal team, but Max (*above*) still lost both his legs within the same year.

The Kibale team has hired hunters from local villages to work with them to remove snares; they also try to teach the villagers about the chimpanzees, hoping that if they know more about them they will care more about their well-being.

Across the country in the Budongo Forest Reserve, a similar percentage of chimpanzees has lost limbs to snares, leading the researchers there to try a creative intervention with local hunters: In exchange for agreeing not to use their snares, the hunters each receive two goats and veterinary care for them. With funds from California's Oakland Zoo, Budongo now hires four people to remove snares, and they've seen the numbers drop dramatically. "It's had real success," says Vernon Reynolds, a retired anthropologist from the University of Oxford in the United Kingdom who started the Budongo chimp research project. The Jane Goodall Institute also has a snare-removal program that employs former poachers and educates locals.

But the battle never ends. "I don't know if it's a no-win situation," says Otali. "We just have to continue, hoping to make a change, no matter how small it is."

–J.C.

CREDITS (TOP TO BOTTOM): KYLE B. WILD; MALCOLM LINTON

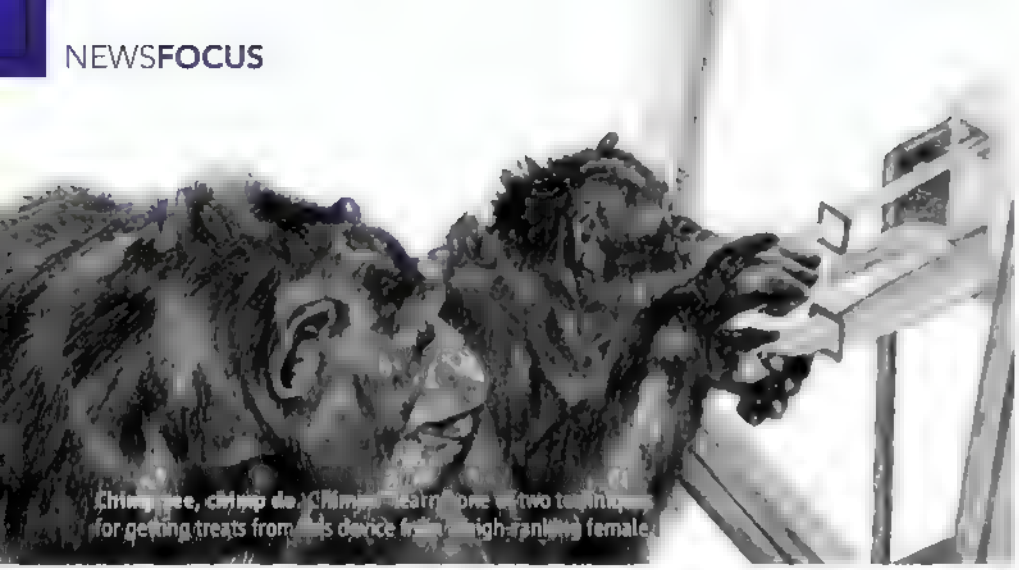

Chimp see, chimp do. Chimps learn one of two techniques for getting treats from a device from high-ranking females.

The Spread of Culture, Primitive as It Is

LAWRENCEVILLE, GEORGIA—It wasn't until 35 years ago that chimp researchers from Gombe visited the nearby project in the Mahale Mountains and noticed a startling difference in grooming techniques. This led to the idea that chimpanzee communities had unique "cultures," but field studies have had difficulty proving that chimps transmit social behaviors. So in 2003, with a freshly minted Ph.D. in hand from the University of St. Andrews in the United Kingdom, Victoria Horner came to Yerkes National

a major supporter of captive chimp populations for research, no longer funds breeding, which means the 1000 or so research chimps now in U.S. primate colonies will disappear within 30 years, according to one estimate (*Science*, 26 January 2007, p. 450) "It's a big concern," says Frans de Waal, an ethologist at Emory University in Atlanta.

De Waal studies chimps at the nearby Yerkes National Primate Research Center, which Emory has run for many years with substantial NIH support. Yerkes is now one of the only places left in the United States that houses chimpanzees for behavioral and cognitive research. "We have to fight here to keep the colony alive and going for research purposes," de Waal says. "And the current financial climate is not ideal."

Psychologist Sally Boysen of Ohio State University, Columbus, has an especially bleak view of the future of captive chimp studies. "It's pretty grim," says Boysen, who for more than 20 years had chimps on campus until her university said in 2006 that it no longer had enough funding to keep them. Despite Boysen's loud protests, she had to let go of her nine chimps, and the six surviving ones now live at Chimp Haven near Keithville, Louisiana, a sanctuary for retired research animals "The message for all of us is, 'Hey, it's not worth it to focus your career on this,' " Boysen says. She also laments what she sees as "the convergence of the animal-rights movement and the political zeitgeist" undercutting the value of chimp research.

The Max Planck model of linking zoos to academic institutions may become more commonplace. The Edinburgh Zoo in the United Kingdom opened the state-of-the-art Budongo Trail exhibit in May 2008 that has 40 chimps and welcomes researchers from the University of St. Andrews. The zoo also supports field studies in Budongo, Uganda. "Zoo funding is better than research grants because zoos are going to stay there and keep funding you if they like your work," says Vernon Reynolds, an anthropologist emeritus at the University of Oxford who started the Budongo project in Uganda. "A grant is up in 3 years."

Some zoos also allow academics to do research without directly supporting them. But this has its limits, cautions de Waal, who did groundbreaking chimp work at Burgers' Zoo in Arnhem, Netherlands, and bonobo studies at the San Diego Zoo. "Zoos can be very constraining," he says.

Biological anthropologist Brian Hare of

"Sanctuaries are the future for ape research. We have far better research resources for a fraction of the cost."

—BRIAN HARE, DUKE UNIVERSITY

Duke University in Durham, North Carolina, has opened a new avenue for studies by tapping into the African sanctuaries that now house bonobos and chimpanzees, many of them confiscated from animal traders or orphaned when their mothers were slaughtered by bushmeat hunters (*Science*, 7 September 2007, p. 1338). According to the Pan African Sanctuary Alliance, more than 850 chimps now live in sanctuaries there, which is more than all the chimps in Europe's zoos and three times the number held by accredited U.S. zoos. "Sanctuaries are the future for ape research," Hare says. "We have far better research resources for a fraction of the cost, and we are helping conservation and welfare organizations on the ground in ape-habitat countries while training African researchers."

Long-term sites where researchers study wild chimpanzees and bonobos have nearly doubled during the past decade (p. 31), but given the rapid pace of the populations' decline from habitat destruction, the bushmeat trade, and disease—some transmitted from humans—many researchers worry that their days are numbered, too. Boesch, who has studied wild chimpanzees in the Taï National Park in Côte d'Ivoire since 1979, argues that the need for more long-term field studies is urgent. "Whenever we go to look, we observe new behavior in chimpanzees that we didn't know before," says Boesch, who recently started a project in Gabon As the wild chimp population dwindles the best estimate now puts the population at 200,000 to 300,000 individuals those opportunities are lost forever, he says.

One particularly productive new site is the Goualougo Triangle Ape Project in the Nouabalé-Ndoki National Park in the Republic of Congo. The remote area, which has 1000 gorillas and 500 or so chimpanzees in more than a dozen communities, wasn't studied until David Morgan went there in 1999. "Ndoki was one of the best kept secrets," says Morgan, who is now a fellow at the Lincoln Park Zoo in Chicago, Illinois, and runs the project with his wife, biological anthropologist Crickette Sanz of Washington University in St. Louis. "We've had more observations of chimps and gorillas interacting than anyone." They have also taken advantage of several high-tech tools, setting up sensor-activated video cameras at termite mounds and fruiting trees and sensors to help detect poachers.

The new generation of chimp researchers has one other trove of data to mine: Studies can now be done with little more than a computer and an Internet connection Anyone can scour the chimpanzee genome and compare it to those of other species. The recently launched Center for Academic

CREDIT: DRAWING BY AMY WHITEN

Primate Research Center of Emory University to exploit its unique culture: Its 47-hectare field station in this Atlanta suburb houses two groups of chimps that live in separate but nearly identical conditions, an ideal experimental setting to study transmission of culture in a controlled environment. "There's no other facility in the world like this," says Horner, who works here with Frans de Waal of Emory.

Two years after arriving, Horner, de Waal, and her then–postdoc adviser Andrew Whiten of St. Andrews published a landmark study that provided the most convincing evidence yet that a new "culture" could spread through groups of chimpanzees. The experiment resembled the children's game "Telephone," in which a message is passed down a chain of individuals. In this case, they taught one chimp in each group how to use a new tool and assessed whether the technique—the culture—spread.

The study relied on a clever device that held a treat, which the chimps could retrieve by either lifting a handle or poking a release lever. Horner taught one high-ranking female in each group a different method. As she and her co-authors described in the 29 September 2005 issue of *Nature*, the other chimps observed their "local expert" and copied the technique. The team subsequently published similar studies that taught one individual in each group to either slide or lift a door in a box that held fruit, or to gather tokens and place them in either a bucket or a pipe to receive a food reward. These experiments again demonstrated that the behaviors were transmitted in their respective groups, creating cultures.

Yes, human culture is much more sophisticated, Horner acknowledges. But she says these experiments unequivocally demonstrate that the ability to transmit a culture is not uniquely human, as some anthropologists have argued. "At what point are people going to be able to give up and say, 'Yes, we are apes,' and be able to handle that?" she asks.

–J.C.

Research and Training in Anthropogeny at the University of California, San Diego, is currently digitizing and putting online one of the largest collections of chimpanzee skeletons ever available for study (p. 43). Although they are not public, many long-term sites have massive amounts of data that researchers can probe. Anne Pusey, a behavioral ecologist at Duke University who formerly ran the Gombe site for the Jane Goodall Institute, says they have 600 hours of videotaped recordings over 11 years of 100 or so wild chimps in three different communities. "We've only looked at the tip of the iceberg," Pusey says.

Perhaps the most pronounced change that has occurred since Goodall first wowed the world with her Gombe observations is one that she ushered in: Protecting chimps is now intimately tied to research. Today, many researchers who complete their Ph.D.s find themselves having to choose between conducting further studies and moving into conservation full-time. And those who stay in research face a different ethical landscape from the one their predecessors faced, in terms of the types of experiments they can conduct, the housing they provide captive chimps, and their responsibility to protect the wild communities they study. "I've seen radical changes," says Masaki Tomonaga, who for 2 decades has studied chimp cognition at Japan's PRI. "Twenty years ago, most researchers didn't think about the ethical issues and the future of these animals. Now we have such an accumulation of findings about them and such a high level of understanding, we have to apply them to animal welfare and conservation. This research is to better understand humans and chimpanzees, but it also has to be used to conserve their lives for the next generations."

–JON COHEN

The Chimpanzee Genome Project's Seedy Origins

WHEN THE HUMAN GENOME PROJECT SET out to unravel the entire DNA of *Homo sapiens*, researchers decided to take blood and sperm from donors with diverse backgrounds to create a "consensus" sequence. The hundreds of donors recruited for the project did not know whether their DNA made it into the final sequence, and the scientists were blinded to the identity of the donors. For the Chimpanzee Genome Project, the DNA came mainly from one chimp, Clint, of Yerkes National Primate Research Center in Atlanta, and he was chosen for the most haphazard of reasons.

DNA donor. Clint was chosen to represent the genetics of his species for an X rated reason that had nothing to do with his chromosomes

For his Ph.D. thesis at Baylor College of Medicine in Houston, Texas, in the 1990s, Evan Eichler studied stretches of DNA that repeat themselves, which are tricky to sort out from sequencing errors. After he completed his doctorate, he wanted to unravel a particularly confusing repeat on the human X chromosome, which he thought he could sort out by comparing it with chimpanzee DNA. The process required a few scientific tricks he did not know—specifically, the then-new technique of cloning stretches of DNA into what are known as bacterial artificial chromosomes (BACs). So he did a stint in the lab of BAC guru Pieter de Jong, then at Roswell Park Cancer Institute in Buffalo, New York. To begin, de Jong asked Yerkes for a sample of chimp sperm, and researchers there chose Clint—not because he was a hardy male representative of *Pan troglodytes* or had some other meaningful attribute. Clint, it turns out, became the genome chimp because he was particularly fond of providing sperm samples.

Eichler did not make much progress, but after he left the lab, de Jong, now with Children's Hospital Oakland Research Institute in California, decided to continue trying with samples of Clint's blood instead of sperm. His lab eventually succeeded, and they stored the clones in a freezer. When Eichler and a small group of colleagues in 2002 decided to sequence the entire chimpanzee genome, they fished out Clint's DNA.

In 2004, the year before the first draft of the chimpanzee genome was published, Clint, then 24, died from heart failure. But his sequence lives on in databases that Eichler, now at the University of Washington, Seattle, and scores of other researchers continue to mine for surprising insights about chimpanzees and how they relate to humans and other species. "Science never goes a straight path," says de Jong.

–J.C.

CREDIT: YERKES NATIONAL PRIMATE RESEARCH CENTER

Say what? Cathy Crockford plans to stage playback experiments in which she watches animals' reactions to recordings of different vocalizations.

CREDIT: MALCOLM LINTON

Talking Chimp to Chimp

Language may be unique to humans, but our closest relatives do a lot of vocalizing, and researchers are trying to figure out what they're yakking about

BUDONGO FOREST RESERVE, UGANDA—As Cathy Crockford wound her way through the dense trees to observe chimpanzees here, she bore more than a little resemblance to a young Jane Goodall. Crockford, who specializes in chimpanzee communication and is based at the University of St. Andrews in the United Kingdom, has Goodall's lanky build and, like Goodall, wore her long, blonde hair pulled back. She is also a native of England and speaks with a purposeful British accent. But Goodall for many months walked around Gombe alone with little more than a notepad, binoculars, and a satchel over her shoulder. Crockford works with her husband, Roman Wittig, and in addition to their binoculars and hip packs, they each have their own field assistants. They often cover adjacent terrain and communicate using walkie-talkies. They tap in their locations and observations on palm-held electronic devices. And most important, each of them totes a state-of-the-art Marantz digital tape recorder strapped around their neck with a high-end microphone covered by a foam windscreen.

Crockford and Wittig, along with their St. Andrews colleagues Klaus Zuberbühler and Katie Slocombe, are conducting the most intensive studies ever done to try to unravel the meaning of chimpanzee pant-hoots, grunts, screams, and whimpers. Although much work has been done studying communication in wild monkeys and captive chimps, wild chimpanzee vocalizations have received surprisingly little formal analysis. "There's almost everything to still find out about the chimpanzee communicative system," said Vernon Reynolds, an anthropologist emeritus at the University of Oxford in the United Kingdom, who started the Budongo site in 1990. "It's ridiculous that we've done so much works on chimps and have not broken the code of their communication."

Decoding chimpanzee communication has proven much trickier than decoding that of other primate species in part because of their forested habitat. "A lot of communication is exchanged between these parties of chimps that can't even see each other," Crockford explained. "It makes it difficult for us to figure out who is giving this particular call and who is responding. But that's one of the things that we're hoping to get a handle on."

Crockford and Wittig's work builds on chimpanzee studies they did in the Taï National Park with Christophe Boesch while working on their Ph.D.s, including Crockford discovering that different communities there used different pant-hoots and that she could distinguish specific barks tied to specific contexts such as traveling or hunting. They then went on to do postdocs studying baboons in Botswana with Dorothy Cheney and Robert Seyfarth, two pioneers in primate communication based at the University of Pennsylvania. Cheney and Seyfarth, another husband-and-wife team, first received international attention for studies in the 1970s with wild vervet monkeys, which they showed had distinctive alarm calls for snake, eagle, and leopard. Their convincing evidence came from playing recordings of the monkeys' own calls through amplifiers they had hidden around the vervet's habitat in Kenya's Amboseli National Park and carefully documenting how the animals responded. Crockford and Wittig began making recordings of the Budongo chimps in 2008 to conduct similar playback experiments.

Cheney said she and her husband have "great admiration" for Crockford and Wittig's "exciting and imaginative" research. "All work on ape cognition was conducted, and in large part continues to be conducted, on captive animals under conditions that lack ecological validity and typically involve the same individuals tested over and over again in

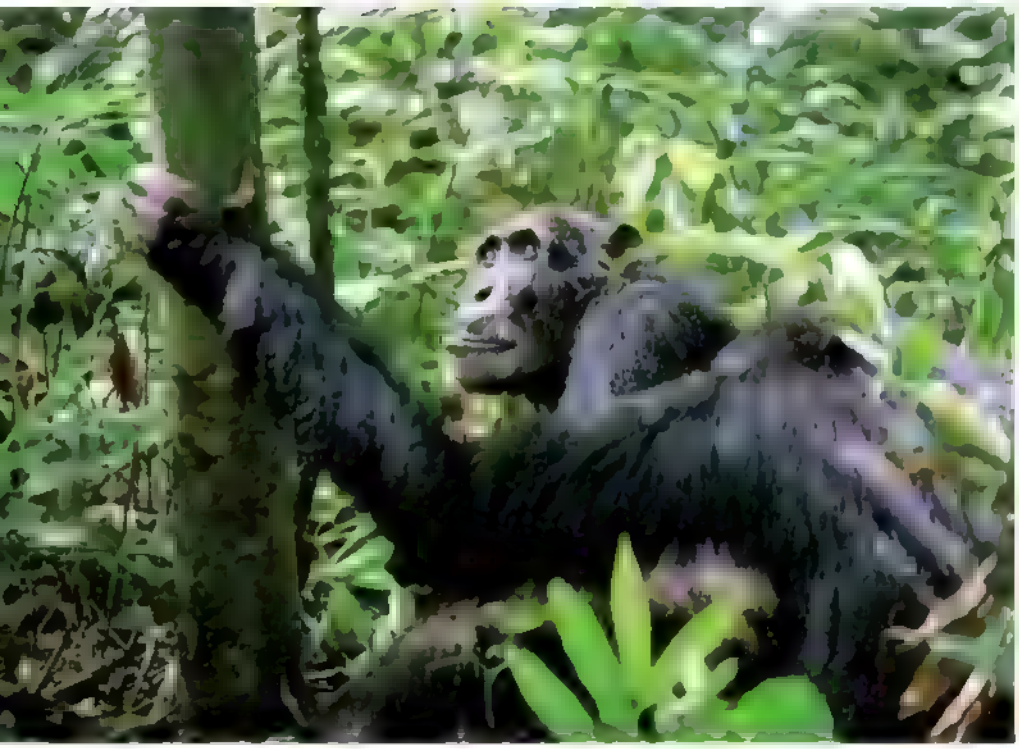

Listen up. Roman Wittig says chimps in the dense forest often figure out the intentions of others, whether a warning or aggression, based on the vocalizations they hear.

CREDITS (LEFT TO RIGHT): MALCOLM LINTON

multiple experiments," Cheney said. "Cathy and Roman are some of the first investigators to attempt to apply the experimental techniques developed by scientists working with monkeys to wild chimpanzees."

Crockford and Wittig have far more ambitious aims than simply decoding vocalizations that approximate words or capture an emotional state. They want to figure out how chimpanzees navigate their complex social environment. "What do they know about the relationships that others have?" Wittig asked. "Do they know who is friends with whom? Vocalizations in the closed, dense forest are probably the main information they have to understand what intentions others have."

While Wittig and Crockford followed the Budongo chimps this morning in May 2008, a drama unfolded that they dubbed the Return of Zefa. "It's like a daily soap opera," Wittig said. Zefa was the second-ranking male in this community until he disappeared 3 months earlier, leading the researchers to fear that he might have died. But he returned in full force this day, triggering repeated challenges from the new alpha male, Nick, and confrontations with other males that Zefa initiated. Crockford looked up as a racket erupted from the treetops where Zefa was hanging out, took a few steps closer, turned on the recorder, and pointed her microphone toward the piercing noise. "That was pant-grunts and screams coming from where Nick just drummed," she said into her mic. Nick apparently had moved on, and Zefa came down from the tree, leading to another outburst from a lower-ranking male, and it sounded as though he was being tortured and screaming for mercy. As the pant-hoots began to fade, they were replaced by a building stream of pant-grunts. "That's a submissive greeting," Crockford explained, noting that the first vocalization had "graded" into the second.

> ***"There are little nuances in their vocalizations that may have completely different meaning."***
>
> —ROMAN WITTIG, UNIVERSITY OF ST. ANDREWS

Wittig believes that the key to making sense of chimp chatter is noticing combinations of calls and other subtleties. "There are little nuances in their vocalizations that may have completely different meaning," Wittig said. "They might have a little faster increase in the beginning or a higher frequency at the end. What would be great to find out is whether they are meaningful, and not only to the guy who is vocalizing, but to an audience as well."

Crockford stressed that the pant-hoots, grunts, barks, and screams are not words but still communicate specific ideas. "These vocalizations are very context-tied, so an individual that is away can probably work out quite a lot of what's happening if he hears this sort of exchange," Crockford said. "But I don't think that necessarily means that it's symbolic, which it would have to be if this were equivalent to words."

Crockford and Wittig plan to use the sound catalog of individuals that they're amassing for playback experiments to analyze the types of complex communications they explored while working with baboons. For example, they found that after a female baboon was attacked, if the victim heard a friendly grunt from one of her attacker's relatives, it sped reconciliation with the aggressor.

Until now, Wittig said, researchers who study wild chimpanzees have relied mainly on observation, rarely conducting experiments. "I think it's time to take one step further and try and hypothesize in a clear way and create a playback experiment where chimps can show what their knowledge is about things," said Wittig. "It's a big puzzle because we're not able to go there and ask the chimps direct questions."

Crockford and Wittig have yet to publish any of their findings from Budongo but expect to soon have a lot to say about an area of chimpanzee research that until now has been remarkably quiet.

–JON COHEN

1 to 1. Rob Shumaker has taught Azy, an orangutan, to communicate with photos and symbols.

CREDIT: MALCOLM LINTON

Boxed About the Ears, Ape Language Research Field Is Still Standing

A once-thriving field now has only a single outpost, the Great Ape Trust, which continues to teach bonobos and orangutans to communicate with humans

DES MOINES—In the heyday of ape language research 3 decades ago, Washoe the chimpanzee, Koko the gorilla, and the scientists who taught them American Sign Language won international fame. But then a 1979 paper in *Science* concluded that researchers had been duped by these and other "talking" apes: Yes, they could learn words, but none could form a sentence, the authors argued, and all excelled at imitating their teachers Defenders of the work suffered mounting criticism and even ridicule, and the field sputtered out. Yet today, one bastion of ape language research remains, the Great Ape Trust, improbably set in a rural neighborhood outside this midwestern city in Iowa.

Established in 2004 with a $25 million gift from a local heir to a hot dog fortune, the Great Ape Trust today has eight bonobos, including the world-renowned Kanzi, and six orangutans. (The trust hoped to house more orangutans, as well as gorillas and chimpanzees, but a flood in June 2008 forced the institution to reconsider its ambitious building plans.) Evolutionary biologist Rob Shumaker, one of five scientists who work full-time at the trust, says he does not feel besieged by the endless skepticism and outright criticism the endeavor attracts. "The people I work with, they don't think I'm out in left field, they don't think I'm crazy," says Shumaker, who does language studies with the orangutans. "We're like-minded and remarkably supportive and interested in what each other is doing." The trust also provides these researchers with something of a cloister atmosphere. "It's not really a sanctuary for the apes," jokes Shumaker. "It's a sanctuary for the researchers."

Built on 90 hectares that includes a humanmade lake, the trust has separate, state-of-the-art housing for its bonobos and orangutans that features touch-screen computers, which display symbols, or lexigrams, that the apes use to communicate. In addition to language, researchers from the trust and grad students working with anthropologist Jill Pruetz at nearby Iowa State University (who studies wild chimps in Senegal) also investigate ape behavior and cognition. And in a similar philosophy to that of Japan's Primate Research Institute (p. 41), all apes must "volunteer" to take part, says psychologist Karyl Swartz of the trust. "They choose minute by minute, day by day, problem by problem, whether they want to participate in the research," says Swartz, who has studied different apes and monkeys for 30 years. So the researchers can lead the apes to computers but can't make them communicate. "We believe that they're our partners in research. It sounds a little over the top and trite, but it's an amazing philosophy."

The trust came about after philanthropist Ted Townsend read that Duane Rumbaugh, who conducted pioneering ape language research at Georgia State University (GSU) in Atlanta with his then-wife Sue Savage-Rumbaugh, was a native of Iowa. Townsend cold-called Rumbaugh and introduced himself, and in time sold him and Savage-Rumbaugh on his vision to build the trust. All the bonobos at the trust came from GSU's Language Research Center, which still has four great apes and conducts studies, but does not teach them language. Savage-Rumbaugh has since retired, and Rumbaugh is now a professor emeritus at the trust and Georgia State University

Although no one disputes that apes can communicate and even learn words, much of the debate that surrounds ape language research focuses on the definition of language. "You can't be an ape language researcher unless you take on what language is," says William Fields, an ethnographer who worked with Savage-Rumbaugh in Georgia and took over the bonobo work at the trust when she retired.

Whereas many linguists define language as using words with the rules of grammar and syntax, Fields argues that it is more about understanding words than producing them. He points to Kanzi a bonobo that Savage-Rumbaugh once claimed had "acquired linguistic and cognitive skills far beyond those achieved by any other nonhuman animal in previous research" and his half-sister Panbanisha Both communicate with lexigram boards that have more than 300 symbols. A controlled 1992 study with Kanzi showed that more than two-thirds of the time he accurately recognized 660 novel sentences like "Put the raisins in the water," and "Pour the juice on your ball." In 2007, Savage-Rumbaugh went so far as to include Panbanisha and Kanzi as co-authors of a paper published on appropriate captive environments for apes in the *Journal of Applied Animal Welfare Science*. (Savage-Rumbaugh was the first and corresponding author, and she gave the apes the last name of Wamba, a long-term research site of wild bonobos.)

Fields's office sits across from the bonobo enclosure, and although a concrete block wall separates him from the animals, he whispers when he compares Kanzi and Panbanisha's language skills. "At some point, Kanzi will have to share the limelight with the real ape

Bonobo banter. Kanzi (*left*) and his half sister Panbanisha (*right*) use lexigrams to communicate with handler Liz Pugh.

CREDITS: (LEFT TO RIGHT) MALCOLM LINTON

of genius," says Fields, explaining that he is often surprised by what the animals hear and comprehend. "I don't have the scientific data to prove it to you, but Sue and I know when we have specific critical conversation about certain things, we have to make sure we're at a certain distance or they're going to hit you with it," says Fields.

In demonstrations, Kanzi and Panbanisha easily identify dozens of words on their lexigram boards. Panbanisha also goes for a walk outside on a leash in an enclosed area and, with the lexigram board, tells her handler that she wants to make a campfire, which she has done many times before. Panbanisha gathers sticks, and when handed matches, successfully lights a fire. She then asks for marshmallows, which her handler gives her on a stick, and she roasts them.

Psychologist David Premack, once a leader in the ape language research field and now a professor emeritus at the University of Pennsylvania, has reviewed the few published studies with Kanzi and remains underwhelmed. "It all can be boiled down to next to nothing," says Premack, reflecting the reaction of many critics. "What looks complicated is not."

Premack contends that apes do not have anything approaching human language. Only humans can construct infinitely long sentences that embed ideas into ideas, a process called recursion. As he explained in an article that compared human and animal cognition in the 28 August 2007 issue of the *Proceedings of the National Academy of Sciences*, "One can talk of 'Ida the red-haired women who left her hat in the theater, the old one that burned down, because arguing with Henry, her husband of forty years, who still has all his hair, wears a maroon smoking jacket in the evenings and is as broke as ever, had rattled her.' " What's more, there is scant evidence that apes teach, he notes, and that is critical to human children learning vocabulary. And apes like Washoe and Koko that learned sign language have severe limitations because they do not have the necessary facial control used for critical functions such as tone and grammar.

Shumaker, who moved to the trust from the Smithsonian Institution's National Zoological Park in Washington, D.C., groans at these distinctions. The field, or at least what is left of it, has matured, says Shumaker, and he wants to move past the bad old days. "What's the next step?" he asks. "Do we get out of this mode of saying, 'Are apes capable of language or not,' and having these big fiery debates about it? I hope so. I don't think it's interesting. I don't really think it's productive. What I would much rather do is focus on the capabilities [apes] have. Are we going to argue forever about the word language? Let's get on with it. Let's really study what's going on mentally for these guys."

> ***"Do we get out of this mode of saying, 'Are apes capable of language or not,' and having these big fiery debates about it? I hope so."***
>
> **—ROB SHUMAKER, GREAT APE TRUST**

Shumaker readily acknowledges that neither the orangutans nor the bonobos have human language skills but says ape language research ultimately opens a window into their minds. "I think language allows us to do things that you simply could not do otherwise and allows us to ask and answer questions that you could not approach with an ape in any other circumstance," he said. "It has tremendous value. Language is a great platform for exploring greater cognitive skills."

Comparative psychologist Benjamin Beck, another National Zoo veteran who now heads the trust's conservation efforts with wild apes, stresses that ape language research remains an important field that attracts broad interest. The fact that so few investigators still do it, he says, simply reflects that it's a costly, long-term endeavor. "Most academic organizations are unwilling to take on the ethical and financial commitment of supporting apes for 40 or more years of their life span," says Beck. But the trust is determined to keep the field alive. Adds Shumaker, "The fact that we're still here speaks to its vitality."

Then again, the trust has had to reassess its original vision since *Science*'s March 2008 visit. Following the flood that June, the U.S. Army Corps of Engineers decided that the trust could not safely expand its orangutan facility as planned, and Shumaker is now in final negotiations to move with those animals to a zoo in 2013. The trust says it will continue to conduct bonobo language research, but the flood sends a loud message: The ape language research field is not built on the firmest of grounds. **–JON COHEN**

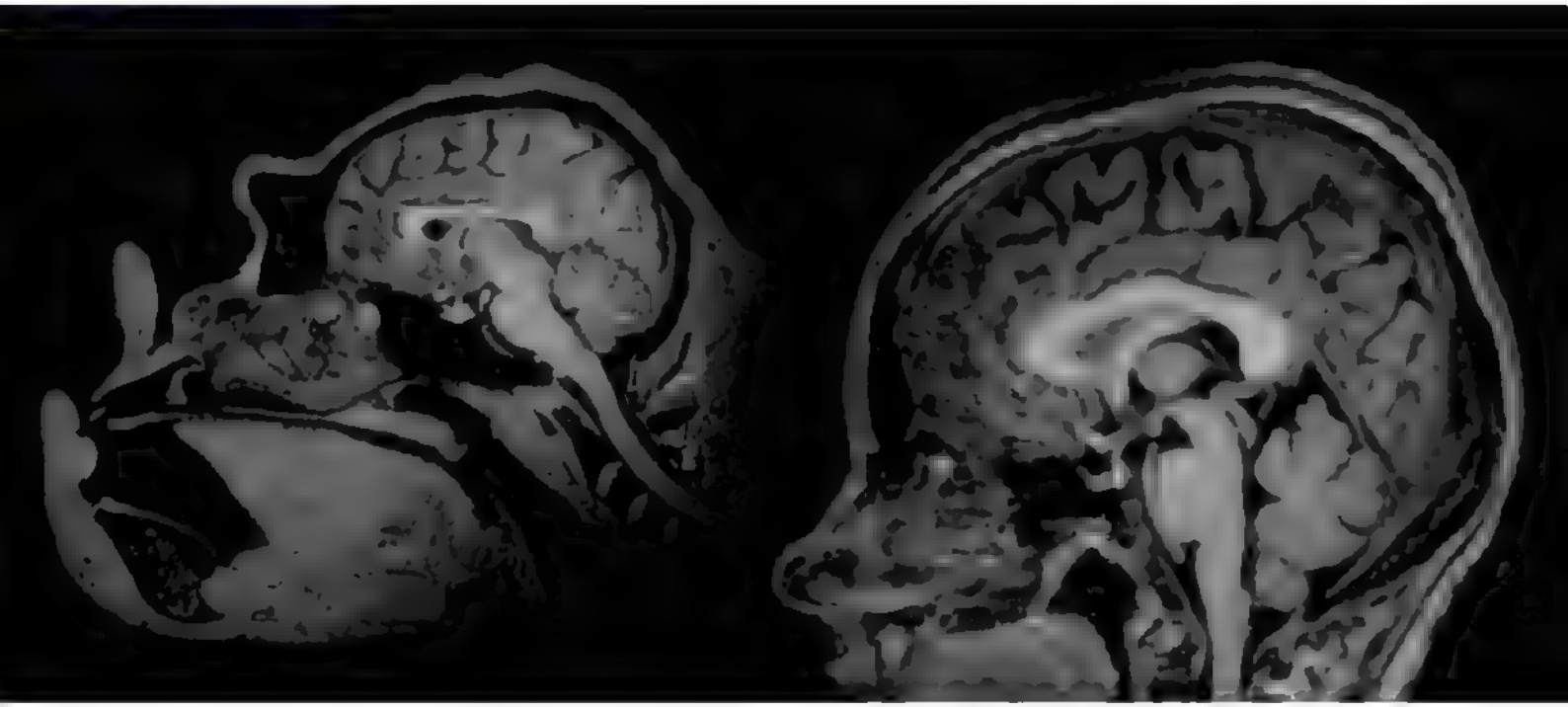

The Inner Workings of the Chimpanzee Brain

Using a noninvasive magnetic resonance imaging scanner, investigators have launched a pathbreaking cerebral journey to probe everything from cognition to disease

ATLANTA—"HO-OW! HO-OW! HO-OW!"

The Siemens Trio 3 Tesla in the imaging center at Yerkes National Primate Research Center of Emory University is a noisy beast of a machine. It weighs in at 13 tons, much of which is an electromagnet that pulses radio frequencies to make protons in water molecules resonate. Lying inside the missilelike MRI tube this morning while foghornlike blasts of sound fill the room is a 26-year-old female chimpanzee named Melinda. The 74-kilogram, hairy hulk rests on a gurney, with a heating pad over her chest and an intubation tube delivering a sedative gas. The only thing visible is the top of her skull, which has been outfitted with a helmet called a "head coil" that transmits and receives the radio frequencies. A veterinarian, wearing a face mask, gloves, and surgical scrubs, stares at a machine with LED numbers that chart Melinda's vitals.

This bizarre scene might look like something out of a sci-fi horror flick, but as Yerkes neuroanatomist Todd Preuss emphasizes, appearances can be deceptive—especially in the emotionally freighted arena of biomedical research with chimpanzees. The MRI emits no radiation and is something of a gentle giant, affording researchers a unique view into the hidden architecture of the body's soft tissues without causing harm. "This is completely noninvasive," says Preuss. "It's the kind of procedure we'd do with a human."

It's November 2008, and Melinda is the 29th chimpanzee that Preuss and anthropologist James Rilling of Emory have scanned as part of a study that will examine the aging of their brains in relationship to humans, including people with Alzheimer's, a disease that does not appear to afflict chimps. "No one has ever compared human brain aging with brain aging in our closest living relative to identify what's really distinctive about humans," says Rilling. Because Melinda and the other chimps in the study have lived at Yerkes for most, if not all, of their lives, the researchers also have extensive behavioral and cognitive data from the animals that they hope to link to their structural and functional MRI findings. "They are excellent researchers, and the work they're doing is unique," says neurobiologist Pasko Rakic of Yale University. "Unfortunately, we don't know much of anything about the differences that emerged in the cerebral cortex during the last stages of primate evolution."

Today, they plan to do what is called diffusion tensor imaging (DTI), which reveals the direction that water molecules move, allowing the researchers to infer the location of fiber tracts in the white matter that carry signals from one place to another. Traditional MRI has nowhere near the resolution of DTI, nor does it show the direction of

Dead or alive. Todd Preuss does brain scans of living animals and autopsied ones.

Brain *Pan*. MRIs of chimp (*left*) and human heads reveal dramatic differences and similarities

CREDIT: JON COHEN

the pathways. A study they published in the April 2008 issue of *Nature Neuroscience* shows the power of the technique. Rilling, Preuss, and colleagues scanned brains to analyze the white matter fiber tract called the arcuate fasciculus, which connects two prominent language areas of the human brain, Wernicke's and Broca's. A comparative DTI revealed that humans have a pronounced projection of axons off the arcuate fasciculus that was much smaller in chimps and absent in monkeys. The researchers suspect that this projection plays a key role in our unique ability to use language.

Before DTI starts, they scan Melinda's head for known landmarks. "You can see just how small the chimpanzee brain is," says Preuss, pointing to a computer monitor that shows black-and-white, x-ray like images. "The big gray thing to the left is the tongue, and their tongues are bigger than their brains." Another odd site in the image turns out to be a vitamin E capsule taped to the left side of her head: Unlike most human brains, which typically have asymmetrical hemispheres, left and right look the same in a chimp, so the researchers need the capsule to orient themselves. Once they know where they are, DTI begins its foghorn "HO-OWs" and scans Melinda's brain in 60 different directions at once; computer software will later crunch those scans into a composite image. "You don't really see much until you average them out," says Preuss.

A key question they want to address is whether white matter declines with age in chimps, as it appears to do in humans. They also want to use these data to tackle a more fundamental problem: The components of the chimp brain remain hazy, so they want to construct an atlas of all its white matter pathways, which can then be compared with human pathways to help clarify what makes our brains tick. "If you look in anatomy textbooks, they show you white matter tracts that are mostly inferred from monkeys," says Rilling. "We know next to nothing about chimps."

Both Rilling and Preuss lament that biomedical research with chimpanzees is moving toward extinction, and they staunchly defend the ethics and significance of their work. Says Rilling: "The biggest and most important differences in neurobiology between humans and other species are going to come down to how the brain is wired and connectivity."

–JON COHEN

Getting Intimate With the Chimp Mind, Japanese Style

At Kyoto University's Primate Research Institute in Inuyama, researchers conduct cognitive experiments with 14 animals that are taking the field to new heights

INUYAMA, JAPAN—Located between Tokyo and Kyoto, this quaint town has attracted people from all over the country for more than 50 years to visit the Japan Monkey Centre, a mix of a zoo and a cheesy amusement park that features 650 primates from more than 70 species and a magic carpet ride. But just down the hill from the monkey park, 14 chimpanzees live far from the public eye—although they have grabbed the attention of scientists worldwide. The chimpanzees are research subjects at the Primate Research Institute (PRI), part of Kyoto University, and since 1978, Director Tetsuro Matsuzawa and his 13 co-workers have conducted cognitive studies here that have stretched *human* minds about the capabilities of our closest animal relatives.

Matsuzawa stands on a high balcony of PRI's research annex and looks down at the chimpanzees ambling about a monumental, tangled, five-story climbing tower. "Look at that!" Matsuzawa says, as a chimp tightropes between two portions of the tower's top. It is an astonishing sight. Yet even more impressive is what goes on inside the research annex.

A series of catwalks connects the outside enclosure to laboratory rooms inside the research annex, and each weekday morning, chimps amble through an enclosed metal catwalk to take part in a variety of experiments. The chimps enter a Plexiglas-walled booth within each room. Holes in the Plexiglas enable them to reach the touch-screen computers used in experiments. This morning, a chimpanzee named Ai and her son Ayumu enter the same room, and each begins tests on different computer screens.

The first experiment has received inter-

national media attention: Both mother and son have learned to recognize Arabic numerals in sequence and can remember their order even when the numbers are obscured milliseconds after they flash on the screen. When humans try the same task, we fail miserably. "This experiment clearly shows in this one cognitive domain, chimpanzees are superior to humans," says Matsuzawa. "No one can deny it; it's not a trick. We can repeat our findings in front of you. The highest standards of science are here. This is not ape-language research."

In a newer study, Matsuzawa and his team of graduate and postdoctoral students use a staple in experimental psychology known as the "Stroop task." The chimps have learned to touch a color that corresponds with specific Kanji symbols; the Stroop test will assess whether they have simply mastered the association of symbol to color or if they understand the word's meaning. The test relies on the fact that if the word for the color blue is written in red it takes longer for humans to read than if blue is written in blue. The computer tracks their success, and the researchers also videotape each chimp individually.

When the chimps are done, Matsuzawa dons what looks like a race-car driver's suit over his clothes, puts gloves on his hands, and enters the booth. Ayumu, a randy 8-year-old, obeys Matsuzawa's commands as he checks his teeth and weighs him, although he play-fights a little too hard at one point and receives a stern reprimand. Ai receives the same checkup, and when she urinates on the floor, Matsuzawa wipes it up with a paper towel so they can later extract hormone levels and assess whether ovulation affects her cognitive performance. "For 30 years, I've been in the same room with chimpanzees, and I still have all 10 of my fingers," boasts Matsuzawa.

The intimate relationship that Matsuzawa and his team have with their chimps is a key feature of PRI. Few of the researchers actually handle the chimps the way he does, but they share a philosophy that defines the institute. "The most important part of our research here is the chimpanzees are our partners," says Masayuki Tanaka, who did his graduate work at PRI and has remained there for 10 years studying perception. As Tanaka conducts a touch-screen experiment with Pan and her daughter Pal that gauges their ability to connect symbols to photographs, he emphasizes that both crawled through the catwalk and came to his lab by their own volition. "All we can do is call their names," he says. "Everything is voluntary."

> ***"We can repeat our findings in front of you. The highest standards of science are here. This is not ape-language research."***
>
> —TETSURO MATSUZAWA, PRI

Of course, the chimpanzees depend on the researchers for their food, and the experiments all involve treats. "It gives us so much power over them," acknowledges Laura Martinez, a French-Mexican graduate student who came here 3 years ago to study the ability of chimpanzees to connect voices to faces. Martinez, who before coming to PRI did a census study of wild chimps in Guinea and Mali, says people who study captive chimps must also confront whether their relationships with the animals affect their findings. "You love them as much as you love your family and you spend more time with them than you do with your family—so finally how objective can you be?" she asks.

Martinez, who ultimately wants to return to Africa to do chimpanzee conservation and sees a Ph.D. as a means to that end, is not simply criticizing her colleagues. She, too, has been swept away by her chimps. "Every morning, I wake up and all I'll want to do is come see these chimps," says Martinez. She is especially fascinated by Pan, the only chimpanzee in the world, says Martinez, that so far has demonstrated an ability to match voice to face. "I really wonder what she sees in me," Martinez says. "Does she realize how close I am to her species the way I see how close she is to mine?"

No studies, of course, can answer that question. But given the unusual glimpses into the chimp mind that have already come out of the innovative experiments at PRI, is it so far-fetched that an investigator would think to ask?

–JON COHEN

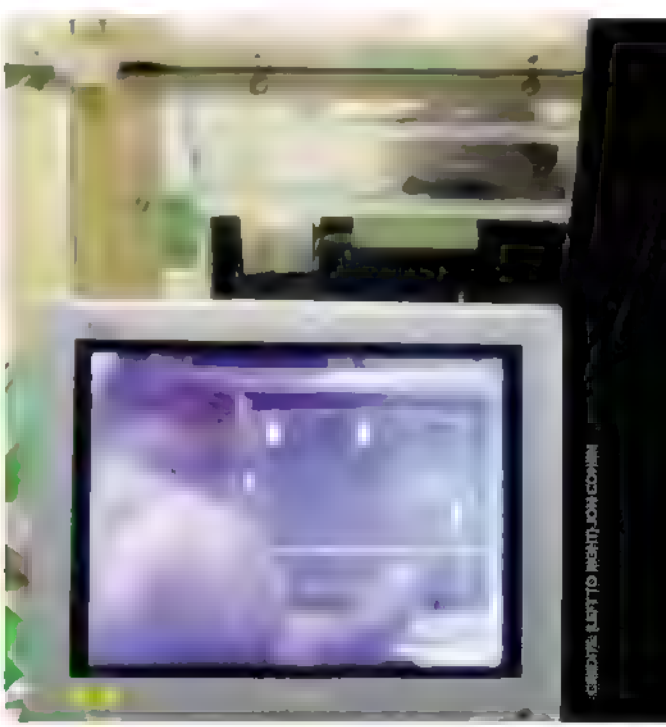

Cutting to the Bone Of Human Origins

Computed tomography scans of a large collection of skeletons from closely monitored captive chimpanzees will soon become part of UCSD's growing "anthropogeny" database

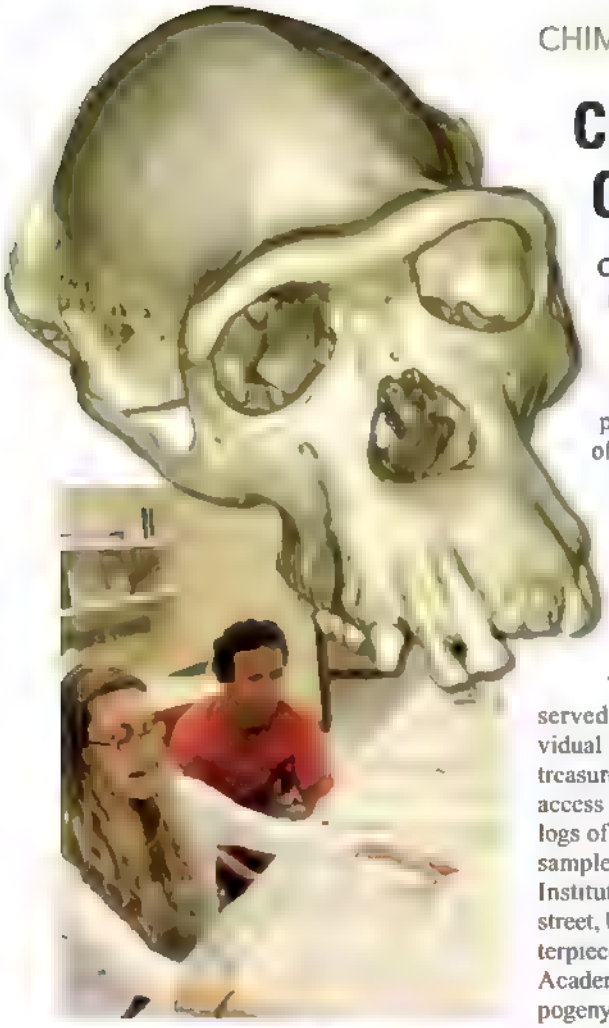

CREDITS (TOP TO BOTTOM): JOHN MORELAND, SAN DIEGO SUPERCOMPUTER CENTER; JON COHEN, 3)

Grateful dead. Froehle (*center*), Crittenden, and Gagneux (*top*) were thrilled that CARTA inherited bones and will post images like this skull online.

SAN DIEGO, CALIFORNIA—Over the past 2 years, the Primate Foundation of Arizona has sent the University of California, San Diego (UCSD), 51 of its chimpanzees. UCSD has no housing for chimpanzees or any other primates on campus. But this group did not require special caging or experienced animal handlers: They were dead.

The meticulously cleaned and preserved chimpanzee skeletons, each individual kept in a separate acid-free box, is a treasure trove for researchers, who can also access the medical records and observation logs of the animals, as well as stored serum samples. And in conjunction with the Salk Institute for Biological Studies across the street, UCSD is making the collection a centerpiece of its recently launched Center for Academic Research and Training in Anthropogeny (CARTA), which is now doing computed tomography scans of the bones and plans to make the digitized images available on the Internet. "The collection is really extraordinary," says Alyssa Crittenden, a postdoc in biological anthropology who is helping with the project. "We're so privileged and thankful to have it."

The atmosphere in the former lab room that holds the bones is more arty, Day of the Dead, than macabre. As part of the digitization project, Crittenden and biological anthropology grad student Andrew Froehle have spread out individual skeletons on tabletops. Froehle is wrapping each bone in plastic bubble wrap, which does not show up on the MRI and protects the skeletons during the scans. The walls feature photos of a few of the chimps now on the tables or inside the stacks of yellow boxes, as well as old chimp-centric poster art, all gifts from Primate Foundation of Arizona Director Jo Fritz, who once bred the animals for the U.S. National Institutes of Health (they died from natural causes) but is closing up shop because funding ran out.

UCSD evolutionary biologist Pascal Gagneux, the associate director of CARTA, holds up the skull of a 2-month-old chimpanzee and points to the nearly fused sutures that separate its plates. "If you have to do an autopsy on a neonate chimp, you need a hacksaw," says Gagneux, who previously studied wild chimps in the Taï National Park in Côte d'Ivoire and now does lab studies of chimpanzee reproduction. "On a human neonate skull, you can just peel it open." The earlier fusion of the chimp skull reflects an important biological difference between us and them: Our brains are less developed at birth and complete their growth much later, which means human children have a longer period of time in which to wire their brains, possibly explaining why we have such unusually sophisticated social skills.

It's questions like these that CARTA hopes to bring into sharper focus. Spearheaded by UCSD glycobiologist and evolutionary biologist Ajit Varki, UCSD anthropologist Margaret Schoeninger, and Salk neurogeneticist Fred Gage, CARTA evolved from a project that since 1998 has gathered together the world's leading chimpanzee researchers with colleagues from diverse disciplines who study human origins (the meaning of "anthropogeny"). These CARTA "members," who hold public talks when they come to town for symposia several times each year, contribute to a Museum of Comparative Anthropogeny that has the ambitious aim of cataloging every difference between humans and other great apes; to date, they have compiled more than 500 entries, fewer than 10% of which are anatomical. "CARTA has snowballed into a productive and incredibly interdisciplinary group of scientists with a shared interest in human origins," says Gagneux. "We're far from reciprocal fluency in each other's scientific languages, but all sides are making admirable efforts at translating." CARTA also offers graduate-level classes and hopes to launch a journal, *Anthropogeny*.

The birth of CARTA, as Varki stresses, illustrates that two of the oldest questions about humans—where do we come from and how did we get here—"have become tractable issues for scientific inquiries." The fledgling center also demonstrates that an academic institution doesn't need living chimpanzees to become a locus to advance what science knows about them.

–JON COHEN

To Enrich or Not To Enrich:

How Target Enrichment Can Advance Your Research

WEBINAR

Several methodologies for performing DNA target enrichment prior to next generation sequencing have been developed and utilized in a growing number of experimental studies. As the price of next gen sequencing continues to fall, the debate around whether to perform some type of selection is ongoing.

A number of variables must be considered to make the best decision, including the number of samples, the amount of DNA available, the sequencing platform used, budget, reproducibility requirements, and the availability of automation. To clarify some of these issues, you are invited to view a discussion of the strategies for DNA target enrichment with our panel of distinguished thought leaders in a video webinar being presented online and live at the AAAS headquarters in Washington, D.C.

During the broadcast, the presenters will:

- provide a general introduction to the target enrichment methods they use
- discuss how these technologies can be applied to the next gen sequencing workflow
- share data from studies that have benefited from their approaches
- answer your questions live!

Monday, April 19, 2010
7 p.m. Eastern;
4 p.m. Pacific;
11 p.m. GMT

Join our panel of experts in a live discussion. Register to participate.

Questions can be submitted live to the panel during the webinar or in advance via e-mail provided with registration. To register, visit

www.sciencemag.org/webinar

Participating Experts:

Dr. Dale Hedges
Hussman Institute for Human Genomics
Miami, FL

Dr. Elaine Mardis
Washington University in St. Louis
St. Louis, MO

Dr. Jun S. Wei
National Institutes of Health
Bethesda, MD

Sponsored by:
Agilent Technologies

Science
AAAS

Brought to you by the *Science* AAAS Business Office

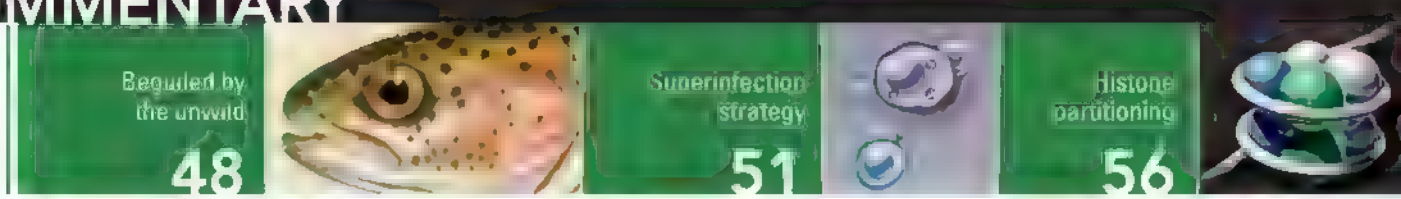

LETTERS

edited by Jennifer Sills

Consent Contraindicated?

THE POLICY FORUM BY B. A. LIANG AND T. MACKEY ("REFORMING OFF-LABEL promotion to enhance orphan disease treatment," 15 January, p. 273) provides a thoughtful and provocative roadmap for the rational development of drugs that are approved for one indication and prescribed "off-label" for another.

However, we wonder whether the preclinical toxicological assessment, combined with the post-marketing safety assessment, provides adequate assurance of safety for the proposed off-label use. We are particularly concerned about the intrathecal and epidural (spinal), and perineural (next to a nerve) delivery of drugs developed for systemic administration. Preclinical research and human experience have taught us that such neuraxial drugs can evoke tissue toxicity unique to the spinal space (*1*, *2*).

We agree that clinical trials are necessary to determine the efficacy of off-label uses. However, a universal requirement of such trials is that the subjects are permitted to make an informed risk assessment. Yet if preclinical safety data by the proposed route of drug administration do not exist—as is frequently the case for neuraxial and perineural administration—then there are no data to guide the subject in making the informed decision. In our experience, local institutional review boards (IRBs) often do not realize the unique risks of neuraxial or perineural administration, and studies are approved that cannot have provided subjects with required information.

The journals *Anesthesiology* and *Anesthesia and Analgesia*, where two of us are editors-in-chief (J.C.E. and S.L.S., respectively), have frequently received submissions describing studies, approved by local IRBs, that involve neuraxial or perineural drugs not previously assessed for safety by these routes. It has raised the journals' concerns, leading to editorial policies requiring regulatory approval for all studies of off-label neuraxial administration, unless there is overwhelming evidence of safety through accepted or widespread use (e.g., intrathecal fentanyl) (*3*).

Liang and Mackey's recommendations are rational and will provide physicians with better therapies and more informed treatment decisions for many illnesses. However, in expanding off-label use, adequate preclinical safety data must exist when route, dose, indication, or population (e.g., adult versus neonate) are fundamentally different from those for which the drug has been approved.

TONY L. YAKSH,[1]* JAMES C. EISENACH,[2] STEVEN L. SHAFER[3]

[1]Department of Anesthesiology and Pharmacology, University of California, San Diego, La Jolla, CA 92093, USA. [2]Department of Anesthesiology, Wake Forest University, Winston-Salem, NC 27103, USA. [3]Department of Anesthesiology, Columbia University, New York, NY 10032, USA.

*To whom correspondence should be addressed. E-mail: tyaksh@ucsd.edu

References

1. T. L. Yaksh *et al.*, *Anesthesiology* **99**, 174 (2003)
2. K. Drasner, *Br. J. Anaesth.* **102**, 729 (2009)
3. S. L. Shafer, *Anesth. Analg.* **105**, 13 (2007)

Response

YAKSH, EISENACH, AND SHAFER RAISE AN important issue associated with off-label drug use. As they point out, many IRB-approved studies do not take into account populations or route of administration when assessing disclosure adequacy and informed consent. Basing clinical drug research project approvals on work that uses different routes of administration or patient populations than that proposed cannot and should not be the basis for safety evaluations. If they are, IRBs are acting on inappropriate information, and through such faulty project approval would not be fulfilling their key role of ensuring study participant safety. We applaud *Anesthesiology* and *Anesthesia and Analgesia* for their policies addressing IRB limitations, and would strongly advocate that all journals adopt similar policies.

BRYAN A. LIANG[1,2]* AND TIM MACKEY[1]

[1]Institute of Health Law Studies, California Western School of Law, San Diego, CA 92101, USA. [2]San Diego Center for Patient Safety, Department of Anesthesiology, University of California, San Diego School of Medicine, San Diego, CA 92103, USA.

*To whom correspondence should be addressed. E-mail: baliang@alum.mit.edu

Polystyrene Overestimated

THE RANDOM SAMPLES PIECE "MAGIC MUSHroom" (11 December 2009, p. 1463) cited data that polystyrene is now 25% of landfill volume. Overestimates of polystyrene (PS) in the waste stream have abounded since in the mid-1980s. Various surveys of waste generators and disposal facilities have found that PS is actually a very small part of the overall waste stream. The latest survey we found (*1*) reported that expanded PS was 0.8% of wastes disposed in Connecticut, by weight. EPA's modeling (*2*) estimated that there were 2.6 million tons of PS discarded in 2008, which is a substantial amount. However, that tonnage is only 1.6% of all estimated discards. Even though PS is a low-density material, it is hard to believe that these relatively small masses could amount to 25% of the volume of discards in landfills. That's a good thing, because the stability of those landfills depends on more massive, cohesive materials comprising most of the wastes.

DAVID J. TONJES[1,2]* AND R. L. SWANSON[2]

[1]Department of Technology and Society, Stony Brook University, Stony Brook, NY 11794–3760, USA. [2]Waste

Reduction and Management Institute, Stony Brook University, Stony Brook, NY 11794–5000, USA.

*To whom correspondence should be addressed. E-mail: david.tonjes@stonybrook.edu

References

1 DSM Environmental Services, Inc., Cascadia Consulting Group, Inc., Mid-Atlantic Solid Waste Consultants, "Waste characterization study. Results of first round of sampling" (2009), p. 17; www.ct.gov/dep/lib/dep/waste_management_and_disposal/solid_waste/wastecharstudy/final_interim_report_july_6_to_ctdep_7_10.pdf

2 U.S. Environmental Protection Agency, "Municipal solid waste generation, recycling, and disposal in the United States. Detailed tables and figures for 2008" (EPA, 2009), Tables 2 and 7; www.epa.gov/osw/nonhaz/municipal/pubs/msw2008data.pdf

Suitability of Artificial Nests

THE REPORT "LOWER PREDATION RISK FOR migratory birds at high latitudes" by L. McKinnon *et al.* (15 January, p. 326) describes a massive artificial nest experiment spanning 29 degrees of latitude in the high Arctic. The authors suggest that artificial nests are appropriate for this sort of investigation because they allow a controlled study of predation risk. However, several studies show that artificial nests are not representative of real nests (*1*–*4*), including one by the authors of the Report, which found that predators of artificial nests included arctic foxes, jaegers, and gulls, whereas predators of real nests were confined to foxes (*4*). The studies in *Conservation Biology* (*1*–*3*), which compare artificial nests and real nests in the same location, show different predation rates and completely different dominant predators. Such substantial differences indicate that meaningful ecological or conservation statements cannot be made on the basis of artificial nest studies. McKinnon *et al.* did not even attempt to correlate their findings with data from real nests from that region [e.g., (*5*, *6*)].

JOHN FAABORG

Division of Biological Sciences, University of Missouri, Columbia, MO 65211–7400, USA. E-mail: faaborgj@missouri.edu

References

1 F. R. Thompson III, D. E. Burhans, *Conserv. Biol.* **18**, 373 (2004).
2 D. M. Burke *et al.*, *Conserv. Biol.* **18**, 381 (2004).
3 P. Batáry, A. Báldi, *Conserv. Biol.* **18**, 389 (2004).
4 L. McKinnon, J. Bêty, *J. Field Ornithol.* **80**, 280 (2009).
5 P. A. Smith, H. G. Gilchrist, J. N. M. Smith, *Condor* **109**, 15 (2007).
6 J. R. Jehl Jr., *Ecology* **52**, 169 (1971).

Response

FAABORG PRESENTS A VALID CONCERN THAT ARTIficial nests should not be used to infer real nest success. For our study, we chose artificial nests to provide a controlled measure of relative predation risk across latitudes, not to infer real nest success. In real nests, success is not determined by predation risk alone, but by a combination of factors including nest defense capabilities (*1*), the degree of parental care (*2*), incubation duration (*3*) and break frequency (*4*), and nest density. Artificial nest experiments permit us to control for these sources of heterogeneity to make meaningful ecological statements concerning predation risk in arctic-nesting birds (*5*, *6*).

It is true that when artificial nests are not physically representative of real nests, differences in predation rates and dominant predators may arise (*7*–*9*). This critique has merit in temperate and tropical regions where bird nest structure is often complicated and difficult to mimic and the diversity of potential predators is high. On the Arctic tundra, where we conducted our study, this critique is not compelling. Arctic-nesting shorebirds excavate a small depression (scrape) in the tundra, upon

which uncovered eggs are laid. To mimic a real nest, artificial shorebird nests require no structural material, just eggs placed upon a depression with a small marker hidden underneath. In addition, the diversity of potential predators is low in the Arctic. Limited camera monitoring at both real and artificial shorebird nests in the Arctic has revealed the arctic fox (*Alopex lagopus*) as the dominant predator (*10*–*12*), with avian predators such as jaegers (*Stercocarius spp.*) and gulls (*Larus spp.*) depredating both real (*11*) and artificial nests (*12*) in smaller proportions. That detection of avian predators can be higher at artificial nests (*12*) could demonstrate that shorebirds' defense of their nests from avian predators is more effective (*13*).

Estimates of real nest success may permit us to evaluate the effectiveness of anti-predator strategies, but the underlying risk of predation may remain masked if these strategies are indeed efficient. Measurements of anti-predator behavior along with the full suite of factors influencing the survival of real nests would be a better complement to our study than would measures of real nest success alone.

L. MCKINNON,[1]* P. A. SMITH,[2] E. NOL,[3] J. L. MARTIN,[4] F. I. DOYLE,[5] K. F. ABRAHAM,[6] H. G. GILCHRIST,[7] R. I. G. MORRISON,[3] J. BÊTY[1]

[1]Département de Biologie, Université du Québec à Rimouski and Centre d'Etudes Nordiques, Rimouski, QC G5L 3A1, Canada. [2]Environment Canada, National Wildlife Research Centre, Ottawa, ON K1A 0H3, Canada. [3]Ecology and Conservation Group, Environment and Life Sciences Graduate Program and Biology Department, Trent University, Peterborough, ON K9J 7B8, Canada. [4]Département Dynamique des Systèmes Ecologiques, Centre d'Ecologie Fonctionnelle et Evolutive, Centre National de la Recherche Scientifique, Montpellier, France. [5]Wildlife Dynamics Consulting, Telkwa, BC V0J 2X0, Canada. [6]Wildlife Research and Development Section, Ontario Ministry of Natural Resources, Peterborough, ON K9J 7B8, Canada. [7]Environment Canada, National Wildlife Research Centre and Department of Biology, Carleton University, Ottawa, ON K1S 5B6, Canada.

*To whom correspondence should be addressed. E-mail: laura.mckinnon3@gmail.com

References

1. J. Kis, A. Liker, T. Szekely, *Ardea* **88**, 155 (2000).
2. P. A. Smith, H. G. Gilchrist, J. N. M. Smith, *Condor* **109**, 15 (2007).
3. D. Schamel, D. M. Tracy, *J. Field Ornithol.* **58**, 126 (1987).
4. T. E. Martin, J. Scott, C. Menge, *Proc. Biol. Sci.* **267**, 2287 (2000).
5. J. Bêty, G. Gauthier, J.-F. Giroux, E. Korpimäki, *Oikos* **93**, 388 (2001).
6. J. Bêty, G. Gauthier, E. Korpimäki, J.-F. Giroux, *J. Anim. Ecol.* **71**, 88 (2002).
7. F. R. Thompson III, D. E. Burhans, *Conserv. Biol.* **18**, 373 (2004).
8. D. M. Burke *et al.*, *Conserv. Biol.* **18**, 381 (2004).
9. P. Batáry, A. Báldi, *Conserv. Biol.* **18**, 389 (2004).
10. R. V. Cartar, R. D. Montgomerie, *Behaviour* **95**, 261 (1985).
11. J. R. Liebezeit, S. Zack, *Arctic* **61**, 153 (2008).
12. L. McKinnon, J. Bêty, *J. Field Ornithol.* **80**, 280 (2009).
13. T. Larsen, T. A. Sordahl, I. Byrkjedal, *Biol. J. Linn. Soc.* **58**, 409 (1996).

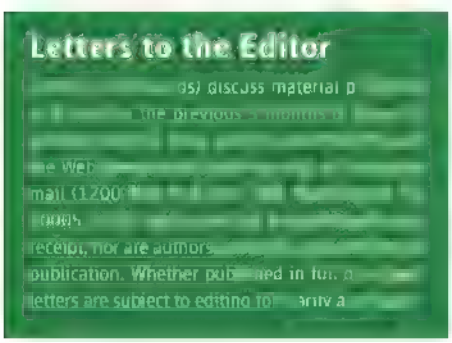

CORRECTIONS AND CLARIFICATIONS

News of the Week: "Polish science reforms bring fear and hope" by E. Pain (19 March, p. 1442). Stanisław Karpiński's name was incorrect. The name has been corrected in the online HTML version.

Random Samples: "Magic mushroom" (11 December 2009, p. 1463). The statistic that polystyrene is now 25% of landfill volume was incorrectly attributed to the EPA. The EPA does not measure volume, only weight. The data were from a San Francisco State University study.

ECOLOGY

Hatching a Mongrel Species

Jared Farmer

Rainbow trout (*1*) used to be a Pacific Rim fish. In historic times, the numerous discrete populations from Baja California to the Kamchatka Peninsula could be grouped into two ecological types, stream trout and anadromous trout (which migrate from the sea to freshwater to spawn). In America, the latter populations became known as steelhead. Starting in the late 19th century, Americans added a third type, hatchery trout. Like the original rainbows, these fish could travel long distances to spawn, but they expended no energy of their own to do so. Instead, people served as their vector, transporting them in trains, trucks, airplanes, and milk cans. Today, rainbow trout can be found on every continent and in every climate; it is the most ubiquitous stocked game fish on Earth. These planned introductions, like all things human, have produced unplanned consequences.

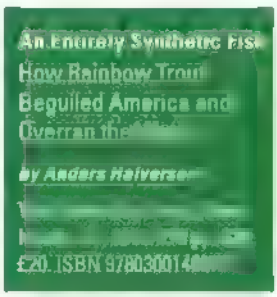

According to Anders Halverson, almost all hatchery rainbows share some ancestry in a Northern California broodstock from the McCloud River—now an arm of Shasta Lake. There, in the 1870s, the U.S. Fish Commission established a hatchery, initially for Pacific salmon. Conservationists back East wanted to import western fish to restock streams degraded by agriculture, logging, and industry. After the failure of Pacific salmon introductions, the station experimented with rainbow trout (a congener). Agents placed fertilized eggs between layers of wet moss in boxes with ice blocks and shipped them by transcontinental railroad.

Rainbows became successful invaders for three main reasons: they make good game; they can tolerate warmer and siltier waters than can other game fish; and they grow well in hatcheries. In the 19th century, the species appealed to acclimatization societies (who wanted to increase what we now call species richness) and river renovationists (who shared the goals, if not the techniques, of later restorationists). Eastern anglers, predominantly elite white males, also wanted to encourage sport fishing as a way of promoting "American" values and manliness. Rainbows had a Goldilocks effect on fly fishermen, notes Halverson. European brown trout were too hard to catch, eastern brook trout too easy. Rainbows were "just right." After biting easily at the surface, they fought the reel with aerial displays.

In the 20th century, a governmental apparatus grew up alongside trout stocking. The state-level hatchery system in the United States can be compared to its local highway system, in which taxes on gasoline funded road construction, which encouraged more fuel consumption. Similarly, state hatcheries were funded from fishing licenses and a special sales tax on fishing equipment. The more people fished, the more money there was for making fish. Hatcheries became popular fixtures throughout the West. Halverson quotes an official from Washington state who courted controversy when he proposed closing more than one hatchery—what you get if "you cross a sacred cow with a military base."

Until recently, hatcheries cared more about self-perpetuation and customer satisfaction than science. Their measure of success was the "return to creel"—the number of fish taken home by anglers. To increase the return, fish and game departments got in the habit of announcing the dates and times of rainbow releases. Thus, in the span of a few hours, a fish might travel the full circuit from hatchery pond to delivery truck to open water to outdoor grill. In 1949, California pioneered the use of surplus military aircraft to aerially stock alpine lakes with rainbow, brook, and golden trout. This kind of biological bombing is still practiced throughout the West. Thankfully, state officials no longer eradicate native fish using chemicals such as rotenone. Alverson chronicles one egregious episode from 1962 when Utah and Wyoming poisoned the entire upper watershed of the Green River (some 15,000 square miles), creating a clean slate to be filled with trout. They called it "rehabilitation."

Before environmentalists made an issue of rainbows, Trout Unlimited complained about annual stocking. The group had no beef with non-native fish; it just wanted "wild" rainbows rather than the latest hatchery product. As Halverson explains, much of the restocking was in fact a waste. Bureaucrats assumed that streams needed to be replenished each year, and they had the budget to do that, so they did. A contrarian fish biologist employed by the state of Montana demonstrated through electroshock censuses in the 1960s and 1970s that the maintenance of population levels came not from restocking per se, but

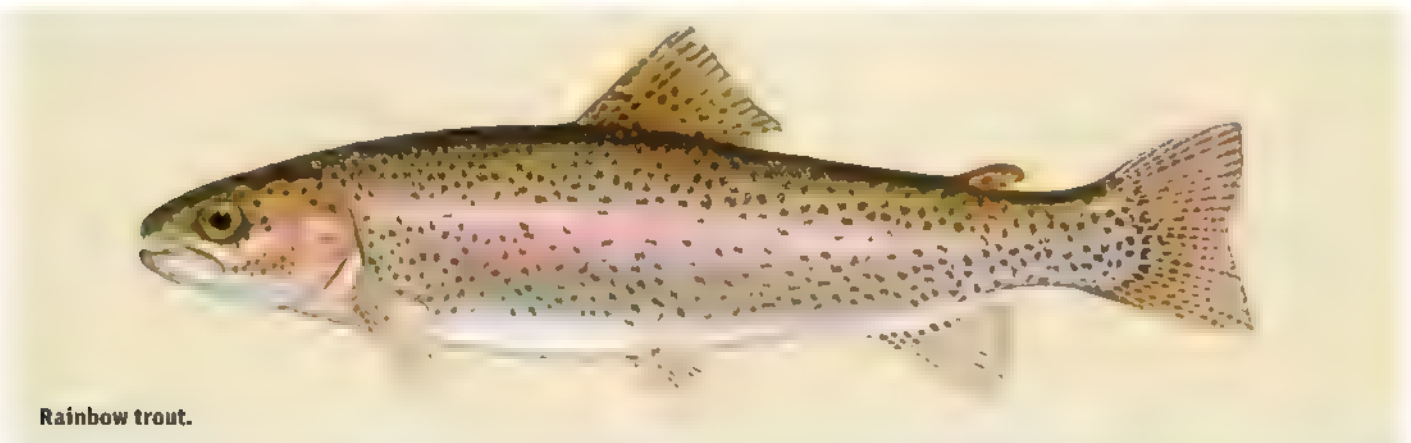

Rainbow trout.

CREDIT: U.S. FISH AND WILDLIFE SERVICE

The reviewer is at the Department of History, State University of New York, Stony Brook, NY 11794, USA. E-mail: jared.farmer@stonybrook.edu

from attrition caused by the contest between resident and incoming trout. After some wild public hearings, Montana conceded to science, stopped stocking its rivers, and focused instead on reservoirs where rainbows could not reproduce. Montana has since developed a healthy tourist economy around the quality of its catch-and-release river fishing rather than its gross creel rate.

Colorado did things differently. It stuck by its hatcheries even after their rainbows became infected with whirling disease. The Centennial State now stocks a new rainbow hybrid that is disease-resistant. The hope is that the hybrid will pass on its resistance to rainbows in the wild. Meanwhile, Colorado's greenback cutthroat swims in dangerous waters. The greenback is one of numerous subspecies of cutthroat trout native to the interior West, island populations left from wetter geologic periods. Several of the cutthroats, including the greenback, are federally listed as threatened. The legality of this is debatable, because it is hard to define what the species is anymore. DNA testing has shown that nearly every cutthroat population has to some degree hybridized with rainbows. In Halverson's words, "Rainbow genes have become their own entity." He repeats a 1988 warning from cutthroat experts that the trout of the North American West could homogenize into a single taxon, "*Salmo ubiquiti*" (*2*).

In the wake of environmentalism and conservation biology, some agencies (notably the U.S. Fish and Wildlife Service and the California Department of Fish and Game) have tried to ameliorate the damage caused by trout introductions. In the high Sierra Nevada, native amphibians, especially frogs, cannot coexist with non-native fish. Paradoxically, California still stocks many Sierran lakes, and advertises their locations, even as it actively removes all fish from other nondisclosed lakes. Fishers legitimately question whether it is fair to apply their user fees and tax dollars toward the eradication of their favorite catch

Halverson, an avid angler, seems well equipped to tackle his topic: he has a Ph.D. in aquatic ecology and experience in journalism What he lacks is training in history, and that shows. Broad-scale cultural, political, and economic developments get shallow treatment Halverson prefers to use biographical figures to propel his narrative. It is surprising, then, that he writes so little about the pervasive stocking done by private citizens—characters such as Finis Mitchell, the Wyoming man who almost single-handedly stocked hundreds of fishless lakes in the Wind River Mountains (*3*). In spite of the book's subtitle, which promises a discussion of the rainbow's global diaspora (including self-sustaining populations in New Zealand and South Africa), Halverson rarely ventures outside the United States. The author is mainly concerned with the impacts of hatchery rainbows on fisheries in the inland West. He merely nods to the issue of genetically modified farmed trout. Chile, the world's leader in rainbow aquaculture, appears nowhere in the text.

Halverson works best in his journalistic mode when he travels to western alpine watersheds to interact with "fish squeezers," wardens, and ichthyologists. Through trips and interviews, Halverson entertainingly introduces some of the most tangled questions in conservation biology: What is a species? What is native? What is natural? What is wild? His account does not pretend to be a source for definitive answers or theoretical contexts. For a deeper discussion of many of the same issues, the curious can seek out several recent books on Pacific salmon (*4*-*7*). But for casual readers, including undergraduates and trout enthusiasts, *An Entirely Synthetic Fish* may have gotten it "just right" sciency enough, not too scientific.

References and Notes

1 Scientific names of taxa mentioned in the text: rainbow and steelhead trout, *Oncorhynchus mykiss* (formerly *Salmo mykiss*); golden trout, *O. m. aguabonita*; Pacific salmon, collectively, six species (chum, *O. keta*; pink, *O gorbuscha*; sockeye, *O. nerka*, chinook, *O. tshawytscha*; coho, *O. kisutch*; and masu, *O. masou*); cutthroat trout, *O. clarki*; greenback cutthroat, *O. c. stomias*; brown trout, *Salmo trutta*; brook trout, *Salvelinus fontinalis*.
2 W Allendorf, R. F Leary, *Conserv Biol* 2, 170 (1988.
3 J Nichols, in *Preserving Western History*, A. Gulliford, Ed. (Univ. New Mexico Press, Albuquerque, 2005), pp. 263–271
4 J. E Taylor, *Making Salmon. An Environmental History of the Northwest Fisheries Crisis* (Univ. Washington Press, Seattle, 1999)
5 J Lichatowich, *Salmon Without Rivers: A History of the Pacific Salmon Crisis* (sland, Washington, DC, 1999,
6 R. Scarece, *Fishy Business. Salmon, Biology, and the Social Construction of Nature* (Temple Univ Press, Philadelphia, 1999).
7 T P Quinn, *The Behavior and Ecology of Pacific Salmon and Trout* (Univ Washington Press, Seattle, 2005)

10.1126/science.1188526

BROWSINGS

Oceanic Anglerfishes: Extraordinary Diversity in the Deep Sea. Theodore W Pietsch. University of California Press, Berkeley, 2009. 569 pp. $85, £59. ISBN 9780520255425.

The cold, dark, nutrient-poor ocean waters below 1 km are home to a surprisingly abundant and diverse clade of anglerfish, the ceratioids. These bizarre predators use a bacterial light organ on the tip of their first dorsal spine to lure prey within reach of their gaping mouth of raptorial teeth. They are also extremely sexually dimorphic; males attach themselves (sometimes permanently) to the much larger, blobbike bodies of females. After detailing "seadevil" diversity, evolution, and distribution, Pietsch discusses bioluminescence, locomotion, feeding, and reproduction. He then comprehensively reviews the suborder's families, genera, and 160 known species (such as *Himantolophus appelii*, left). Although written for fish biologists, this profusely illustrated account should inspire wider interest in these fascinating hobgoblin fish.

Fishes of the Open Ocean: A Natural History and Illustrated Guide. Julian Pepperell; illustrated by Guy Harvey. University of New South Wales Press, Sydney, Australia, 2009. 272 pp. A$54.50. ISBN 9780868407005. University of Chicago Press, Chicago, 2010. $35, £22.50. ISBN 9780226655390.

Relatively few fish species are found in surface waters (down to 200 m) far from land. But these include the largest, swiftest, most prolific, and farthest migrating fish. Some are permanent residents, some spend part of their life cycles at sea, and others are only occasional visitors. Pepperell begins with short discussions of food webs, morphologic adaptations that have independently evolved in several groups, and the impacts of commercial and sports fisheries. The remainder of the book summarizes the identification, distribution, and biology of all major open ocean species, including billfish, tuna, mackerels, jacks, and pelagic sharks and rays. Harvey has painted each species; many are also presented in informative underwater photographs (right, yellowfin tuna, *Thunnus albacares*, prowling the surface).

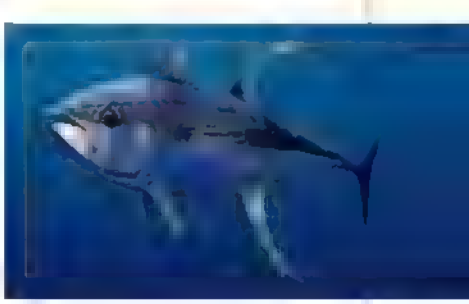

CREDITS (LEFT) THEODORE W PIETSCH/UNIVERSITY OF WASHINGTON (RIGHT) C. & M FALLOWS/SEAPICS.COM/COURTESY UNIVERSITY OF NEW SOUTH WALES PRESS

ENVIRONMENT

China's Road to Sustainability

Complex interactions of various forces create a bumpy road to environmental sustainability in China.

Jianguo Liu

Although China has achieved exceptional economic growth and has endeavored to protect the environment since its founding in 1949, it ranked 133rd among 146 countries assessed for environmental sustainability in 2005 (*1*). Many forces (e.g., socioeconomic, political, demographic, and technological) influence China's environmental sustainability. Any individual force can cause positive and negative impacts on sustainability directly or indirectly. This forum illustrates the complexity of forces that have affected China's sustainability over the past six decades and offers perspectives for the future.

Both internal and external forces vary across space and time. They can enhance or offset each other differently depending on the context, which often leads to nonlinear and unexpected consequences. During the past 60 years, negative impacts have been stronger than positive ones, with most environmental conditions worsening and few improving. The "Great Leap Forward" movement (1958–1961) the loss of at least 10% of China's forests to fuel backyard furnaces for steel production (*2*). The "Learn from Dazhai in Agriculture" movement (1964–1978) transformed numerous landscapes and filled countless lakes, wetlands, and coastal areas for crop production with little regard for topographic, climatic, and socioeconomic conditions (*3*). Since the economic reform and open-door policy started in 1978, the massive production of many export goods has caused further resource depletion and environmental pollution.

Of the >100 environmental laws and policies enacted since the 1970s, most have ineffective implementation and enforcement. Although sustainable development has been a national strategy since 1994, short-term economic gain still has priority. Some positive actions, such as the calculation of green GDP in 2004–2005 (*4*) (i.e., discounting gross domestic product by incorporating environmental costs) were short-lived because many government officials were concerned about their jobs and promotions, which were solely or mainly based on economic performance. The widespread ideology of "development first, environmental protection later" or "pollute first, then clean up" is a root cause of China's low ranking in environmental sustainability (*5*).

Center for Systems Integration and Sustainability, Michigan State University, East Lansing, MI 48823, USA. E-mail: jliu@panda.msu.edu

There are some positive signs, however. The nature reserve system now occupies 15.1% of China's territory (higher than the world average) (*6*). The Natural Forest Conservation Program (*7*) banned logging of natural forests after the devastating floods of 1998 that were widely believed to be the result of deforestation and soil erosion. China's economy, dominated by polluting, low-efficiency industry, is gradually being replaced by a circular economy that applies the principles of "reduce, reuse, and recycle" and uses one facility's waste as another facility's input. Since attending the 1972 United Nations Conference on the Human Environment, China has begun to recognize environmental problems, signed international environment-related treaties, imported green technologies, and collaborated with foreign countries and international organizations to undertake environmental actions in China. The National Climate Change Program has aimed to lower energy consumption per unit of GDP by 20% between 2006 and 2010 (*8*) through economic restructuring and closing outdated factories. Furthermore, China plans to reduce CO_2 emissions per unit of GDP by 40 to 45% from its 2005 level by 2020 through developing a low-carbon economy and more renewable energy (*9*).

In many cases, the government's intention has been good but has been met with surprises. Extensive efforts to plant trees in many arid and semiarid regions have caused environmental deterioration because trees consume too much of the limited soil moisture, reduce overall vegetation cover, and lead to more severe wind erosion (*10*). The one-child policy, started in 1979, responded to inaction that had led to a population of 975 million, 80% higher than in 1949 (*11*). It averted more than 300 million births by 2005 (*8*), which has had debatable social effects but can be seen as beneficial to the environment. However, the number of households has increased much faster than the population since 1979 owing to such factors as more divorces and a lower proportion of multigenerational households. Reduction in household size alone added 80 million households from 1985 to 2000 (*12*). More households consume more resources and generate more waste, and smaller households lower the efficiency of resource use.

What will China's future road to sustainability look like? It will depend on the timing, durations, strength, and complex interactions of existing and emerging forces in China and elsewhere. Bolder actions are needed to weaken negative impacts and to strengthen positive ones. Here are two examples: Efforts to promote environmental sustainability should be a major criterion for evaluating government officials nationwide (*13*). More sustainability actions should take place in households, the basic socioeconomic units of consumption. Households can increase resource use efficiency and reduce emissions in many ways (*14*). Formation of new households can be slowed by discouraging divorce (e.g., implementing a longer waiting period for couples seeking to divorce) (*15*). Government incentives such as tax credits and subsidies can promote co-housing and thus increase sharing of household goods.

China's transition to sustainability should take advantage of its ability to implement massive programs that can infiltrate every aspect of society rapidly. Furthermore, China's economic strength gives it an unprecedented opportunity to become a global leader in sustainability through institutional, scientific, and technological innovations.

References and Notes

1. 2005 Environmental Sustainability Index; www.yale.edu/esi
2. J. Shapiro, *Mao's War against Nature* (Cambridge Univ. Press, Cambridge, 2001)
3. J. Zhao, J. Woudstra, *Landsc. Res.* **32**, 171 (2007)
4. Chinese Academy for Environmental Planning (CAEP), *China Green National Accounting Study Report 2004* (CAEP, Beijing, 2006).
5. Y. Pan, *Thoughts about China's Environmental Issues* [in Chinese] (Environmental Culture Promotion Association, Beijing, 2007)
6. Ministry of Environmental Protection (MEP), *Bulletin of National Environmental Statistics 2008* [in Chinese] (MEP, Beijing, 2009)
7. J. Liu, S. Li, Z. Ouyang, C. Tam, X. Chen, *Proc. Natl. Acad. Sci. U.S.A.* **105**, 9477 (2008).
8. National Development and Reform Commission (NDRC), *China's National Climate Change Program* [in Chinese] (NDRC, Beijing, 2007)
9. "China announces targets on carbon emission cuts," Xinhua News Agency, http://news.xinhuanet.com/english/2009-11/26/content_12544181.htm.
10. S. Cao, *Environ. Sci. Technol.* **42**, 1826 (2008)
11. China Population and Development Research Center, "1949–1998 total population of China" (CPDRC, Beijing, 2010), www.cpirc.org.cn/en/totpope.htm.
12. J. Liu *et al.*, *Nature* **421**, 530 (2003)
13. Q. Tang, *J. Hunan Admin. Inst.* **2009**, 9 (2009)
14. T. Dietz, G. T. Gardner, J. Gilligan, P. C. Stern, M. P. Vandenbergh, *Proc. Natl. Acad. Sci. U.S.A.* **106**, 18452 (2009)
15. J. Liu, J. Diamond, *Nature* **435**, 1179 (2005).

16. I thank anonymous reviewers; J. Broderick, S. Cao, X. Chen, P. Esselman, K. Frank, J. Gong, S. Li, Y. Li, W. Liu, J. Luo, W. McConnell, J. Millington, W. Taylor, M. Tuanmu, A. Vina, and W. Yang for comments and assistance; and NSF, National Aeronautics and Space Administration, and Michigan Agricultural Experiment Station for financial support.

10.1126/science.1186234

VIROLOGY

A Vaccine Monkey Wrench?

The mechanism by which monkeys succumb to secondary infection by a herpesvirus may explain the difficulty in developing a human vaccine.

Hartmut Hengel[1] and Ulrich H. Koszinowski[2]

Cytomegalovirus (CMV) is an enveloped DNA virus that, like other herpes viruses, establishes life-long latency in its host after infection. Reactivation of latent virus or secondary infection by the same (or similar) virus frequently occurs, confounding the host's ability to establish immune protection. In industrialized countries, primary, recurrent, and secondary infection during pregnancy is the greatest cause of many congenital diseases such as childhood deafness, and neurological handicaps, including mental retardation. Hence, development of a vaccine against human CMV is a high priority (*1*). On page 102 of this issue, Hansen *et al.* (*2*) elucidate how CMV reinfects its human host despite the immune system's capacity to control primary infection.

CMVs are species-specific and express proteins that modulate host functions to enhance their survival. This includes inhibiting the process by which T cells are presented viral antigen to specify their reactivity. Antigen presentation involves loading viral antigen fragments onto major histocompatibility complex (MHC) class I molecules for display on the surface of host cells. The MHC class I–antigen complex is presented to cytotoxic $CD8^+$ T cells. These T cells can prevent viral spread by destroying infected cells. CMV proteins block MHC class I antigen presentation (*3*), and although the underlying molecular mechanisms are known (*4*), it has been difficult to pinpoint their role during primary infection in vivo (*5*, *6*).

The genomes of rhesus macaque and human CMV are very similar. To determine whether viral regulators of host MHC class I affect secondary infection, Hansen *et al.* engineered rhesus CMV lacking the genes that inhibit MHC class I–restricted antigen presentation, and then infected rhesus monkeys that already had a primary infection by the wild-type version of the same strain. By monitoring the macaques for up to 700 days, the authors show that the superinfecting virus was maintained. A successful secondary infection required either down-regulation of MHC class I expression by the secondary virus, or transient depletion of $CD8^+$ T cells during the secondary infection. Thus, viral modulators of host MHC class I molecules govern reinfection, providing a new research direction for human CMV superinfection.

A note of caution is required, however. The chronic shedding of virus from infected monkeys, and frequent reinfection in the rhesus CMV model, show that in this animal model, the virus-host balance is tilted toward chronic virus production. Human adults infected with CMV usually shed virus only when there is immune suppression or deficiency, and during lactation. Chronic human CMV shedding is seen only after perinatal infection. Thus, the rhesus macaque model seems to reflect human perinatal CMV acquisition. The salient question regarding medical risks of CMV is not reinfection per se, but infection of the fetus. Although human CMV strains can reach the fetus, preconceptional immunity reduces this risk and the severity of congenital disease (*7*). But if reinfection requires that the virus evades the $CD8^+$ T cell response (by down-regulating MHC-I expression), then vaccine concepts that rely on $CD8^+$ T cell immunity may fail, at least as far as reducing the risk of reinfection. Such vaccines may not be effective if the risk of superinfection is identical to that of fetal infection. Hansen *et al.* address the ease of superinfection but not of fetal infection, which may not be identical.

Which protective immune options remain if T cells are excluded? Studies in mice show that B cell immunity (antibody production) is critical to control recurrent CMV infection (*8*). Passive antibody intervention — the transfer of pathogen-specific antibodies from one individual to another — is not without effect on fetal infection in humans (*9*). Although superinfection with human CMV occurs more frequently than thought (*10*), and even though

[1]Institute for Virology, Heinrich Heine University, Düsseldorf, Germany. [2]Max von Pettenkofer-Institute, Ludwig Maximilians University, Munich, Germany. E-mail: koszinowski@mvp.uni-muenchen.de

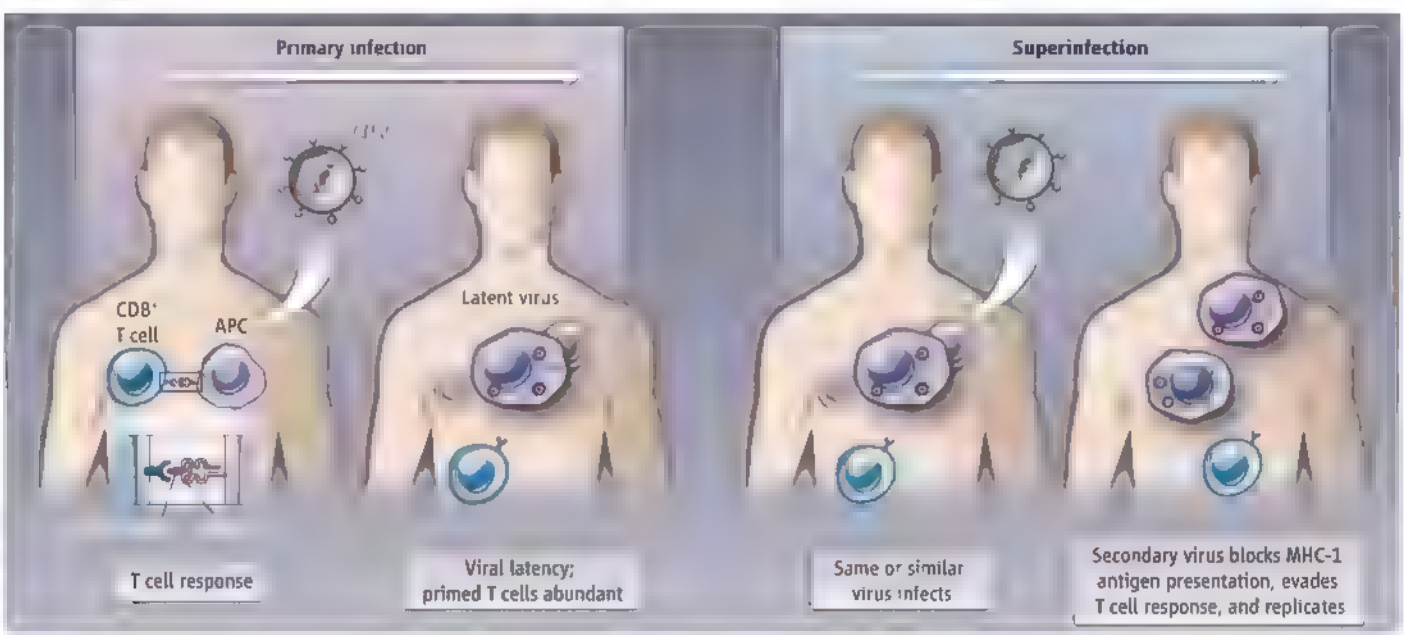

CREDIT: V. GREENMAN/SCIENCE

Superinfection. CMV infection triggers the activation and expansion of cytotoxic $CD8^+$ T cells. The virus persists mainly in the latent form. A secondary infection by the same or similar CMV occurs if the secondary virus blocks MHC class I antigen presentation to the virus-specific $CD8^+$ T cells.

human CMV can attenuate antibody responses (*11*), strain-specific antibodies do have a protective role in this setting. The macaque model could provide a test for antibody-based intervention concepts.

Secondary infection in the Hansen *et al.* study was carried out by subcutaneous injection of CMV. Biting may be a mode of rhesus CMV transmission, but this is unusual in human societies. It will be of interest to address the barrier effect of the mucosa, in particular, because the authors also observed that rhesus CMV induces mucosal immunity (*12*). In addition to affecting antigen presentation to T cells, human CMV devotes other genes to preempt immune responses, including effector functions of natural killer cells, chemokines, interferons, and antibodies (*13*). The findings of Hansen *et al.* show that elucidating a viral principle does not define its in vivo role. The advantage of rhesus macaque CMV is that defined viral functions can be assessed in a primate model.

References

1. A. M. Arvin *et al.*, *Clin. Infect. Dis.* **39**, 233 (2004).
2. S. G. Hansen *et al.*, *Science* **328**, 102 (2010).
3. M. Del Val *et al.*, *J. Exp. Med.* **176**, 729 (1992).
4. B. N. Lilley, H. L. Ploegh, *Immunol. Rev.* **207**, 126 (2005).
5. R. Holtappels *et al.*, *J. Exp. Med.* **199**, 131 (2004).
6. A. K. Pinto, A. B. Hill, *Viral Immunol.* **18**, 434 (2005).
7. A. Kenneson, M. J. Cannon, *Rev. Med. Virol.* **17**, 253 (2007).
8. S. Jonjic *et al.*, *J. Exp. Med.* **179**, 1713 (1994).
9. G. Nigro *et al.*, *N. Engl. J. Med.* **353**, 1350 (2005).
10. S. A. Ross *et al.*, *J. Infect. Dis.* **201**, 386 (2010).
11. R. Atalay *et al.*, *J. Virol.* **76**, 8596 (2002).
12. S. G. Hansen *et al.*, *Nat. Med.* **15**, 293 (2009).
13. C. Powers *et al.*, *Curr. Top. Microbiol. Immunol.* **325**, 333 (2008).

10.1126/science.1188578

APPLIED PHYSICS

Why Thick Can Be Slick

Martin H. Müser and Dmitry Shakhvorostov

Studies of various lamellar materials show a general trend between thickness and friction irrespective of the material.

A main impediment to the development and commercialization of micro- and nanoelectromechanical systems has been the difficulty in effectively lubricating the small-scale moving parts. Greasing the sliding interfaces in the usual way, with liquids, fails because they are readily squeezed out of the contact region. The resulting friction and wear have catastrophic consequences for the functionality of the device. To keep the lubricant within the contact region, molecules can be functionalized so that they self-assemble into a protective and strongly adhering coating on the surface. But problems still remain, primarily insufficient antiwear performance and the difficulty of scaling up the coating process to the size of a wafer (*1*). An alternative strategy based on solid lubricants such as graphite or layered MoS_2 is already being used for macroscopic systems (*2*), but thickness becomes a variable in ways that would not be seen with liquid lubricants. On page 76 of this issue, Lee *et al.* (*3*) unravel a systematic trend of friction with the thickness of the solid lubricant that, surprisingly, is a general effect independent of the material.

The thickness of a material can affect the electronic transport in a fundamental fashion by limiting the degrees of freedom in which the charge carriers can move, in particular when the solid is so thin that it becomes a two-dimensional object. For example, a single layer of carbon atoms, graphene, is a semiconductor, whereas three-dimensional graphite is a conductor (*4*). Should one expect related trends for mechanical properties as the thickness is varied? Filleter *et al.* (*5*) showed that single graphene layers grown on SiC lead to higher friction with another surface than double layers. They correlated the large friction with the large coupling between vibrations and electrons in single layers. Vibrations are produced when an object is slid over a surface that is not perfectly smooth, and ultimately convert into heat. Electrons also heat up when their coupling to vibrations is large, which results in larger drag forces and possibly larger friction.

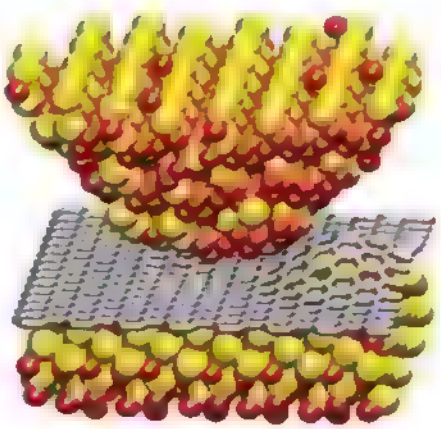

Here's the rub. A single graphene sheet bends out of plane when a friction force microscope tip rubs against it. The thicker the sheet, the more difficult it becomes for it to pucker or ripple, which decreases the contact area and ultimately the friction. Lee *et al.* (*3*) show this thickness-dependent deformation and its influence on friction to be a general effect irrespective of the material.

Lee *et al.* exfoliated flakes from various lamellar materials: metallic $NbSe_2$, semiconducting MoS_2, insulating hexagonal BN, and graphite. The flakes were then deposited onto an oxidized silicon wafer or suspended over a circular hole that had been cut into the substrate. Friction was then measured with a friction force microscope (FFM). Different FFM tip radii and chemistries were investigated; the externally imposed load, the humidity, and the scanning speeds were varied as well. Identical behavior was observed in all samples: The friction decreased with increasing number of layers, until it converged to the bulk value. Purely mechanical reasons can explain the observed trend. The thinner the sheet, the more easily it bends out of plane and thus the larger is the counterface against which the tip is rubbing (see the figure). These conclusions were supported by numerical modeling of the contact.

The results of Lee *et al.* revitalize an old scenario for the origin of friction. To explain why solids manage to interlock so generally (which is counterintuitive, as the surface roughness of one solid should in most cases not match that of another), Coulomb (*6*) had speculated that surface molecules of two opposing planes contract because of their proximity into a coherence (a locally similar corrugation), which needs to be overcome to produce motion. This and related interlocking ideas have long been dismissed, in particular as a result of experiments by Hardy (*7*). He showed that transferring a single monolayer of a fatty acid to a glass surface did not change its corrugation but did reduce its friction by a factor of 10. However, what matters is the thickness of the object. The greater its thickness, generally the more difficult it becomes to deform it, and thus the less it can interlock with a counterface (*8*). Two-dimensional solids, such as graphene, are particular in that regard, as their resistance to in-plane deformation does not depend on the spatial extent of the deformation and bending them is easy. This is why single layers can accommodate the tip geometry much better than several layers can. To fully

CREDIT: DMITRY SHAKHVOROSTOV

Materialwissenschaft und Werkstofftechnik, Universität des Saarlandes, Campus C6 3, 66123 Saarbrücken, Germany. E-mail: martin.mueser@mx.uni-saarland.de; dshakh@mx.uni-saarland.de

understand the experiments, it is necessary to characterize what instabilities occur within the area of contact. Simply having enhanced contact due to puckering does not suffice to convey shear (without instabilities, one could translate the deformed structure adiabatically with extremely small forces) (*9*). One mechanism would be in-plane elastic instabilities within the sheet in addition to the bending, which seems possible given the quite large 10% stretching of graphene observed in the experiments. Whatever the nature of the local interlocking between the two surfaces, Lee *et al.*'s work demonstrates that single graphene layers are not good lubricants, whereas, a five-layer-thick coating will make the contacts as slick as if they were greased with bulk solid lubricants. This might form a guideline in the production of new microelectromechanical systems with moving parts.

References

1. R. Mabaudian *et al.*, *Tribol. Lett.* **12**, 95 (2002)
2. C. Donnet, A. Erdemir, *Surf. Coat. Tech.* **180–181**, 76 (2004)
3. C. Lee *et al.*, *Science* **328**, 76 (2010)
4. A. K. Geim, K. S. Novoselov, *Nat. Mater.* **6**, 183 (2007)
5. T. Filleter *et al.*, *Phys. Rev. Lett.* **102**, 086102 (2009)
6. C. A. Coulomb, "Theorie des machines simples," in *Memoires de Mathematique et de Physique de l'Academie Royale* (Bachelier, Paris, 1785), pp. 161–342
7. W. B. Hardy, *Collected Works*, E. K. Ridea., Ed. (Cambridge Univ. Press, Cambridge, 1923)
8. M. H. Müser, *Europhys. Lett.* **66**, 97 (2004)
9. L. Prandtl, *Z. Angew. Math. Mech.* **8**, 85 (1928)

10.1126/science.1188086

GEOCHEMISTRY

Ocean Chemistry and Early Animals

Chemical changes in the world's oceans were key to the early evolution of animals.

Guy M. Narbonne

During the Neoproterozoic Era (1000 to 542 million years ago), the prokaryote microbial communities that had previously dominated Earth were supplemented by the diverse communities of animals and other eukaryotes that have characterized Earth since then. Chemical changes in the world's oceans were central to this transition. After more than a billion years of euxinic (sulfidic anoxic) oceans, deep-water conditions turned ferruginous (iron-rich anoxic) in the late Neoproterozoic (see the figure) (*1*). This ferruginous ocean may have also been a substantial reservoir for dissolved organic carbon (*2*). On page 80 of this issue, Li *et al.* (*3*) elucidate redox conditions in the late Neoproterozoic Doushantuo Formation of southern China. These strata contain superbly preserved eggs, embryos, and probable resting cysts that are generally regarded as the oldest-known microscopic animals (*4*).

The Doushantuo Formation (635 to 551 million years ago) (*5*) spans most of the Ediacaran Period. Li *et al.* use multiple redox indicators to show that anoxia prevailed throughout the deposition of all sampled shallow-water strata, with the main variation being between ferruginous and sulfidic (euxinic) conditions. The few deep-water samples studied show ferruginous and at least intermittently anoxic conditions (*3*). By correlating these redox conditions with various proxies for water depth, the authors conclude that a wedge of sulfidic water positioned over the Doushantuo midramp was sandwiched between ferruginous waters (see the figure).

Li *et al.* did not observe the third member of the trilogy—the oxygen-rich surface layer—but they infer that atmospheric diffusion would have resulted in a thin layer of oxygenated surface water above the anoxic ferruginous and sulfidic water masses documented in their study. The boundaries between these water masses would move both horizontally and vertically in response to sea-level rises and falls, preserving a complex mosaic of redox conditions in the sediment. The conclusions seem robust for the Doushantuo Formation and may help to explain some of the global heterogeneity of the ferruginous ocean, which was overwhelmingly ferruginous, but with euxinic and even oxic conditions present locally (*1*, *6*).

Li *et al.*'s geochemical studies elucidate the critical link between the Neoproterozoic chemical evolution of the oceans and atmosphere and the early evolution of animals. Animals require oxygen. Frequent anoxia is evident even in agitated surface waters up to 740 million years ago (*6*); this scarcity of free oxygen probably lim-

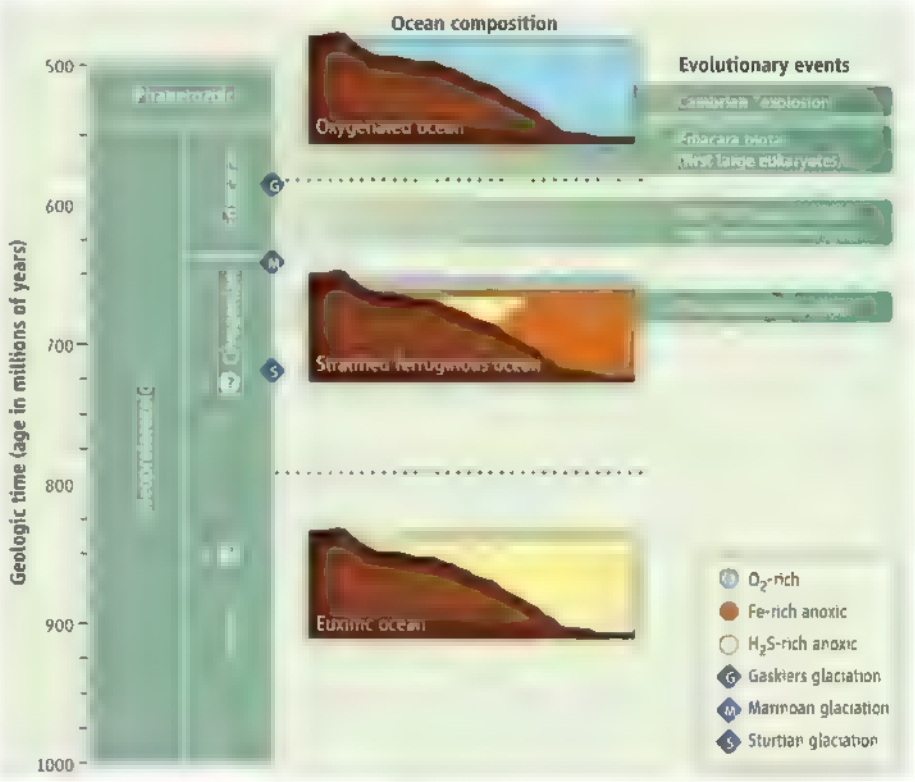

Ocean chemistry and early animal evolution. Dashed lines imply gradual transitions between Neoproterozoic chemical ocean states. The position of the Tonian-Cryogenian boundary is under discussion. The structure of the ferruginous ocean, with stratified layers and lenses of ferruginous, sulfidic, and oxygenated waters, is from Li *et al.* (*3*).

Department of Geological Sciences and Geological Engineering, Queen's University, Kingston, ON K7L 3N6, Canada. E-mail: narbonne@geol.queensu.ca

ited animal evolution throughout most of the Neoproterozoic. Li *et al.* infer that the abundant animal microfossils in the Doushantuo Formation lived in a surface oxygenated layer and were transported into nearby anoxic deposits, where they were exceptionally preserved. Many of the microfossils show morphological features that may reflect periodic anoxia or euxinia (*7*), implying that the early Ediacaran oxygen layer may not have been well developed. Large animals are unknown from these or any other early Ediacaran strata. The mid-ramp wedge of hydrogen sulfide-rich waters documented by Li *et al.* would have severely restricted animal life in this setting. Furthermore, their model predicts that the oxygen-rich surface layer reached the sea bottom only near the shoreline, where high turbulence and fluctuating salinities may have been deleterious to early benthic animals.

Multiple geochemical proxies worldwide show that this stratified ferruginous ocean rich in dissolved organic carbon (*1*–*3*) began to give way to oxygenated deep oceans about 580 million years ago (*8*, *9*). It is probably not a coincidence that the oldest large and architecturally complex eukaryotes are rangeomorphs (*10*), an extinct clade of mainly deep-water, stem-group animals whose self-similar branching favored direct adsorption of dissolved organic carbon from sea water (*11*). Rangeomorphs dominated the earliest Ediacara biota but declined later in the Ediacaran and are unknown from Cambrian deposits worldwide (*10*–*12*), perhaps mimicking the demise of the Neoproterozoic reservoir of dissolved organic carbon that had fueled their origin and early evolution (*13*). Their gradual replacement by segmented and mobile animals in late Ediacaran, well-oxygenated seas marks the end of the Neoproterozoic ferruginous ocean and the biological prelude to the Cambrian "explosion" of animals and the beginnings of our modern world (*10*, *12*).

References

1. D. E. Canfield *et al.*, *Science* **321**, 949 (2008)
2. D. H. Rothman, J. M. Hayes, R. E. Summons, *Proc. Natl. Acad. Sci. U.S.A.* **100**, 8124 (2003)
3. C. Li *et al.*, *Science* **328**, 80 (2010)
4. L. Yin *et al.*, *Nature* **446**, 661 (2007)
5. D. Condon *et al.*, *Science* **308**, 95 (2005)
6. D. T. Johnston *et al.*, *Earth Planet. Sci. Lett.* **290**, 64 (2010).
7. P. A. Cohen, A. H. Knoll, R. B. Kodner *Proc. Natl. Acad. Sci. U.S.A.* **106**, 6519 (2009)
8. D. A. Fike *et al.*, *Nature* **444**, 744 (2006)
9. D. E. Canfield *et al.*, *Science* **315**, 92 (2007)
10. G. M. Narbonne, *Annu. Rev. Earth Planet. Sci.* **33**, 421 (2005)
11. M. Laflamme, S. Xiao, M. Kowalewski, *Proc. Natl. Acad. Sci. U.S.A.* **106**, 14438 (2009)
12. S. Xiao, M. Laflamme, *Trends Ecol. Evol.* **24**, 31 (2009).
13. E. A. Sperling, D. Pisani, K. J. Peterson, in *The Rise and Fall of the Ediacaran Biota*, P. Vickers-Rich, P. Komarower, Eds. (Geological Society of London, Spec. Publ. 286, 2007), pp. 355–368.

10.1126/science.1188688

GEOPHYSICS

What Lies Beneath

Convection in Earth's hot mantle plays a key role in determining ocean depth.

Maya Tolstoy

Since Archimedes shouted "Eureka!" more than 2200 years ago, Eurasia and North America have moved ~55 m further away from each other as the sea floor has spread at the Mid-Atlantic Ridge. The slow but steady process of sea-floor spreading takes hot young lithosphere at the ridge axis and gradually moves it away as it cools, thickens, and sinks. Archimedes' principle of buoyancy rules much of these plate tectonic processes. On page 83 of this issue, Adam and Vidal (*1*) remind us that it is not just what sits atop that matters, but also what lies beneath. They show that mantle flow beneath the oceanic crust influences the depth of the Pacific Ocean. Taking advantage of new, easily accessible global geophysical data sets, the authors offer a new explanation for a long-standing mystery in the variation of sea-floor depth with crustal age.

When Wegener proposed continental drift (the predecessor of the theory of plate tectonics) in 1912, his hypothesis was rejected, in part because it seemed impossible that continents could plow through fixed crust. Decades later, mid-ocean ridges were discovered, and magnetic studies revealed quasi-regular switches in magnetic polarity in the ocean crust (*2*). This observation clinched the debate for plate tectonics, showing that crust moves away from the ridge crest on a conveyor belt–like system. Mantle convection was invoked to drive plate spreading, with upwelling at the ridge axes, horizontal flow pulling the plates apart, and downwelling at subduction zones.

With the Cold War firmly under way, the U.S. Navy invested heavily in mapping the deep sea floor, and plate tectonics explained much of what was observed. Once the long mountain chains on the sea floor were understood to be sites of new crustal formation, attention turned to the gradual deepening of the sea floor away from these volcanic centers. This deepening was soon described in terms of a simple model (*3*) and shown to vary linearly with the square-root of the age of oceanic crust (*4*), defining a cooling, sinking lithosphere as it moved away from the ridge axis (see the figure, panel A). This classic relationship is commonly referred to as root-*t* (where *t* is time).

However, closer examination of the data showed a flattening of sea-floor depth in older lithosphere (*5*), which was expected to keep sinking. For decades, debate has continued as to what might cause the oldest sections of ocean basin to behave in this way. Because the older lithosphere sits higher than anticipated, explanations focused largely on how the lithospheric cooling might be hampered or how the lithosphere might be buoyed up by unanticipated mantle forces (*5*–*10*). Yet, resolution of this question remained elusive (*11*).

The lithosphere is the thermal boundary layer of a convecting mantle (*12*)—the thin skin atop a hot base. In this simple view, what lies beneath the lithosphere must be the key driving force behind lithospheric thickness and depth. With this image in mind, Adam and Vidal take a new approach to the problem of lithospheric depth changes with age. Focusing on the Pacific lithosphere, they consider how changes in the direction of plate spreading, and the resulting reorganization of mantle flow, have altered the location of older lithosphere relative to the mantle it was originally above. Thus, they consider the depth of the lithosphere along mantle flow lines, rather than along crustal age lines perpendicular to the ridge. The resulting fit is remarkable: Root-*t* works all the way to the edge of the oldest oceanic crust if you account for mantle "age."

It thus appears that the lithosphere, with enough time, will adjust to the structure of a thermal boundary layer appropriate for the mantle that underlies it (see the figure, panel B). In this model, the lithosphere does not passively cool as it moves away from the ridge axis, but rather is a dynamic feature. Attempts to explain the flattening through changes in the heat input from the mantle had the right idea (*8*–*11*), but no complex change in mantle dynamics had to be invoked to account for this. It simply required considering the four-dimensional dynamic character of plate tectonics.

After decades of debate about why root-*t* fails on older oceanic crust, it is heartening to learn that it may be valid after all, as long

Lamont-Doherty Earth Observatory, Columbia University, Palisades, NY 10964, USA. E-mail: tolstoy@ldeo.columbia.edu

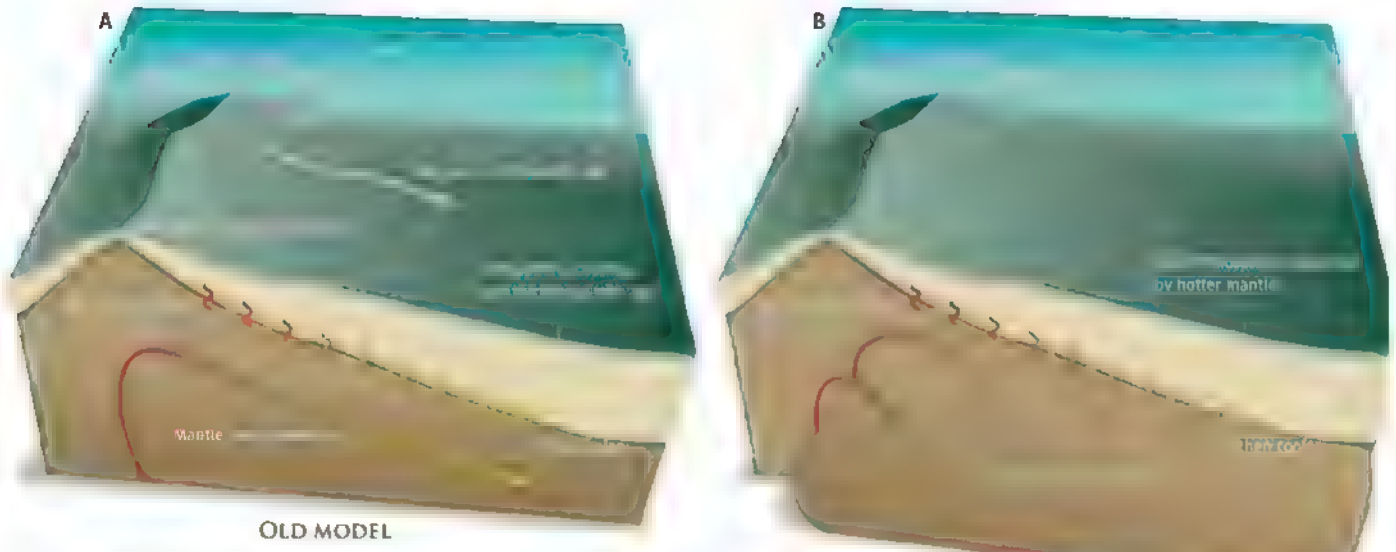

Accounting for mantle flow. (**A**) In the root-*t* model, mantle flow is assumed to cool parallel to the plate-spreading direction. (**B**) Mantle flow lines that are skewed relative to the plate-spreading direction may reheat older lithosphere, as proposed by Adam and Vidal.

as the distance from the upwelling point of the mantle beneath is considered. The result is a testament to the value of large, easily accessible global geophysical data sets. More work is needed to show that this explanation is globally applicable, given that the Pacific depth profile is simpler than those in other ocean basins (*13*). The model should also be refined to consider the implications for overall mantle convective processes, and what flow reorganization can tell us about dynamic mantle coupling to the lithosphere.

References

1. C. Adam, V. Vidal, *Science* **328**, 83 (2010).
2. F. D. Vine, D. H. Matthews, *Nature*, **199**, 947 (1963).
3. R. L. Parker, D. W. Oldenburg, *Nature* **242**, 384 (1973).
4. E. E. Davis, C. R. B. Lister, *Earth Planet. Sci. Lett.* **21**, 405 (1974).
5. B. Parsons, J. G. Sclater, *J. Geophys. Res.* **82**, 803 (1977).
6. R. N. Anderson, M. A. Hobart, *J. Geophys. Res.* **81**, 2968 (1976).
7. C. A. Stein, S. Stein, *Nature* **359**, 123 (1992).
8. B. Parsons, D. McKenzie, *J. Geophys. Res.* **83**, 4485 (1978).
9. E. Humler, C. Langmuir, V. Daux, *Earth Planet. Sci. Lett.* **173**, 7 (1999).
10. W. Schroeder, *J. Geophys. Res.* **89**, 9873 (1984).
11. M.-P. Doin, L. Fleitout, *Geophys. J. Int.* **143**, 582 (2000).
12. T. Turcotte, G. Schubert, *Geodynamics* (Cambridge Univ. Press, Cambridge, UK, ed. 2, 2002).
13. D. E. Hayes, *J. Geophys. Res.* **93**, 2937 (1988).

10.1126/science.1188090

PHYSICS

Fishing Antihypernuclei Out of a Quark-Gluon Soup

Rare antimatter hypernuclei can form when an ultrahigh-energy plasma of quarks and gluons cools down.

Thomas D. Cohen

Quantum field theory is the general framework for combining special relativity and quantum mechanics; it is the formalism that describes the standard model of particle physics. The mathematical structure of quantum field theory requires that all types of particles have antiparticles of the same mass but the opposite electric charge. In fact, the implications are broader: Any physical system describable in quantum field theory—no matter how complex or exotic—has an antimatter analog with an identical mass. Thus, a version of quantum field theory rich enough to allow for the existence of elephants must equally allow for antielephants. On page 58 of this issue, The STAR Collaboration (*1*, *2*) discusses the formation of a complex particle, an antihypertriton, an exotic relative of the nucleus of tritium that contains a particular variety of elementary particle known as the strange quark.

Of course, antielephants have yet to be seen; our universe has a vast preponderance of ordinary matter over antimatter. It is not completely understood why our universe displays this asymmetry, but because it does, it is very hard to make complicated states of antimatter. Antiparticles can be made and even used. For example, positrons—positively charged electrons—are emitted in certain nuclear decay processes and used in imaging. However, antiparticles usually encounter normal matter soon after they form, which results in their annihilation by conversion into neutral particles such as photons. In practice, even if one had the vast number of positrons, antiprotons, and antineutrons needed for an antielephant, they would be annihilated long before they could be arranged into an antielephant.

Antielephants may not be practical to create, but it is possible to create relatively complex antimatter systems. One way to create such systems is via extremely energetic heavy-ion collisions such as those produced at the Relativistic Heavy-Ion Collider (RHIC) at Brookhaven National Laboratory. The STAR Collaboration was able to form and detect an antihypertriton, which may crudely be thought of as a variant of an ordinary triton, or tritium nucleus ^{3}H, the heavy isotope of hydrogen with one proton and two neutrons (see the figure)

Maryland Center for Fundamental Physics and Physics Department, University of Maryland, College Park, MD 20742, USA. E-mail: cohen@umd.edu

Strange quarks make nuclei hyper. In principle, all complex matter, even elephants (**top**), can exist in matter or antimatter forms. (**Middle**) Schematic representations of the tritium nucleus, or triton, depicts its up (u) and down (d) quark constituents (antimatter is indicated by a bar over a symbol). The white circles indicate the baryons (protons and neutrons) into which quarks are bound. (**Bottom**) The hypernuclear partner of the triton has one of the down quarks in a neutron replaced by a strange (s) quark to create a hyperon.

In the hypertriton, one of the ordinary down quarks in one of the neutrons is replaced with a strange quark. The particle that replaces the neutron is the hyperon.

This result is noteworthy because it is the first observation of any antinucleus with net strangeness (an antihypernucleus). Although not quite an antielephant, the antihypertriton is a complicated structure. To form it, nine antiquarks (four up, four down, and one strange), must come within a distance of a couple of femtometers (10^{-15} m) of each other without encountering ordinary quarks and annihilating.

The formation of antihypertritons requires extreme conditions that create numerous antiquarks in close proximity. Such conditions can be found in the ultrarelativistic heavy-ion collisions that are studied at RHIC. Two heavy nuclei, such as gold, are each accelerated to ultrarelativistic speeds—0.9995 times the speed of light. They then undergo a nearly head-on collision, and numerous collisions between the constituents of the nuclei occur on a very rapid time scale. These collisions create numerous interacting gluons, quarks, and antiquarks. Within a time of less than 10^{-23} s, the system is believed to achieve thermal equilibrium and forms a "fireball" at a temperature of a few times 10^{15} degrees Kelvin. Quarks and gluons are normally confined inside particles that feel the strong force, such as protons or pions, but at temperatures this high, they are thought to escape their confinement in a strongly interacting quark-gluon plasma (QGP) (*1*, *3*, *4*).

To a high level of accuracy, this QGP has an equal number of quarks and antiquarks; its temperature is high enough so that strange quarks, which are comparatively heavy and require much energy to produce, are abundant. This fireball expands and cools, ultimately to the point where quarks and gluons "hadronize" and are again confined into ordinary hadrons. The details of how this hot soup of quarks, antiquarks, and gluons form into ordinary hadrons is not completely understood. Most of the quarks and antiquarks combine to form mesons. A small fraction of the time, three quarks (or antiquarks) are sufficiently close together during hadronization to form baryons (protons, neutrons, or hyperons) or antibaryons.

The production rates of these various particles are used to infer both the properties of the QGP and the dynamics of how it expands, cools, and hadronizes (*1*, *3*). Statistically, it is much less likely that larger combinations of antiquarks form into antinuclei because this outcome requires correlations where numerous antiquarks are close enough to combine. However, the very large number of quarks in the QGP, and the large number of collisions produced at RHIC, means that even very unlikely final states, such as $\bar{\Lambda}$ antinuclei antihypernuclei, can form and be observed (*2*).

The discovery of the antihypertriton is significant for a number of reasons. First, it confirms our understanding that every physical system has an antimatter analog of the same mass in a new context, that of hypernuclei. The accuracy of the mass determination is far less precise than in many other antimatter systems, in part because of limited statistics and because antihypertriton is unstable and decays through weak interactions. Nevertheless, to within measurement uncertainties, hypertriton and antihypertriton have the same mass. Second, the result is noteworthy purely as a matter of technical virtuosity. In RHIC experiments, interesting physics must be pulled out of the extraordinarily complicated environments created in these collisions. The antihypertriton are a minuscule fraction of the total particles produced. The success in finding this needle in a haystack is remarkable. Finally, and perhaps most importantly, hypertriton and antihypertriton provide a new window for exploring the dynamics of ultrarelativistic heavy-ion collisions.

References

1. K. H. Ackermann *et al.*, *Nucl. Instrum. Methods A* **499**, 624 (2003).
2. The Star Collaboration, *Science* **328**, 58 (2010); published online 4 March 2010 (10.1126/science.1183980).
3. J. Adams *et al.*, *Nucl. Phys. A* **757**, 102 (2005).
4. P. Braun-Munzinger, J. Stachel, *Nature* **448**, 302 (2007).

10.1126/science.1187769

MOLECULAR BIOLOGY

Mixing or Not Mixing

Dominique Ray-Gallet and Geneviève Almouzni

How are parental and newly synthesized histones distributed into nucleosomes during eukaryotic cell division?

Beyond DNA information, the organization of the proteins and DNA that constitute chromatin represents a means to regulate genome function (*1*). The inheritance and maintenance of the DNA sequence has been explained by a semiconservative mechanism of replication in which a complementary new strand of DNA is synthesized along each parental strand, resulting in an inherited double-stranded molecule that contains old and new DNA. But how is the inheritance of epigenetic traits—modifications of chromatin proteins (histones) and DNA that do not alter the sequence—affected by dynamic changes in chromatin organization during eukaryotic cell division? On page 94 of this issue, Xu *et al.* (*2*) explore how parental (old) and newly synthesized histones associate after replication.

The basic unit of chromatin, the nucleosome, has a core particle of eight histones—two pairs of histone H3-H4 as a tetramer flanked by two dimers of histone H2A-H2B. Histones can be present in distinct forms or variants, and they may harbor specific posttranslational modifications that can define a given epigenome (*1*, *3*). How do these particular markings sustain passage through

Laboratory of Nuclear Dynamics and Genome Plasticity, UMR218 CNRS/Institut Curie, 26 rue d'Ulm, 75248 Paris Cedex 05, France. E-mail: Genevieve.Almouzni@curie.fr

replication? An attractive hypothesis has been a semiconservative mechanism in which parental histones are combined with newly synthesized histones within the same core nucleosome. The presence of parental information as a template to reproduce the same marks on new histones provides a convenient means to ensure accurate reproduction of the initial marking at the same place. But can parental and new histones mix?

Histones H2A-H2B readily exchange as dimers, but H3-H4 tetramers are thought not to split (*4*). However, newly synthesized H3 and H4 can exist as dimers when associated with histone chaperones (*5*–*8*), spurring the debate.

Xu *et al.* use isotope labeling and mass spectrometry analysis of histone content to explore how new and old H3-H4 dimers associate after replication. Their model system is based on conditional expression in cultured human cells of tagged versions of distinct variants of histone H3: H3.1 and H3.3. H3.1 is a replicative histone variant, with a peak of expression in S phase of the cell division cycle, and is mostly incorporated into duplicated chromatin in a manner that is coupled to DNA replication (*3*). H3.3, known as a replacement variant, is expressed throughout all phases of the cell cycle and in quiescence, and can be incorporated into chromatin independently of DNA synthesis (*3*).

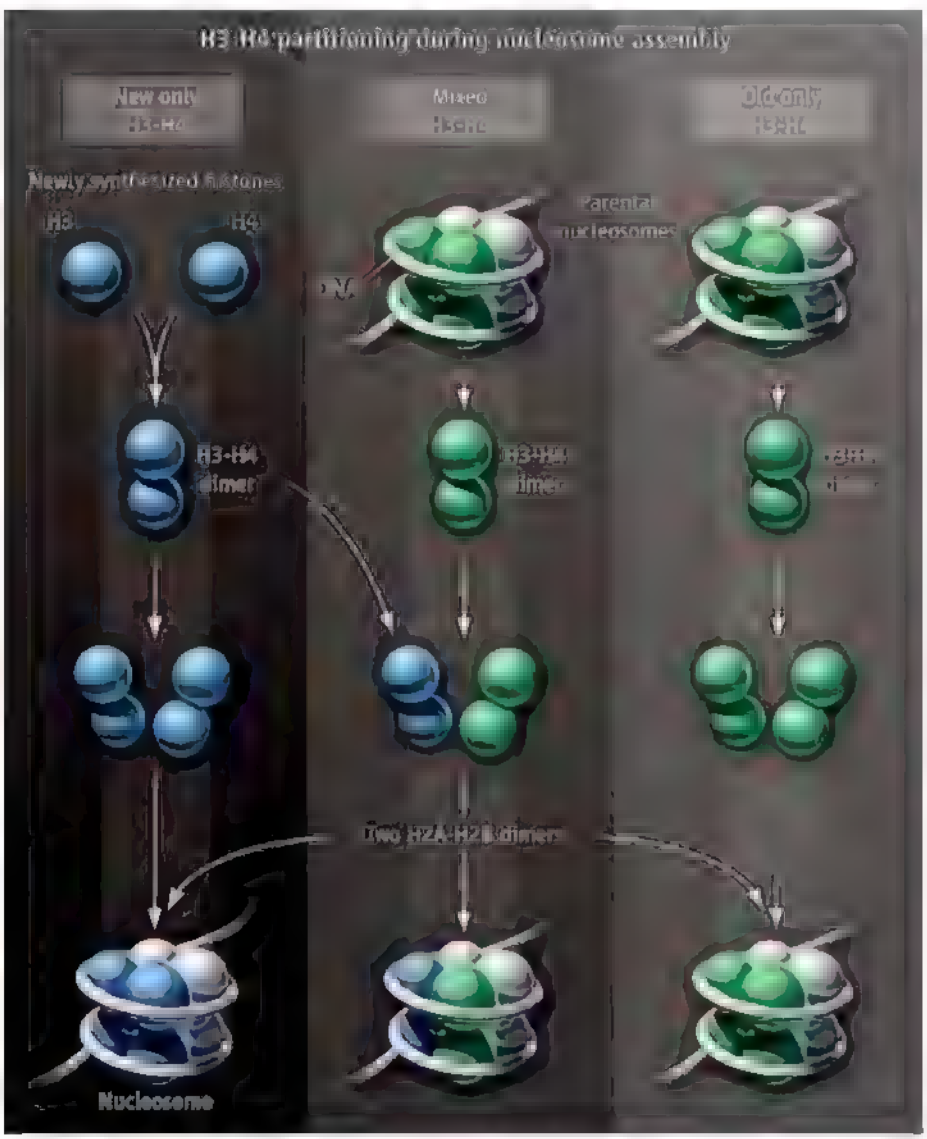

CREDIT: C. BICKEL/SCIENCE

Histone partitioning. New nucleosomes result from de novo assembly using newly synthesized H3 and H4 histones in the form of two H3-H4 dimers, after association with two H2A-H2B dimers, the result is a nucleosome containing only new H3-H4 dimers. Mixed particles will form using a newly synthesized H3-H4 dimer and an H3-H4 dimer recycled from a disrupted parental nucleosome. Old nucleosomes will form either by self-reassociation of two H3-H4 dimers recycled from a transiently disrupted parental nucleosome, or according to the generally accepted view, by inheritance of a stable H3-H4 tetramer from a parental nucleosome. [Adapted from (*10*) with permission from Cold Spring Harbor Laboratory Press]

Xu *et al.* did a genome-wide analysis of H3.1 incorporation into nucleosomes and observed no splitting of the H3.1-H4 tetramer, confirming earlier work on H3. Yet the H3.3-H4 tetramer did split. Both H3.1 and H3.3 variants were found in new and old nucleosomes and in mixed nucleosomes for H3.3. The authors considered the possibility that when selecting cells with H3.1 or H3.3 for analysis, they may have examined different populations of nucleosomes arising from distinct genomic regions. This is particularly critical for H3.3, which has been associated with actively transcribed regions. The question is whether splitting is region-specific or variant-specific. A previous analysis showed that in the vicinity of H3.3, H3.1 presented modifications similar to those found on H3.3 (*9*). In this case, what would the fate be of H3.1 nucleosomes that flank H3.3—would they split or not? It may be that H3.1 has a similar splitting feature when it is in the vicinity of H3.3.

Clearly, histone splitting is part of the histone inheritance picture during chromatin duplication, and three alternative modes for H3-H4 partitioning (*10*) can be considered as real (see the figure). The next challenge is to explore how these modes of distribution become articulated with the transmission of histone marks. The nonmixing options are compatible with proposed models in which histone marks are copied from neighboring histones, as observed with tightly packed heterochromatin regions (*1*, *10*–*12*). Yet, the possibility of an intranucleosome histone template for modifications may apply to particular genomic regions to ensure memory of critical active marks (*12*, *13*). Future work will investigate how the choice between histone splitting and nonsplitting is made within a cell and whether this is regulated during cellular life or during development.

References

1. C. D. Allis, T. Jenuwein, D. Reinberg, *Epigenetics* (Cold Spring Harbor Laboratory Press, New York, 2006)
2. M. Xu *et al.*, *Science* **328**, 94 (2010)
3. K. Sarma, D. Reinberg, *Nat. Rev. Mol. Cell Biol.* **6**, 139 (2005)
4. A. T. Annunziato, *J. Biol. Chem.* **280**, 12065 (2005)
5. H. Tagami, D. Ray-Gallet, G. Almouzni, Y. Nakatani, *Cell* **116**, S1 (2004)
6. C. M. English, N. K. Maluf, B. Tripet, M. E. Churchill, J. S. Tyler, *Biochemistry* **44**, 13673 (2005)
7. L. J. Benson *et al.*, *J. Biol. Chem.* **281**, 9287 (2006)
8. R. Natsume *et al.*, *Nature* **446**, 338 (2007)
9. A. Loyola *et al.*, G. Almouzni, *Mol. Cell* **24**, 309 (2006)
10. Y. Nakatani, D. Ray-Gallet, J. P. Quivy, H. Tagami, G. Almouzni, *Cold Spring Harb. Symp. Quant. Biol.* **69**, 273 (2004)
11. J. Nakayama *et al.*, *Science* **292**, 110 (2001)
12. A. V. Probst, E. Dunleavy, G. Almouzni, *Nat. Rev. Mol. Cell Biol.* **10**, 192 (2009)
13. S. Henikoff, J. G. Henikoff, A. Sakai, G. B. Loeb, K. Ahmad, *Genome Res.* **19**, 460 (2008)

10.1126/science.1188653

Observation of an Antimatter Hypernucleus

The STAR Collaboration*†

Nuclear collisions recreate conditions in the universe microseconds after the Big Bang. Only a very small fraction of the emitted fragments are light nuclei, but these states are of fundamental interest. We report the observation of antihypertritons—comprising an antiproton, an antineutron, and an antilambda hyperon—produced by colliding gold nuclei at high energy. Our analysis yields 70 ± 17 antihypertritons ($^{3}_{\Lambda}\overline{\mathrm{H}}$) and 157 ± 30 hypertritons ($^{3}_{\Lambda}$H). The measured yields of $^{3}_{\Lambda}$H ($^{3}_{\Lambda}\overline{\mathrm{H}}$) and ^{3}He ($^{3}\overline{\mathrm{He}}$) are similar, suggesting an equilibrium in coordinate and momentum space populations of up, down, and strange quarks and antiquarks, unlike the pattern observed at lower collision energies. The production and properties of antinuclei, and of nuclei containing strange quarks, have implications spanning nuclear and particle physics, astrophysics, and cosmology.

Nuclei are abundant in the universe, but antinuclei that are heavier than the antiproton have been observed only as products of interactions at particle accelerators (*1*, *2*). Collisions of heavy nuclei at the Relativistic Heavy-Ion Collider (RHIC) at Brookhaven National Laboratory (BNL) briefly produce hot and dense matter that has been interpreted as a quark gluon plasma (QGP) (*3*, *4*) with an energy density similar to that of the universe a few microseconds after the Big Bang. This plasma contains roughly equal numbers of quarks and antiquarks. As a result of the high energy density of the QGP phase, many strange-antistrange ($s\bar{s}$) quark pairs are liberated from the quantum vacuum. The plasma cools and transitions into a hadron gas, producing nucleons, hyperons, mesons, and their antiparticles.

Nucleons (protons and neutrons) contain only up and down valence quarks, whereas hyperons (Λ, Σ, Ξ, Ω) contain at least one strange quark in their three-quark valence set. A hypernucleus is a nucleus that contains at least one hyperon in addition to nucleons. All hyperons are unstable, even when bound in nuclei. The lightest bound hypernucleus is the hypertriton ($^{3}_{\Lambda}$H), which consists of a Λ hyperon, a proton, and a neutron. The first observation of any hypernucleus was made in 1952 using a nuclear emulsion cosmic ray detector (*5*). Here, we present the observation of an antimatter hypernucleus.

Production of antinuclei. Models of heavy-ion collisions have had good success in explaining the production of nuclei by assuming that a statistical coalescence mechanism is in effect during the late stage of collision evolution (*4*, *6*). Antinuclei can be produced through the same coalescence mechanism and are predicted to be present in cosmic rays. An observed high yield could be interpreted as an indirect signature of new physics such as dark matter (*7*, *8*). Heavy-ion collisions at RHIC provide an opportunity for the discovery and study of many antinuclei and antihypernuclei.

The ability to produce antihypernuclei allows the study of all populated regions in the three-dimensional chart of the nuclides. The conventional two-dimensional chart of the nuclides organizes nuclear isotopes in the (N, Z) plane, where N is the number of neutrons and the Z is the number of protons in the nucleus. This chart can be extended to the negative sector in the (N, Z) plane by including antimatter nuclei. Hypernuclei bring a third dimension into play, based on the strangeness quantum number of the nucleus. The present study probes the territory of antinuclei with nonzero strangeness (Fig. 1), where proposed ideas (*9*–*12*) related to the structure of nuclear matter can be explored.

Hypernuclei—formation and observation. The hyperon-nucleon (YN) interaction, responsible in part for the binding of hypernuclei, is of fundamental interest in nuclear physics and nuclear astrophysics. For example, the YN interaction plays an important role in attempts to understand the structure of neutron stars. Depending on the strength of the YN interaction, the collapsed stellar core could consist of hyperons, strange quark matter, or a kaon condensate (*13*). Whereas the hyperons or strange particles inside a dense neutron star would not decay because of local energy constraints, free hypernuclei decay into ordinary nuclei with typical lifetimes of a few hundred picoseconds, which is still 13 orders of magnitude longer than the lifetimes of the shortest-lived particles. The lifetime of a hypernucleus depends on the strength of the YN interaction (*14*, *15*). Therefore, a precise determination of the lifetime of hypernuclei provides direct information on the YN interaction strength (*15*, *16*).

The experiment was carried out by the STAR collaboration (*17*) at the RHIC facility. The main detector of the STAR experiment is a gas-filled cylindrical time projection chamber (TPC) with an inner radius of 50 cm, an outer radius of 200 cm, and a length of 420 cm along the beamline (*18*). The TPC is a device for imaging, in three dimensions, the ionization left along the path of charged particles. It resolves more than 50 million pixels within its active volume. The present analysis is based on interactions produced by colliding two Au beams at an energy of 200 GeV per nucleon-nucleon collision in the center-of-mass system. About 89 million collision events were collected using a trigger designed to accept, as far as possible, all impact parameters (minimum-bias events), and an additional 22 million events were collected using a trigger that preferentially selects near-zero impact parameter (or "head-on") collisions. The accepted collisions are required to occur within 30 cm of the center of the TPC along the beamline. Charged particle tracks traversing the TPC are reconstructed in an acceptance that is uniform in azimuthal angle. The precise coverage in terms of polar angle is somewhat complicated (*18*), but roughly speaking, charged tracks emerging at angles with respect to the beam axis in the range of $45° < \theta < 135°$ are reconstructed.

Figure 2 depicts a typical Au + Au collision reconstructed in the STAR TPC. The tracks are curved by a uniform magnetic field of 0.5 T parallel to the beamline. The event of interest here includes a $^{3}_{\Lambda}\overline{\mathrm{H}}$ candidate created at the

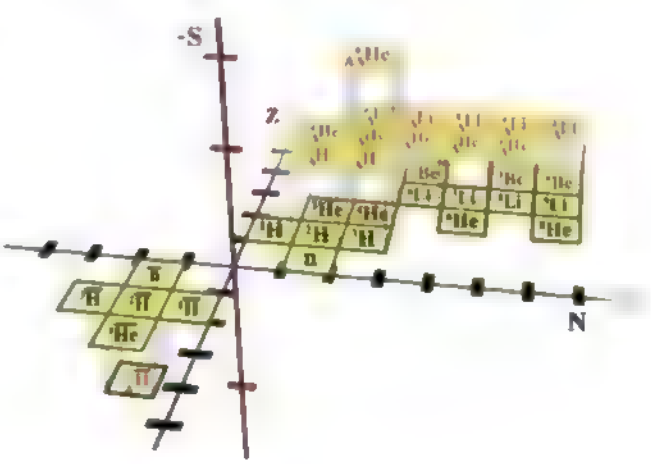

Fig. 1. A chart of the nuclides showing the extension into the strangeness sector. Normal nuclei lie in the (N, Z) plane. Antinuclei lie in the negative sector of this plane. Normal hypernuclei lie in the positive (N, Z) quadrant above the plane. The antihypertriton $^{3}_{\Lambda}\overline{\mathrm{H}}$ reported here extends this chart into the strangeness octant (S) below the antimatter region in the (N, Z) plane.

*Address for correspondence: starpapers-l@lists.bnl.gov
†All authors and their affiliations appear at the end of this paper.

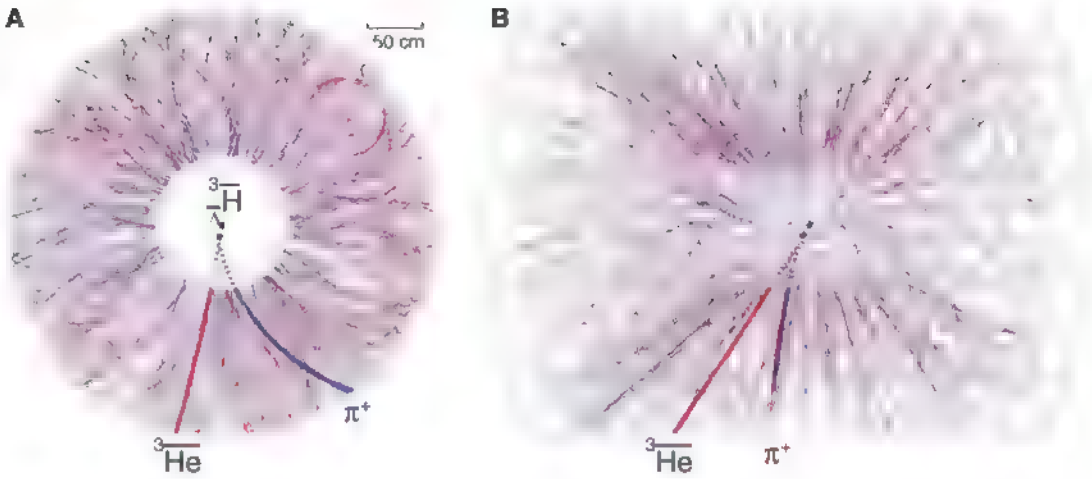

Fig. 2. A typical event in the STAR detector that includes the production and decay of a $^3_{\bar{\Lambda}}\bar{H}$ candidate: **(A)** with the beam axis normal to the page, **(B)** with the beam axis horizontal. The dashed black line is the trajectory of the $^3_{\bar{\Lambda}}\bar{H}$ candidate, which cannot be directly measured. The heavy red and blue lines are the trajectories of the ^3He and π^+ decay daughters, respectively, which are directly measured.

primary collision vertex near the center of the TPC. The $^3_{\bar{\Lambda}}\bar{H}$ travels a few centimeters before it decays. One of the possible decay channels is $^3_{\Lambda}H \rightarrow {}^3He + \pi^-$, which occurs with a branching ratio of 25% (assuming that this branching fraction is the same as that for $^3_{\Lambda}H$) (*15*). The two daughter particles then traverse the TPC along with the hundreds of other charged particles produced in the primary Au + Au collision. The trajectories of the daughter particles are reconstructed from the ionization trails they leave in the TPC gas volume (shown in Fig. 2 as thick red and blue lines for $^3\bar{He}$ and π^+, respectively). The energy loss by these particles to ionization in the TPC, $\langle dE/dx\rangle$, depends on the particle velocity and charge. Particle identification is achieved by correlating the $\langle dE/dx\rangle$ values for charged particles in the TPC with their measured magnetic rigidity, which is proportional to the inverse of the curvature of the trajectory in the magnetic field. With both daughter candidates directly identified, one can trace back along the two helical trajectories to the secondary decay point, and thereby reconstruct the location of the decay vertex as well as the parent momentum vector.

Particle identification. Figure 3 presents results from the antihypertriton analysis outlined above, along with results from applying the same analysis to measure the normal matter hypertritons in the same data set; only the sign of the curvature of the decay products is reversed. Figure 3C shows $\langle dE/dx\rangle$ for negative tracks as a function of the magnetic rigidity; the different bands result from the different particle species. The measured $\langle dE/dx\rangle$ of the particles is compared to the expected value from the Bichsel function (*19*), which is an extension of the usual Bethe-Bloch formula for energy loss. A new variable, z, is defined as $z = \ln(\langle dE/dx\rangle/\langle dE/dx\rangle_B)$, where $\langle dE/dx\rangle_B$ is the expected value of $\langle dE/dx\rangle$ for the given particle species and momentum. The measured $z(^3He)$ distributions for ^3He and $^3\bar{He}$ tracks (Fig. 3D) include 5810 ^3He and 2168 ^3He candidates with $|z(^3He)| < 0.2$. The first few ^3He candidates were observed at the Serpukhov accelerator laboratory (*20*), followed by confirmation from the European Organization for Nuclear Research (CERN) (*21*). In 2001, a sample of 14 $^3\bar{He}$ antinuclei was reported by the STAR collaboration (*22*). The ^3He and ^3He samples in the present analysis are so cleanly identified that misidentification from other weak decays is negligible. However, because of the $\langle dE/dx\rangle$ overlap between ^3H and ^3He at low momenta, we can identify the ^3He nuclei only at relatively high momenta (i.e., above ~2 GeV/c). The daughter pions from $^3_{\bar{\Lambda}}\bar{H}$ decays usually have momenta of ~0.3 GeV/c and can be cleanly identified (*23*).

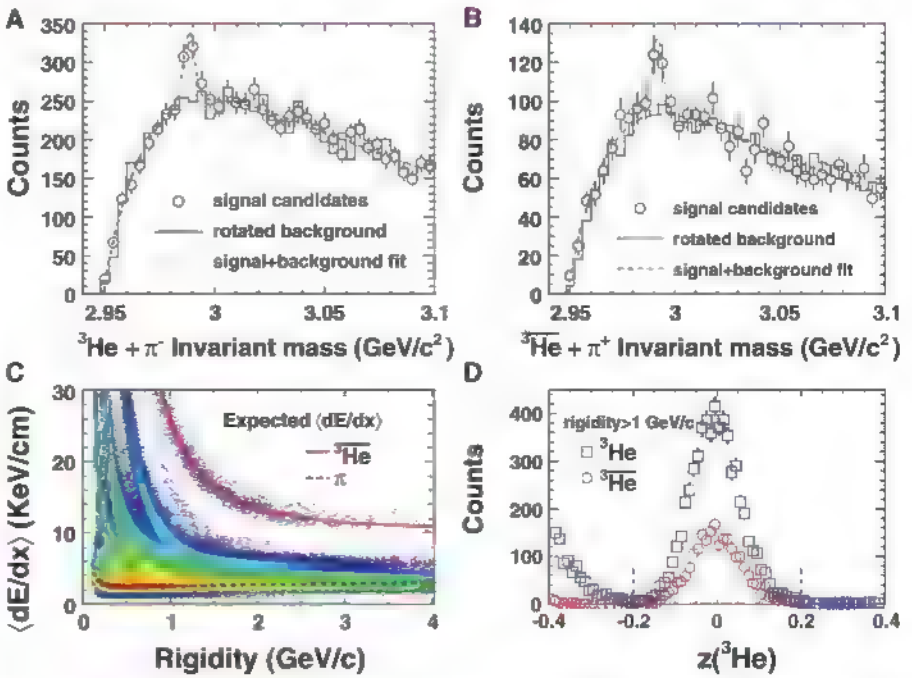

Fig. 3. **(A** and **B)** Invariant mass distribution of the daughter $^3He + \pi$. Open circles represent the signal candidate distributions; solid black lines are background distributions. Blue dashed lines are signal (Gaussian) plus background (double-exponential) combined fit (see text for details). **(A)** $^3_{\Lambda}H$ candidate distributions; **(B)** $^3_{\bar{\Lambda}}\bar{H}$ candidate distributions. **(C)** $\langle dE/dx\rangle$ versus rigidity (momentum/nuclear charge units) for negative tracks. Also plotted are the expected values for ^3He and π tracks. The color indicates the number of tracks on a relative scale. **(D)** Measured $z(^3He)$ distributions for ^3He and $^3\bar{He}$ tracks. (C) and (D) demonstrate that the ^3He and $^3\bar{He}$ tracks ($|z(^3He)| < 0.2$) are identified essentially without background.

Topological reconstruction. A set of topological cuts is invoked to identify and reconstruct the secondary decay vertex positions with a high signal-to-background ratio. These cuts involve the distance at the decay vertex between the tracks for the $^3\bar{He}$ and π^+ (<1 cm), the distance of closest approach (DCA) between the $^3_{\bar{\Lambda}}\bar{H}$ candidate and the event primary vertex (<1 cm), the decay length of the $^3_{\bar{\Lambda}}\bar{H}$ candidate vertex from the event primary vertex (>2.4 cm), and the DCA between the π track and the event primary vertex (>0.8 cm). The cuts are optimized on the basis of full detector response simulations (*24*). Several different cut criteria are also applied to cross-check the results and to estimate the systematic errors. The signal is always present, and the

differences in the total yields using different cuts are found to be less than 15%. The total systematic error in the present analysis is 15%.

The parent candidate invariant mass is calculated on the basis of the momenta of the daughter candidates at the decay vertex. The results are shown as the open circles in Fig. 3A for the hypertriton, ${}^{3}_{\Lambda}\mathrm{H} \rightarrow {}^{3}\mathrm{He} + \pi^-$, and in Fig. 3B for the antihypertriton, ${}^{3}_{\Lambda}\overline{\mathrm{H}} \rightarrow {}^{3}\overline{\mathrm{He}} + \pi^+$. There remains an appreciable combinatorial background in this analysis, which must be described and subtracted. A track rotation method is used to reproduce this background. This approach involves the azimuthal rotation of the daughter ${}^{3}\mathrm{He}$ (${}^{3}\overline{\mathrm{He}}$) track candidates by 180° with respect to the event primary vertex. In this way, the event is not changed statistically, but all of the secondary decay topologies are destroyed because one of the daughter tracks is rotated away. This provides an accurate description of the combinatorial background. The resulting rotated invariant mass distribution is consistent with the background distribution, as shown by the solid histograms (Fig. 3, A and B). The rotated background distribution is fit with a double-exponential function: $f(x) \propto \exp[-(x/p_1)] + \exp[-(x/p_2)]$, where $x = m - m({}^{3}\mathrm{He}) - m(\pi)$, and p_1, p_2 are fit parameters. Finally, the counts in the signal are calculated after subtraction of this fit function derived from the rotated background. In total, 157 ± 30 ${}^{3}_{\Lambda}\mathrm{H}$ and 70 ± 17 ${}^{3}_{\Lambda}\overline{\mathrm{H}}$ candidates are thus observed. The quoted errors are statistical.

Production and properties. We can use the measured ${}^{3}_{\Lambda}\mathrm{H}$ yield to estimate the expected yield of ${}^{3}_{\Lambda}\mathrm{H}$, assuming symmetry between matter and antimatter, in the following manner: ${}^{3}_{\Lambda}\overline{\mathrm{H}} = {}^{3}_{\Lambda}\mathrm{H} \times {}^{3}\overline{\mathrm{He}}/{}^{3}\mathrm{He} = 59 \pm 11$. This indicates a 5.2σ projection of the number of ${}^{3}_{\Lambda}\mathrm{H}$ that is expected in the same data set where ${}^{3}_{\Lambda}\mathrm{H}$, ${}^{3}\mathrm{He}$, and ${}^{3}\overline{\mathrm{He}}$ are detected. An additional check involves fitting the ${}^{3}\mathrm{He} + \pi^-$ invariant mass distribution with the combination of a Gaussian "signal" term plus the double-exponential background function (blue dashed lines in Fig. 3, A and B). The resulting mean values and widths of the invariant mass distributions are consistent with the results from the full detector response simulations. Our best-fit values (from χ^2 minimization) are $m({}^{3}_{\Lambda}\mathrm{H}) = 2.989 \pm 0.001 \pm 0.002$ GeV/c^2 and $m({}^{3}_{\Lambda}\overline{\mathrm{H}}) = 2.991 \pm 0.001 \pm 0.002$ GeV/c^2. These values are consistent with each other within the current statistical and systematic errors, and are consistent with the best value from the literature [i.e., $m({}^{3}_{\Lambda}\mathrm{H}) = 2.99131 \pm 0.00005$ GeV/c^2 (*16*)]. Our systematic error of 2 MeV/c^2 arises from well-understood instrumental effects that cause small deviations from ideal helical ionization tracks in the TPC.

Lifetimes. The direct reconstruction of the secondary decay vertex in these data allows measurement of the ${}^{3}_{\Lambda}\mathrm{H}$ lifetime, τ, via the equation $N(t) = N(0)\exp(-t/\tau)$, where $t = l/(\beta\gamma c)$, $\beta\gamma c = p/m$, l is the measured decay distance, p is the particle momentum, m is the particle mass, and c is the speed of light. For better statistics in our fit, the ${}^{3}_{\Lambda}\mathrm{H}$ and ${}^{3}_{\Lambda}\overline{\mathrm{H}}$ samples are combined, as the matter-antimatter symmetry requires their lifetimes to be equal. Separate measurements of the lifetimes for the two samples show no difference within errors. The signal is then plotted in three bins in $l/\beta\gamma$. The yield in each bin is corrected for the experimental tracking efficiency and acceptance. The total reconstruction efficiency for the ${}^{3}_{\Lambda}\overline{\mathrm{H}}$ and ${}^{3}_{\Lambda}\mathrm{H}$ is on the order of 10%, considering all sources of loss and the analysis cuts. The three points are then fit with the exponential function to extract the parameter $c\tau$, and the best-fit result is displayed as the solid line in Fig. 4A. To arrive at the optimum fit, we performed a χ^2 analysis (Fig. 4A, inset). The $c\tau$ parameter that is observed in this analysis is $c\tau = 5.5^{+2.7}_{-1.4} \pm 0.8$ cm, which corresponds to a lifetime τ of $182^{+89}_{-45} \pm 27$ ps. As an additional cross-check, the Λ hyperon lifetime was extracted from the same data set using the same approach, for the $\Lambda \rightarrow p + \pi^-$ decay channel. The result obtained is $\tau = 267 \pm 5$ ps, which is consistent with $\tau = 263 \pm 2$ ps compiled by the Particle Data Group (*19*).

The ${}^{3}_{\Lambda}\mathrm{H}$ lifetime measurements to date (*25*–*31*) are not sufficiently accurate to distinguish between models, as depicted by Fig. 4B. The present measurement is consistent with a calculation using a phenomenological ${}^{3}_{\Lambda}\mathrm{H}$ wave function (*14*) and is also consistent with a more recent three-body calculation (*15*) using a more modern description of the baryon-baryon force. The present result is also comparable to the lifetime of free Λ particles within the uncertainties, and is statistically competitive with the earlier experimental measurements.

Coalescence calculations. The coalescence model makes specific predictions about the ratios of particle yields. These predictions can be checked for a variety of particle species. To determine the invariant particle yields of ${}^{3}_{\Lambda}\overline{\mathrm{H}}$ and ${}^{3}_{\Lambda}\mathrm{H}$, we apply corrections for detector acceptance and inefficiency. The ${}^{3}_{\Lambda}\overline{\mathrm{H}}$ and ${}^{3}_{\Lambda}\mathrm{H}$ yields are measured in three different transverse momentum (p_t) bins within the analyzed transverse momentum region of $2 < p_t < 6$ GeV c and then extrapolated to the unmeasured regions ($p_t < 2$ GeV/c and $p_t > 6$ GeV/c). This extrapolation assumes that both ${}^{3}_{\Lambda}\overline{\mathrm{H}}$ and ${}^{3}_{\Lambda}\mathrm{H}$ have the same spectral shape as the high-statistics ${}^{3}\mathrm{He}$ and ${}^{3}\mathrm{He}$ samples from the same data set (see Table 1). If the ${}^{3}_{\Lambda}\overline{\mathrm{H}}$ and ${}^{3}_{\Lambda}\mathrm{H}$ are formed by coalescence of $(\overline{\Lambda} + \overline{p} + \overline{n})$ and $(\Lambda + p + n)$, then the production ratio of ${}^{3}_{\Lambda}\overline{\mathrm{H}}$ to ${}^{3}_{\Lambda}\mathrm{H}$ should be proportional to $[(\overline{\Lambda}/\Lambda) \times (\overline{p}/p) \times (\overline{n}/n)]$. The latter value can be extracted from spectra already measured by STAR, and the value obtained is $0.45 \pm 0.08 \pm 0.10$ (*23*, *24*). The measured ${}^{3}_{\Lambda}\overline{\mathrm{H}}/{}^{3}_{\Lambda}\mathrm{H}$ and ${}^{3}\mathrm{He}/{}^{3}\mathrm{He}$ ratios are consistent with the interpretation that the ${}^{3}_{\Lambda}\overline{\mathrm{H}}$ and ${}^{3}_{\Lambda}\mathrm{H}$ are formed by coalescence of $(\overline{\Lambda} + \overline{p} + \overline{n})$ and $(\Lambda + p + n)$, respectively.

Discussion. As the coalescence process for the formation of (anti)hypernuclei requires that (anti)nucleons and (anti)hyperons be in proximity in phase space (i.e., in coordinate and momentum space), (anti)hypernucleus production is sensitive to the correlations in phase-space distributions of nucleons and hyperons (*6*). An earlier two-particle correlation measurement published by STAR implies a strong phase-space correlation between protons and Λ hyperons (*32*). Equilibration among the strange quark flavors and light quark flavors is one of the proposed signatures of QGP formation (*33*), which would result in high (anti)hypernucleus

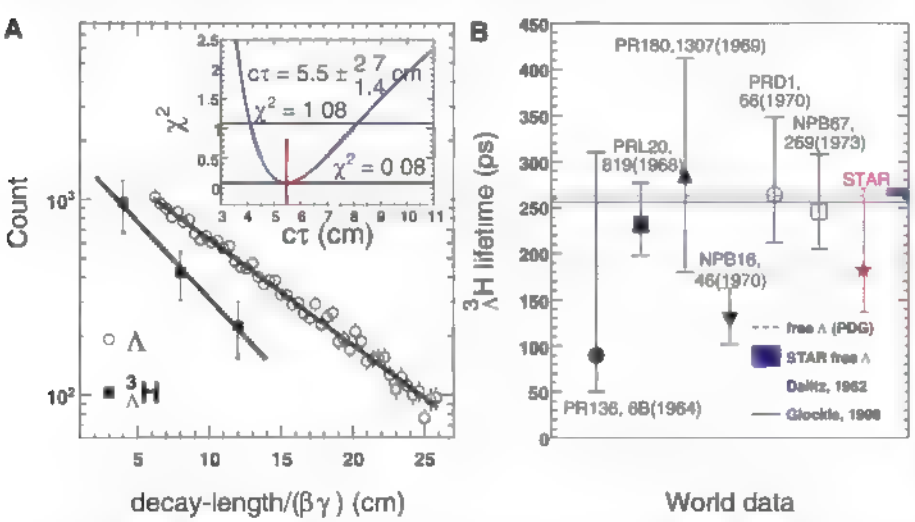

Fig. 4. (A) The ${}^{3}_{\Lambda}\mathrm{H}$ (solid squares) and Λ (open circles) yield distributions versus $c\tau$. The solid lines represent the $c\tau$ fits. The inset depicts the χ^2 distribution of the best ${}^{3}_{\Lambda}\mathrm{H}$ $c\tau$ fit. **(B)** World data for ${}^{3}_{\Lambda}\mathrm{H}$ lifetime measurements. The data points are from (*26*–*31*). The theoretical calculations are from (*14*, *15*). The error bars represent the statistical uncertainties only.

Table 1. Particle ratios from Au + Au collisions at 200 GeV.

Particle type	Ratio
${}^{3}_{\Lambda}\overline{\mathrm{H}}/{}^{3}_{\Lambda}\mathrm{H}$	$0.49 \pm 0.18 \pm 0.07$
${}^{3}\overline{\mathrm{He}}/{}^{3}\mathrm{He}$	$0.45 \pm 0.02 \pm 0.04$
${}^{3}_{\Lambda}\mathrm{H}/{}^{3}\overline{\mathrm{He}}$	$0.89 \pm 0.28 \pm 0.13$
${}^{3}_{\Lambda}\mathrm{H}/{}^{3}\mathrm{He}$	$0.82 \pm 0.16 \pm 0.12$

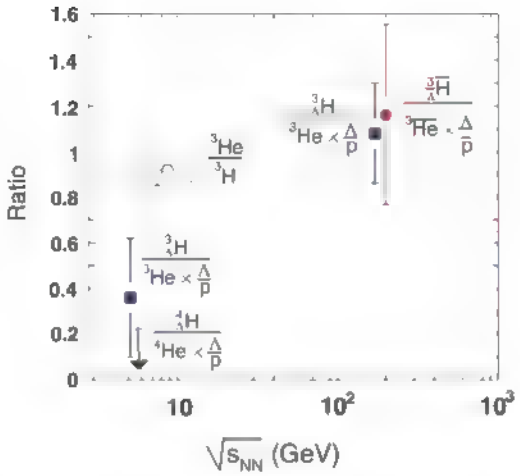

Fig. 5. Particle ratios as a function of center-of-mass energy per nucleon-nucleon collision. The data at lower energies are from (*38*–*40*). The $^4_\Lambda H/(^4He \times \Lambda/p)$ ratio is corrected for the spin degeneracy factor (*38*). The error bars represent statistical uncertainties only.

yields. In addition, recent theoretical studies motivate a search for the onset of QGP by studying the evolution of the baryon-strangeness correlation as a function of collision energy (*34*–*36*). The $^3_\Lambda H$ yields provide a natural and sensitive tool to extract this correlation (*6*, *37*), as they can be compared to the yields of ^3He and ^3H, which have the same atomic mass number. Besides $4u + 4d$ valence quarks, the valence quark content of these species includes one additional u, d, and s quark for ^3He, ^3H, and $^3_\Lambda H$, respectively. Recent nuclear transport model calculations (*37*) support the expectation that the strangeness population factor, $S_3 = {}^3_\Lambda H/({}^3He \times \Lambda/p)$, can be used as a tool to distinguish the QGP from a purely hadronic phase.

Figure 5 depicts various particle ratios as a function of the collision energy. The $^3He/^3H$ ratio at a center-of-mass energy of 5 GeV obtained at the Alternating Gradient Synchrotron (AGS) at BNL is much closer to unity than the ratio $^3_\Lambda H/^3He$ at the same energy. The values of S_3 are about 1/3 at AGS energies and near unity at RHIC energies, although with large uncertainties. The AGS value is further constrained to be relatively low by the measured upper limit on the $^4_\Lambda H/^4He$ ratio (*38*), indicating that the phase-space population for strangeness is very similar to that for the light quarks in high-energy heavy-ion collisions at RHIC, in contrast to the situation at AGS.

Individual relativistic heavy-ion collisions produce abundant hyperons containing one (Λ, Σ), two (Ξ), or three (Ω) strange (anti)quarks. The coalescence mechanism for hypernucleus production in these collisions thus provides a source for other exotic hypernucleus searches. This should allow an extension of the three-dimensional chart of the nuclides (Fig. 1) further into the antimatter sectors. An order-of-magnitude larger sample of similar collisions will allow detailed studies of masses and lifetimes, as well as stringent tests of production rates compared to predictions based on coalescence models.

Concluding remarks. Evidence for the observation of an antihypernucleus, the $^3_\Lambda H$, with a statistical significance of 4.1σ has been presented; consistency checks and constraints from a $^3_\Lambda H$ analysis in the same event sample, with 5.2σ significance, support this conclusion. The lifetime is observed to be $\tau = 182^{+89}_{-45} \pm 27$ ps, which is comparable to that of the free Λ hyperon within current uncertainties. The $\frac{^3\overline{H}}{^3_{\overline{\Lambda}}\overline{H}}$ ($^3_{\overline{\Lambda}}\overline{H}$) to $^3\overline{He}$ ($^3\overline{He}$) ratio is close to unity and is significantly larger than that measured at lower beam energies, indicating that the strangeness phase-space population is similar to that of light quarks. The antihypernucleus observation demonstrates that RHIC is an ideal facility for producing exotic hypernuclei and antinuclei.

References and Notes

1. J. Alcaraz *et al.*, *Phys. Lett. B* **461**, 387 (1999).
2. H. Fuke *et al.*, *Phys. Rev. Lett.* **95**, 081101 (2005).
3. J. Adams *et al.*, *Nucl. Phys. A* **757**, 102 (2005).
4. P. Braun-Munzinger, J. Stachel, *Nature* **448**, 302 (2007), and references therein.
5. M. Danysz, J. Pniewski, *Philos. Mag.* **44**, 348 (1953).
6. H. Sato, K. Yazaki, *Phys. Lett. B* **98**, 153 (1981).
7. S. Ahlen *et al.*, *Nucl. Instrum. Methods A* **350**, 351 (1994).
8. F. Donato, N. Fornengo, D. Maurin, *Phys. Rev. D* **78**, 043506 (2008).
9. W. Greiner, *Int. J. Mod. Phys. E* **5**, 1 (1996).
10. U. Heinz, P. R. Subramanian, H. Stocker, W. Greiner, *J. Phys. G* **12**, 1237 (1986).
11. C. Greiner, D.-H. Rischke, H. Stöcker, P. Koch, *Phys. Rev. D* **38**, 2797 (1988).
12. J. Schaffner, C. Greiner, H. Stöcker, *Phys. Rev. C* **46**, 322 (1992).
13. J. M. Lattimer, M. Prakash, *Science* **304**, 536 (2004).
14. R. H. Dalitz, G. Rajasekharan, *Phys. Lett.* **1**, 58 (1962).
15. H. Kamada, J. Golak, K. Miyagawa, H. Witała, W. Glöckle, *Phys. Rev. C* **57**, 1595 (1998).
16. M. Juric *et al.*, *Nucl. Phys. B* **52**, 1 (1973).
17. K. H. Ackermann *et al.*, *Nucl. Instrum. Methods A* **499**, 624 (2003).
18. M. Anderson *et al.*, *Nucl. Instrum. Methods A* **499**, 659 (2003).
19. C. Amsler *et al.*, *Phys. Lett. B* **667**, 1 (2008).
20. Y. Antipov *et al.*, *Sov. J. Nucl. Phys.* **12**, 171 (1971).
21. K. Pretzl *et al.*, *Heavy Ion Phys.* **14**, 297 (2001).
22. C. Adler *et al.*, *Phys. Rev. Lett.* **87**, 262301 (2001).
23. B. I. Abelev *et al.*, *Phys. Rev. Lett.* **97**, 152301 (2006).
24. J. Adams *et al.*, *Phys. Rev. Lett.* **98**, 062301 (2007).
25. M. M. Block *et al.*, *Proceedings of the International Conference on Hyperfragments at St. Cergue 1963, CERN Report 64-1* (1964), p. 63.
26. R. J. Prem, P. H. Steinberg, *Phys. Rev.* **136**, B1803 (1964).
27. G. Bohm *et al.*, *Nucl. Phys. B* **16**, 46 (1970).
28. G. Keyes *et al.*, *Phys. Rev. Lett.* **20**, 819 (1968).
29. R. E. Phillips, J. Schneps, *Phys. Rev.* **180**, 1307 (1969).
30. G. Keyes *et al.*, *Phys. Rev. D* **1**, 66 (1970).
31. G. Keyes, J. Sacton, J. H. Wickens, M. M. Block, *Nucl. Phys. B* **67**, 269 (1973).
32. J. Adams *et al.*, *Phys. Rev. C* **74**, 064906 (2006).
33. J. Rafelski, B. Muller, *Phys. Rev. Lett.* **48**, 1066 (1982).
34. V. Koch, A. Majumder, J. Randrup, *Phys. Rev. Lett.* **95**, 182301 (2005).
35. A. Majumder, B. Muller, *Phys. Rev. C* **74**, 054901 (2006).
36. R. V. Gavai, S. Gupta, *Phys. Rev. D* **73**, 014004 (2006).
37. S. Zhang *et al.*, *Phys. Lett. B* **684**, 224 (2010).
38. T. A. Armstrong *et al.*, *Phys. Rev. C* **70**, 024902 (2004).
39. T. A. Armstrong *et al.*, *Phys. Rev. C* **61**, 064908 (2000).
40. V. I. Kolesnikov, *J. Phys. Conf. Ser.* **110**, 032010 (2008).

41. We thank K. Synder for providing Fig. 1, and the RHIC Operations Group and RCF at BNL, the NERSC Center at LBNL, and the Open Science Grid consortium for providing resources and support. Supported by the Offices of NP and HEP within the U.S. DOE Office of Science; NSF; the Sloan Foundation, the DFG cluster of excellence "Origin and Structure of the Universe," CNRS/IN2P3, STFC and EPSRC of the United Kingdom; FAPESP CNPq of Brazil; Ministry of Education and Science of the Russian Federation; MNSFC, CAS, MoST, and MoE of China; GA and MSMT of the Czech Republic; FOM and NOW of the Netherlands; DAE, DST, and CSIR of India; Polish Ministry of Science and Higher Education; Korea Research Foundation; Ministry of Science, Education and Sports of the Republic of Croatia; and Russian Ministry of Science and Technology and RosAtom of Russia.

The STAR Collaboration

B. I. Abelev,[1] M. M. Aggarwal,[2] Z. Ahammed,[3] A. V. Alakhverdyants,[4] I. Alekseev,[5] B. D. Anderson,[6] D. Arkhipkin,[7] G. S. Averichev,[4] J. Balewski,[8] L. S. Barnby,[9] S. Baumgart,[10] D. R. Beavis,[7] R. Bellwied,[11] M. J. Betancourt,[8] R. R. Betts,[1] A. Bhasin,[12] A. K. Bhati,[2] H. Bichsel,[13] J. Bielcik,[14] J. Bielcikova,[15] B. Biritz,[16] L. C. Bland,[7] B. E. Bonner,[17] J. Bouchet,[6] E. Braidot,[18] A. V. Brandin,[19] A. Bridgeman,[20] E. Bruna,[10] S. Bueltmann,[21] I. Bunzarov,[4] T. P. Burton,[9] X. Z. Cai,[22] H. Caines,[10] M. Calderón,[23] O. Catu,[10] D. Cebra,[23] R. Cendejas,[16] M. C. Cervantes,[24] Z. Chajecki,[25] P. Chaloupka,[15] S. Chattopadhyay,[3] H. F. Chen,[26] J. H. Chen,[22] J. Y. Chen,[27] J. Cheng,[28] M. Cherney,[29] A. Chikanian,[10] K. E. Choi,[30] W. Christie,[7] P. Chung,[15] R. F. Clarke,[24] M. J. M. Codrington,[24] R. Corliss,[8] J. G. Cramer,[13] H. J. Crawford,[31] D. Das,[23] S. Dash,[32] A. Davila Leyva,[33] L. C. De Silva,[11] R. R. Debbe,[7] T. G. Dedovich,[4] M. DePhillips,[7] A. A. Derevschikov,[34] R. Derradi de Souza,[35] L. Didenko,[7] P. Djawotho,[24] S. M. Dogra,[12] X. Dong,[26] J. L. Drachenberg,[24] J. E. Draper,[23] J. C. Dunlop,[7] M. R. Dutta Mazumdar,[3] L. G. Efimov,[4] E. Elhalhuli,[9] M. Elnimr,[11] J. Engelage,[31] G. Eppley,[17] B. Erazmus,[37] M. Estienne,[37] L. Eun,[38] O. Evdokimov,[1] P. Fachini,[7] R. Fatemi,[39] J. Fedorisin,[4] R. G. Fersch,[39] P. Filip,[4] E. Finch,[10] V. Fine,[7] Y. Fisyak,[7] C. A. Gagliardi,[24] D. R. Gangadharan,[16] M. S. Ganti,[3] E. J. Garcia-Solis,[1] A. Geromitsos,[37] F. Geurts,[17] V. Ghazikhanian,[16] P. Ghosh,[3] Y. N. Gorbunov,[29] A. Gordon,[7] O. Grebenyuk,[36] D. Grosnick,[40] B. Grube,[30] S. M. Guertin,[16] A. Gupta,[12] N. Gupta,[12] W. Guryn,[7] B. Haag,[23] A. Hamed,[24] L.-X. Han,[22] J. W. Harris,[10] J. P. Hays-Wehle,[8] M. Heinz,[10] S. Heppelmann,[38] A. Hirsch,[41] E. Hjort,[36] A. M. Hoffman,[8] G. W. Hoffmann,[39] D. J. Hofman,[1] R. S. Hollis,[1] B. Huang,[26] H. Z. Huang,[16] T. J. Humanic,[25] L. Huo,[24] G. Igo,[16] A. Iordanova,[1] P. Jacobs,[36] W. W. Jacobs,[42] P. Jakl,[15] C. Jena,[32] F. Jin,[22] C. L. Jones,[8] P. G. Jones,[9] J. Joseph,[6] E. G. Judd,[31] S. Kabana,[37] K. Kajimoto,[33] K. Kang,[28] J. Kapitan,[15] K. Kauder,[1] D. Keane,[6] A. Kechechyan,[4] D. Kettler,[13] D. P. Kikola,[36] J. Kiryluk,[36] A. Kisiel,[43] S. R. Klein,[36] A. G. Knospe,[10] A. Kocoloski,[8] D. D. Koetke,[40] T. Kollegger,[44] J. Konzer,[41] M. Kopytine,[6] I. Koralt,[21] L. Koroleva,[5] W. Korsch,[39] L. Kotchenda,[19] V. Kouchpil,[15] P. Kravtsov,[19] K. Krueger,[20] M. Krus,[14] L. Kumar,[2] P. Kurnadi,[16] M. A. C. Lamont,[7] J. M. Landgraf,[7] S. LaPointe,[11] J. Lauret,[7] A. Lebedev,[7] R. Lednicky,[4] C.-H. Lee,[30] J. H. Lee,[7] W. Leight,[8] M. J. Levine,[7] C. Li,[26] L. Li,[33] N. Li,[27] W. Li,[22] X. Li,[41] Y. Li,[28] Z. Li,[27] G. Lin,[10] S. J. Lindenbaum,[45*] M. A. Lisa,[25] F. Liu,[27] H. Liu,[23] J. Liu,[17] T. Ljubicic,[7] W. J. Llope,[17] R. S. Longacre,[7] W. A. Love,[7] Y. Lu,[26] X. Luo,[26] G. L. Ma,[22] Y. G. Ma,[22] D. P. Mahapatra,[32] R. Majka,[10] O. I. Mal,[42] L. K. Mangotra,[12] R. Manweiler,[40] S. Margetis,[6] C. Markert,[33] H. Masui,[36] H. S. Matis,[36] Yu. A. Matulenko,[34] D. McDonald,[17] T. S. McShane,[29] A. Meschanin,[34] R. Milner,[8] N. G. Minaev,[34] S. Mioduszewski,[24] A. Mischke,[18] M. K. Mitrovski,[44] B. Mohanty,[3] M. M. Mondal,[3] B. Morozov,[5] D. A. Morozov,[34] M. G. Munhoz,[46] B. K. Nandi,[47] C. Nattrass,[10] T. K. Nayak,[3] J. M. Nelson,[9] P. K. Netrakanti,[41] M. J. Ng,[31] L. V. Nogach,[34] S. B. Nurushev,[34]

G. Odyniec,[36] A. Ogawa,[7] H. Okada,[7] V. Okorokov,[19] D. Olson,[35] M. Pachr,[14] B. S. Page,[42] S. K. Pal,[3] Y. Pandit,[6] Y. Panebratsev,[4] T. Pawlak,[43] T. Peitzmann,[18] V. Perevoztchikov,[7] C. Perkins,[31] W. Peryt,[43] S. C. Phatak,[32] P. Pile,[7] M. Planinic,[48] M. A. Ploskon,[35] J. Pluta,[43] D. Plyku,[21] N. Poljak,[48] A. M. Poskanzer,[35] B. V. K. S. Potukuchi,[12] C. B. Powell,[35] D. Prindle,[13] C. Pruneau,[11] N. K. Pruthi,[2] P. R. Pujahari,[17] J. Putschke,[10] H. Qiu,[49] R. Raniwala,[30] S. Raniwala,[30] R. L. Ray,[33] R. Redwine,[8] R. Reed,[23] H. G. Ritter,[35] J. B. Roberts,[17] O. V. Rogachevskiy,[4] J. L. Romero,[23] A. Rose,[35] C. Roy,[37] L. Ruan,[7] R. Sahoo,[37] S. Sakai,[35] I. Sakrejda,[35] T. Sakuma,[8] S. Salur,[35] J. Sandweiss,[50] E. Sangaline,[23] J. Schambach,[33] R. P. Scharenberg,[41] N. Schmitz,[51] T. R. Schuster,[44] J. Seele,[8] J. Seger,[29] I. Selyuzhenkov,[42] P. Seyboth,[51] E. Shahaliev,[4] M. Shao,[26] M. Sharma,[11] S. S. Shi,[27] E. P. Sichtermann,[35] F. Simon,[51] R. N. Singaraju,[3] M. J. Skoby,[41] N. Smirnov,[50] P. Sorensen,[7] J. Sowinski,[42] H. M. Spinka,[20] B. Srivastava,[41] T. D. S. Stanislaus,[40] D. Staszak,[16] J. R. Stevens,[42] R. Stock,[44] M. Strikhanov,[19] B. Stringfellow,[41] A. A. P. Suaide,[46] M. C. Suarez,[1] N. L. Subba,[6] M. Sumbera,[15] X. M. Sun,[35] Y. Sun,[26] Z. Sun,[49] B. Surrow,[8] D. N. Svirida,[3] T. J. M. Symons,[35] A. Szanto de Toledo,[46] J. Takahashi,[35] A. H. Tang,[7] Z. Tang,[26] L. H. Tarini,[11] T. Tarnowsky,[52] D. Thein,[33] J. H. Thomas,[35] J. Tian,[22] A. R. Timmins,[11] S. Timoshenko,[19] D. Tlusty,[15] M. Tokarev,[4] T. A. Trainor,[13] V. N. Tram,[35] S. Trentalange,[16] R. E. Tribble,[24] O. D. Tsai,[16] J. Ulery,[41] T. Ullrich,[7] D. G. Underwood,[20] G. Van Buren,[7] M. van Leeuwen,[18] G. van Nieuwenhuizen,[8] J. A. Vanfossen Jr.,[6] R. Varma,[47] G. M. S. Vasconcelos,[35] A. N. Vasiliev,[34] F. Videbaek,[7] Y. P. Viyogi,[3] S. Vokal,[4] S. A. Voloshin,[11] M. Wada,[33] M. Walker,[8] F. Wang,[41] G. Wang,[16] H. Wang,[52] J. S. Wang,[49] Q. Wang,[41] X. L. Wang,[26] Y. Wang,[28] G. Webb,[39] J. C. Webb,[40] G. D. Westfall,[9] C. Whitten Jr.,[16] H. Wieman,[35] E. Wingfield,[33] S. W. Wissink,[42] R. Witt,[53] Y. Wu,[27] W. Xie,[41] H. Xu,[49] N. Xu,[35] Q. H. Xu,[54] W. Xu,[16] Y. Xu,[26] Z. Xu,[7] L. Xue,[22] Y. Yang,[49] P. Yepes,[17] K. Yip,[7] I.-K. Yoo,[30] Q. Yue,[28] M. Zawisza,[43] H. Zbroszczyk,[43] W. Zhan,[49] J. Zhang,[27] S. Zhang,[22] W. M. Zhang,[6] X. P. Zhang,[35] Y. Zhang,[35] Z. P. Zhang,[26] J. Zhao,[22] C. Zhong,[22] J. Zhou,[17] W. Zhou,[54] X. Zhu,[28] Y. H. Zhu,[22] R. Zoulkarneev,[4] Y. Zoulkameeva[4]

[1]University of Illinois, Chicago, IL 60607, USA. [2]Panjab University, Chandigarh 160014, India. [3]Variable Energy Cyclotron Centre, Kolkata 700064, India. [4]Joint Institute for Nuclear Research, Dubna 141 980, Russia. [5]Alikhanov Institute for Theoretical and Experimental Physics, Moscow, Russia. [6]Kent State University, Kent, OH 44242, USA. [7]Brookhaven National Laboratory, Upton, NY 11973, USA. [8]Massachusetts Institute of Technology, Cambridge, MA 02139, USA. [9]University of Birmingham, Birmingham, UK. [10]Yale University, New Haven, CT 06520, USA. [11]Wayne State University, Detroit, MI 48201, USA. [12]University of Jammu, Jammu 180001, India. [13]University of Washington, Seattle, WA 98195, USA. [14]Czech Technical University in Prague, FNSPE, Prague, 115 19, Czech Republic. [15]Nuclear Physics Institute AS CR, 250 68 Řež, Prague, Czech Republic. [16]University of California, Los Angeles, CA 90095, USA. [17]Rice University, Houston, TX 77251, USA. [18]NIKHEF and Utrecht University, Amsterdam, Netherlands. [19]Moscow Engineering Physics Institute, Moscow, Russia. [20]Argonne National Laboratory, Argonne, IL 60439, USA. [21]Old Dominion University, Norfolk, VA 23529, USA. [22]Shanghai Institute of Applied Physics, Shanghai 201800, China. [23]University of California, Davis, CA 95616, USA. [24]Texas A&M University, College Station, TX 77843, USA. [25]Ohio State University, Columbus, OH 43210, USA. [26]University of Science and Technology of China, Hefei 230026, China. [27]Institute of Particle Physics, CCNU (HZNU), Wuhan 430079, China. [28]Tsinghua University, Beijing 100084, China. [29]Creighton University, Omaha, NE 68178, USA. [30]Pusan National University, Pusan, Republic of Korea. [31]University of California, Berkeley, CA 94720, USA. [32]Institute of Physics, Bhubaneswar 751005, India. [33]University of Texas, Austin, TX 78712, USA. [34]Institute of High Energy Physics, Protvino, Russia. [35]Universidade Estadual de Campinas, Sao Paulo, Brazil. [36]Lawrence Berkeley National Laboratory, Berkeley, CA 94720, USA. [37]SUBATECH, Nantes, France. [38]Pennsylvania State University, University Park, PA 16802, USA. [39]University of Kentucky, Lexington, KY 40506, USA. [40]Valparaiso University, Valparaiso, IN 46383, USA. [41]Purdue University, West Lafayette, IN 47907, USA. [42]Indiana University, Bloomington, IN 47408, USA. [43]Warsaw University of Technology, Warsaw, Poland. [44]University of Frankfurt, Frankfurt, Germany. [45]City College of New York, New York, NY 10031, USA. [46]Universidade de Sao Paulo, Sao Paulo, Brazil. [47]Indian Institute of Technology, Mumbai, India. [48]University of Zagreb, Zagreb, HR-10002, Croatia. [49]Institute of Modern Physics, Lanzhou, China. [50]University of Rajasthan, Jaipur 302004, India. [51]Max-Planck-Institut für Physik, Munich, Germany. [52]Michigan State University, East Lansing, MI 48824, USA. [53]United States Naval Academy, Annapolis, MD 21402, USA. [54]Shandong University, Jinan, Shandong 250100, China. *Deceased.

29 October 2009; accepted 18 February 2010
Published online 4 March 2010
10.1126/science.1183980
Include this information when citing this paper

Functional Hierarchy and Reversibility Within the Murine Spermatogenic Stem Cell Compartment

Toshinori Nakagawa,[1]* Manju Sharma,[2] Yo-ichi Nabeshima,[1] Robert E. Braun,[2] Shosei Yoshida[1,3,4]†

Stem cells support tissue maintenance by balancing self-renewal and differentiation. In mice, it is believed that a homogeneous stem cell population of single spermatogonia supports spermatogenesis, and that differentiation, which is accompanied by the formation of connected cells (cysts) of increasing length, is linear and nonreversible. We evaluated this model with the use of lineage analysis and live imaging, and found that this putative stem cell population is not homogeneous. Instead, the stem cell pool that supports steady-state spermatogenesis is contained within a subpopulation of single spermatogonia. We also found that cysts are not committed to differentiation and appear to recover stem cell potential by fragmentation, and that the fate of individual spermatogonial populations was markedly altered during regeneration after damage. Thus, there are multiple and reversible paths from stem cells to differentiation, and these may also occur in other systems.

Maintenance of adult tissues is supported by a small number of undifferentiated stem cells that self-renew to maintain their population and produce differentiating progeny for normal tissue function. It has generally been accepted that differentiating daughter cells progress unidirectionally toward terminal differentiation. This view has recently been challenged by data suggesting that under some circumstances, differentiating cells can revert to the self-renewing stem cell pool (*1*–*8*). This apparent plasticity may add robustness to maintenance of the stem cell population during normal tissue maintenance and may play a crucial role in tissue regeneration after injury. However, the nature of the self-renewing stem cells and the plasticity of differentiating cells in the maintenance of tissue homeostasis and regeneration are mostly unknown, particularly in mammals.

Germ cells share a characteristic feature across all animal species. Although the most primitive cells in adult gonads are singly isolated, their differentiating progeny remain connected by intercellular bridges to form syncytial cysts of 2^n cells (*9*, *10*). Thus, the length of the cysts reflects their cell division history or lineage. This unique feature has made the germ line one of the most tractable systems to study adult stem cell self-renewal and differentiation (*2*, *3*). The study of the spermatogenic stem cell compartment in mammals also relies on heterogeneity in the cyst length (*9*, *11*, *12*). In the mouse testis, the most primitive subset of diploid germ cells (spermatogonia) includes A_{single} (A_s, single isolated spermatogonia), A_{paired} (A_{pr}, interconnected spermatogonial pairs), and $A_{aligned}$ (A_{al}, consisting of 4, 8, or 16 interconnected spermatogonia, specifically termed A_{al4}, A_{al8}, and A_{al16}, respectively). A vast majority of stem cell function, if not all, resides in this population. These cells transform without cell division into more differentiating A_1 spermatogonia, which subsequently undergo six mitotic and two meiotic divisions to form haploid spermatids (*10*, *13*) (fig. S1).

The prevailing rodent stem cell model (*14*, *15*) (Fig. 1A) assumes that the stem cell population resides in the A_s population and that cyst length reflects the extent of differentiation in a linear manner (*9*, *11*). A corollary of this "A_s model" is that A_s spermatogonia are functionally homogeneous, that all A_s cells are stem cells, and that all cells are equivalent in each morphological cat-

[1]Department of Pathology and Tumor Biology, Graduate School of Medicine, Kyoto University, Kyoto 606-8501, Japan. [2]The Jackson Laboratory, Bar Harbor, ME 04609, USA. [3]Division of Germ Cell Biology, National Institute for Basic Biology, National Institutes for Natural Sciences, Okazaki 444-8787, Japan. [4]Department of Basic Biology, School of Life Science, Graduate University for Advanced Studies (SOKENDAI), Okazaki 444 8585, Japan.

*Present address: Department of Immunobiology and Hematology, Institute for Frontier Medical Sciences, Kyoto University, Kyoto 606-8507, Japan.

†To whom correspondence should be addressed. E-mail: shosei@nibb.ac.jp

egory (*9*, *10*). This simple and attractive model, proposed in 1971, has provided the framework for years of germline stem cell research in mice and other animals. However, the lack of appropriate molecular markers and experimental tools has hindered its critical evaluation.

In recent years, substantial progress has been made in identifying genes that are expressed in A_s cells and cysts of A_{pr} and A_{al} [e.g., *GFRα1*, *PLZF*, *E-CAD* (E-cadherin), and *NGN3*] (*16*–*23*). Heterogeneity in gene expression among cysts of the same length has suggested possible functional heterogeneity within cells of the same cyst length (*21*–*23*). Here, we used gene expression, cyst length, lineage analysis (*6*), and live imaging (*24*) to revisit the long-held assumptions of the functionality of the spermatogonial population in mice.

Stratification of spermatogonia by morphology and gene expression. Comparison of expression patterns of genes that mark the A_s, A_{pr}, and/or A_{al} population (*16*–*23*) by whole-mount double staining of seminiferous tubules, the spermatogenic center of the testis, revealed that the two genes *PLZF* (*17*, *18*) and *E-CAD* (*21*) have essentially identical expression patterns and are found in essentially all the A_s, A_{pr}, and A_{al} spermatogonia (fig. S2 and supporting online text). In contrast, two other genes, *GFRα1* and *NGN3*, were expressed in minor and major subpopulations of the E-CAD$^+$ total A_s, A_{pr}, and A_{al} population, respectively, with the same gene expression observed in all the cells within an individual cyst (Fig. 1, B and C). Intriguingly, all the E-CAD$^+$ cysts expressed either or both of these genes (Fig. 1E). Thus, spermatogonial cysts were heterogeneous in the expression of GFRα1 and NGN3 even in the same morphological fraction, except for $A_{al\text{-}16}$, which was essentially all NGN3$^+$ (Fig. 1D).

Thus, the A_s, A_{pr}, and A_{al} populations can be stratified by both morphology (cyst length) and gene expression (GFRα1 single-positive, GFRα1-NGN3 double-positive, and NGN3 single-positive). These two parameters are mutually correlated. Shorter cysts have a greater probability of being GFRα1 single-positive, whereas longer cysts tend to be NGN3 single-positive.

A functional hierarchy between the GFRα1$^+$ and NGN3$^+$ subpopulations. The observation that GFRα1$^+$ cells are largely A_s or A_{pr}, whereas NGN3$^+$ cells are mainly A_{al} (Fig. 1D), suggests that cells make a transition from GFRα1$^+$ → NGN3$^+$ → A_1 spermatogonia. To investigate this possibility, we used pulse-chase and live-imaging experiments.

First, we analyzed the fate of NGN3$^+$ cells that were irreversibly labeled with green fluorescent protein (GFP) by a single administration of 4-OH-tamoxifen (Fig. 2A) (*6*). Two days after the pulse, a majority of the GFP-tagged cells were E-CAD$^+$ GFRα1$^-$ KIT$^-$ (KIT is a marker for A_1 spermatogonia through early spermatocytes) (*25*) (Fig. 2, B to D). The labeling efficiency of the NGN3$^+$ cells was ~30% for all morphological fractions (fig. S3 and supporting online text). Ten days after the pulse, most of the GFP-tagged cells were present in large cysts (>16 cells) that were E-CAD$^+$ GFRα1$^-$ KIT$^+$ (Fig. 2, E to H), indicating that most NGN3$^+$ cells left the E-CAD$^+$ compartment and went on to differentiate. Eventually, all KIT$^+$ spermatogonia were derived from NGN3$^+$ cells, as they retained the GFP in the transgenic mice that express GFP under the control of the *Ngn3* regulatory sequence (Ngn3-GFP) (*16*) (fig. S4). Second, live imaging of the testis of the same Ngn3-GFP mice (*16*, *24*) was used to directly show that a gain of GFP signal, which reflects an induction of NGN3, was frequently observed in GFP$^-$ (i.e., GFRα1 single-positive) A_s, A_{pr}, and A_{al} spermatogonia (Fig. 2I, fig. S5, and movie S1). The minor GFRα1-NGN3 double-positive cells are likely to be in transition from GFRα1 single-positive to NGN3 single-positive cells, because both signals were weaker in double-positive cells than in either of the single-positive populations.

Functional hierarchy within the A_s spermatogonia. We then asked whether A_s spermatogonia are functionally heterogeneous. After a single pulse of 4-OH-tamoxifen to permanently label NGN3$^+$ cells with GFP, the contribution of the GFP-tagged cells to the entire A_s population rapidly decreased (Fig. 3A), indicating that the majority of the NGN3$^+$ A_s cells left the A_s compartment. Live imaging showed that NGN3$^+$ A_s cells mostly became NGN3$^+$ A_{pr}, while a few of them divided into two A_s cells (Fig. 2I, fig. S5, and movie S1). In addition, 2 days after the pulse, a small number of labeled single cells were KIT$^+$ (Fig. 3C), which suggested direct conversion of NGN3$^+$ A_s into A_1 spermatogonia, although they might represent a novel and unique population. We conclude that A_s cells are not equivalent, and that a vast proportion of NGN3$^+$ A_s cells are essentially transit-amplifying cells rather than self-renewing stem cells.

However, by day 20, a small number of GFP-tagged cells were still present in the A_s compartment (Fig. 3A). A majority of these persisting GFP-tagged A_s cells were also GFRα1$^+$ (Fig. 3B). These data suggest that a small fraction of the NGN3$^+$ cells can revert to GFRα1$^+$ A_s cells. Theoretically, such "reverted" GFRα1$^+$ A_s cells could be derived from NGN3$^+$ A_s or from NGN3$^+$ A_{pr} and A_{al}, although the latter events would require cyst fragmentation.

Fragmentation of spermatogonial clones observed by live imaging. Live imaging of Ngn3-GFP transgenic mouse testes, in which

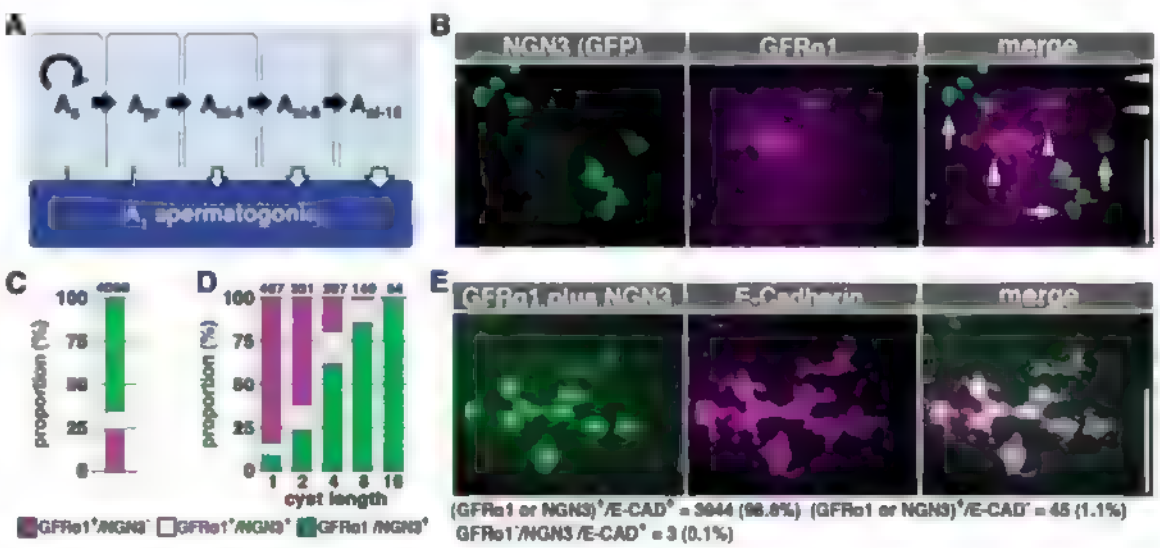

Fig. 1. The "A_s model" and hierarchical gene expression in cysts of A_s, A_{pr}, and A_{al} spermatogonia. (**A**) Schematic representation of the "A_s model." Arrows indicate the proposed flows of the cells in each cyst type. The width of the open vertical arrows reflects the relative probability of each cyst type to differentiate. (**B**) Whole-mount immunofluorescence for GFP (green) and GFRα1 (magenta) in Ngn3-EGFP mouse seminiferous tubules. Arrows and arrowheads indicate NGN3$^+$ (GFP$^+$) and GFRα1$^+$ cells, respectively. Scale bar, 100 μm. (**C** and **D**) Summarized cell counts from immunostaining shown in (B), shown as total frequency of single- and double-positive spermatogonia regardless of cyst length (C) and frequency of single- and double-positive cysts harboring the indicated number of cells (D). Numbers of counted cells (C) and cysts (D) are shown above each bar. In (D), cysts of other than 2^n cells are omitted. (**E**) Whole-mount immunofluorescence using a mixture of antibodies to GFP and GFRα1 (green) and antibody to E-CAD (magenta) in Ngn3-EGFP mouse seminiferous tubules. Summarized counts are shown under the panel. Scale bar, 100 μm.

$NGN3^+$ cells were labeled with GFP, provided direct evidence of spermatogonial cyst fragmentation (Fig. 4 and fig. S5). The frequency of this fragmentation was much lower than that of the normal divisions that double the cyst length (fig. S5, B and C). In one case out of the three observed (Fig. 4 and movie S2), a GFP^+ (i.e., $NGN3^+$) A_{a-8} cyst divided synchronously and then fragmented into two pairs of interconnected cells, which later divided into A_{al-4}, whereas the remainder of the 12-cell cyst underwent synchronized death. The other two cysts showed different patterns of fragmentation, excluding the possibility of a stereotypic fragmentation pattern (fig. S5C and movies S3 and S4). In these instances, the GFP signal decreased in many of the resultant shorter cysts and A_s, prompting us to postulate that they might have become $GFR\alpha1$ single-positive. Cysts with lengths other than 2^n cells were also generated as a result of cyst fragmentation.

Capture of latent stem cell potential during tissue regeneration. During steady-state spermatogenesis, the A_s, A_{pr}, and A_{al} subpopulations are constant by definition. However, during regeneration after damage, self-renewal is favored over differentiation (*11*). We investigated the fate of the A_s, A_{pr}, and A_{al} subpopulations during regeneration after administration of busulfan, a drug preferentially toxic to spermatogonia including stem cells (Fig. 5, A to D). About 8 days after busulfan treatment, a majority of E-CAD cells had died, although some had formed small regenerating clusters. By day 18, such clusters became prominent and the local density of $E\text{-}CAD^+$ spermatogonia had recovered to a level comparable to that in untreated testes, although their average density was still low (Fig. 5B). During the recovery period, we found that both cyst length and gene expression were altered, the average cyst length became shorter and a greater percentage of cells were $GFR\alpha1^+$ (Fig. 5, C and D).

A change in these two parameters during recovery could reflect preferential elimination of longer $NGN3^+$ cysts, a decrease in their formation, an increase in cyst fragmentation, and/or reversion from $NGN3^+$ to $GFR\alpha1^+$. Although the first possibility is not excluded, fate analysis of

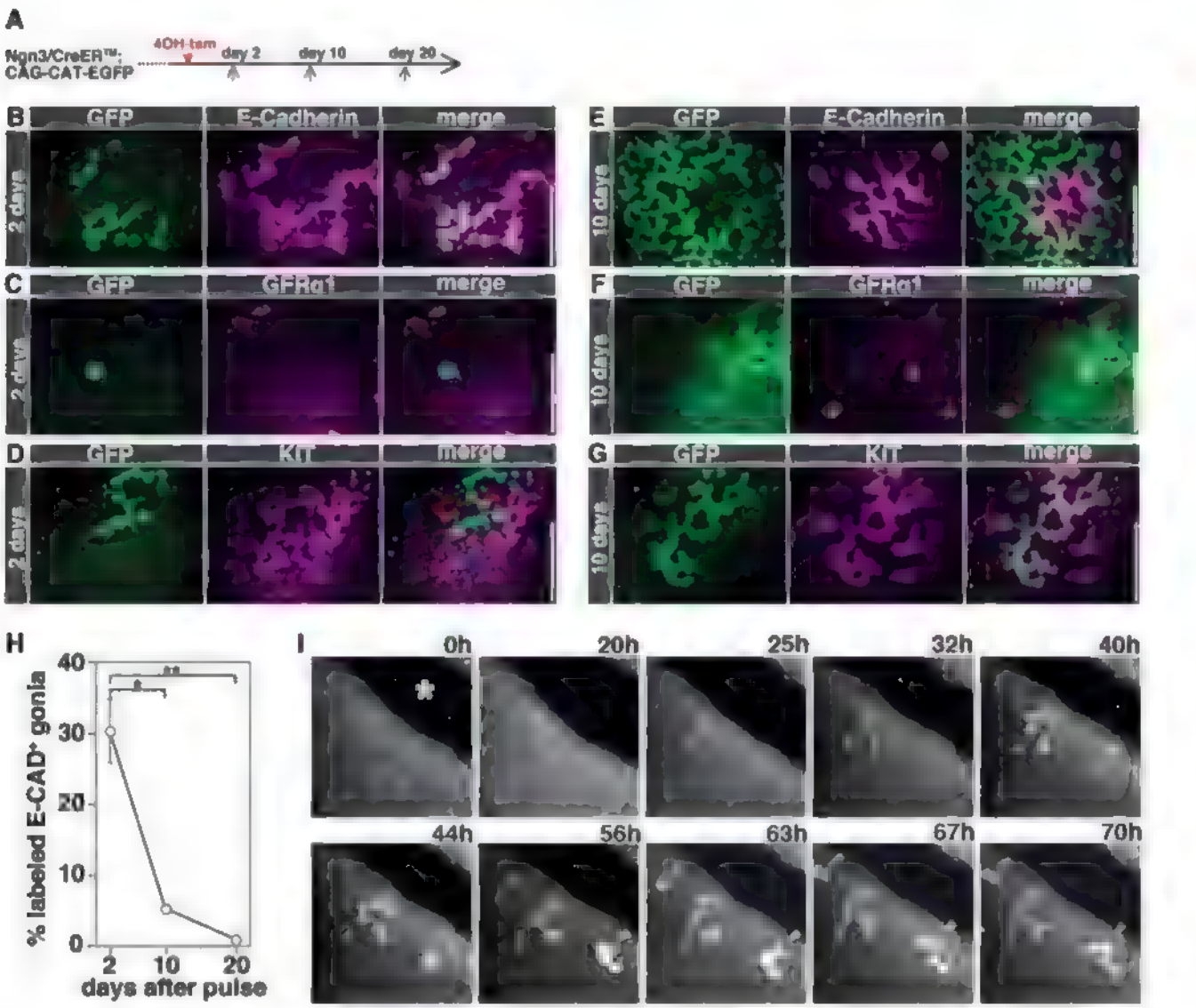

Fig. 2. Behavior of the $NGN3^+$ population in steady-state spermatogenesis. (**A**) Schedule for (B) to (G). Ngn3/CreER™;CAG-CAT-EGFP mice were administrated 4-OH-tamoxifen; their testes were analyzed 2, 10, and 20 days after pulse. (**B** to **G**) Whole-mount staining of the seminiferous tubules for EGFP (green) and E-CAD [(B) and (E)], $GFR\alpha1$ [(C) and (F)], or KIT [(D) and (G)] (magenta) 2 days or 10 days after pulse. Scale bars, 100 μm. (**H**) Contribution of pulse-labeled cells to the $E\text{-}CAD^+$ total population. Averages ± SEM from 5, 3, and 5 testes for days 2, 10, and 20, respectively, are shown; $^*P = 0.006$, $^{**}P < 0.001$, respectively, against the values of day 2 (Student's *t* test). (**I**) Selected frames from live imaging (movie S1) in Ngn3-GFP mouse testes. Orange, yellow, and green arrowheads indicate the gain of GFP fluorescence in A_s, A_{al-4}, and probable A_{al-8}, respectively. The indicated A_s cell divided into an A_{pr}; asterisk denotes a blood vessel.

the pulse-labeled NGN3$^+$ cells is compatible with the other three scenarios (Fig. 5, E to I). A higher percentage of labeled GFP$^+$ cells (which had been NGN3$^+$ at the time of labeling) were retained in the E-CAD$^+$ population during regeneration than during steady-state spermatogenesis (Fig. 5F). Moreover, a significantly higher percentage of the labeled cells contributed to the E-CAD$^+$ A_s fraction (Fig. 5G) and were positive for GFRα1 (Fig. 5H). We also found that the percentage of labeled cells in the GFRα1$^+$ A_s population increased during regeneration (Fig. 5I). These findings indicate that either the labeled NGN3$^+$ A_s cells remained as A_s and "reverted" back to being GFRα1$^-$, or alternatively, that NGN3$^+$ A_{pr} or A_{al} cells gave rise to GFRα1$^-$ A_s cells through cyst fragmentation.

In addition, the frequency of GFRα1$^+$ $A_{al\text{-}8}$ and $A_{al\text{-}16}$ cells, which were observed in steady-state spermatogenesis only rarely, was elevated during regeneration (fig. S7). This indicates a delay of the GFRα1$^+$ → NGN3$^+$ transition, a NGN3$^+$ → GFRα1$^+$ reversion in long cysts, or both. Finally, as observed previously (*6*), the contribution of the labeled cells to the long-term stem cell pool in regeneration was much higher than in steady-state spermatogenesis.

We conclude that the A_s, A_{pr}, and A_{al} spermatogonial subpopulations markedly change their behavior during regeneration, thus enabling a quicker recovery of the stem cell pool.

Extending the "A_s model." Our results demonstrate a variety of different properties of the A_s, A_{pr}, and A_{al} subpopulations that constitute the stem cell compartment (Fig. 6). Differentiation does not follow a strictly linear process where gene expression is coupled to lineage (cyst length); rather, it includes multiple pathways along the two parameters. For example, NGN3$^+$ $A_{al\text{-}4}$ can be generated either by division of NGN3$^+$ A_{pr} or by gain of NGN3 expression in GFRα1$^+$ $A_{al\text{-}4}$.

This model proposes a number of important extensions to the A_s model (Fig. 1A). First, regardless of cyst length, the NGN3$^+$ subpopulations including A_s are destined for differentiation. Thus, not all A_s cells act equivalently as stem cells. Second, A_{pr} and A_{al} spermatogonia are not committed unidirectionally to differentiation but are capable of reverting to A_s or shorter cysts by clone fragmentation. In some cases this may also be accompanied by reversion in gene expression. Clone fragmentation has been previously proposed in mice (*11*, *26*) and primates (*27*, *28*) and demonstrated in *Drosophila* (*4*, *5*), and we have directly observed this event by live imaging in vivo. Third, of the two parameters, gene expression appears to be the better indicator of the fate of individual cells over the cyst length. For example, GFRα1$^+$ cells transform directly into KIT$^+$ spermatogonia only occasionally (fig. S4), and eventually all the KIT$^+$ spermatogonia are generated from the NGN3$^+$ population, regardless of their cyst length. On the basis of increasing transformation frequency into A_1 spermatogonia along the cyst length, it has been proposed that the differentiation potential increases gradually (Fig. 1A) (*29*). Our data suggest that this is a reflection of the increasing content of NGN3$^+$ cells.

Implications for the definition of a stem cell. It has been generally assumed that A_s cells represent the entire spermatogenic stem cell population and that they support both steady-state spermatogenesis and regeneration after tissue damage or transplantation (*9*, *12*, *30*). However, our findings challenge this assumption.

We have demonstrated that NGN3$^+$ cells can revert to being GFRα1$^+$ A_s cells and can even act as long-lasting stem cells. The frequency of these events increases when tissue is damaged and regeneration takes place. This suggests that these "differentiating" cells can act as "potential stem cells," defined as cells that do not normally self-renew during steady-state spermatogenesis but nonetheless retain latent self-renewing potential (*6*, *31*). Live imaging of clone fragmentation suggests that the potential stem cells include not only the NGN3$^+$ A_s cells, but also A_{pr} and A_{al} (either NGN3$^+$ or GFRα1$^+$) cells. Indeed, the NGN3$^+$ cell population, most of which are present in con-

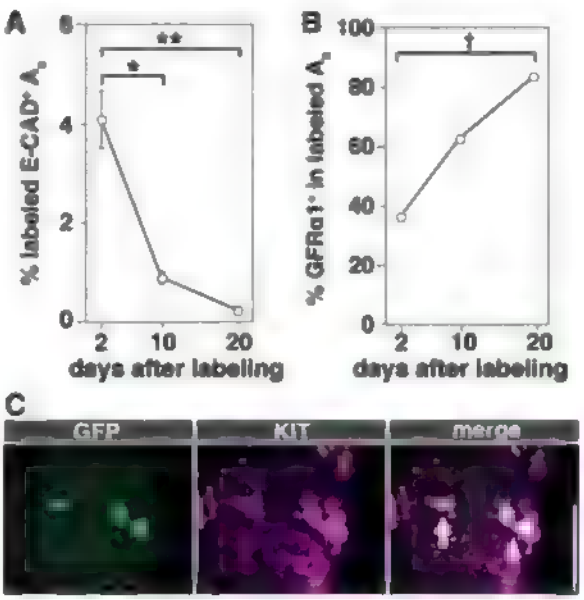

Fig. 3. Behavior of NGN3$^+$ A_s cells in steady-state spermatogenesis. **(A)** Percentage of labeled A_s in E-CAD$^+$ A_s in testes of Ngn3/CreER^{TM};CAG-CAT-EGFP mice 2, 10, and 20 days after pulse labeling. Averages ± SEM from 5, 3, and 5 testes for days 2, 10, and 20, respectively, are shown; *P = 0.006, **P < 0.001 (Student's t test). **(B)** Percentage of GFRα1$^+$ cells in labeled A_s spermatogonia. Total numbers of GFP-tagged A_s cells for days 2, 10, and 20 are 171, 8, and 6, respectively; †P < 0.02 (χ^2 test). **(C)** Whole-mount seminiferous tubules stained for GFP (green) and KIT (magenta) 2 days after pulse labeling, indicating rare examples of GFP-KIT double-positive single (arrow) and paired (arrowhead) cells, observed at a frequency of 1 out of ~10 to 20 GFP-tagged E-CAD$^+$ A_s cells. Scale bar, 100 μm.

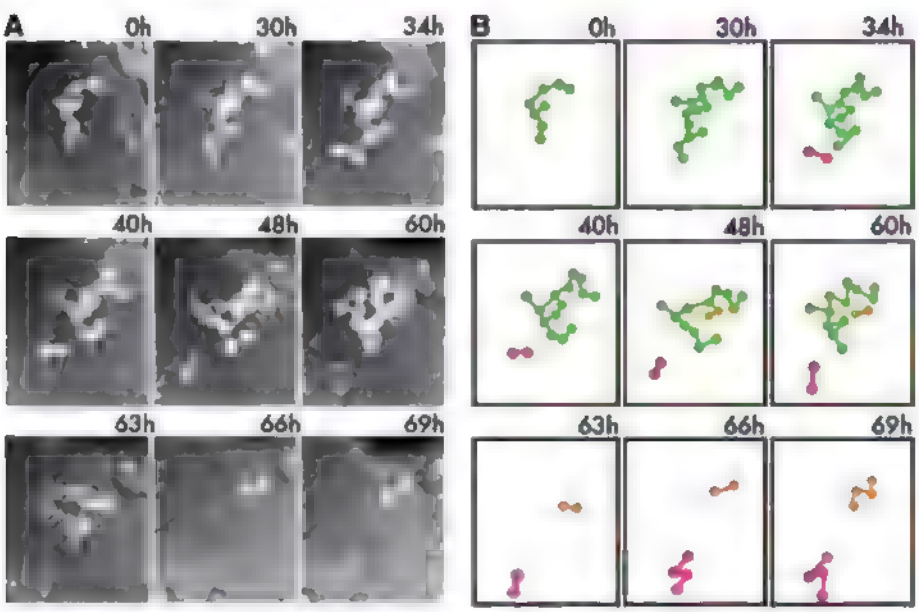

Fig. 4. Clone fragmentation of NGN3$^+$ A_{al} spermatogonia. **(A and B)** Selected frames from live imaging of an Ngn3-GFP transgenic mouse testis (movie S2) (A) and their schematic representation (B), indicating fragmentation of NGN3$^+$ A_{al} spermatogonia. After synchronous division of an $A_{al\text{-}8}$ cyst, two pairs of connected cells, indicated by magenta and orange arrowheads in (A) and dots in (B), survive; the remaining cells in the large chain subsequently died [small, light blue arrowheads in lower left panel of (A)]. Elapsed time is indicated.

nected cysts, exhibits colony formation and contribution to regeneration (*6*).

On the other hand, the population of GFRα1$^+$ A_s cells, which is positioned at the top of both hierarchies, is best related to the "actual stem cells" that support normal steady-state spermatogenesis (*6*, *31*). In the pulse-labeling experiment in undisturbed testes, however (Figs. 2 and 3), the absolute number of GFP-tagged GFRα1$^+$ A_s cells (which were originally NGN3$^+$ at the time of labeling) decreased by day 20. This was still larger than the number of persistent patches observed 3 months after the pulse, which represent the long-lasting stem cells (fig. S6). Similarly, during regeneration after damage, the number of persistent patches, which was significantly larger than that found in steady-state spermatogenesis, was smaller than the count of GFP-tagged GFRα1$^+$ A_s cells (fig. S6). Thus, only a part of the GFRα1$^+$ A_s population persists for a long period to serve as functional stem cells, and a majority of this population do not self-renew continually and may act as "potential stem cells" as well. The recent report of colony-forming activity in a small fraction of KIT$^+$ spermatogonia (*8*) may also represent "potential stem cells," which could reside in the minor populations of GFRα1$^+$ KIT$^-$ spermatogonia (fig. S4) or in the populations of single and paired KIT$^+$ spermatogonia that have been converted directly from NGN3$^+$ A_s and A_{pr} (Fig. 3C).

The concept of a single homogeneous cell population serving both steady-state spermatogenesis and regeneration is unnecessarily constraining. Rather, cells seem to possess a variable level of potential to act as stem cells. How their potential is manifested can be greatly influenced by the state of the tissue. Steady-state spermatogenesis favors the GFRα1$^+$ A_s population, which may have the greatest potential, whereas regeneration after transplantation or damage relies on the NGN3$^+$ and cyst (A_{pr} and A_{al}) spermatogonia as well, whose potential seems to be lower.

Regulation of the stem cell compartment. The molecular mechanisms governing the transition between the GFRα1$^+$ and NGN3$^+$ populations have yet to be defined. In this regard, the finding that GDNF (glial cell line–derived neurotrophic factor), the ligand for GFRα1, regulates the spermatogonial expression of GFRα1 and NGN3 in a reciprocal manner (i.e., positively and negatively, respectively) (*32*) suggests that GDNF may be an important determinant of stem cell behavior. Indeed, Sertoli cells, an essential player for the maintenance of the spermatogenic stem cell population, express GDNF, which is essential for the long-term maintenance of spermatogenic stem cell activity in vivo (*19*) and crucial for spermatogonial cultures to maintain the ability to form colonies after transplantation (*33*, *34*).

Comparison with other stem cell systems. In *Drosophila*, male and female germ cells appear to differentiate along a linear pathway with respect to lineage and gene expression. Their differentiation state is geographically

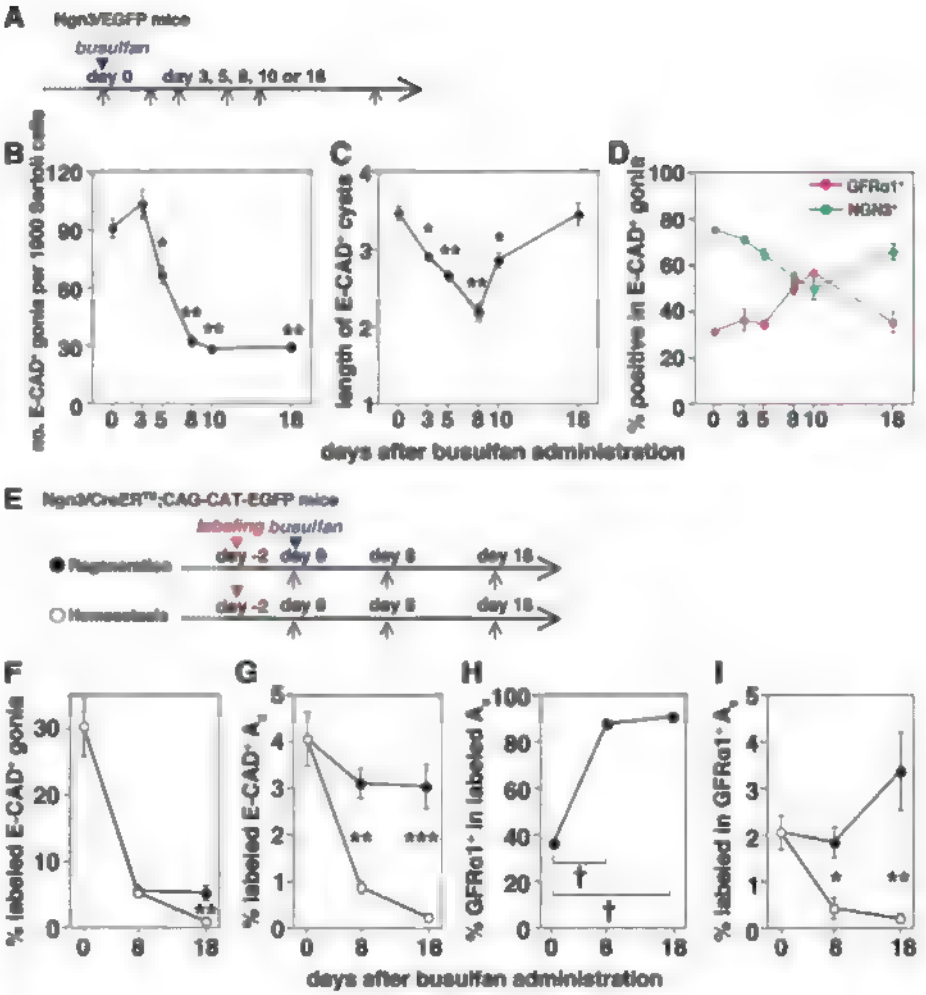

Fig. 5. Behavior of spermatogonial subpopulations during regeneration. (**A** to **D**) Analysis of the A_s, A_{pr}, and A_{al} subpopulations after administration of a submarginal dose of busulfan into Ngn3-EGFP adult mice. According to the schedule in (A), testes were processed for cell counting by whole-mount immunofluorescence. Shown in (B), (C), and (D) are numbers of total (E-CAD$^+$) A_s, A_{pr}, and A_{al} spermatogonia per 1000 Sertoli cells, the average length of E-CAD$^+$ cysts, and the percentage of GFRα1$^+$ (magenta) and NGN3$^+$ (green) A_s, A_{pr}, and A_{al} spermatogonia within the total E-CAD$^+$ population, respectively. Values are shown as average + SEM [$n = 6$, 6, and 3, for all the data points in (B), (C), and (D), respectively]; $^*P < 0.006$, $^{**}P < 0.001$, respectively, against the values of day 0 (Student's t test). (**E** to **I**) Pulse-label analyses of NGN3$^+$ spermatogonia during regeneration (solid circles) and steady-state spermatogenesis (open circles). Two days after the pulse, Ngn3/CreER^{TM};CAG-CAT-EGFP doubly transgenic mice were injected with busulfan to induce regeneration. In the control steady-state group, busulfan treatment was omitted. (F) and (G) Percentage of labeled cells in the E-CAD$^+$ total population (A_s, A_{pr}, and A_{al}) and the E-CAD$^+$ A_s population, respectively, following the schedule in (E). (H) Percentage of GFRα1$^+$ A_s cells in the total GFP-labeled A_s population. Total numbers of GFP-tagged A_s cells for 0, 8, and 18 days were 171, 24, and 108, respectively; $\dagger P < 0.006$ (χ^2 test). (I) Percentage of GFP-labeled cells within the GFRα1$^+$ A_s population. Averages ± SEM from 5, 3, and 5 testes for days 0, 8, and 18, respectively, are shown in (F), (G), and (I); $^*P < 0.03$, $^{**}P < 0.006$, $^{***}P < 0.001$ (Student's t test). Data for steady-state spermatogenesis in (F) and (G) are reproduced from Figs. 2 and 3, respectively.

recapitulated in the polarized gonad as a consequence of localized specialized supporting cells and extracellular factors that control self-renewal and differentiation (*3*). In contrast, in mouse testis, the stem cell compartment (Fig. 6) does not appear to be spatially constrained. Rather, while showing biased localization to the blood vessels and interstitium (*24*), the A_s, A_{pr}, and A_{al} spermatogonia are intermingled among more differentiating germ cells and seemingly uniform supporting Sertoli cells. Given these anatomical differences, it is not surprising that flies and mice exhibit distinct controlling mechanisms.

Within mammals, the primate stem cell compartment appears to differ from that in mice. In primates, primitive spermatogonia, referred to as A_{dark} and A_{pale} according to nuclear morphology, are generally assumed to represent the stem cell pool (*11*, *28*). The A_{dark} cells are the presumptive reserve stem cells that rarely proliferate; the A_{pale} cells represent the active stem cell pool and are continuously cycling. Whereas NGN3$^+$ spermato-

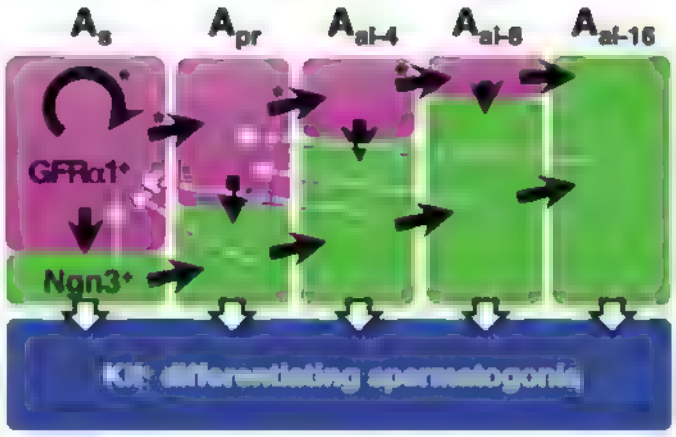

Fig. 6. Proposed spermatogonial subpopulations and their behavior with respect to their morphology (cyst length) and gene expression (GFRα1$^+$ and NGN3$^+$). Black arrows indicate the proposed flow of the majority of cells in each morphological group. Dashed lines show the observed modes of "reversion." Arrows without asterisks were actually observed; those with asterisks were not observed but are proposed to occur with high probability.

gonia proliferate actively, the cell cycle status of GFRα1$^+$ population is yet to be elucidated. It is an intriguing question whether there exists a reserve population of GFRα1$^+$ cells in mice, equivalent to the A_{dark} cells in primates, or whether a reserve population of stem cells is unique to primates.

The biological importance of the syncytial nature of spermatogonial proliferation across animal species remains a mystery. Nonetheless, it provides a powerful tool to monitor gene expression in the context of cell lineage. In other stem cell systems, especially in mammals, stem and progenitor cell compartments are often classified on the basis of gene expression and location; correlation of lineage and gene expression has generally not been feasible. Our study demonstrates that lineage is not strictly and linearly correlated with gene expression and that there may be multiple and reversible paths from stem cells to differentiation in other systems.

References and Notes

1. S. J. Morrison, A. C. Spradling, *Cell* **132**, 598 (2008)
2. G. Seydoux, R. E. Braun, *Cell* **127**, 891 (2006)
3. M. T. Fuller, A. C. Spradling, *Science* **316**, 402 (2007)
4. C. Brawley, E. Matunis, *Science* **304**, 1331 (2004)
5. T. Kai, A. Spradling, *Nature* **428**, 564 (2004)
6. T. Nakagawa, Y. Nabeshima, S. Yoshida, *Dev. Cell* **12**, 195 (2007)
7. J. Cheng *et al.*, *Nature* **456**, 599 (2008)
8. V. Barroca *et al.*, *Nat. Cell Biol.* **11**, 190 (2008)
9. D. G. de Rooij, L. D. Russell, *J. Androl.* **21**, 776 (2000)
10. L. Russell, R. Ettlin, A. Sinha Hikim, E. Clegg, *Histological and Histopathological Evaluation of the Testis* (Cache River Press, Clearwater, FL, 1990)
11. M. L. Meistrich, M. E. van Beek, in *Cell and Molecular Biology of the Testis*, C. Desjardins, L. L. Ewing, Eds (Oxford Univ. Press, New York, 1993), pp. 266–295.
12. S. Yoshida, *Cold Spring Harb. Symp. Quant. Biol.* **73**, 25 (2008)
13. D. G. de Rooij, *Reproduction* **121**, 347 (2001)
14. C. Huckins, *Anat. Rec.* **169**, 533 (1971)
15. E. F. Oakberg, *Anat. Rec.* **169**, 515 (1971)
16. S. Yoshida *et al.*, *Dev. Biol.* **269**, 447 (2004)
17. F. W. Buaas *et al.*, *Nat. Genet.* **36**, 647 (2004)
18. J. A. Costoya *et al.*, *Nat. Genet.* **36**, 653 (2004)
19. X. Meng *et al.*, *Science* **287**, 1489 (2000)
20. M. C. Hofmann, L. Braydich-Stolle, M. Dym, *Dev. Biol.* **279**, 114 (2005)
21. M. Tokuda, Y. Kadokawa, H. Kurahashi, T. Marunouchi, *Biol. Reprod.* **76**, 130 (2007)
22. H. Suzuki, A. Sada, S. Yoshida, Y. Saga, *Dev. Biol.* **336**, 222 (2009)
23. K. Zheng, X. Wu, K. H. Kaestner, P. J. Wang, *BMC Dev. Biol.* **9**, 38 (2009)
24. S. Yoshida, M. Sukeno, Y. Nabeshima, *Science* **317**, 1722 (2007)
25. B. H. Schrans-Stassen, H. J. van de Kant, D. G. de Rooi, A. M. van Pelt, *Endocrinology* **140**, 5894 (1999)
26. B. H. Erickson, *Radiat. Res.* **86**, 34 (1981)
27. J. Ehmcke, C. M. Luetjens, S. Schlatt, *Biol. Reprod.* **72**, 293 (2005)
28. J. Ehmcke, S. Schlatt, *Reproduction* **132**, 673 (2006)
29. D. G. de Rooij, *Int. J. Exp. Pathol.* **79**, 67 (1998)
30. R. L. Brinster, *Science* **296**, 2174 (2002)
31. C. S. Potten, M. Loeffler, *Development* **110**, 1001 (1990)
32. J. M. Oatley, M. R. Avarbock, A. I. Telaranta, D. T. Fearon, R. L. Brinster, *Proc. Natl. Acad. Sci. U.S.A.* **103**, 9524 (2006)
33. M. Kanatsu-Shinohara *et al.*, *Biol. Reprod.* **69**, 612 (2003)
34. H. Kubota, M. R. Avarbock, R. L. Brinster, *Proc. Natl. Acad. Sci. U.S.A.* **101**, 16489 (2004)

35. We thank J. Miyazaki, T. Noce, and A. Imura for materials; T. Ogawa, R. Sugimoto, Y. Kitadate, K. Hara, and H. Mizuguchi-Takase for comments; T. Fujimori for discussion and technical advice; and M. Sukeno for technical assistance. Supported by a Grant-in-Aid for Scientific Research (KAKENHI) on Innovative Areas, "Regulatory Mechanism of Gamete Stem Cells" (S.Y.), NICHD/NIH Contraceptive Development Research Centers Program grant U54 HD4254 (R.E.B.), the Uehara Memorial Foundation, and the Naito Foundation.

Supporting Online Material

www.sciencemag.org/cgi/content/full/science.1182868/DC1
Materials and Methods
SOM Text
Figs. S1 to S7
Movies S1 to S4
References

5 October 2009; accepted 1 March 2010
Published online 18 March 2010;
10.1126/science.1182868
Include this information when citing this paper.

A Gating Charge Transfer Center in Voltage Sensors

Xiao Tao,[1] Alice Lee,[1] Walrati Limapichat,[2] Dennis A. Dougherty,[2] Roderick MacKinnon[1]*

Voltage sensors regulate the conformations of voltage-dependent ion channels and enzymes. Their nearly switchlike response as a function of membrane voltage comes from the movement of positively charged amino acids, arginine or lysine, across the membrane field. We used mutations with natural and unnatural amino acids, electrophysiological recordings, and x-ray crystallography to identify a charge transfer center in voltage sensors that facilitates this movement. This center consists of a rigid cyclic "cap" and two negatively charged amino acids to interact with a positive charge. Specific mutations induce a preference for lysine relative to arginine. By placing lysine at specific locations, the voltage sensor can be stabilized in different conformations, which enables a dissection of voltage sensor movements and their relation to ion channel opening.

Voltage sensors are membrane proteins that change their conformation in response to voltage differences across the cell membrane. They are best known as components of voltage-dependent ion channels, in which voltage sensor conformational changes regulate channel opening. Voltage-dependent K^+ (Kv) and Na^+ (Nav) channels produce nerve impulses, and voltage-dependent Ca^{2+} (Cav) channels initiate muscle contraction and many other cellular processes (*1*). Certain enzymes also have voltage sensors, which allow the membrane voltage to regulate catalytic activity (*2*, *3*).

Voltage sensors can exhibit a nearly switch-like dependence on membrane voltage, changing from "off" to "on" over a few hundredths of a volt. Such a steep dependence on voltage exists because a large quantity of electric charge (known as gating charge) is transferred across the membrane voltage difference when a sensor switches off to on (*4*). In the Shaker Kv channel, the total gating charge is 12 to 14 elementary charges per channel, or 3.0 to 3.5 elementary charges from each of four voltage sensors (*5*–*7*). The charges originate from amino acids carrying a positive charge—mostly arginine but occasionally lysine—located on the fourth membrane-spanning helix (S4) of the voltage sensor (*5*, *6*).

[1]Laboratory of Molecular Neurobiology and Biophysics, Rockefeller University, Howard Hughes Medical Institute, 1230 York Avenue, New York, NY 10065, USA. [2]Division of Chemistry and Chemical Engineering, California Institute of Technology, 1200 East California Boulevard, Pasadena, CA 91125, USA.

*To whom correspondence should be addressed. E-mail: mackinn@rockefeller.edu

Crystal structures of voltage sensors from Kv channels show that they consist of only four transmembrane helices surrounded by the lipid membrane (*8–11*). The seemingly simple structure of the voltage sensor presents an apparent paradox. How does the voltage sensor transfer a large quantity of charge across the low-dielectric and charge-destabilizing interior of the membrane when there are only four helices to "shield" the charges? Some explanations have posited that the sensor does not physically move its charges very far across the membrane, but rather that it somehow restructures the electric field relative to the charges (*12–17*). However, other studies suggest that charged amino acids on S4 move 15 to 20 Å across the membrane (*18–20*). Such large movements would seem to require a specific mechanism to stabilize the charges as they cross the membrane center.

Voltage sensors of Kv channels. Kv channels consist of a central ion conduction pore surrounded by four voltage sensors (Fig. 1A) (*8, 11*). Each voltage sensor contacts the pore through two functionally important interfaces, one located near the extracellular (top) surface of helix S1 and another near the intracellular surface at the S4-S5 linker (*21*). The segments of the voltage sensor colored red in Fig. 1A (S3b, S4, and the S4-S5 linker) are proposed to move relative to the more static segments colored gray (S1, S2, and S3a) (*18, 22*). The crystal structure of the closed conformation has not been determined, but in a proposed mechanism, a hinge between S3a and S3b would allow the voltage sensor paddle (S3b and S4) to undergo movement, which would exert force on the S4-S5 linker to close or open the pore as modeled in Fig. 1B (*10, 11, 21*). The voltage difference across the membrane drives the conformational change by acting on positively charged residues on S4 (Fig. 1, C and D).

In the crystal structure of the Kv1.2-Kv2.1 chimera (paddle chimera), the pore is open, and the voltage sensors adopt a membrane depolarized (positive inside relative to outside) conformation (Fig. 1, A to C) (*11*). We refer to this depolarized voltage sensor conformation as the open voltage sensor and the hyperpolarized conformation as the closed voltage sensor. In the open crystal structure, positively charged amino acids are labeled according to their position on S4 from outside to inside, 0 to 5 (Fig. 1, C and D). Position 1 is Gln in paddle chimera but Arg in Kv1 channels such as the Shaker channel. The outermost charged amino acids, labeled R0 to R4 (*23*), are located either near the phospholipid head group layer (R0 and R1) or in an aqueous cleft created because the paddle is tilted away from S1 and S2 (R2 to R4) (Fig. 1C). R0 to R4 are, therefore, in or near an extracellular surface-exposed environment. The next positively charged amino acid, K5, is different, because it is isolated from the external aqueous surface by a phenylalanine side chain, Phe^{233} (Fig. 1C, green side chain). The Phe is highly conserved among voltage sensors from many different proteins, including Kv, Nav, Cav, voltage-dependent H^+ (Hv) channels, and voltage-dependent phosphatase (VSP) enzymes (Fig. 1E) (*24, 25*). What role does this Phe play?

Effects of mutating Phe^{233}. To address this question, we introduced mutations in this Phe by substituting 19 other amino acids (*23, 26*) (Fig. 2, A and B). These experiments were carried out with the Shaker K^+ channel instead of the paddle chimera channel because the Shaker channel is highly expressed in *Xenopus* oocytes, and it is the most extensively studied Kv channel with respect to gating function (*27–31*). Even though the crystal structure of the Shaker K^+ channel has not been determined, the paddle

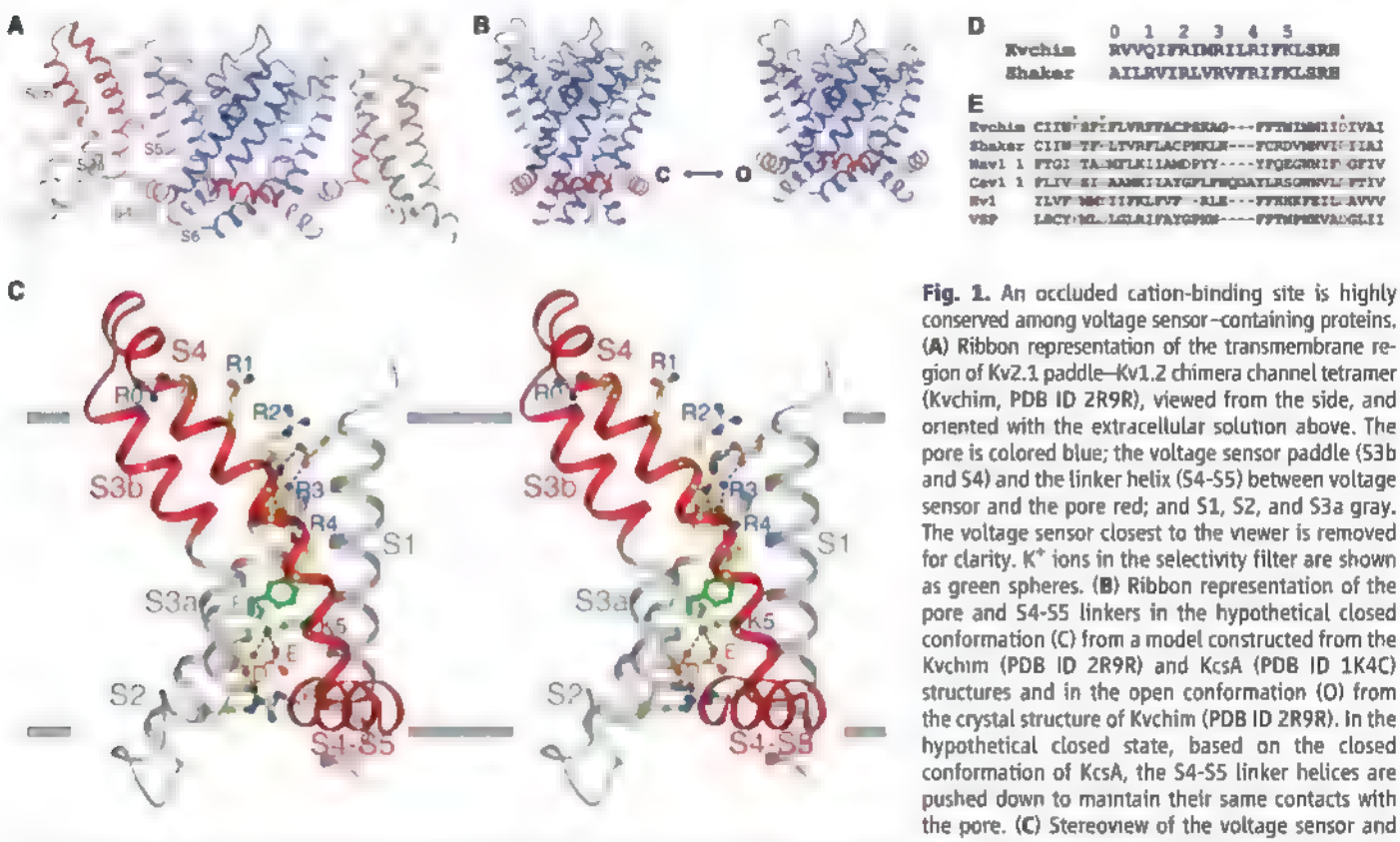

Fig. 1. An occluded cation-binding site is highly conserved among voltage sensor–containing proteins. (**A**) Ribbon representation of the transmembrane region of Kv2.1 paddle–Kv1.2 chimera channel tetramer (Kvchim, PDB ID 2R9R), viewed from the side, and oriented with the extracellular solution above. The pore is colored blue; the voltage sensor paddle (S3b and S4) and the linker helix (S4-S5) between voltage sensor and the pore red; and S1, S2, and S3a gray. The voltage sensor closest to the viewer is removed for clarity. K^+ ions in the selectivity filter are shown as green spheres. (**B**) Ribbon representation of the pore and S4-S5 linkers in the hypothetical closed conformation (C) from a model constructed from the Kvchim (PDB ID 2R9R) and KcsA (PDB ID 1K4C) structures and in the open conformation (O) from the crystal structure of Kvchim (PDB ID 2R9R). In the hypothetical closed state, based on the closed conformation of KcsA, the S4-S5 linker helices are pushed down to maintain their same contacts with the pore. (**C**) Stereoview of the voltage sensor and S4-S5 linker helix of the open conformation from Kvchim. Side chains of the positively charged residues on S4 (labeled as R0, R1, R2, R3, R4, and K5) and the negatively charged residues forming ionizing hydrogen bonds (dashed black lines) with the positive charges, as well as those of the three residues (labeled F, E, and D) forming an occluded binding site in the voltage sensor, are shown as sticks and colored according to atom types (yellow, carbon; blue, nitrogen; red, oxygen; and green, phenylalanine). (**D**) Sequence alignment of the S4 segment of Kvchim (GI: 160877792) and Shaker Kv (GI: 13432103). The positively charged residues are colored blue. Numbers [0 to 5, equivalent to those in (C)] above the sequences are used to indicate the positive charges on S4 throughout the text. (**E**) Sequence alignment of Kvchim (GI: 160877792), Shaker Kv (GI: 13432103), human Nav1.1 (GI: 115583677), human Cav1.1 (GI: 110349767), human Hv1 (GI: 91992155), and ciona VSP (GI: 76253898). Only the segment of S2 and S3a forming the occluded binding site is included. The three highly conserved residues forming the site are highlighted: F, green, and E and D, red. F corresponds to Phe^{233} in Kvchim.

chimera channel shares high sequence identity and, therefore, should serve as an accurate model for designing and analyzing experiments on the Shaker channel. The mutants fall into four groups, according to the level of expressed current and the midpoint voltage (V_m) of the activation curve (Fig. 2, A and B). Only two substitutions, Tyr and Trp, produced currents near wild-type levels with negative V_m (Fig. 2B).

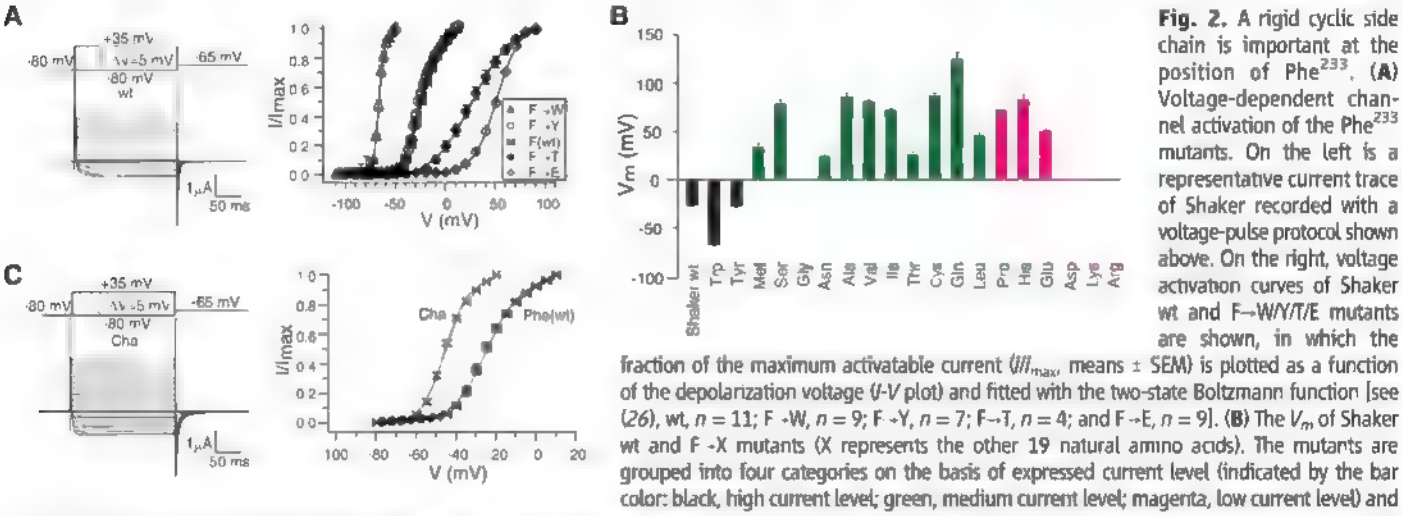

Fig. 2. A rigid cyclic side chain is important at the position of Phe^{233}. **(A)** Voltage-dependent channel activation of the Phe^{233} mutants. On the left is a representative current trace of Shaker recorded with a voltage-pulse protocol shown above. On the right, voltage activation curves of Shaker wt and F→W/Y/T/E mutants are shown, in which the fraction of the maximum activatable current (I/I_{max}, means ± SEM) is plotted as a function of the depolarization voltage (*I-V* plot) and fitted with the two-state Boltzmann function [see (*26*), wt, $n = 11$; F→W, $n = 9$; F→Y, $n = 7$; F→T, $n = 4$; and F→E, $n = 9$]. **(B)** The V_m of Shaker wt and F→X mutants (X represents the other 19 natural amino acids). The mutants are grouped into four categories on the basis of expressed current level (indicated by the bar color: black, high current level; green, medium current level; magenta, low current level) and the value of V_m (indicated by the bar height). Oocytes expressing the Lys or Arg mutants did not produce any AgitoxinZ-sensitive current. The expressed current level of the Asp mutant was too low to generate a usable *I-V* plot. V_m of the Gly mutant was not determined, as its *I-V* plot cannot be fitted with the two-state Boltzmann function. **(C)** Voltage-dependent channel activation of the Phe to cyclohexylalanine (Cha) mutant. (Left) A representative current trace of the Cha mutant recorded with a voltage-pulse protocol shown above. (Right) The voltage activation curves of Shaker wt and the Cha mutant. The curves are fitted with the two-state Boltzmann function [see (*26*), wt, $n = 11$; Cha, $n = 15$].

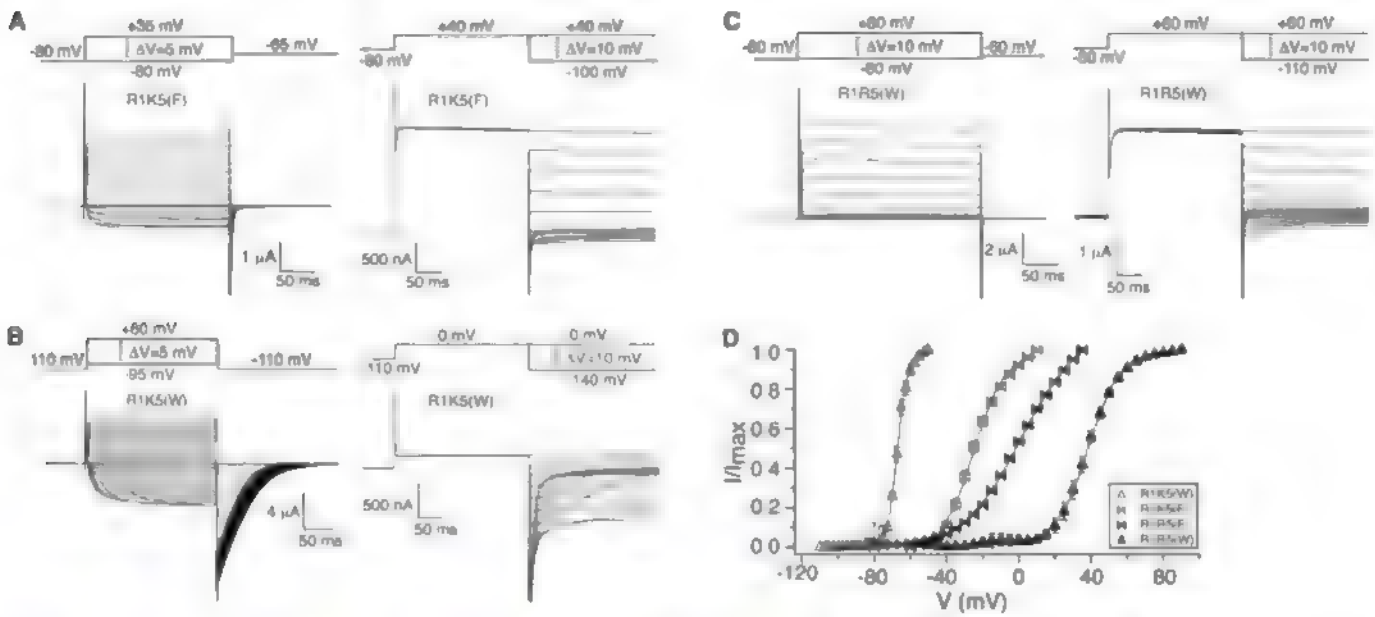

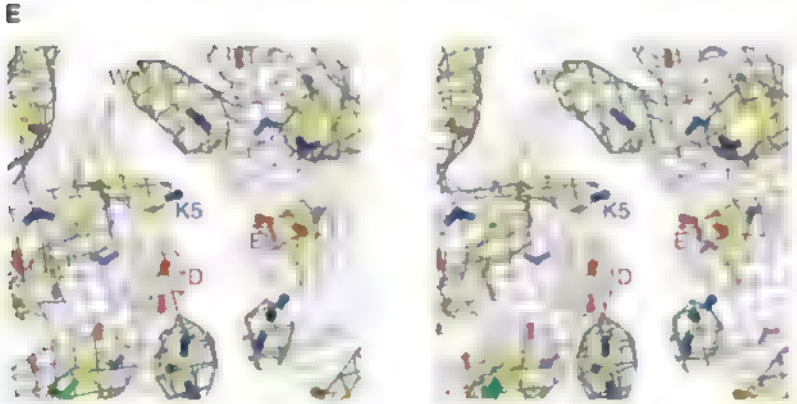

Fig. 3. Effects of the Phe to Trp mutation depend on the amino acid at position 5. **(A to C)** Representative current traces of voltage-dependent channel opening (left) and closing (right) of R1K5(F) (i.e., Shaker wt), R1K5(W), and R1R5(W). The corresponding pulse protocols are shown above the traces. **(D)** The voltage-activation curves of R1K5(F) (i.e., Shaker wt), R1K5(W), R1R5(F), and R1R5(W). Fraction of the maximal current (I/I_{max}, means ± SEM) is plotted as a function of the depolarization voltage and fitted with the two-state Boltzmann function [see (*26*), R1K5(F), $n = 11$; R1K5(W), $n = 9$; R1R5(F), $n = 12$, and R1R5(W), $n = 5$]. **(E)** Stereo representation of electron density (gray wire mesh, $2F_{obs} - F_{calc}$, calculated from 50 to 2.9 Å by using phases from the final model and contoured at 0.8 σ) for the occluded binding site in the crystal structure of the Kvchim F233W mutant [equivalent to R1K5(W)]. The protein is shown as sticks and colored according to atom types (yellow, carbon; blue, nitrogen; and red, oxygen).

The three amino acids with a permanent aromatic side chain (Phe, Tyr, and Trp) support the highest current levels and negative V_m. To test the importance of aromaticity and the possible existence of a cation-π interaction, we substituted Phe with cyclohexylalanine (Cha), which has a rigid cyclic side chain but is not aromatic. This mutant yielded functional channels with a negative V_m, much like channels with Phe, Tyr, and Trp (Fig. 2C). In addition, a variety of unnatural amino acid analogs of Phe, including 3,5-difluoro-Phe (F_2Phe), 4-methyl-Phe (MePhe), 4-cyano-Phe (CNPhe), and 4-bromo-Phe (BrPhe), consistently produced negative V_m values but did not show a systematic correlation with the negative electrostatic potential on the surface of the aromatic ring (fig. S1). These results suggest that a rigid cyclic side chain is important at this position, but aromaticity is not.

The channel containing Trp activates with the most negative V_m (Fig. 2, A and B). The channel kinetics underlying the more negative V_m in the Trp mutant can be seen with a voltage protocol in which the membrane is depolarized to open the channels and then hyperpolarized to close them; the rate of closure is extremely slow (Fig. 3, A and B). In general, the rate of closure is voltage dependent; it becomes faster as the membrane voltage is made more negative (right side of Fig. 3, A and B). In the wild-type channel [R1K5(F), corresponding to Arg at position 1 and Lys at position 5 on S4 (Fig. 1D), and Phe at the equivalent position of Phe^{233} on S2 (Fig. 1E)], closure is so rapid that a voltage of −65 mV is sufficient to close channels in a brief period of time (Fig. 3A). But when Phe^{233} is replaced by Trp [R1K5(W)] even at −110 mV (a voltage at which closure is expected to be much faster than at −65 mV), the channels take much longer to close (Fig. 3B). The negative V_m and slow closure suggest that the Phe to Trp mutation energetically favors the open channel relative to the closed channel.

Effects of the Phe to Trp mutation depend on the K5 amino acid. The effects of mutating Phe to Trp depend on the nature of the amino acid at position 5 (Fig. 3, A to C). This dependence can be seen through a comparison of double mutants: The R1K5(W) channel has a more negative V_m and a slower rate of closure compared with the R1K5(F) channel (Fig. 3, A, B, and D), but the R1R5(W) channel has a more positive V_m and a faster rate of closure than the R1R5(F) channel (Fig. 3, C and D, and fig. S2A). Thus, the Trp residue slows closure in the background of Lys and speeds it in the background of Arg.

The crystal structure of the open channel shows that the side chain of K5 is isolated from the external and internal solutions in an occluded binding site formed by Phe above and Glu and Asp below. Glu and Asp form ionized hydrogen bonds with the Lys amino group (Fig. 1C) (*11*). Because K5 is in direct contact with the Phe, it is understandable that the functional consequence of mutating Phe to Trp could depend on whether Lys or Arg is present at position 5. High conservation of all three amino acids, Phe, Glu, and Asp, among Kv, Nav, Cav, and Hv channels, as well as VSP enzymes, suggests that the occluded site is an important feature of voltage sensors in general (Fig. 1E). A crystal structure of the Phe to Trp mutant of the paddle chimera channel was determined to 2.9 Å (table S1) and shows that the open conformation of the voltage sensor is preserved and that the occluded site remains intact, with the K5 side chain present and Trp replacing Phe (Fig. 3E).

The observations described above lead us to the following hypothesis: The occluded site affects the conformation of the voltage sensor through the strength of its interaction with Lys relative to Arg at position 5. Mutation of either the binding site (Phe to Trp) or the Lys (Lys to Arg) influences gating. The more negative V_m and slower rate of closure observed with the mutation R1R5(W) to R1K5(W) would suggest that Lys binds more tightly relative to Arg in the presence of Trp in the occluded site, which causes the voltage sensor to be stabilized in its open conformation (Fig. 3, B to D).

Lys substitutions stabilize specific conformations of the voltage sensor. If Lys is favored relative to Arg in the occluded site when Phe is mutated to Trp and if the voltage sensor transfers its positively charged residues through this site when it undergoes a conformational change, then it should be possible to stabilize the voltage sensor in specific conformations by substituting Lys at different positions while Trp is present in the binding site. In the presence of Phe with Lys at position 1 [K1R5(F)], the channels open and close rapidly, but in the presence of Trp with Lys at position 1 [K1R5(W)], the channels open slowly and close rapidly (Fig. 4, A and B). That

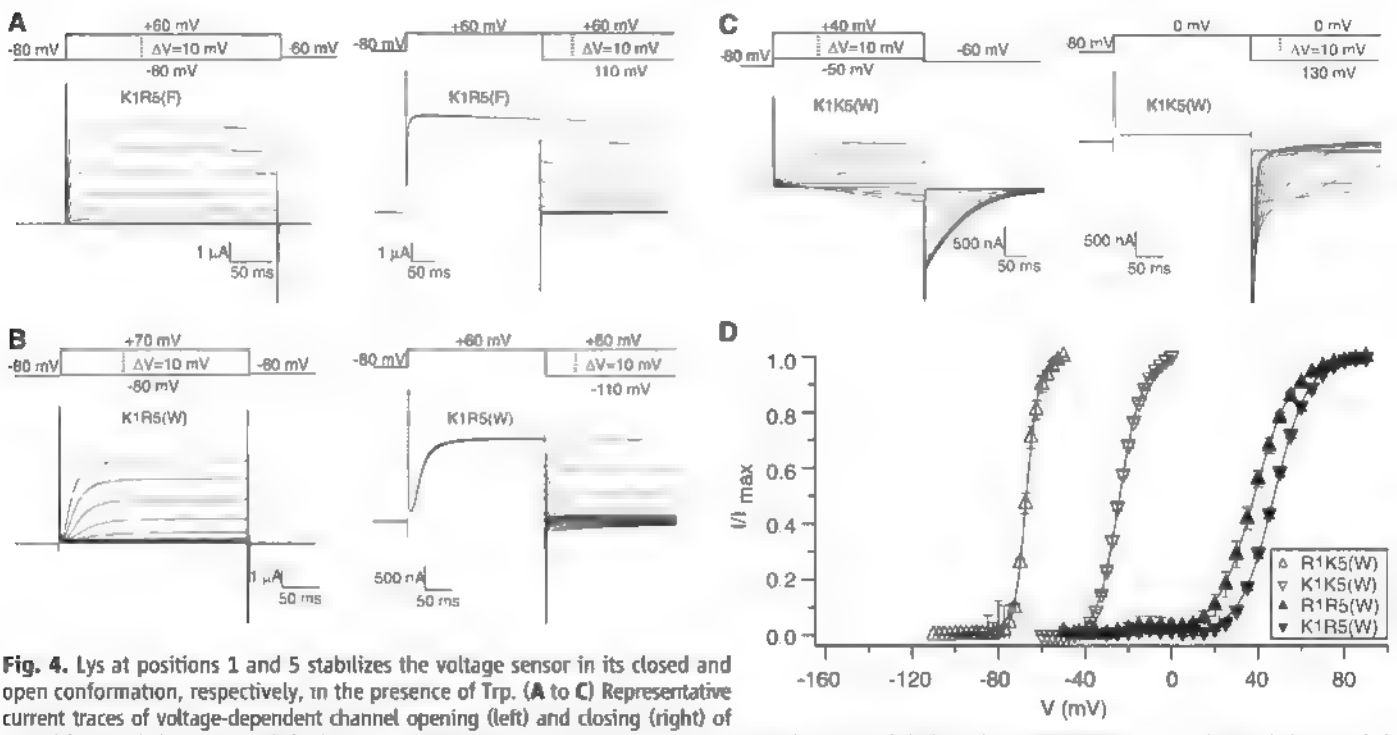

Fig. 4. Lys at positions 1 and 5 stabilizes the voltage sensor in its closed and open conformation, respectively, in the presence of Trp. (**A** to **C**) Representative current traces of voltage-dependent channel opening (left) and closing (right) of K1R5(F), K1R5(W), and K1K5(W). The corresponding pulse protocols are shown above the traces. (**D**) The voltage activation curves of R1K5(W), K1K5(W), R1R5(W), and K1R5(W). Fraction of the maximal current (I/I_{max}, means + SEM) is plotted as a function of the depolarization voltage and fitted with the two-state Boltzmann function [see (*26*), R1K5(W), n = 9; K1K5(W), n = 11; R1R5(W), n = 5; and K1R5(W), n = 7].

is, the Phe to Trp mutation slows opening (but not closing) when Lys is present at position 1, and it slows closing (but not opening) when Lys is present at position 5. When Lys is present at positions 1 and 5 simultaneously, both channel opening and closing are slowed (Fig. 4C and fig. S2B). The activation curve midpoint voltage, V_m, is most negative for R1K5(W), most positive for K1R5(W), and intermediate for K1K5(W) (Fig. 4D). These results are consistent with the hypothesis that Lys at position 5 favors the open conformation and Lys at position 1 favors the closed conformation.

Voltage sensor conformations assessed through gating currents. Ionic currents associated with pore opening and closing, as described above, provide an indirect measure of voltage sensor conformational change. Gating currents, however, provide a direct measure, because they result directly from the displacement of the charged amino acids in the voltage sensor when it changes its conformation (*4*). Gating currents are measurable as a component of the transient current that follows a membrane voltage step (fig. S3) (*6*). Agitoxin2 was used to prevent ionic (K^+) currents, because this toxin blocks the pore but does not interfere with voltage sensor movements (fig. S3B) (*6*, *32*). Integration of the remaining transient current gives the total charge associated with each voltage step, which can be graphed as a function of membrane voltage in a *Q-V* plot (fig. S3, C and D). *Xenopus* oocytes not expressing Kv channels show a linear *Q-V* plot (fig. S3C), which reflects the charge required to bring the membrane to its new voltage (the linear capacitive charge). Oocytes expressing Kv channels show the same linear component as well as a nonlinear component. The nonlinear component—the gating charge—corresponds to the displacement of charged amino acids as the voltage sensor undergoes its conformational change (fig. S3D).

Transient currents during a single voltage step are shown in Fig. 5, A to D, for the four mutants analyzed in Fig. 4D. In the R1R5(W) channel, the transient currents associated with opening (voltage stepped from hyperpolarized to depolarized value) and closing (voltage stepped back to hyperpolarized value) are brief, and consequently, the gating current is buried within the linear capacitive current (Fig. 5A). In contrast, the transient current associated with closing the R1K5(W) channel has a prolonged component that extends beyond the duration of the linear capacitive current (Fig. 5B). This is direct evidence that the voltage sensor is being delayed in its transition from its open to closed conformation. The K1R5(W) channel has a prolonged component associated with channel opening (Fig. 5C), and the K1K5(W) channel has a prolonged component associated with both opening and closing (Fig. 5D). Therefore, the voltage sensor is delayed in its closed-to-open transition when Lys is present at position 1 and delayed in its open-to-closed transition when Lys is present at position 5. The time course of the transient current during opening and closing in Fig. 5D is consistent with a conformational change of the voltage sensor that involves multiple sequential steps after an initial delay (Fig. 6, A and B).

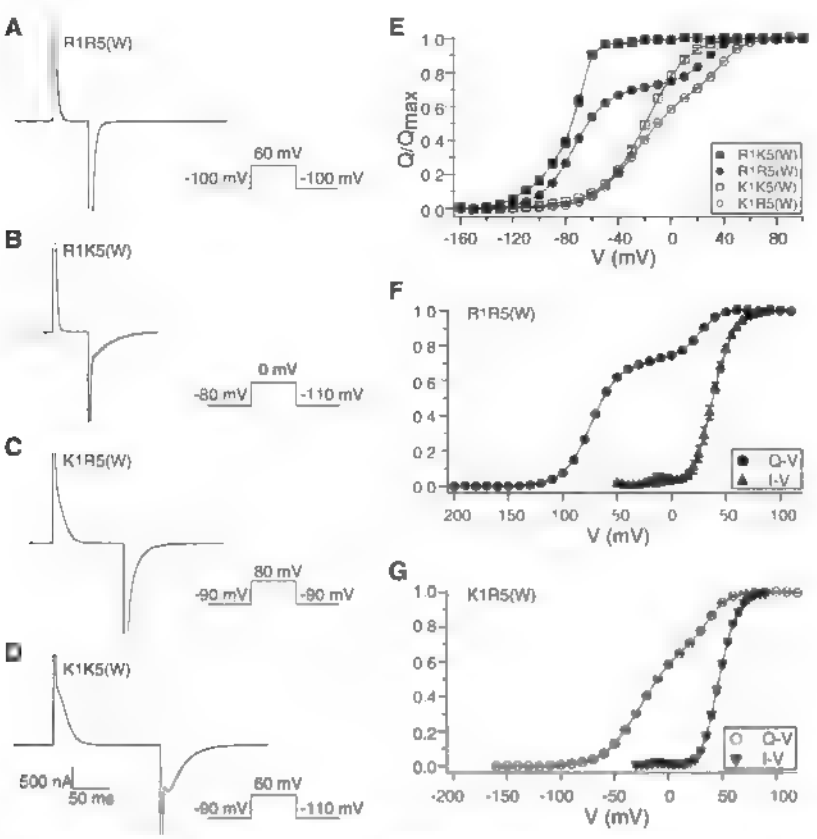

Fig. 5. Voltage-sensor movements assessed by gating currents (**A** to **D**) Representative transient current traces after voltage steps are shown for R1R5(W), R1K5(W), K1R5(W), and K1K5(W). Corresponding pulse protocols are shown next to the traces. Ionic currents are blocked using at least 50 μM Agitoxin2, and baselines were corrected by subtracting the Agitoxin2-insensitive current (*26*). (**E**) *Q-V* plots of the four mutants in (A to D). Total gating charges, calculated by integrating the repolarization-induced transient currents over time and subtracting the linear capacitive component, were plotted as a function of the step voltage [see (*26*), R1R5(W), $n = 11$; R1K5(W), $n = 13$; K1R5(W), $n = 24$; and K1K5(W), $n = 22$]. (**F**) *Q-V* (Q/Q_{max}) and *I-V* (I/I_{max}) plots of the R1R5(W) channel. Note that I/I_{max} in the *I-V* plot does not represent the true open probability of the channel, and the same applies to (G). (**G**) *Q-V* and *I-V* plots of the K1R5(W) channel.

The *Q-V* plots with the linear capacitive component subtracted are shown in Fig. 5E for the same mutant channels. The quantity Q/Q_{max} is the fraction of total gating charge following a voltage step. When Q/Q_{max} is small, corresponding to small displacements of the voltage sensor from its closed conformation, the four plots fall into two groups: one that shows charge movement at very negative voltages (around −100 mV) and another that begins to move charge at less negative voltages (around −50 mV) (Fig. 5E). The two groups correspond to voltage sensors with Arg (more negative, filled symbols) or Lys (less negative, empty symbols) at position 1. When Q/Q_{max} is large, corresponding to small displacements of the voltage sensor from its open conformation, again two groups are observed, but this time depending on the residue at position 5. Voltage sensors with Arg at position 5 (Fig. 5E, circles) exhibit a distinct second component of charge movement compared with voltage sensors with Lys at position 5 (Fig. 5E, squares).

The *Q-V* plots are consistent with the hypothesis that Lys relative to Arg interacts more favorably with the occluded site (Fig. 5E). Near the voltage sensor's closed conformation the occluded site presumably binds to positively charged S4 amino acids near position 1. If Lys is present at position 1 and binds more favorably than Arg, then a more depolarized membrane voltage (i.e., less negative) should be required to drive the voltage sensor away from its closed and to its open conformation. Near the voltage sensor's open conformation, the occluded site presumably binds to positively charged S4 amino acids near position 5. Therefore, Lys at position 5 should stabilize the open conformation, whereas Arg should destabilize it. As a consequence, in the presence of Arg at position 5, a more positive membrane voltage should be required to force the voltage sensor through its final transition to its

open conformation. This final transition appears to correlate with a distinct second component of charge movement. The second component, visible in both the R1R5(W) and K1R5(W) channels, accounts for ~25% of the total gating charge movement. In both channels, the pore opens, and ions begin to conduct only in association with this second component (Fig. 5, F and G).

Discussion. In summary, the data support the following conclusions: (i) Phe^{233} forms the extracellular lid on an occluded binding site in voltage sensors into which S4 positive charges bind. (ii) Mutating Phe to Trp alters the relative strength of interaction between Arg or Lys and this site. (iii) Lys appears to interact more favorably compared to Arg in the presence of Trp: At position 5, Lys stabilizes the open voltage sensor conformation; at position 1, Lys stabilizes the closed voltage sensor conformation. (iv) Given that Lys at position 1 and at position 5 appears to interact with the site in the closed and open conformations, respectively, we propose that the occluded site serves as a catalytic center to lower the energy associated with the transfer of each of the voltage sensor charges as they cross the membrane. (v) Arg at position 5 isolates the last 25% of gating charge as a separate component in the *Q-V* plot, which occurs concomitantly with pore opening. The association of this last component of gating charge with pore opening suggests that binding of the charged residue at position 5 into the occluded site is required for pore opening.

A simple-state model of voltage sensor transitions is shown (Fig. 6A). Each of the five states, connected by four transitions, corresponds to conformations of a single voltage sensor associated with the positively charged residue at positions 1 through 5 inside the occluded site. Thus, state 1 represents the fully closed voltage sensor, in which the positive charge of the position 1 amino acid binds to the occluded site, and state 5 represents the open voltage sensor, in which the positive charge of the position 5 amino acid binds to the occluded site. The data do not uniquely define each transition in this model, so the following simplifying assumptions are made. A single value for the forward rate constants and a single value for the backward rate constants are used except for the rate constants describing the fourth transition connecting states 4 and 5. Voltage dependence is distributed over the four transitions equally, with 25% of the total gating charge in each. It is further assumed that the open pore corresponds to the condition in which all four voltage sensors are open (i.e., all four have reached state 5) and that four voltage sensors undergo independent conformational changes.

For illustrative purposes, the graphs below the state model depict chemical free energy as a function of voltage sensor reaction coordinate in a channel in which Phe has been mutated to Trp (Fig. 6A). The presence of Lys in the occluded site is represented as a deeper energy well relative to Arg. One physical interpretation is that Lys binds more tightly to the occluded site. Another interpretation is that the energy barriers and wells are higher for Arg relative to Lys. Equations for the scheme in Fig. 6A (*26*) generate the main features observed in the electrophysiology data (Fig. 6, B to D). Notably, by changing only the well depth of state 5 by ~4.6 RT (R is the gas constant, T is the absolute temperature) relative to all other barriers and wells, the qualitative features of both the gating current time course and the *Q-V* plots of R1K5(W) and R1R5(W) are recapitulated (Fig. 6, B to D). In particular, relative stabilization of state 5 with Lys in the presence of Trp [R1K5(W)] prolongs the gating current associated with channel closing and gives it the correct time-dependent shape (Fig. 6, B and C), whereas destabilization of state 5 with Arg in the presence of Trp [R1R5(W)] speeds the gating current and separates the *Q-V* plot into two components (Fig. 6, B and D).

The model captures an important feature of gating, most explicitly displayed in channels with Arg at position 5 [R1R5(W) and K1R5(W)]: multiple transitions occur within each voltage sensor (connecting states 1 through 4 in the model) before a final transition (state 4 to 5), which is closely associated with pore opening (Fig. 5, F and G, and Fig. 6D). Thus, according to the model, the closed channel is actually associated with a distribution of conformations (states 1 through 4 within each voltage sensor), which is a function of the degree to which the membrane is hyperpolarized. The more negative the voltage, the closer the distribution comes to state 1. The open channel, however, is associated with a specific conformation (state 5) that must be achieved by all four voltage sensors. In order to approximate the behavior of the electrophysiology data, we found it necessary to use unique forward and backward rate constants for the fourth (final) voltage sensor transition (*26*). We speculate that this final transition is very different because it is associated with opening the pore.

In the context of the crystal structure, the model can explain a discrepancy between the total gating charge per channel (~14 elementary charges) and the sum of reduced charges when each of the five positions is mutated to a neutral amino acid one at a time (~18 elementary charges) (*6*). Because of the presence of two carboxylate ligands, the occluded binding site probably requires a positive charge in it at all times—except during brief transitions between states driven by voltage. Therefore, mutations that remove a positive charge from a particular position should reduce measured gating charge for two reasons: because the number of charges transported by the voltage sensor is reduced, and because the distribution of states before and/or after the voltage step is altered (i.e., the starting

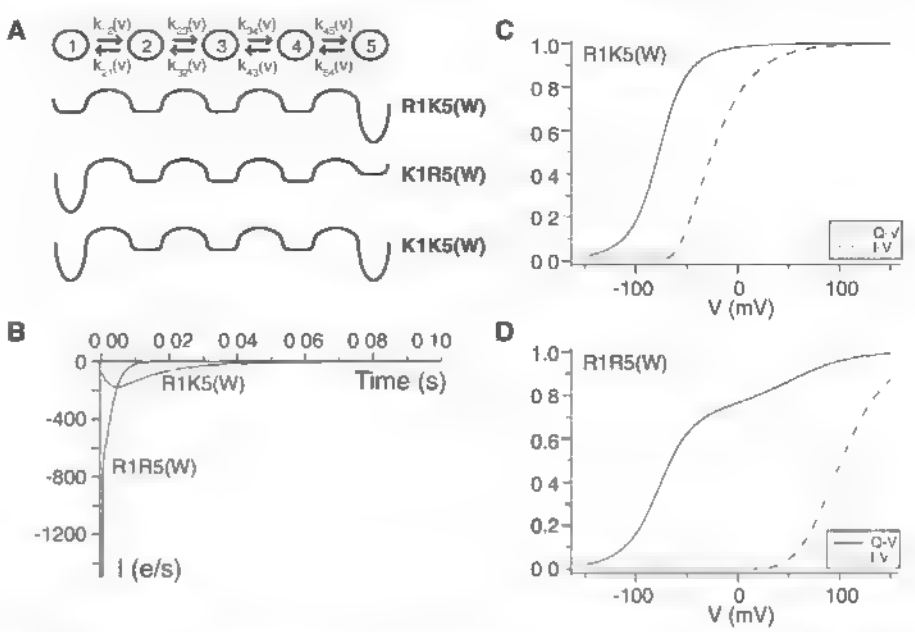

Fig. 6. State model of voltage-sensor conformational change captures qualitative gating behavior. (**A**) A simple model consists of five voltage-sensor states (state 1 though 5) within each voltage sensor connected by four transitions before the final pore opening step. For each state, a different positively charged S4 residue (indicated by the number) is located in the occluded binding site (indicated by the surrounding circle). When all four voltage sensors are in state 5, the pore opens, and ions conduct. The model assumes equal distribution of voltage dependence over the four transitions, and a single forward and a single backward rate constant for the first three transitions. Below the model is a depiction of the energy as a function of the voltage-sensor reaction coordinate in R1K5(W), K1R5(W), and K1K5(W) channels, which illustrates the qualitative effect of Lys on energy well depth when bound in the occluded binding site with Trp. (**B**) The gating current time courses generated from the above model are shown for R1K5(W) and R1R5(W) channels in association with a 100 mV to −120 mV voltage step. (**C** and **D**) The *Q-V* and *I-V* plots of R1K5(W) and R1R5(W) channels generated from the model.

and/or ending positions of all the charges is altered). The two reasons combined can account for the apparent discrepancy between total gating charge and the sum of reduced gating charge by mutation.

We do not know the physical basis of Lys versus Arg discrimination by the occluded site in the Phe to Trp mutant. The case in which Lys binds more favorably to the occluded site is indistinguishable from that in which Arg binds less favorably, because the Boltzmann distribution of states depends only on the relative energy differences among the available states. We favor the idea that Trp causes Arg to bind in the site with lower affinity and also, perhaps, raises the barrier for an Arg to enter the site because Trp is larger than Phe and would be expected to constrict the site, which destabilizes the larger Arg guanidinium group relative to the smaller Lys amino group. A correlation between the size of substituted groups on the Phe side chain (Br > CN > Me > H) and the value of V_m is consistent with this idea (fig. S1).

The data imply a specific distance over which S4 charged amino acids move across the membrane with gating. In the crystal structures of the open conformation, Lys at position 5 is located in the occluded binding site (Figs. 1C and 3E) (*11*). The electrophysiological data suggest that Lys at position 1 binds in the occluded site in the fully closed (strongly hyperpolarized) conformation (Fig. 4). The α-carbon distance between positions 1 and 5 is 21 Å along the S4 helix and 18 Å perpendicular to the membrane (fig. S4). This distance falls within the range 15 to 20 Å inferred independently by biotin-avidin accessibility studies on a prokaryotic Kv channel (*18*, *19*).

This study identifies an occluded site, conserved in voltage sensors, that catalyzes the transfer of positive charges across the membrane field in the process of voltage sensing. By manipulating the structure of the site, we have altered its selectivity between Arg and Lys. This selectivity is used to stabilize the voltage sensor in specific conformations and to dissect the relation between the voltage sensor and pore conformational changes.

References and Notes

1. B. Hille, *Ion Channels of Excitable Membranes* (Sinauer, Sunderland, MA, 2001)
2. Y. Okamura, Y. Murata, H. Iwasaki, M. Sasaki, *Tonpakushitsu Kakusan Koso* **51**, 18 (2006)
3. Y. Murata, H. Iwasaki, M. Sasaki, K. Inaba, Y. Okamura, *Nature* **435**, 1239 (2005)
4. C. M. Armstrong, F. Bezanilla, *J. Gen. Physiol.* **63**, 533 (1974)
5. S. A. Seoh, D. Sigg, D. M. Papazian, F. Bezanilla, *Neuron* **16**, 1159 (1996)
6. S. K. Aggarwal, R. MacKinnon, *Neuron* **16**, 1169 (1996)
7. N. E. Schoppa, K. McCormack, M. A. Tanouye, F. J. Sigworth, *Science* **255**, 1712 (1992)
8. Y. Jiang *et al.*, *Nature* **423**, 33 (2003)
9. S. B. Long, E. B. Campbell, R. MacKinnon, *Science* **309**, 897 (2005)
10. S. B. Long, E. B. Campbell, R. MacKinnon, *Science* **309**, 903 (2005)
11. S. B. Long, X. Tao, E. B. Campbell, R. MacKinnon, *Nature* **450**, 376 (2007)
12. C. A. Ahern, R. Horn, *Neuron* **48**, 25 (2005)
13. A. Cha, G. E. Snyder, P. R. Selvin, F. Bezanilla, *Nature* **402**, 809 (1999)
14. B. Chanda, O. K. Asamoah, R. Blunck, B. Roux, E. Bezanilla, *Nature* **436**, 852 (2005)
15. K. S. Glauner, L. M. Mannuzzu, C. S. Gandhi, E. Y. Isacoff, *Nature* **402**, 813 (1999)
16. D. J. Posson, P. Ge, C. Miller, F. Bezanilla, P. R. Selvin, *Nature* **436**, 848 (2005)
17. D. M. Starace, F. Bezanilla, *Nature* **427**, 548 (2004).
18. V. Ruta, J. Chen, R. MacKinnon, *Cell* **123**, 463 (2005)
19. Y. Jiang, V. Ruta, J. Chen, A. Lee, R. MacKinnon, *Nature* **423**, 42 (2003)
20. H. P. Larsson, O. S. Baker, D. S. Dhillon, E. Y. Isacoff, *Neuron* **16**, 387 (1996)
21. S. Y. Lee, A. Banerjee, R. MacKinnon, *PLoS Biol.* **7**, e47 (2009)
22. A. Banerjee, R. MacKinnon, *J. Mol. Biol.* **381**, 569 (2008)
23. Single-letter abbreviations for the amino acid residues are as follows: A, Ala; C, Cys; D, Asp; E, Glu; F, Phe; G, Gly; H, His; I, Ile; K, Lys; L, Leu; M, Met; N, Asn; P, Pro; Q, Gln; R, Arg; S, Ser; T, Thr; V, Val; W, Trp; and Y, Tyr
24. I. S. Ramsey, M. M. Moran, J. A. Chong, D. E. Clapham, *Nature* **440**, 1213 (2006)
25. M. Sasaki, M. Takagi, Y. Okamura, *Science* **312**, 589 (2006)
26. Materials and methods are available as supporting material on *Science* Online
27. N. E. Schoppa, F. J. Sigworth, *J. Gen. Physiol.* **111**, 313 (1998)
28. L. D. Islas, F. J. Sigworth, *J. Gen. Physiol.* **114**, 723 (1999)
29. W. N. Zagotta, T. Hoshi, R. W. Aldrich, *J. Gen. Physiol.* **103**, 321 (1994)
30. W. N. Zagotta, T. Hoshi, J. Dittman, R. W. Aldrich, *J. Gen. Physiol.* **103**, 279 (1994)
31. T. Hoshi, W. N. Zagotta, R. W. Aldrich, *J. Gen. Physiol.* **103**, 249 (1994)
32. M. L. Garcia, M. Garcia-Calvo, P. Hidalgo, A. Lee, R. MacKinnon, *Biochemistry* **33**, 6834 (1994).

33. We thank members of D. Gadsby's laboratory (Rockefeller University) for assistance with oocyte preparation, members of the MacKinnon laboratory for assistance; the staff at beamline X29 (National Synchrotron Light Source, Brookhaven National Laboratory) for advice at the synchrotron; and A. Banerjee, J. A. Letts, G. von Heijne (Stockholm University), and J. Chen (Purdue University) for helpful discussions. R.M. is the Investigator in the Howard Hughes Medical Institute. D.A.D. is a George Grant Hoag Professor of Chemistry. Supported by NIH GM43949 to R.M and N5 34407 to D.A.D. The x-ray crystallographic coordinates and structure factor files have been deposited in the Protein Data Bank with accession ID 3LNM.

Supporting Online Material

www.sciencemag.org/cgi/content/full/328/5974/67/DC1
Materials and Methods
Figs. S1 to S4
Table S1
References

14 December 2009; accepted 16 February 2010
10.1126/science.1185954

REPORTS

Evidence for Strong Extragalactic Magnetic Fields from Fermi Observations of TeV Blazars

Andrii Neronov* and Ievgen Vovk

Magnetic fields in galaxies are produced via the amplification of seed magnetic fields of unknown nature. The seed fields, which might exist in their initial form in the intergalactic medium, were never detected. We report a lower bound $B \geq 3 \times 10^{-16}$ gauss on the strength of intergalactic magnetic fields, which stems from the nonobservation of GeV gamma-ray emission from electromagnetic cascade initiated by tera–electron volt gamma rays in intergalactic medium. The bound improves as $\lambda_B^{-1/2}$ if magnetic field correlation length, λ_B, is much smaller than a megaparsec. This lower bound constrains models for the origin of cosmic magnetic fields.

The problem of the origin of 1- to 10-μG magnetic fields in galaxies and galaxy clusters is one of the long-standing problems of astrophysics and cosmology [see (*1*–*4*) for reviews]. It is assumed that the observed magnetic fields result from the amplification of much weaker seed fields. However, the nature of the initial weak seed fields is largely unknown. There are two broad classes of models for the seed fields: astrophysical models, which assume that the seed fields are generated by motions of the plasma in (proto)galaxies, and cosmological models, in which the seed fields are produced in the early universe (*1*–*4*).

Extremely weak unamplified extragalactic magnetic fields (EGMFs) have escaped detection up to now. Measurements of the Faraday rotation in the polarized radio emission from distant quasars (*1*, *5*, *6*) and/or distortions of the spectrum and polarization properties in the cosmic microwave background (CMB) radiation (*7*, *8*) imply upper limits on EGMF strengths at the level of ~10^{-9} G. Numerical modeling of magnetic field formation in galaxy clusters implies a theoretical upper bound of the order of

ISDC Data Centre for Astrophysics, Geneva Observatory, Ch. d'Ecogia 16, Versoix 1290, Switzerland

*To whom correspondence should be addressed. E-mail: Andrii.Neronov@unige.ch

$\sim 10^{-12}$ G on EGMF strength (*19*, *20*). Bounds on the EGMF strength depend on the field correlation length, λ_B, which is also unknown. A lower limit on λ_B is set by the requirement that the resistive magnetic diffusion time scale has to be larger than the age of the Universe (*2*), whereas an upper limit is set only by the size of the visible part of the Universe, R_H.

Here, we report a lower bound for the EGMF strength, derived from the data of Fermi and High Energy Stereoscopic System (HESS) gamma-ray telescopes. Similarly to the existing upper bounds, the lower bound depends on the unknown EGMF configuration parameters, such as the typical correlation length and spectrum.

Gamma rays with energies above ~1 TeV cannot propagate over cosmological distances because of absorption resulting from interactions with diffuse extragalactic background light (EBL) (*21*–*24*). The mean free path of gamma rays of energy $E_{\gamma 0}$ through EBL is $D_\gamma \simeq 80\kappa\,(E_{\gamma 0}/10\ \mathrm{TeV})^{-1}$ Mpc, where $\kappa \sim 1$ is a numerical factor that accounts for uncertainties of the measurements and modeling of the EBL (*25*). Interactions of multi-TeV gamma rays with the EBL lead to the deposition of electron-positron pairs in the intergalactic space. These e^+e^- pairs emit secondary cascade gamma rays via inverse Compton (IC) scattering of CMB photons. Typical energies for the IC photons emitted by electrons of energy $E_e \sim E_{\gamma 0}/2$ are $E_\gamma \sim (4/3)\epsilon_{CMB}(E_e/m_ec^2)^2 \sim 88(E_{\gamma 0}/10\ \mathrm{TeV})^2$ GeV, where $\epsilon_{CMB} = 6 \times 10^{-4}$ eV is the typical energy of CMB photons and E_e and m_e are the energy and mass, respectively, of an electron. Pairs lose energy on IC scattering on the distance scale $D_e \sim 10^{23}(E_e/10\ \mathrm{TeV})^{-1}$ cm, which is much smaller than the gamma ray mean free path D_γ. Power removed from the primary gamma-ray beam is transferred to the cascade gamma-ray emission.

If magnetic fields, which deviate electron and positron trajectories, are negligibly small, the IC emission from the electromagnetic cascade contributes to the primary point gamma-ray source flux (*26*–*29*). Otherwise, if magnetic fields along the path of development of the cascade are strong enough to deviate the trajectories of the pairs, the cascade emission appears as extended emission around the initial point source (*25*, *30*–*33*).

The deflection angle δ depends on the correlation length of the magnetic field. If $\lambda_B \gg D_e$, the motion of electrons or positrons can be approximated by the motion in a homogeneous magnetic field. In this case $\delta \simeq D_e/R_L \simeq 3 \times 10^{-4}(B/10^{-15}G)(E_e/10\ \mathrm{TeV})^{-2}$ is a ratio of D_e to the Larmor radius, R_L. If $\lambda_B \ll D_e$, electron deflections are describable by diffusion in angle, so that the deflection angle is $\delta = \sqrt{D_e\lambda_B}/R_L \simeq 5 \times 10^{-5}(E_e/10\ \mathrm{TeV})^{3/2}(B/10^{-16}\ \mathrm{G})(\lambda_B/1\ \mathrm{kpc})^{1/2}$. The size of the extended cascade source is estimated as $\Theta_{ext} \simeq \delta/\tau$, where $\tau = D/D_\gamma$ is the optical depth for gamma rays from a source at a distance D with respect to absorption on EBL (*25*).

Because lower energy electrons are deviated by larger angles, the size of the extended cascade source Θ_{ext} is larger at low energies. The energy of cascade photons, $E_{\gamma,min}$, below which the extended source size becomes larger than the point spread function (PSF) of a telescope, depends on the EGMF strength and correlation length. In the case of the Fermi telescope, the PSF depends on the photon energy, decreasing as $\Theta_{PSF} \simeq 2°(E_\gamma/1\ \mathrm{GeV})^{-0.8}$ (95% of the signal) below $E_\gamma \cong 1$ GeV and improving from ~2° at 1 GeV to $\Theta_{PSF} \simeq 0.2°$ at $E_\gamma \sim 10$ GeV (*34*). Taking the photon energy $E_\gamma \sim 10$ GeV as a reference, one finds that $\Theta_{ext} \geq \Theta_{PSF}$ if

$$B \gtrsim B_{PSF} \simeq \begin{cases} 6 \times 10^{-17}\tau(E_{\gamma,min}/10\ \mathrm{GeV}) \\ \quad \times\ \mathrm{G}, \lambda_B > D_e \\ 8 \times 10^{-16}\tau(E_{\gamma,min}/10\ \mathrm{GeV})^{3/4} \\ \quad \times\ (\lambda_B/1\ \mathrm{kpc})^{-1/2}\mathrm{G}, \lambda_B < D_e \end{cases} \quad (1)$$

To constrain the presence of a cascade contribution in the spectra of distant TeV blazars, we have analyzed Fermi/LAT (Large Area Tele-

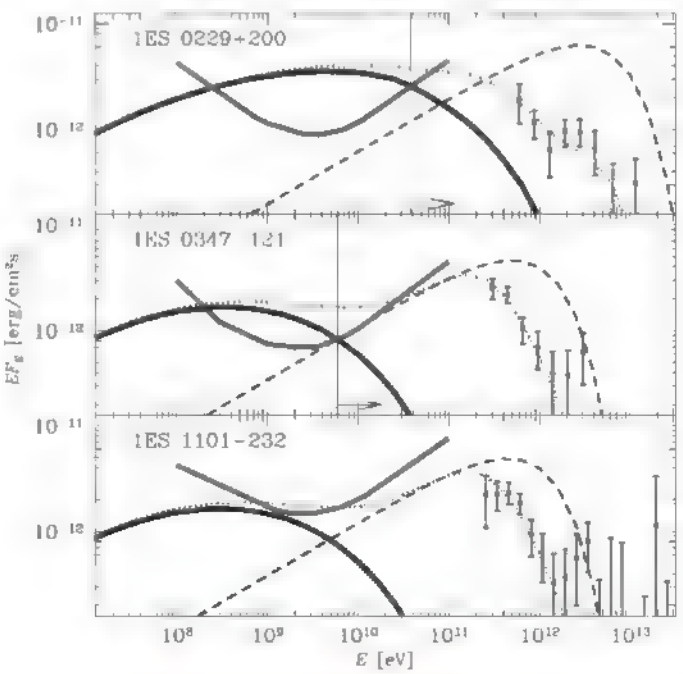

Fig. 1. A comparison of models of cascade emission from TeV blazars (thick solid black curves) with Fermi upper limits (gray curves) and HESS data (gray data points). Thin dashed curves show the primary (unabsorbed) source spectra. Dotted curves show the overall (cascade plus direct) spectra after propagation through the EBL. Vertical lines with arrows show the energies below which the cascade emission should be suppressed. HESS data points (with SEM error bars) are taken from (*23*, *36*, *37*).

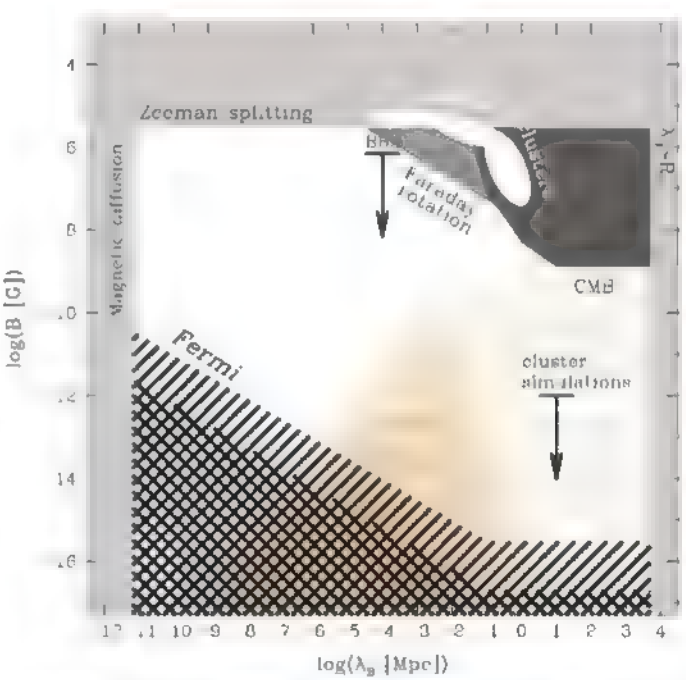

Fig. 2. Light, medium, and dark gray: known observational bounds on the strength and correlation length of EGMF, summarized in (*25*). The bound from Big Bang nucleosynthesis (BBN) is from (*2*). The black hatched region shows the lower bound on the EGMF derived from observations of 1ES 0347-121 (cross-hatching) and 1ES 0229+200 (single diagonal hatching) in this paper. Orange hatched regions show the allowed ranges of B and λ_B for magnetic fields generated at the epoch of inflation (horizontal hatching), the electroweak phase transition (dense vertical hatching), QCD phase transition (medium vertical hatching), and epoch of recombination (light vertical hatching) (*25*). White ellipses show the range of measured magnetic field strengths and correlation lengths in galaxies and galaxy clusters.

scope) data on the blazars 1ES 1101-232, 1ES 0229+200, 1ES 0347-121, and H 2356-309, obtained during the Fermi's first year of operation. These sources were selected on the basis of their high redshifts ($z = 0.14$ for 1ES 0229+200, $z = 0.165$ for H 2356-309, $z = 0.186$ for 1ES 1101-232, and $z = 0.188$ for 1ES 0347-121) and hard TeV band spectra (*22*, *23*, *35*–*38*).

Minimal possible cascade signal from 1ES 1101-232 and H 2356-309 are below the Fermi upper bounds [see supporting online material (SOM) for details]. The nondetection of 1ES 0229+200 and 1ES 0347-121 with Fermi imposes restrictions on the contribution to the flux from the low-energy tail of the cascade (*40*). In order to determine these restrictions, we have developed a numerical model of electromagnetic cascade in intergalactic space, initiated by the absorption of TeV gamma rays on EBL photons. The model solves the one-dimensional kinetic equations for concentrations of gamma rays and of e^+e^- pairs, taking into account the injection of pairs by the absorbed gamma rays (*41*), the injection of secondary cascade gamma rays via IC emission by the e^+e^- pairs, and the cooling of the e^+e^- pairs via IC scattering energy losses (*42*). The cosmological photon backgrounds with which our gamma rays and e^+e^- pairs interact include CMB and EBL taken from (*24*).

The initial gamma-ray spectra at the source, shown by dashed thin curves in Fig. 1, were chosen in the form of a cutoff power law, $dN_\gamma/dE \sim E^{-\Gamma}\exp(-E/E_{cut})$. The cascade emission power is equal to the fraction of the power of the primary gamma-ray beam absorbed on the way from the source to Earth. Because almost 100% of the power initially injected at the energies above TeV is absorbed, the luminosity of cascade emission is roughly equal to the integral primary source luminosity in the multi-TeV energy band. Primary source spectra shown in Fig. 1 correspond to the minimal value of E_{cut} compatible with HESS data, to minimize total flux of the cascade contribution (see details in the SOM).

Assumption of zero magnetic field along the cascade development path is in contradiction with Fermi upper bounds on the source fluxes (Fig. 1). Although the model spectra deviate from simple power laws, the deviations are small, meaning that Fermi bounds on the power law type spectra could be applied.

The cascade emission has to be suppressed below an energy $E_{\gamma,min}$ (marked by a vertical line in the top two graphs of Fig. 1) at which the Fermi upper bound becomes higher than the model cascade flux. Suppression of the cascade flux at low energies could be achieved if trajectories of low-energy e^+e^- pairs are deviated by magnetic fields. The cascade emission does not contribute to the point source flux below the energy $E_{\gamma,min}$ if EGMF is stronger than B_{PSF} given by Eq. 1. The values of B_{PSF} corresponding to $E_{\gamma,min}$ found for each source are given in table S1.

The best bound $B \geq B_{PSF}$ imposed by Fermi limits on the flux from 1ES 0229+200 (black hatched region in Fig. 2), suffers from a number of uncertainties and therefore should be considered as an order-of-magnitude estimate.

Suppression of the cascade contribution to the point source flux below the energy $E_{\gamma,min}$ results in a deviation of the model source flux from the power law at the energies $E \lesssim E_{\gamma,min}$. This means that the Fermi upper bounds on the power law type spectra shown in Fig. 1 could provide only rough estimates of $E_{\gamma,min}$ and B_{PSF}. Additional uncertainty is introduced in the estimate of B_{PSF} by the uncertainty of the measurements of EBL, which result in the uncertainty of the optical depth τ in Eq. 1. Further uncertainty is introduced in the derivation of $E_{\gamma,min}$ from nonsimultaneous data in GeV and TeV bands. Both HESS and Fermi measurements refer to the source spectra averaged over year(s) time scale. The reported HESS observations of the sources took place in the period from 2005 to 2006 (*22*, *23*, *36*), whereas Fermi measurements were taken in 2008 and 2009. Up to now, no long-term variability was found in HESS observations (*22*, *23*, *36*, *43*).

The mean free path of primary multi-TeV gamma rays is of the order of ~ 80κ Mpc. The largest structures in the universe, galaxy clusters, have typical sizes of the order of several Mpc, and their volume filling factor is small. Most of the volume of the sphere of radius ~ 80κ Mpc around 1ES 0229+200 and 1ES 0347-121 is occupied by the voids in the Large-Scale Structure.

Evidence for existence of magnetic fields in the voids provides a strong argument in favor of a cosmological origin of the fields serving as seeds for subsequent amplification in galaxies and galaxy clusters. Weak magnetic fields produced in the early universe are expected to fill the whole universe, including the voids. Contrarily, in the astrophysical models, the weak seed fields are created locally in (proto)galaxies, and the field outside these structures should be close to zero.

Cosmological magnetogenesis models consider generation of magnetic fields with a correlation length that does not exceed the size of the cosmological horizon and with energy density that does not exceed the critical density of the universe at the moment of magnetogenesis. Four broad classes of cosmological magnetogenesis scenaria are considered: magnetogenesis at the epoch of inflation, at the electroweak phase transition, at the epoch of quantum chromodynamics (QCD) phase transition, and at the epoch of recombination (*1*–*3*, *44*–*51*). The lower bound reported here excludes substantial parts of allowed parameter space for all the classes of cosmological magnetogenesis models (Fig. 2).

References and Notes

1. P. P. Kronberg, *Rep. Prog. Phys.* **57**, 325 (1994).
2. D. Grasso, H. R. Rubinstein, *Phys. Rep.* **348**, 163 (2001).
3. L. M. Widrow, *Rev. Mod. Phys.* **74**, 775 (2002).
4. R. M. Kulsrud, E. G. Zweibel, *Rep. Prog. Phys.* **71**, 0046091 (2008).
5. P. Blasi, S. Burles, A. V. Olinto, *Astrophys. J.* **514**, L79 (1999).
6. J. P. Vallee, *N. Astron. Rev.* **48**, 763 (2004).
7. J. D. Barrow, P. G. Ferreira, J. Silk, *Phys. Rev. Lett.* **78**, 3610 (1997).
8. K. Subramanian, J. D. Barrow, *Phys. Rev. Lett.* **81**, 3575 (1998).
9. R. Durrer, P. G. Ferreira, T. Kahniashvili, *Phys. Rev. D* **61**, 043001 (2000).
10. K. Jedamzik, V. Katalinic, A. V. Olinto, *Phys. Rev. Lett.* **85**, 700 (2000).
11. T. R. Seshadri, K. Subramanian, *Phys. Rev. Lett.* **87** 101301 (2001).
12. A. Mack, T. Kahniashvili, A. Kosowsky, *Phys. Rev. D* **65**, 123004 (2002).
13. A. Lewis, *Phys. Rev.* **70**, 043011 (2004).
14. D. G. Yamazaki, K. Ichiki, T. Kajino, G. Mathews, *Phys. Rev. D* **77**, 043005 (2008).
15. M. Giovannini, K. E. Kunze, *Phys. Rev. D* **77**, 063003 (2008).
16. J. R. Kristiansen, P. G. Ferreira, *Phys. Rev. D* **77**, 123004 (2008).
17. T. Kahniashvili, T. Maravin, A. Kosowsky, *Phys. Rev. D* **80**. 023009 (2009).
18. T. R. Seshadri, K. Subramanian, *Phys. Rev. Lett.* **103**, 081303 (2009).
19. K. Dolag, M. Bartelmann, H. Lesch, *Astron. Astrophys.* **348**, 351 (1999).
20. K. Dolag, D. Grasso, V. Springel, I. Tkachev, *J. Cosmol. Astropart. Phys.* **0501**, 009 (2005).
21. R. J. Gould, G. P. Schréder, *Phys. Rev. Lett.* **16**, 252 (1967).
22. F. A. Aharonian *et al.*, *Nature* **440**, 1018 (2006).
23. F. A. Aharonian *et al.*, *Astron. Astrophys.* **475**, L9 (2007).
24. A. Franceschini, G. Rodighiero, M. Vaccari, *Astron. Astrophys.* **487**, 837 (2008).
25. A. Neronov, D. Semikoz, *Phys. Rev. D* **80**. 123012 (2009).
26. R. Plaga, *Nature* **374**, 430 (1995).
27. Y. Z. Fan, Z. G. Dai, D. M. Wei, *Astron. Astrophys.* **415**, 483 (2002).
28. P. D'Avezac, G. Dubus, B. Giebels, *Astron. Astrophys.* **469**, 857 (2007).
29. K. Murase, K. Takahashi, S. Inoue, K. Ichiki, S. Nagataki, *Astrophys. J.* **686**, L67 (2008).
30. F. A. Aharonian, P. S. Coppi, H. J. Volk, *Astrophys. J.* **423**, L5 (1994).
31. A. Neronov, D. V. Semikoz, *J. Exp. Theor. Phys. Lett.* **85**, 473 (2007).
32. A. Elyiv, A. Neronov, D. V. Semikoz, *Phys. Rev. D* **80**, 023010 (2009).
33. K. Dolag, M. Kachelrieß, S. Ostapchenko, R. Tomàs, *Astrophys. J.* **703**, 1078 (2009).
34. www-glast.slac.stanford.edu/software/IS/glast_lat_performance.htm
35. F. A. Aharonian *et al.*, *Astron. Astrophys.* **455**, 461 (2006).
36. F. A. Aharonian *et al.*, *Astron. Astrophys.* **470**, 475 (2007).
37. F. A. Aharonian *et al.*, *Astron. Astrophys.* **473**, L25 (2007).
38. When this paper was ready for publication, we became aware of analysis of the signal from TeV blazars reported by the Fermi collaboration (*39*). Our analysis is consistent with the one of (*39*) and extends the results obtained in (*39*).
39. A. A. Abdo *et al.*, *Astrophys. J.* **707**, 1310 (2009).
40. The cut-off energies of intrinsic spectra of H 2356-309 and 1ES 1101-232 could be so low that the flux of the cascade emission could be below Fermi upper bounds on GeV source flux. This is illustrated in the bottom graph of Fig. 1 for the case of 1ES 1101-232. See SOM for more details.
41. R. J. Gould, G. P. Schréder, *Phys. Rev.* **155**, 1404 (1967).
42. G. R. Blumenthal, R. J. Gould, *Rev. Mod. Phys.* **42**, 237 (1970).
43. F. A. Aharonian *et al.*, *Astron. Astrophys.* **478**, 387 (2008).
44. M. S. Turner, L. M. Widrow, *Phys. Rev. D* **37**, 2743 (1988).
45. J. Quashnock, A. Loeb, D. Spergel, *Astrophys. J.* **344**, L49 (1989).
46. C. J. Hogan, *Phys. Rev. Lett.* **51**, 1488 (1983).
47. T. Vachaspati, *Phys. Lett. B* **265**, 258 (1991).
48. B. Ratra, *Astrophys. J.* **391**, L1 (1992).
49. G. Sigl, A. V. Olinto, K. Jedamzik, *Phys. Rev. D* **55**, 4582 (1997).
50. A. Díaz-Gil, J. García-Bellido, M. G. Pérez, A. González-Arroyo, *Phys. Rev. Lett.* **100**, 241301 (2008).
51. V. Demozzi, V. Mukhanov, H. Rubinstein, *J. Cosmol. Astropart. Phys.* **8**, 25 (2009).

Supporting Online Material

www.sciencemag.org/cgi/content/full/328/5974/73/DC1
Materials and Methods
Fig. S1
Table S1
References

3 November 2009; accepted 2 March 2010
10.1126/science.1184192

Frictional Characteristics of Atomically Thin Sheets

Changgu Lee,[1]* Qunyang Li,[2]* William Kalb,[1] Xin-Zhou Liu,[3] Helmuth Berger,[4] Robert W. Carpick,[2]† James Hone[1]

Using friction force microscopy, we compared the nanoscale frictional characteristics of atomically thin sheets of graphene, molybdenum disulfide (MoS_2), niobium diselenide, and hexagonal boron nitride exfoliated onto a weakly adherent substrate (silicon oxide) to those of their bulk counterparts. Measurements down to single atomic sheets revealed that friction monotonically increased as the number of layers decreased for all four materials. Suspended graphene membranes showed the same trend, but binding the graphene strongly to a mica surface suppressed the trend. Tip-sample adhesion forces were indistinguishable for all thicknesses and substrate arrangements. Both graphene and MoS_2 exhibited atomic lattice stick-slip friction, with the thinnest sheets possessing a sliding-length–dependent increase in static friction. These observations, coupled with finite element modeling, suggest that the trend arises from the thinner sheets' increased susceptibility to out-of-plane elastic deformation. The generality of the results indicates that this may be a universal characteristic of nanoscale friction for atomically thin materials weakly bound to substrates.

The development of materials and structures with nanoscale features highlights the need to understand how such materials behave in contact. The high relative surface area at small scales renders adhesion, friction, and wear consequential for nanoscale data storage devices, nanocomposites, and nanoeletromechanical systems (NEMS). Two-dimensional (2D) architectures are of particular interest, because their planar geometry is compatible with wafer-level processing. How material behavior depends on structural dimensionality is relevant scientifically, particularly at the nanoscale: Quasi-0D materials (quantum dots, nanoparticles) and quasi-1D materials (nanowires, nanotubes) behave very differently from their 3D counterparts (*1*, *2*). Studies of isolated atomic sheets have demonstrated the distinct properties of 2D materials as well. The most widely studied of these is graphene, which exhibits notable electronic, thermal, chemical, and mechanical properties including unrivaled mechanical stiffness and strength (*3*). This motivates considering graphene for next-generation electronic devices and NEMS (*4*, *5*).

For such applications, the mechanical and tribological properties of these materials must be better understood. To this end, four atomically-thin quasi-2D materials—graphene, molybdenum disulfide (MoS_2), hexagonal boron nitride (h-BN), and niobium diselenide ($NbSe_2$)—were separated

[1]Department of Mechanical Engineering, Columbia University, New York, NY 10027, USA. [2]Department of Mechanical Engineering and Applied Mechanics, University of Pennsylvania, Philadelphia, PA 19104, USA. [3]Department of Physics, Leiden University, 2300 RA Leiden, Netherlands. [4]Institute of Physics of Condensed Matter, Ecole Polytechnique Fédérale de Lausanne, CH-1015 Lausanne, Switzerland.

*These authors contributed equally to this work.
†To whom correspondence should be addressed. E-mail: carpick@seas.upenn.edu

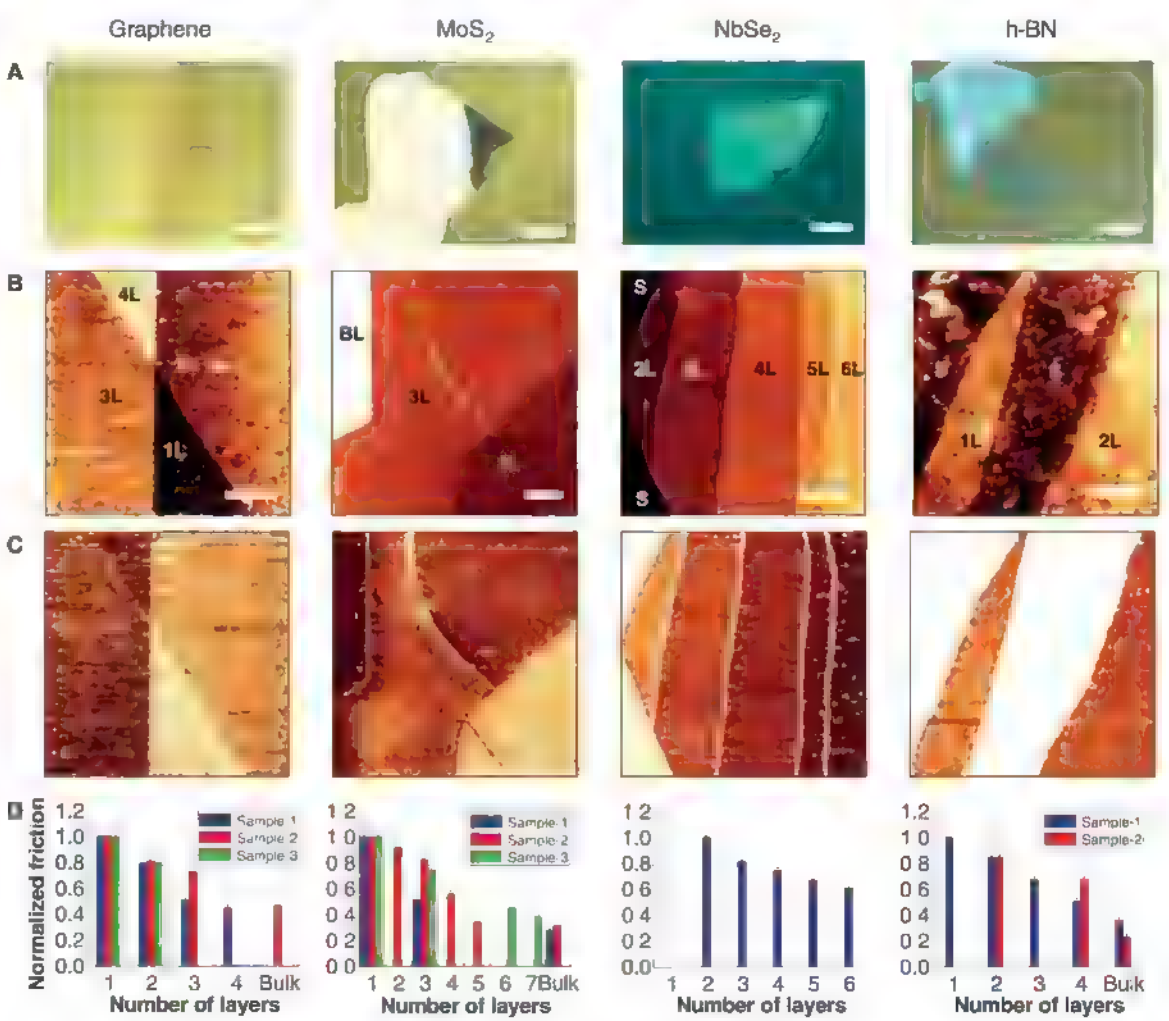

Fig. 1. Optical and AFM images of atomically thin sheets of (from left to right) graphene, MoS_2, $NbSe_2$, and h-BN on silicon oxide. (**A**) Bright field optical microscope images of thin sample flakes. The red dotted squares represent subsequent AFM scan areas. Scale bars, 10 μm. (**B** and **C**) Topographic and friction (forward scan) images measured simultaneously by AFM from the indicated areas. 1L, 2L, 3L, etc., indicate sheets with thicknesses of one, two, three, etc., atomic layers. BL ("bulk-like") denotes an area with a very thick flake, and S represents an area with bare SiO_2 substrate. Scale bars, 1 μm. (**D**) Friction on areas with different layer thicknesses. For each sample, friction is normalized to the value obtained for the thinnest layer. Error bars represent the standard deviation of the friction signals of each area. In each chart, the same color represents data from the same sample

from their bulk sources by mechanical exfoliation (*6*) and their nanotribological properties characterized by friction force microscopy (FFM). These materials have widely varying electronic properties. $NbSe_2$ is metallic; graphene is a zero-bandgap semiconductor or a semimetal (depending on thickness); MoS_2 is a semiconductor; and h-BN is insulating.

The bulk analogs of these lamellar materials, particularly graphite, MoS_2, and h-BN, are widely used as solid lubricant films in critical engineering applications (*7*, *8*). The way in which asperities interact with the lamellar structures in these films, and how lamellae interact with each other, are key areas where molecular-level insights could be valuable.

Recently, FFM measurements found that monolayer epitaxial graphene on SiC exhibits higher friction than bilayer graphene (*9*). Here, we observe that friction on all four quasi-2D materials studied is higher than that of their bulk counterparts. The evolution from monolayer to multiple layers and bulk is quantitatively studied at the micrometer scale and at the atomic-level stick-slip regime. The experiments, and finite element modeling, indicate that the higher friction is related to the low bending stiffness of the thinnest layers.

Graphene, MoS_2, h-BN, and $NbSe_2$ flakes were deposited in ambient conditions by mechanically exfoliating bulk source materials onto SiO_2/Si (SiO_2: 300 nm) substrates in a manner similar to that previously established (*6*). After deposition, the samples did not go through any further treatment, so as-deposited materials were used for all measurements. The thinnest flakes were identified by optical microscopy (Fig. 1A). The exfoliated flakes have typical lateral dimensions of tens of micrometers, consisting of both thin and thick areas.

Micrometer-scale imaging and FFM were performed in contact mode with a Park Systems XE-100 atomic force microscope (AFM) in an ambient environment (25 to 50% relative humidity, 20° to 25°C, unless otherwise noted). Silicon AFM probes [Mikromasch CSC17, specified tip radius R = 5 to 10 nm, and typical normal force constant $k \approx 0.15$ N/m, calibrated using the reference cantilever method (*10*)] were used at an applied force of 1 nN with scan areas several micrometers across. Contact-mode AFM is a reliable method for providing accurate height measurements of atomically thin sheets (*11*). Thicknesses of the monolayer sheets closely matched the interlayer crystal spacings of each material (0.335, 0.615, 1.288, and 0.333 nm for graphene, MoS_2, $NbSe_2$, and h-BN, respectively). Thicker multilayered regions had thicknesses close to integer multiples of the interlayer spacings (fig. S1) (*12*). The topographic AFM images of the thin flakes are shown in Fig. 1B. The regions labeled 1L, 2L, etc., correspond to where the flakes are one-layer, two-layer, etc., thick. Regions labeled BL are very thick (bulk-like, >20 layers). For graphene, the measured thicknesses were independently confirmed by Raman spectroscopy (*13*).

FFM images (Fig. 1C), obtained simultaneously with the topographic images, show a pattern of increasing friction with decreasing thickness. To quantify the observed trend, we calculated the friction force by dividing the friction signal difference between the steady-state values in the forward and reverse scans by two. For all four materials, the friction force is roughly equal to the bulk value for samples thicker than about five layers and increases monotonically with decreasing thickness below that point (Fig. 1D). Monolayer sheets show ~20% greater friction than bilayer sheets, and two to three times higher friction than bulk sheets. Extrinsic factors that can affect the measured friction, such as tip size, shape, and composition, applied load, environment, and scan speed (*14*)–, are kept constant for a given image; for each data set we report friction normalized to the value measured on the thinnest sheet found (one or two layers depending on the material). We also obtained absolute friction values on thick areas (>10 layers) of the four materials with a Si tip calibrated by a diamagnetic lateral force calibrator (*12*, *15*) (fig. S2). We observed that graphene, MoS_2, and h-BN had much lower friction (~1 nN) than $NbSe_2$ (~7 nN).

The trend of increasing friction with decreasing thickness was robust over a large range of experimental conditions. The results were reproduced when distinct Si tips and samples were used for all four materials. The trend did not depend on scan speed from 1 to 10 μm/s, or on normal load from 0.1 to 2 nN. The trend was also seen in graphene for a normal load of 50 nN when a stiffer silicon nitride–coated probe was used [DP15/LS, nonconducting, Mikromasch, R = 20 to 30 nm, k = 45 N/m, calibrated by Sader's method (*16*)]. Friction was also measured with tips made of other materials, including silicon nitride (DP15/LS, Mikromasch) and diamond (ND-CTIR1 "NaDia Probe," nonconducting, Advanced Diamond Technologies). The relative changes in friction were comparable for every tip. Reducing the humidity from ~30 to <5% in N_2 for graphene and MoS_2 led to overall lower friction forces (by ~20 to 30%), but the trend with layer thickness was preserved. Because tip-substrate adhesion can influence friction (*17*), we measured adhesion on samples by carrying out force-displacement spectroscopy. There was no resolvable difference in adhesion between areas of different thicknesses for any of the materials studied.

The observation of increasing friction with decreasing thickness is consistent with experiments on one-layer and two-layer SiC-derived graphene of Filleter *et al.* (*9*), and extends the trend to more layers and additional materials. However, Filleter *et al.* reported that bulk graphite has higher friction than one-layer and two-layer graphene, whereas we observe that friction on graphene approaches that of graphite as the number of layers increases.

Two experiments were next performed to test the role of the substrate in the friction measurements. First, graphene was deposited on substrates with 300-nm-diameter circular holes to form freely suspended membranes. FFM images showed no difference in friction between the suspended and substrate-supported graphene. Figure 2A shows one such sample, in which areas of one-layer and two-layer graphene were suspended over the same hole. Both thicknesses showed the same behavior when suspended and supported. Second, graphene was deposited on muscovite mica, on which it is strongly adherent and atomically flat because of mica's high surface energy (*18*). Graphene was deposited within several seconds after the mica was mechanically cleaved to minimize adsorption of water on the surface; little difference in topography and friction was observed for samples deposited in air or in dry nitrogen. As previously reported (*18*), topographic images [see Supporting Online Material (SOM) (*12*)] reveal two types of behavior: atomically flat areas in intimate contact with the mica, and slightly (0.2 to 0.3 nm) elevated "bubbles," which appear to be caused by gas trapped between the graphene and mica. Figure 2B shows a FFM image of a thick (~9 nm) graphene flake next to a two-layer flake, on mica, separated by a narrow region of bare mica. The friction shown by flat areas of the two-layer region is identical to that of the thick sample, whereas friction shown by the "bubbles" is about twice as large, consistent with behavior on SiO_2 or when suspended.

A second set of measurements was obtained by scanning for only a few nanometers across

Fig. 2. FFM images of suspended graphene (**A**) and graphene deposited on mica (**B**). Scale bars, 0.3 μm. The green lines are profiles of friction force along the black scan lines. In (A), there is no difference in friction between the suspended and supported areas for both 1L and 2L graphene, but friction for 2L is noticeably lower than for 1L. In (B), friction for the thick (BL) and 2L graphene (the topographically lower regions) is the same. The 2L graphene possesses isolated regions of higher friction that are topographically elevated and may be due to trapped gas or liquid.

graphene and MoS_2 samples with a RHK UHV350 AFM (Fig. 3). The ultrahigh-vacuum AFM chamber was purged by clean, dry nitrogen (from vaporized liquid nitrogen) and then sealed. The relative humidity was measured to be <5% and was likely around 1 to 2% based on measurements under similar conditions. For graphene, the normal force was maintained at 4 nN with a silicon probe [CSC37 Mikromasch, force constant 0.18 N/m calibrated using Sader's method (*16*)]. The scan speed was 40 nm/s for 2-nm scan sizes and 100 nm/s for 5-nm scan sizes. For measurements on MoS_2, the normal force was 3.6 nN exerted by a silicon probe (CSC17 Mikromasch, calibrated force constant 0.1 N/m), with scan speeds of 25 nm/s for 5-nm scan sizes and 50 nm/s for 10-nm scan sizes. In both cases, the lateral force was calibrated by a diamagnetic lateral force calibrator (*15*).

Figure 3A shows line traces of the friction force for 2-nm scan widths. The tip exhibits clear, periodic stick-slip motion, similar to that observed previously for bulk graphite and MoS_2, respectively (*19*–*21*). However, on the thinnest sheets, the force at which each slip occurs increases in magnitude during each forward and reverse scan, producing a tilted friction loop. This "strengthening" effect is highlighted by the dotted trend lines in the figure and is strongest for the monolayer. At longer scan lengths of 5 nm, the strengthening effect saturates as the scan proceeds (Fig. 3B).

Because of this friction strengthening, it is more straightforward to report the relative frictional energy dissipated per unit cell as opposed to the average or maximum force (Fig. 3C). This is obtained by first integrating the friction force over the forward and reverse scans and then dividing the result by the number of apparent unit cells scanned. For both graphene and MoS_2, the energy dissipated per unit cell decreases monotonically with an increase in the number of layers, and approaches that of bulk materials. This is consistent with the micrometer-scale measurements (Fig. 1), although the dependence on thickness is slightly less prominent. This could be due to the different scan velocities, tip sizes or shapes, or environments; detailed studies are needed to fully explore these modest differences. The energy dissipated per slip ranges from ~2.5 to 10 eV, which is initially generated at a contact that spans a diameter of several nanometers and therefore involves several hundreds of atoms at the interface.

Atomic-level stick-slip on bulk graphite and MoS_2 yields friction images with threefold symmetric patterns (*22*, *23*). Representative examples of raw and filtered friction images on both one-layer and bulk materials are shown in Fig. 3D. The raw friction signal on one-layer sheets appears darker on the left because of the strengthening effect, whereas the force at which slip occurs is uniform for the bulk materials. Similar threefold symmetric patterns were observed for all the samples, corresponding to the known symmetry of the lattices.

During the strengthening portion of the friction loops, the periodicity for graphene is increased along the fast scanning direction, as seen by comparing the lattice measured from one-layer graphene to that from bulk graphite (Fig. 3D, filled circles). This effect gets weaker as the number of layers increases, and the lattice measured from four-layer graphene is nearly indistinguishable from that of bulk graphite (fig. S5). For one-layer MoS_2, a higher level of drift prevented any similar effect from being resolved.

The stick-slip images allow observation of the crystal orientation of each exposed layer. For graphene, the individual stacked region of a given flake all share the same orientation to within 0.4°, which means that the layers of an exfoliated flake remain commensurate. This relatively straightforward FFM imaging technique may prove useful for characterization of

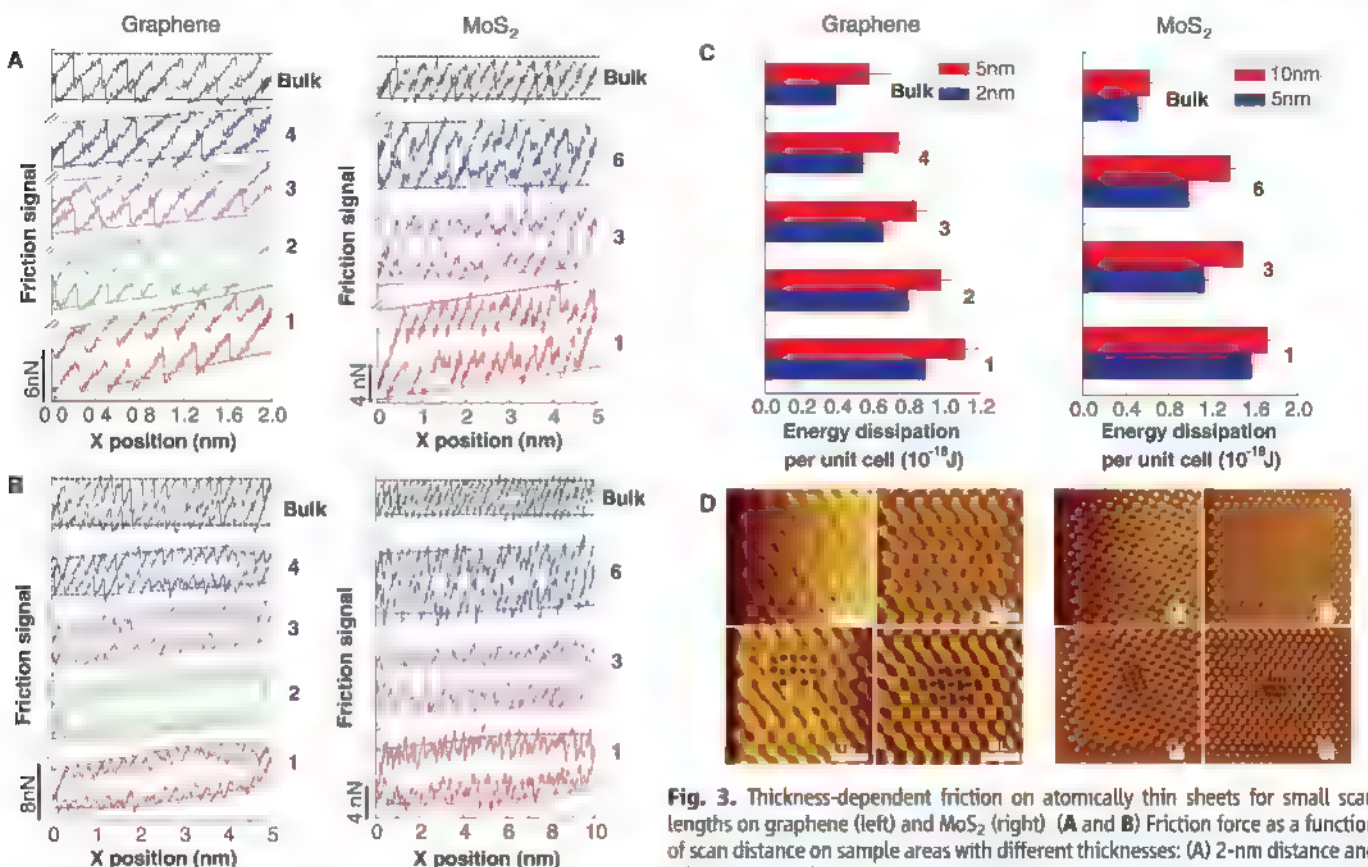

Fig. 3. Thickness-dependent friction on atomically thin sheets for small scan lengths on graphene (left) and MoS_2 (right). (**A** and **B**) Friction force as a function of scan distance on sample areas with different thicknesses: (A) 2-nm distance and (B) 5-nm scan distance. The numbers on the right indicate the corresponding numbers of atomic layers. The friction traces show that the tip moves unstably with stick-slip motion coupled with an unusual "strengthening" effect, which is highlighted by the dotted trend lines. (**C**) Energy dissipation per unit cell of slip as the tip slides over the thin sheets, as well as over the bulk counterparts. (**D**) Raw (upper) and low-pass filtered (lower) images showing the friction signal in the forward sliding direction for 1L (left) and thick (BL) (right) samples. The filtered images show the periodicity of the lattice; black dots represent the periodic sites of the friction force signal. For graphene, the lattice is clearly stretched in the strengthening portion of the friction measurement. Scale bars, 0.5 nm.

structures such as epitaxial graphene and graphene nanoribbons, whose electronic properties depend on their width and angle relative to the crystal axis, as well as the degree of disorder at the nanoribbon edge (*24*, *25*).

We next examine potential mechanisms that can account for the observed trend of decreasing friction with increasing thickness. The similar behavior for four materials with widely varying electronic and vibrational properties, as well as the strong substrate effects, argues against phononic (*26*) and electronic dissipation as the cause (*27*). In particular, the electron-phonon coupling mechanism proposed by Filleter *et al.* cannot account for our results, although our results do not exclude an additional contribution from this mechanism. A recent model of interfacial dislocation-mediated friction (*28*) assumes 3D crystalline materials on both sides of an infinite interface; our finite-sized amorphous tip in contact with atomically thin sheets is incompatible with this. In addition, chemical mechanisms and wear are not at play, as we see no evidence of bond breaking or other irreversible structural changes. Finally, the identical behavior of suspended and SiO_2-supported graphene rules out roughening or interaction with charge traps in the SiO_2.

A number of factors argue against the presence in these experiments of interlayer sliding, which could reduce friction for thicker samples. The flakes are much larger than the tip-sample contact area (micrometers versus nanometers), and the flake edges may interact more strongly with the substrate owing to the presence of dangling bonds or oxide groups. Therefore, even for an overall weak flake-substrate adhesion, the force required to move an entire flake is far larger than that required to slide the tip relative to the sample. The steady-state atomic-scale stick-slip results clearly demonstrate that relative slip consistently occurs between the tip and the top surface of the graphene. However, a transient amount of local sliding between the topmost layer and the material below could be occurring during the strengthening portion of the friction loop, i.e., for the first few nanometers of sliding (Fig. 3, A and D), where the lattice is seen to be distorted. However, this effect is most pronounced in the thinnest samples, indicating that transient interlayer sliding is associated with higher, not lower, friction.

We next consider a mechanical origin for the observed effect, namely, that any material becomes more compliant, especially in bending, as it approaches atomic thickness (the flexural rigidity of an elastic is proportional to its thickness cubed). This is consistent with our observations for four distinct materials, as well as the observed substrate effects: suspended or weakly bonded (i.e., on SiO_2) samples will be more compliant than samples strongly adhered to substrates (i.e., graphene on mica).

To understand the role of the sheet stiffness in friction, we consider a simple model of a tip sliding across a flexible membrane. In this case, when the tip makes contact with the top surface, adhesion causes the sheet to easily pucker locally (*29*) because of the sheet's low bending stiffness compared to its in-plane stiffness. The puckered geometry will be modified at the front edge by tip-sheet friction, as depicted by the cartoon in Fig. 4A. This out-of-plane puckering could explain increased friction because of the increased tip-sheet contact area that results, or because of additional work required to move the puckered region forward. This will become more pronounced as the sheet becomes thinner, and indeed this is observed in finite element modeling.

In this picture, one could expect the thinnest sheets to exhibit a transient behavior each time the tip changes direction. The puckered region of the graphene would rearrange under the tip in response to the change in sliding direction. Some relative sliding between the topmost layer and the material below could then occur. This would increase the spacing of the stick-slip events, and this is indeed what is seen during the strengthening portion of the friction loops (Fig. 3, A, B, and D).

To test the puckering idea further, we performed finite element modeling for a simplified 2D continuum model. In the model, a rigid spherical tip is slid over a thin elastic sheet whose bending stiffness and in-plane rigidity are dependent on its thickness. The tip-sheet interaction is described by an effective adhesive force originating from Lennard-Jones interaction, and a shear stress obtained from contact-size–dependent friction model (see SOM for details) (*12*). Because of adhesion, the elastic sheet snaps to the tip, and locally puckers if the sheet is thin enough. When the tip slides, the symmetry of the puckered region breaks and it piles up mostly at the front edge of the contact (Fig. 4B, left inset); the geometry reverses when the tip changes direction. The enlarged contact area from out-of-plane deformation requires more force to slide the tip forward. For a thicker sheet, the puckering is less prominent owing to the larger bending stiffness of the sheet (Fig. 4B, right inset), and therefore friction is lower. The resulting variation in friction with sheet thickness is given in Fig. 4B. The qualitative agreement with the experiments suggests that the puckering effect is a feasible mechanism for the thickness-dependent friction behavior.

No atomistic theory specifically formulated for asperity contact with a thin material contains mechanisms that cause friction to increase as the atomic limit of thickness is approached. However, a recent atomistic model for flat interfaces predicts that as a material varies from 3D to 2D geometry, friction against that material increases (*30*), owing to weaker scaling of elastic stiffness with size in two dimensions combined with the well-known intrinsic property of atomic lattice stick-slip friction: Stick-slip instabilities and the associated increased frictional dissipation occur when the local elastic stiffness becomes weaker than the gradient of the lateral force arising from the corrugated interfacial potential (*31*). Increased elastic compliance of the puckered thin sheet could therefore be another related aspect contributing to higher friction in these systems. The finite element model presented here is only a first step in analyzing this behavior. Atomistic simulations tailored to these materials and conditions would not only provide substantial further insights into the present experiments, but could potentially provide needed molecular-level insights into the tribological behavior of solid lubricants.

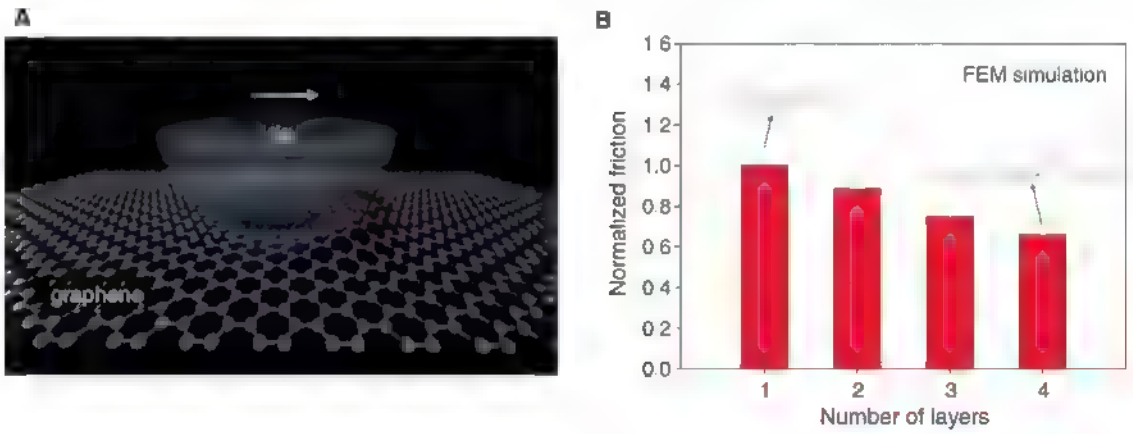

Fig. 4. (**A**) A schematic showing the proposed puckering effect, where adhesion to the sliding AFM tip creates out-of-plane deformation of a graphene sheet, leading to increased contact area and friction; the color scale of the atoms indicates their out-of-plane positions. (**B**) The variation in friction as a function of the sheet thickness based on the FEM simulation. Friction is normalized by the value obtained for a one-layer sheet; the insets indicate the local out-of-plane deformation of the sheets (indicated by the color) around the contact areas for sliding over a one-layer sheet and four-layer sheet.

The consistency of the AFM measurements for four different materials strongly suggests that this phenomenon is universal for atomically thin sheets that are loosely adhered to a substrate or freely suspended. This reveals a new mechanism of enhanced friction for quasi-2D materials based on elastic compliance. Because the effect is suppressed when the sheet is attached to a strongly adhering substrate, the results indicate an avenue to controlling nanoscale friction for these materials. Therefore, these results can potentially aid in the rational design and use of materials for nanomechanical applications, including nanolubricants and components in micro- and nanoeletromechanical systems devices.

References and Notes

1. H. Park *et al.*, *Nature* **407**, 57 (2000)
2. A. I. Yanson, G. R. Bollinger, H. E. van den Brom, N. Agraït, J. M. van Ruitenbeek, *Nature* **395**, 783 (1998)
3. A. K. Geim, *Science* **324**, 1530 (2009)
4. K. S. Novoselov *et al.*, *Science* **306**, 666 (2004)
5. I. Meric *et al.*, *Nat. Nanotechnol.* **3**, 654 (2008)
6. K. S. Novoselov *et al.*, *Proc. Natl. Acad. Sci. U.S.A.* **102** 10451 (2005)
7. C. Donnet, A. Erdemir *Surf. Coat. Tech.* **180-181**, 76 (2004)
8. I. L. Singer, H. M. Pollock, *Fundamentals of Friction: Macroscopic and Microscopic Processes* (Kluwer, Dordrecht, Netherlands, 1992)
9. T. Filleter *et al.*, *Phys. Rev. Lett.* **102**, 86102 (2009)
10. M. Tortonese, M. Kirk, *Proc. Soc. Photo. Opt. Instrum. Eng.* **3009**, 53 (1997)
11. P. Nemes-Incze, Z. Osvath, K. Kamaras, L. P. Biro, *Carbon* **46**, 1435 (2008)
12. Sample preparation, additional measurement results, and finite element modeling are available as supporting material on *Science* Online
13. A. C. Ferrari *et al.*, *Phys. Rev. Lett.* **97**, 187401 (2006)
14. I. Szlufarska, M. Chandross, R. W. Carpick, *J. Phys. D Appl. Phys.* **41**, 123001 (2008)
15. Q. Li, K. S. Kim, A. Rydberg, *Rev. Sci. Instrum.* **77**, 65105 (2006)
16. J. E. Sader, J. W. M. Chon, P. Mulvaney, *Rev. Sci. Instrum.* **70**, 3967 (1999)
17. K. L. Johnson, *Contact Mechanics* (Cambridge Univ. Press, Cambridge, 1985)
18. C. H. Lui, L. Liu, K. F. Mak, G. W. Flynn, T. F. Heinz, *Nature* **462**, 339 (2009)
19. C. M. Mate, G. M. McClelland, R. Erlandsson, S. Chiang, *Phys. Rev. Lett.* **59**, 1942 (1987)
20. S. N. Medyanik, W. K. Liu, I.-H. Sung, R. W. Carpick, *Phys. Rev. Lett.* **97**, 136106 (2006)
21. X. Zhao, S. R. Phillpot, W. G. Sawyer, S. B. Sinnott, S. S. Perry, *Phys. Rev. Lett.* **102**, 186102 (2009)
22. J.-A. Ruan, B. Bhushan, *J. Appl. Phys.* **76**, 5022 (1994)
23. S. Fujisawa, E. Kishi, Y. Sugawara, S. Morita, *Phys. Rev. B* **51**, 7849 (1995)
24. K. Nakada, M. Fujita, G. Dresselhaus, M. S. Dresselhaus, *Phys. Rev. B* **54**, 17954 (1996)
25. M. Y. Han, B. Ozyilmaz, Y. Zhang, P. Kim, *Phys. Rev. Lett.* **98**, 206805 (2007)
26. M. Cieplak, E. D. Smith, M. O. Robbins, *Science* **265** 1209 (1994)
27. B. N. J. Persson, A. I. Volokitin, *J. Chem. Phys.* **103** 8679 (1995)
28. A. P. Merkle, L. D. Marks, *Tribol. Lett.* **26**, 73 (2007).
29. K. R. Shull, *Mater. Sci. Eng. Rep.* **36**, 1 (2002)
30. M. H. Müser, *Europhys. Lett.* **66**, 97 (2004)
31. L. Prandtl, *Z. Angew. Math. Mech.* **8**, 85 (1928)

32. We acknowledge support from the NSF under awards NSF/MRSEC (no. DMR-0520020) (R.W.C.), CMMI-0800154 (R.W.C.), CHE-0117752 (J.H.), and CMMI-0927891 (J.H.), the New York State Office of Science, Technology, and Academic Research (NYSTAR) (J.H.); the Defense Advanced Research Projects Agency (DARPA) Center on Nanoscale Science and Technology for Integrated Micro/Nano-Electromechanical Transducers (iMINT, grant HR0011-06-1-0048) (J.H.); Air Force Office of Scientific Research (AFOSR) (MURI FA955009-1-0705) (J.H.); and the Swiss NSF and its National Centers of Competence in Research (NCCR) MaNEP (H.B.). We thank Momentive Performance Materials, Advanced Diamond Technologies, and C. H. Lui for supplying h-BN powder, diamond-coated AFM probes, and graphene samples on mica, respectively. We acknowledge helpful discussions with J. Li, M. Müser, and L. Forró

Supporting Online Material

www.sciencemag.org/cgi/content/full/328/5974/76/DC1
Materials and Methods
Figs. S1 to S8
References

3 November 2009; accepted 17 February 2010
10.1126/science.1184167

A Stratified Redox Model for the Ediacaran Ocean

Chao Li,[1]* Gordon D. Love,[1] Timothy W. Lyons,[1] David A. Fike,[2] Alex L. Sessions,[3] Xuelei Chu[4]

The Ediacaran Period (635 to 542 million years ago) was a time of fundamental environmental and evolutionary change, culminating in the first appearance of macroscopic animals. Here, we present a detailed spatial and temporal record of Ediacaran ocean chemistry for the Doushantuo Formation in the Nanhua Basin, South China. We find evidence for a metastable zone of euxinic (anoxic and sulfidic) waters impinging on the continental shelf and sandwiched within ferruginous [Fe(II)-enriched] deep waters. A stratified ocean with coeval oxic, sulfidic, and ferruginous zones, favored by overall low oceanic sulfate concentrations, was maintained dynamically throughout the Ediacaran Period. Our model reconciles seemingly conflicting geochemical redox conditions proposed previously for Ediacaran deep oceans and helps to explain the patchy temporal record of early metazoan fossils.

Numerous lines of geochemical and stable isotope evidence have indicated that the Ediacaran (635 to 542 million years ago) ocean underwent a stepwise and protracted oxidation [e.g., (*1*–*4*)]. Some geochemical studies suggested that ocean basins were fully oxygenated by the late Ediacaran (*1*, *2*, *4*), yet others provided seemingly conflicting evidence for anoxic deep waters (*5*, *6*), with ferruginous conditions [Fe(II)-enriched] persisting into the Cambrian (*5*). Although a stratified ocean maintained through the Ediacaran Period (*7*) may help reconcile these seemingly conflicting views, the details remain unclear.

The Doushantuo Formation in the Nanhua Basin, South China, presents a unique opportunity to study Ediacaran ocean chemistry across spatial and temporal scales [e.g., (*8*)]. It is composed of a succession of both shallow- and deep-water siliciclastic, carbonate, and phosphatic sedimentary rocks deposited immediately after the last globally extensive Neoproterozoic glacial episode (*9*), widely known as the Marinoan glaciation. Zircon U-Pb ages indicate that the deposition of Doushantuo Formation lasted from ~635 to ~551 million years ago (*10*), spanning most of the Ediacaran Period.

To investigate the marine redox structure, we characterized the composition of sedimentary Fe mineral species and measured S isotope signatures for sulfides and sulfates (*11*) at four sections of Doushantuo Formation, which encompass the full range of sedimentary facies from continental shelf to slope to deep basin (fig. S1). We focused on quantifying the fractional abundance of Fe in several highly reactive mineral species (Fe_{HR}): pyrite (Fe_{Py}), Fe(III) oxides, magnetite, and carbonate minerals relative to total Fe (Fe_T) contents. High Fe_{HR}/Fe_T ratios indicate anoxic conditions (*12*). If anoxic, low associated Fe_{Py}/Fe_{HR} ratios indicate ferruginous bottom waters, whereas high Fe_{Py}/Fe_{HR} points to euxinic conditions, defined as having an anoxic and H_2S-containing water column (*5*, *12*). In most modern and ancient sediments deposited beneath anoxic bottom waters, Fe_{HR}/Fe_T exceeds 0.38, but this threshold value can be reduced to 0.15 [±0.10 (SD)] for thermally altered ancient sedimentary rocks (*13*) such as Doushantuo Formation because of conversion of Fe_{HR} to nonreactive iron during burial. For a euxinic water column, Fe_{Py}/Fe_{HR} in the underlying sediments usually exceeds 0.8 (*12*). Previous Fe speciation data obtained from Paleo- and Mesoproterozoic sedimentary rocks (*14*, *15*) revealed two distinct redox end members in marine basins characterized by either euxinic or ferruginous deep waters (fig. S2). In contrast, the iron speciation data from Doushantuo Formation are not confined to a single end member (Fig. 1A), suggesting nonuniform redox conditions for deep waters of Nanhua Basin.

The inner shelf Jiulongwan section records sedimentary deposition in the shallowest water

[1]Department of Earth Sciences, University of California, Riverside, CA 92521, USA. [2]Department of Earth and Planetary Sciences, Washington University, St. Louis, MO 63130, USA. [3]Department of Geological and Planetary Sciences, California Institute of Technology, Pasadena, CA 91125, USA. [4]State Key Laboratory of Lithospheric Evolution, Institute of Geology and Geophysics, Chinese Academy of Sciences, Beijing 100029, China.

*To whom correspondence should be addressed. E-mail: chaoli@ucr.edu

facies but well below wave base (*3*) and far from shore, along a broad continental shelf. The associated Fe data from this section plot in both the euxinic and ferruginous fields (Fig. 1A); late Ediacaran black shales from this section all plot in the euxinic zone (table S1). In contrast, samples from the Zhongling section, a deeper shelf margin setting, plot mainly in the ferruginous region, with only three samples having Fe_{Py}/Fe_{HR} ratios > 0.8 (Fig. 1A). The deepest water samples from the slope Minle and basinal Longe sections, which are all early Ediacaran black shales, contain very low levels of pyrite (thus low Fe_{Py}/Fe_{HR}) and yield Fe mineral parameters suggesting ferruginous bottom waters. Considering all the data, the paleoenvironmental trends suggest a co-occurrence of euxinic waters on the shelf with ferruginous deep water toward the center of the basin.

Carbonate lithologies dominate the shallow platform of Nanhua Basin, grading into shales in basinal settings (*16*, *17*), reflecting preferential precipitation of carbonates in shallower waters and enhanced hydrodynamic sorting of fine aluminosilicates into deeper waters. Accordingly, a stratigraphic decrease in carbonate content or, inversely, increasing Al content in samples (fig. S3) from the same site broadly reflects increasing water depth with rising sea level. Doushantuo samples exhibit two dominant trends when Fe_{Py}/Fe_{HR} ratios are viewed in light of Al concentration (Fig. 1B). Almost all inner shelf samples show an increase in Fe_{Py}/Fe_{HR} with increasing Al (path A in Fig. 1B), suggesting generally more sulfidic conditions with higher sea levels (greater distance from shore) but ferruginous conditions when sea level was lower. In contrast, most samples from distal sections show a reverse pattern (path B in Fig. 1B), with low Fe_{Py}/Fe_{HR} values found for samples with moderate-to-high Al content [>1 weight % (wt %)] regardless of organic content, suggesting a dominantly ferruginous and thus sulfate-limited deep-water setting. Taken together, these opposing trends can only be explained by a metastable mid–water-column sulfidic zone located between the inner shelf and the shelf margin nested within a ferruginous water mass (Fig. 2). The location and dimensions of this sulfidic zone would have fluctuated temporally. In most cases, euxinia is suggested independently by diagnostic Mo enrichments (fig. S4) above typical crustal values (*4*).

We did not observe direct evidence for oxic shallow waters in the sections that we sampled, although such conditions are expected in shallow settings given appreciable atmospheric O_2 in the Ediacaran atmosphere (*18*) and early benthic animal fossils at shallow sites (*19*–*22*). Therefore, it is likely that the sulfidic and ferruginous zones in the deep anoxic waters persisted beneath shallower oxic and ferruginous layers (Fig. 2).

It is difficult to envisage that a metastable sulfidic water mass could have coexisted with ferruginous deep water for 84 million years without mixing if seawater SO_4^{2-} concentration in Nanhua Basin was high. Net reduction in the surface S inventory may have limited the resupply of sulfate during the Neoproterozoic (*23*), particularly if reduced weathering during the Neoproterozoic glaciations suppressed the riverine flux (*24*). In combination with efficient sulfate removal from seawater through bacterial sulfate reduction and pyrite formation (*24*–*26*), enhanced by hydrothermal release of dissolved iron (*27*) during the glaciations and thereafter, this reduced delivery of sulfate reset Ediacaran ocean chemistry back to the ferruginous conditions (*5*) with extremely low SO_4^{2-} concentrations that have been prevalent in the Archean (*28*). Under such conditions, the continental sulfate supply was exhausted before reaching the deep basinal areas, resulting in a dynamically maintained lateral sulfate concentration gradient from shore to basin (Fig. 2, bottom inset) and, in turn, a metastable euxinic zone. Lack of sufficient sulfate to support extensive organic matter remineralization in distal marine settings is consistent with the large and long-stable pool of organic matter suggested for the deep Ediacaran ocean by the unusual carbon isotope systematics expressed in carbonate rocks and sedimentary organic matter of this age (*1*, *3*, *29*).

Several lines of evidence support the existence of a persistent sulfate concentration gradient in Nanhua Basin. First, larger ratios of organic C to pyrite S (C_{org}/S_{py}) in the distal sections (mean = 34, n = 49) compared with those of the inner shelf site (mean = 4, n = 42), similar to those found under modern low sulfate conditions (*30*), suggest lower sulfate concentrations in the distal regions (fig. S5). Second, an average offset of 30 per mil (‰) in the S isotope composition of pyrite ($\delta^{34}S_{py}$) was observed between most of the inner shelf and shelf margin sections (Fig. 3A), with ^{34}S-enriched pyrites formed in the deeper water settings. Furthermore, differences in S isotope ratios ($\Delta^{34}S$) between coeval carbonate-associated sulfate ($\delta^{34}S_{CAS}$) and $\delta^{34}S_{py}$ were on average ~10‰ lower for the shelf margin (~20‰) compared

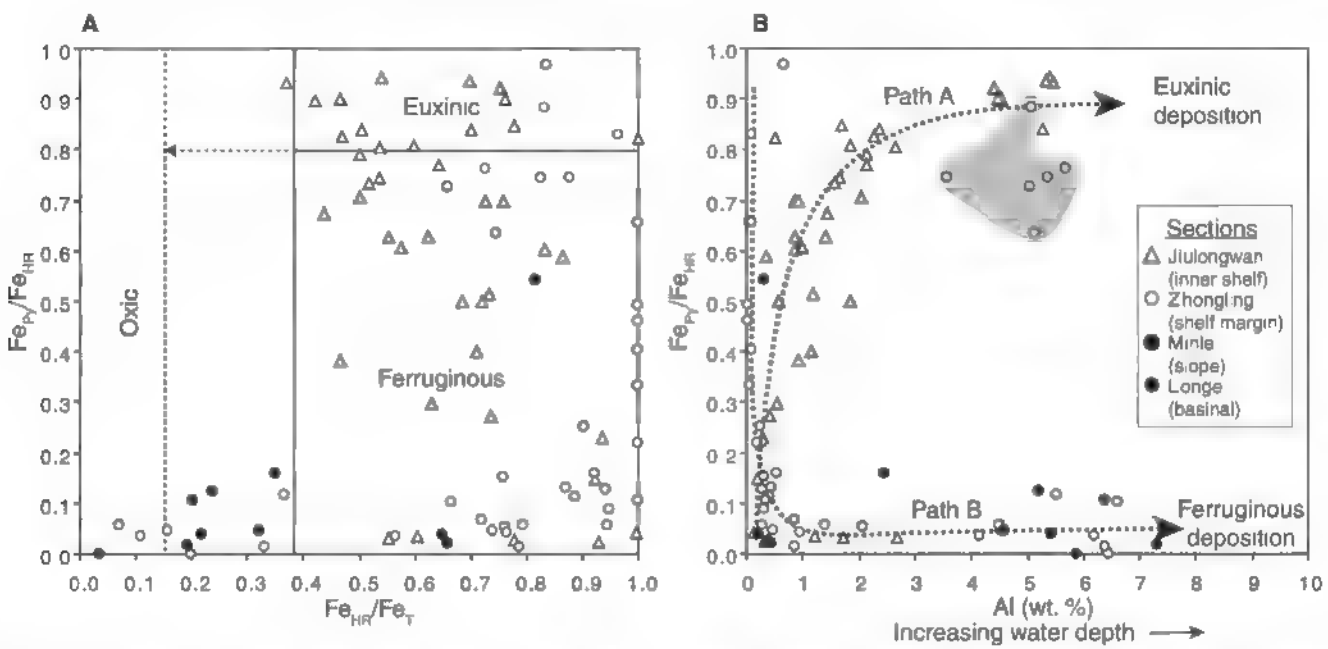

Fig. 1. **(A)** A crossplot of Fe_{Py}/Fe_{HR} versus Fe_{HR}/Fe_T shows a co-occurrence of euxinic with ferruginous conditions for deep waters of Nanhua Basin. Horizontal and vertical (solid for thermally immature and dashed for thermally mature rocks) lines indicate the boundaries for distinguishing euxinic from ferruginous and anoxic from oxic water columns. Dashed lines indicate the most appropriate boundary values for Doushantuo Formation. **(B)** Fe_{Py}/Fe_{HR} versus Al content shows two distinct redox profiles (path A and path B) that constrain the spatial location of the metastable sulfidic water mass to a region between the inner shelf and shelf margin. Samples in the shaded area were deposited in a stratigraphic interval during an early Ediacaran transgressive period and are outliers for path B.

with the inner shelf section (~30‰), suggesting lower SO_4^{2-} concentration availability along the shelf margin (Fig. 3B). Lastly, concentrations of carbonate-associated sulfate were consistently much lower for the shelf margin rocks compared with those from the inner shelf, with concentrations in the deeper sections frequently too low to permit isotopic analysis (table S1).

Modern seawater SO_4^{2-} concentration is ~28 mM, and the isotopic fractionation associated with bacterial sulfate reduction under such high sulfate availability is often large (up to 46‰). In contrast, limited fractionation occurs when sulfate concentration is low, particularly when it falls below a biological threshold of ~200 μM (*28*). These observations provide upper and lower limits for our estimates of SO_4^{2-} concentration in the Ediacaran Nanhua Basin, albeit within a broad range. The $\Delta^{34}S$ in the inner shelf Jiulongwan section increases abruptly from 15‰ in the basal cap carbonate to ~30‰ in the overlying ~40 m and thereafter, with a few samples having $\Delta^{34}S$ > 30‰ in the upper section (Fig. 3B). These trends are consistent with an increase of SO_4^{2-} concentration from <200 μM during post-Marinoan deglaciation to >200 μM thereafter and extending into the late Ediacaran. Although $\Delta^{34}S$ values from the shelf margin section are no more than 24‰, such fractionations are large enough to point to local sulfate levels > 200 μM during the late Ediacaran. The $\Delta^{34}S$ data do not provide a clear upper limit for late Ediacaran sulfate concentrations, but the isotopic and concentration gradients inferred from our study demand a sulfate level that was only a small fraction of the modern 28 mM.

Because the sulfidic zone could expand into previously oxygenated areas of the shelf during transgression and during pulses of high productivity, the generally patchy record of metazoans observed through the Ediacaran (*3*, *19*–*22*) might be explained by fluctuating oceanic redox conditions in and around the continental shelf. The finding of Ediacaran metazoan resting cysts, in the form of large ornamented acritarch fossils most prevalent in lower to middle Ediacaran strata from Doushantuo Formation (*19*) and from Australia and Russia (*22*), has previously been interpreted as an evolutionary response of early benthic metazoans to prolonged episodes of anoxia in shelf and platform bottom waters (*22*). Such a control is broadly consistent with our ocean redox model. For the inner shelf facies of Doushantuo Formation, available data highlight a broad correlation between sedimentary horizons containing the most diverse assemblage of acritarch fossils or animal embryos and intervals with the lowest pyrite contents (fig. S6), suggesting that the presence of hydrogen sulfide, rather than merely the absence of oxygen, hindered colonization of the shelf sea floor by early animals.

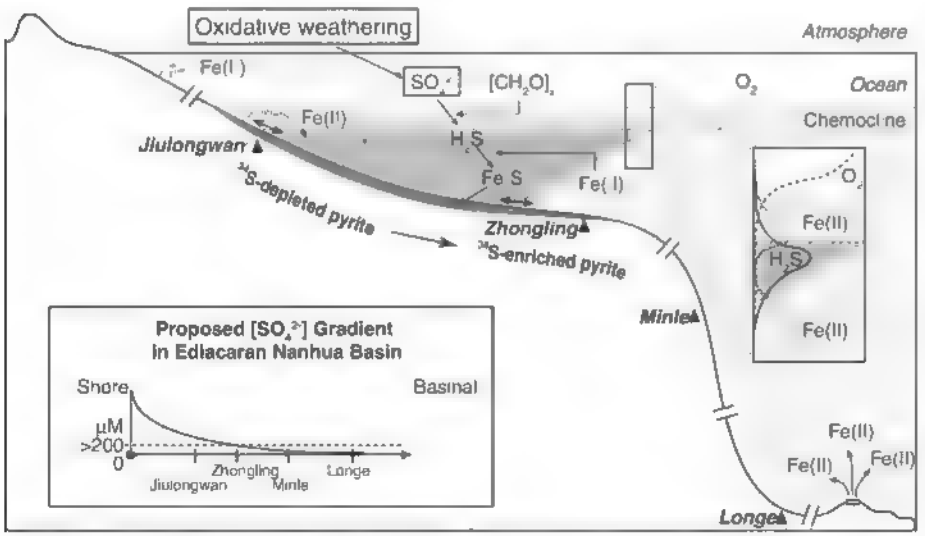

Fig. 2. Schematic representation of a stratified redox model for the Ediacaran Nanhua Basin. Most prevalent is a sulfidic water wedge, located at intermediate water depths within a ferruginous deep water mass and maintained by low riverine sulfate input and consumption of sulfate by bacterial sulfate reduction on the continental shelf. A lateral shore-to-basin sulfate concentration gradient (**bottom inset**) is assumed to be metastable.

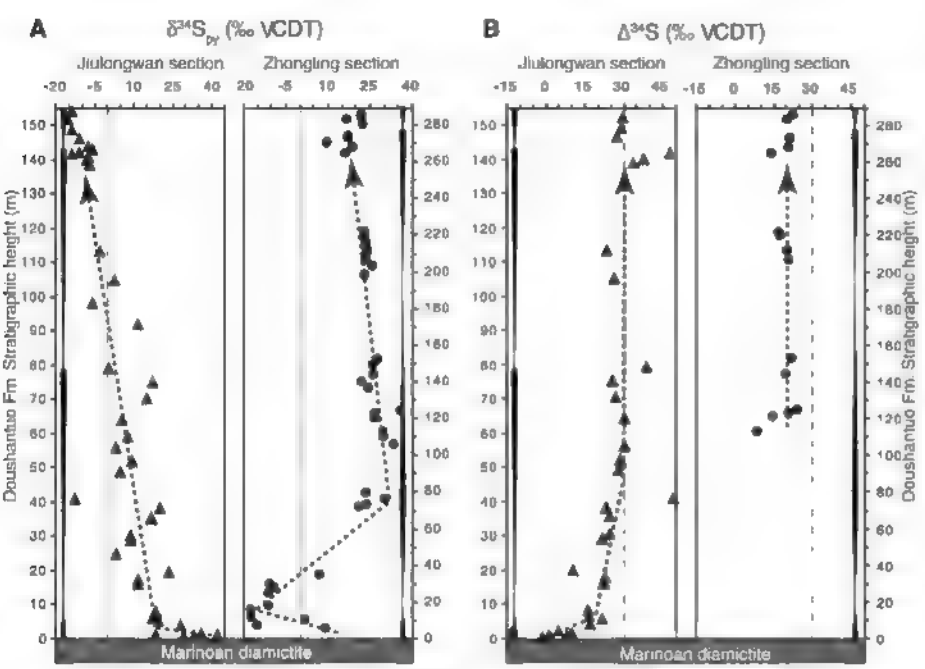

Fig. 3. Chemostratigraphic comparisons of (**A**) $\delta^{34}S_{py}$ and (**B**) $\Delta\delta^{34}S$ for inner shelf (Jiulongwan) and shelf margin (Zhongling) sections. The sections are correlated on the basis of alignment with published sequence stratigraphic data, and three similar transgressive-regressive sedimentary cycles can be identified (*3*, *16*). The lateral S-isotope gradient is also apparent when the sections are aligned by using carbonate C isotope stratigraphy (fig. S7). Values are reported relative to VCDT (Vienna Canon Diablo Troilite) standard.

References and Notes

1. D. A. Fike, J. P. Grotzinger, L. M. Pratt, R. E. Summons, *Nature* **444**, 744 (2006).
2. D. E. Canfield, S. W. Poulton, G. M. Narbonne, *Science* **315**, 92 (2007); published online 7 December 2006 (10.1126/science.1135013).
3. K. A. McFadden *et al.*, *Proc. Natl. Acad. Sci. U.S.A.* **105**, 3197 (2008).
4. C. Scott *et al.*, *Nature* **452**, 456 (2008).
5. D. E. Canfield *et al.*, *Science* **321**, 949 (2008); published online 17 July 2008 (10.1126/science.1154499).
6. Y. Shen, T. Zhang, P. F. Hoffman, *Proc. Natl. Acad. Sci. U.S.A.* **105**, 7376 (2008).
7. G. A. Logan, J. M. Hayes, G. B. Hieshima, R. E. Summons, *Nature* **376**, 53 (1995).
8. G. Jiang, A. J. Kaufman, N. Christie-Blick, S. Zhang, H. Wu, *Earth Planet. Sci. Lett.* **261**, 303 (2007).
9. J. Wang, Z. X. Li, *Precambrian Res.* **122**, 141 (2003).
10. D. Condon *et al.*, *Science* **308**, 95 (2005); published online 24 February 2005 (10.1126/science.1107765).
11. See section of Materials and Methods in supporting material available on *Science* Online.
12. R. Raiswell, D. E. Canfield, *Am. J. Sci.* **298**, 219 (1998).
13. R. Raiswell *et al.*, *Am. J. Sci.* **308**, 105 (2008).
14. Y. Shen, A. H. Knoll, M. R. Walter, *Nature* **423**, 632 (2003).
15. S. W. Poulton, P. W. Fralick, D. E. Canfield, *Nature* **431**, 173 (2004).

16. M. Y. Zhu, J. M. Zhang, A. H. Yang, *Palaeogeogr. Palaeoclimatol. Palaeoecol.* **254**, 7 (2007).
17. E. Vernhet, C. Heubeck, M. Y. Zhu, J. M. Zhang, *Precambrian Res.* **148**, 32 (2006).
18. D. J. Des Marais, H. Strauss, R. E. Summons, J. M. Hayes, *Nature* **359**, 605 (1992).
19. L. Yin *et al.*, *Nature* **446**, 661 (2007).
20. S. Xiao, Y. Zhang, A. H. Knoll, *Nature* **391**, 553 (1998).
21. G. D. Love *et al.*, *Nature* **457**, 718 (2009).
22. P. A. Cohen, A. H. Knoll, R. B. Kodner, *Proc. Natl. Acad. Sci. U.S.A.* **106**, 6519 (2009), and references therein.
23. D. E. Canfield, *Am. J. Sci.* **304**, 839 (2004).
24. J. L. Kirschvink, in *The Proterozoic Biosphere: A Multidisciplinary Study*, J. W. Schopf, C. Klein, D. Des Marais, Eds. (Cambridge Univ. Press, Cambridge, 1992), pp. 51–52.
25. M. T. Hurtgen, M. A. Arthur, N. S. Suits, A. J. Kaufman, *Earth Planet. Sci. Lett.* **203**, 413 (2002).
26. P. Gorjan, J. J. Veevers, M. R. Walter, *Precambrian Res.* **100**, 151 (2000).
27. L. R. Kump, W. E. Seyfried Jr., *Earth Planet. Sci. Lett.* **235**, 654 (2005).
28. K. S. Habicht, M. Gade, B. Thamdrup, P. Berg, D. E. Canfield, *Science* **298**, 2372 (2002).
29. D. H. Rothman, J. M. Hayes, R. E. Summons, *Proc. Natl. Acad. Sci. U.S.A.* **100**, 8124 (2003).
30. R. A. Berner, R. Raiswell, *Geology* **12**, 365 (1984).
31. We are extremely grateful to R. Raiswell, S. Bates, W. Gilhooly, B. Gill, J. Owens, A. Khong, P. Marenco, N. Planavsky, C. Reinhard, M. Rohrssen, C. Scott, S. Severmann, J. Huang, L. Feng, H. Chang, and Q. Zhang for laboratory and field assistance and helpful discussions. The NSF Earth Sciences program (grant EAR-0720362 to G.D.L. and T.W.L. and grant EAR-0719493 to A.L.S.), National Science Foundation of China Fund (grant 40532012 to X.C.), the Chinese Academy of Sciences Fund (grant KZCX3-SW-141 to X.C.), the NASA Astrobiology Institute, and the Agouron Institute provided funding.

Supporting Online Material

www.sciencemag.org/cgi/content/full/science.1182369/DC1
Materials and Methods
Figs. S1 to S7
Table S1
References

23 September 2009; accepted 27 January 2010
Published online 11 February 2010;
10.1126/science.1182369
Include this information when citing this paper.

Mantle Flow Drives the Subsidence of Oceanic Plates

Claudia Adam[1,2]* and Valérie Vidal[3]

The subsidence of the sea floor is generally considered a consequence of its passive cooling and densifying since its formation at the ridge and is therefore regarded as a function of lithospheric age only. However, the lithosphere is defined as the thermal boundary layer of mantle convection, which should thus determine its structure. We examined the evolution of the lithosphere structure and depth along trajectories representative of the underlying mantle flow. We show that along these flow lines, the sea-floor depth varies as the square root of the distance from the ridge (as given by the boundary-layer equation) along the entire plate, without any flattening. Contrary to previous models, no additional heat supply is required at the base of the lithosphere.

At mid-oceanic ridges, hot material rises and then cools while driven away to subduction zones, forming the tectonic plates. The structure of the lithosphere, as the upper thermal boundary layer, is determined by conductive cooling after its formation at the ridge. The lithosphere thickens away from the mid-oceanic ridge and, as rock density increases by cooling, slowly sinks into the underlying mantle. Therefore, the sea-floor depth is regarded as a function of its age only and is studied along trajectories following an age gradient (referred to as "age trajectories"). Several models have been proposed to describe the thermal subsidence of the sea floor with age (*1*–*4*), but no consensus has been reached on the origin of the flattening observed at old ages (*5*). These thermal subsidence models do not directly consider the role of convection in the underlying mantle, which deforms with a velocity on the order of a few centimeters per year. In particular, their description of passive lithosphere cooling ignores any change in plate motion (in other words, in mantle convection).

[1]Institute for Research on Earth Evolution, Japan Agency for Marine-Earth Science and Technology, 2-15 Natsushima, Yokosuka, 237-0061, Japan. [2]Centro de Geofísica, Universidade de Évora, Rua Romão Ramalho 59, 7002 554 Évora, Portugal. [3]Laboratoire de Physique, Université de Lyon, Ecole Normale Supérieure de Lyon–CNRS, 46 Allee d' Italie, 69364 Lyon cedex 07, France.

*To whom correspondence should be addressed. E-mail: adam@uevora.pt

The first model that proposed to explain the variations of sea-floor depth with age—the half-space model (*6*)—considered the lithosphere as the cold upper boundary layer of a cooling mantle, where the depth varies with the square root of the distance from the ridge. By assuming a constant plate velocity, the sea-floor depth varies with the square root of the age of the lithosphere. However, subsequent studies found that the observed sea-floor depth at old ages [>70 million years ago (Ma)] was substantially shallower than the model prediction (*1*, *2*). These studies suggested that the flattening observed at old ages could be accounted for by a model in which the lithosphere is considered as a rigid, cooling conductive plate with a constant basal temperature (plate model) (*2*, *3*, *7*). However, if this constant temperature at the base of the plate is a simple and convenient way to introduce the additional heat supply necessary to explain sea-floor flattening at old ages, there is no physical reason why this should be true for the entire plate. Different physical processes have been proposed to explain the origin of this additional heat supply: small-scale convection (*8*–*11*), upwelling mantle plumes (*12*, *13*), or internal heating, including radiogenic heating as well as the heating from secular cooling (*11*, *14*). Nonetheless, we still do not know which of these physical processes is truly responsible for the observed flattening at old ages.

Previous global models also do not account for possible variations of ridge temperature and depth, either spatial or temporal. Systematic studies of sea-floor subsidence along the East Pacific Rise, for instance, show that the ridge depth varies from 2000 to 3200 m, and the associated subsidence rate from 50 to 450 m/Ma$^{1/2}$ (*15*–*19*). These variations imply spatial mantle temperature variations of about ±100°C (*16*–*18*). Others suggested that the possible change through time of plate motion and plate-driving forces (*20*) [in particular, pulsations in sea-floor spreading rates (*21*), and a higher mean mantle temperature during the Mesozoic (*22*)] could be responsible for higher ridge height and subsidence rate during this period. Estimates of a mantle ~50°C warmer during the Mesozoic, for example, could explain much of the observed flattening relative to a boundary-layer model (*22*).

Regardless of their differences, all previous models are based on the hypothesis that the thermal structure of the oceanic lithosphere is determined entirely by its age—that is, the time elapsed since its creation at the mid-oceanic ridge. However, because mantle convection and plate motion evolve over time, the new thermal conditions imposed on the base of the oceanic lithosphere also change, thus modifying its structure. This lithospheric structure will evolve to adapt to the new thermal conditions imposed at its base, along the entire plate. After a drastic change in the convective system, it will either thicken (or, alternately, become thinner) if the temperature at its base, defined by the new convective system, is cooler (or hotter) than it was previously. After a time long enough (several tens of million years), the lithosphere will tend toward the structure of the thermal boundary layer for the new underlying mantle flow, independently of its initial state.

To test that the structure of the oceanic lithosphere is determined by the underlying mantle convection, we analyzed more than 770 depth profiles, leading to a complete coverage of the Pacific plate (*23*). Several kinematic models have been tested to compute the trajectories representative of the present-day mantle convection (flow lines) (*23*). The Pacific plate is an ideal candidate to test our hypothesis for a number of reasons. First, the Pacific plate velocity has remained constant over the last 47 to 50 million years (My) (*24*), providing sufficient time for the lithosphere to

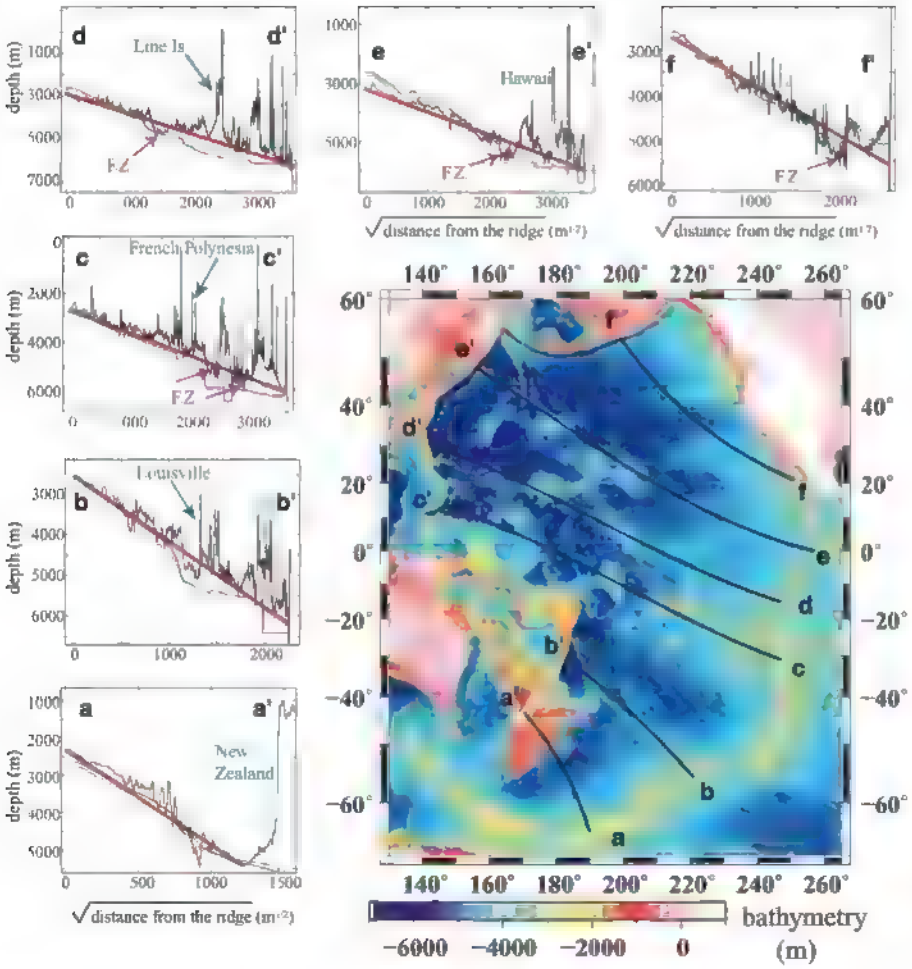

Fig. 1. (Main panel) Bathymetry of the Pacific plate (*27*) corrected for sediment loading and six examples of flow lines aa', bb', cc', dd', ee', and ff' (*23*). **(Side panels)** Profiles along the flow lines indicated in the main panel. Black, sea-floor depth as a function of the square root of the distance from the ridge; red, linear trend $z \propto x^{1/2}$; blue and green, models from (*2*) and (*3*), respectively. Arrows indicate the local geological features responsible for the departure from the linear trend (F.Z. indicates a fracture zone)

adapt to the new thermal conditions. Second, the drastic change in its motion, which is the consequence of a large-scale rearrangement of the mantle convection 47 to 50 million years ago (*24*), has necessarily induced an important change in the thermal conditions applied to the older lithosphere. Therefore, flow lines, which are representative of the underlying mantle convection, strongly differ from age trajectories. Third, the large size of the Pacific plate provides us with the longest observable oceanic lithosphere temporal and spatial evolution on the planet. Finally, because of the strong driving force provided by its slab morphology and trench length, the Pacific has the fastest plate velocity (*25*). If mantle convection is the driving mechanism of sea-floor subsidence, its effects will be most visible over this plate.

Along the flow lines (Fig. 1), we observe a linear relation between the sea-floor depth (z) and the square root of the distance from the ridge ($x^{1/2}$), written as

$$z = z_R + ax^{1/2} \quad (1)$$

where z_R is the ridge depth, and a is the subsidence rate. This relation holds true all along the plate, from the ridge where it forms to the subduction zone where it sinks into the mantle. Departures from the linear trend are localized (Fig. 1) and can be explained by local geophysical processes. The highs are associated with volcanoes (isolated seamounts, hot-spot chains) and swells due to buoyant mantle upwelling (including the South Pacific Superswell). The lows are correlated to the flexure of the lithosphere due to volcano loading or to fracture zones. In all cases, the wavelength of these anomalies is much shorter than the general trend (Fig. 1).

Along the flow lines, no flattening is observed at old ages, far away from the ridge. Despite de-

Fig. 2. (Right) Sea-floor age (*28*), flow lines (black lines), and age trajectories (white lines) (*23*). **(Left)** Depth profiles along the age trajectories. Black, sea-floor depth as a function of the square root of the sea-floor age; red, our model; blue and green, models from (*2*) and (*3*), respectively. Our model (red line) fits the general trend of the bathymetry along the entire plate. Contrary to previous models, there is no need to invoke any flattening at old ages.

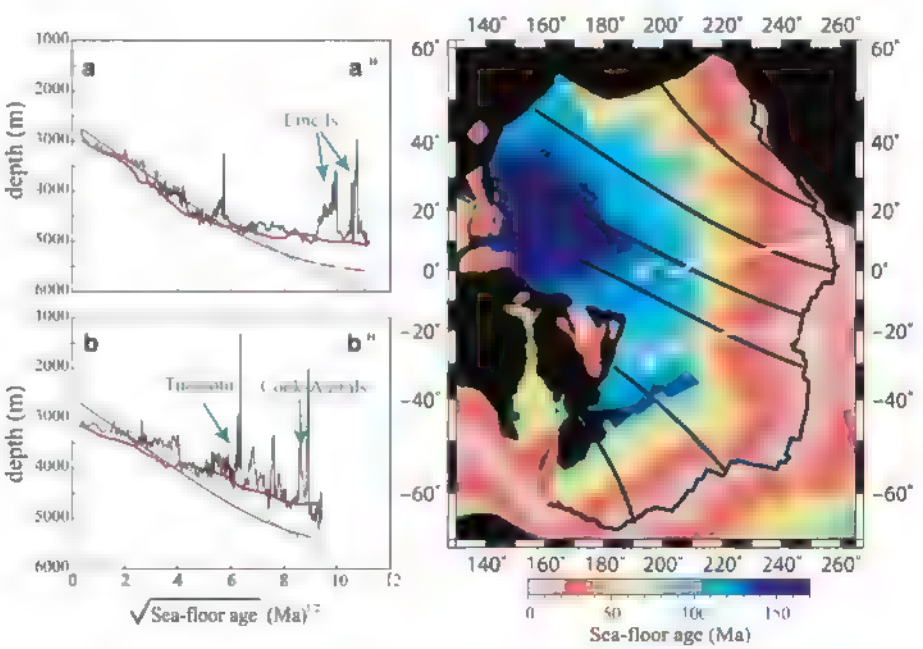

partures from the model due to local processes, the thermal subsidence along the present-day convective motion direction follows the expected trend. Over the Pacific plate, the flow lines strongly differ from the age trajectories (Fig. 2), which is the key point to discriminate our analysis from previous models. Along the age trajectories, the depth profiles represented in Fig. 2 [based on a continuous grid (*23*)] show that there is an apparent flattening. But this flattening is only due to the misleading direction along which the subsidence is investigated. Contrary to previous models (*2*, *3*), our model fits the general trend of the bathymetry along the entire plate. The subsidence rates found in this study vary from 0.5 to 3.5 $m/m^{1/2}$. Rescaling by the constant Pacific plate velocity (9 cm $year^{-1}$) gives values ranging from 200 to 900 $m/Ma^{1/2}$, comparable to the values found in previous studies (*15*, *19*).

The general trend of the sea-floor depth along flow lines, representative of the underlying mantle convection, validates our hypothesis that the lithosphere should be viewed as the upper thermal boundary layer of mantle convection, its true definition (*26*). Because of the steady-state conditions imposed during the last 47 to 50 My (*24*), the Pacific lithosphere had time to readjust, by conduction, to the thermal conditions imposed at its base by the underlying convective mantle. The structure of the lithosphere (and, hence, its thermal subsidence) is therefore driven by the underlying mantle flow. This simple alternative perspective contrasts to the many more complicated explanations that have previously been proposed. In particular, we find that there is no sea-floor flattening at old ages and, therefore, no need to invoke any additional heat supply at the base of the old lithosphere.

References and Notes

1. J. G. Sclater, L. A. Lawver, B. Parsons, *J. Geophys. Res.* **80**, 1031 (1975).
2. B. Parsons, J. G. Sclater, *J. Geophys. Res.* **82**, 803 (1977).
3. C. A. Stein, S. Stein, *Nature* **359**, 123 (1992).
4. M.-P. Doin, L. Fleitout, *Earth Planet. Sci. Lett.* **142**, 121 (1996).
5. M.-P. Doin, L. Fleitout, *Geophys. J. Int.* **143**, 582 (2000).
6. R. L. Parker, D. W. Oldenburg, *Nature* **242**, 137 (1973).
7. A. G. Crosby, D. McKenzie, J. G. Sclater, *Geophys. J. Int.* **166**, 553 (2006).
8. B. Parsons, D. McKenzie, *J. Geophys. Res.* **83**, 4485 (1978).
9. D. A. Yuen, L. Fleitout, *Nature* **313**, 125 (1985).
10. M. A. Eberle, D. W. Forsyth, *Geophys. Res. Lett.* **22**, 473 (1995).
11. J. Huang, S. Zhong, *J. Geophys. Res.* **110**, B05404 (2005).
12. W. Schroeder, *J. Geophys. Res.* **89**, 9873 (1984).
13. G. F. Davies, *J. Geophys. Res.* **93**, 10467 (1988).
14. G. F. Davies, M. A. Richards, *J. Geol.* **100**, 151 (1992).
15. J. C. Marty, A. Cazenave, *Earth Planet. Sci. Lett.* **94**, 301 (1989).
16. B. Lago, A. Cazenave, J. C. Marty, *Phys. Earth Planet. Inter.* **61**, 253 (1990).
17. K. A. Kane, D. E. Hayes, *J. Geophys. Res.* **99**, 21759 (1994).
18. K. Perrot, J. Francheteau, M. Maia, C. Tisseau, *Earth Planet. Sci. Lett.* **160**, 593 (1998).
19. J. R. Cochran, W. R. Buck, *J. Geophys. Res.* **106**, 19233 (2001).
20. C. P. Conrad, C. Lithgow-Bertelloni, *J. Geophys. Res.* **109**, B10407 (2004).
21. S. R. Gaffin, B. C. O'Neill, *Geophys. Res. Lett.* **21**, 1947 (1994).
22. E. Humler, C. Langmuir, V. Daux, *Earth Planet. Sci. Lett.* **173**, 7 (1999).
23. Supporting material is available on *Science* Online.
24. W. D. Sharp, D. A. Clague, *Science* **313**, 1281 (2006).
25. A. E. Gripp, R. G. Gordon, *Geophys. Res. Int.* **150**, 321 (2002).
26. T. Turcotte, G. Schubert, *Geodynamics* (Cambridge Univ. Press, Cambridge, ed. 2, 2002).
27. W. H. F. Smith, D. T. Sandwell, *Science* **277**, 1956 (1997).
28. R. D. Muller, W. R. Roest, J.-Y. Royer, L. M. Gahagan, J. G. Sclater, *J. Geophys. Res.* **102**, 3211 (1997).

29. We thank A. Bonneville, F. Lucazeau, and Y. Fukao for fruitful discussions.

Supporting Online Material

www.sciencemag.org/cgi/content/full/328/5974/83/DC1
SOM Text
Figs. S1 and S2
References

14 December 2009; accepted 18 February 2010
10.1126/science.1185906

Orchestration of Floral Initiation by APETALA1

Kerstin Kaufmann,[1,2]* Frank Wellmer,[3]* Jose M. Muiño,[4] Thilia Ferrier,[5] Samuel E. Wuest,[3] Vijaya Kumar,[6] Antonio Serrano-Mislata,[7] Francisco Madueño,[7] Pawel Krajewski,[8] Elliot M. Meyerowitz,[6] Gerco C. Angenent,[1,9] José Luis Riechmann[5,6,10]†

The MADS-domain transcription factor APETALA1 (AP1) is a key regulator of *Arabidopsis* flower development. To understand the molecular mechanisms underlying AP1 function, we identified its target genes during floral initiation using a combination of gene expression profiling and genome-wide binding studies. Many of its targets encode transcriptional regulators, including known floral repressors. The latter genes are down-regulated by AP1, suggesting that it initiates floral development by abrogating the inhibitory effects of these genes. Although AP1 acts predominantly as a transcriptional repressor during the earliest stages of flower development, at more advanced stages it also activates regulatory genes required for floral organ formation, indicating a dynamic mode of action. Our results further imply that AP1 orchestrates floral initiation by integrating growth, patterning, and hormonal pathways.

Phase transitions in plants require the reprogramming of meristematic identities (*1*). Although several key regulators involved in this process have been identified, their molecular modes of action remain largely elusive. The floral meristem identity gene *APETALA1* (*AP1*) and its paralog *CAULIFLOWER* (*CAL*) control the onset of *Arabidopsis* flower development in a partially redundant manner (*2*). When both genes are mutated, plants do not transition to flowering but instead exhibit massive overproliferation of inflorescence meristems, leading to a cauliflower-like appearance. *AP1* expression is first observed throughout emerging floral primordia and is later confined to the outer whorls of floral buds, where AP1 is involved in the specification of sepals and petals (*3*). Several transcription factors have been identified that bind directly to the *AP1* promoter and control the onset of its expression. These include the floral meristem identity factor LEAFY (LFY) (*4*), the basic leucine zipper (bZIP) protein FD in concert with FLOWERING LOCUS T (FT) (*5*, *6*), as well as members of the SQUAMOSA PROMOTER BINDING PROTEIN-LIKE (SPL) family (*7*, *8*).

Previous studies have provided first insights into AP1 function during early flower development. AP1 directly represses the flowering time genes *SHORT VEGETATIVE PHASE* (*SVP*), *AGAMOUS-LIKE24* (*AGL24*), and *SUPPRESSOR OF OVEREXPRESSION OF CO1* (*SOC1*) in emerging floral primordia (*9*). Furthermore, it represses, directly or indirectly, the shoot identity gene *TERMINAL FLOWER1* (*TFL1*) (*10*), promotes the transcription of *LFY* as part of a positive feedback loop (*10*), and controls the expression of floral homeotic genes (*11*, *12*).

To obtain a detailed understanding of AP1 function during floral initiation, we identified genes that are controlled by it on a genome-wide scale. We used a previously described line expressing a fusion between AP1 and the hormone-binding domain of a glucocorticoid receptor (AP1-GR) in an *ap1 cal* double-mutant

[1]Business Unit Bioscience, Plant Research International, Wageningen 6700 AA, Netherlands. [2]Laboratory of Molecular Biology, Wageningen University, Wageningen 6700 AP, Netherlands. [3]Smurfit Institute of Genetics, Trinity College, Dublin 2, Ireland. [4]Applied Bioinformatics, Plant Research International, Wageningen 6700 AA, Netherlands. [5]Center for Research in Agricultural Genomics (CRAG), Barcelona 08034, Spain. [6]California Institute of Technology, Division of Biology, Pasadena, CA 91125, USA. [7]Instituto de Biología Molecular y Celular de Plantas, Consejo Superior de Investigaciones Científicas–Universidad Politécnica de Valencia, Valencia 46022, Spain. [8]Institute of Plant Genetics, Polish Academy of Sciences, Poznan 60-479, Poland. [9]Centre for BioSystems Genomics (CBSG), Wageningen 6700 AB, Netherlands. [10]Institucio Catalana de Recerca i Estudis Avançats, Barcelona 08010, Spain.

*These authors contributed equally to this work.
†To whom correspondence should be addressed. E-mail: jriechma@caltech.edu

background (*13*). Activation of AP1-GR through treatment with dexamethasone leads to the simultaneous transformation of the inflorescence-like meristems of *ap1 cal* plants into floral primordia. We employed two microarray platforms (*14*) to identify genes that transcriptionally respond within 12 hours after AP1 activation (Fig. 1A) and identified 1366 genes that showed robust expression changes (with a fold change of >1.8 and adjusted *P* value of <0.05) (table S1). Because this set of genes should comprise both direct and indirect targets, we used the same AP1-GR system in chromatin immunoprecipitation (ChIP) experiments with AP1-specific antibodies followed by deep-sequencing (ChIP-Seq) (Fig. 1A and fig. S1) to determine AP1-binding sites on a genome-wide scale. We identified 1942 genomic regions that were significantly enriched in the dataset [with a false discovery rate (FDR) of <0.001] (table S2). In agreement with the observation that these regions were bound by AP1, we found that CArG boxes, the canonical binding motif of MADS-domain transcription factors (*15*), were highly enriched in these sequences (fig. S2). Analysis of the spatial distribution of AP1-binding sites further revealed that they are preferentially located near the transcriptional start site of genes (Fig. 1F). To define a set of potential AP1 targets, we searched for genes that contained one or more binding sites within 3 kb upstream of the 5′ end and 1 kb downstream of the 3′ end of the gene. Using these criteria, we identified 2298 genes as putative AP1 targets (table S2).

It has been demonstrated that in eukaryotes, transcription factor–binding events do not always coincide with changes in transcriptional activity (*16*). A comparison of the microarray and ChIP-Seq results revealed that approximately half (~44%) of the genes in proximity to AP1-binding sites showed expression changes after AP1 activation (fig. S3). However, the transcriptional response of many of these genes was small, and only 249 genes (which we refer to as high-confidence targets) showed robust (>1.8-fold) differential expression (tables S3 and S4). Quantitative reverse transcription polymerase chain reaction and independent ChIP experiments for selected genes confirmed the microarray and ChIP-Seq data (figs. S4 and S5), indicating that the limited overlap between the ChIP-Seq and microarray-selected gene sets was not a result of the methods used.

In agreement with the conjecture that early-response genes are more likely direct AP1 targets than late-response genes (which may include many secondary targets), most of the high-confidence targets were identified as differentially expressed in the earliest time points taken (Fig. 1E). Further evidence for a direct regulation of these genes by AP1 was provided by additional microarray analyses, for which we activated AP1 in the presence of the translational inhibitor cycloheximide (table S5). In these experiments, we found that 44% of the high-confidence targets responded transcriptionally in absence of protein biosynthesis. These results also illustrate the sufficiency of AP1 (in a floral context) to regulate its targets, whereas a comparison of gene expression between *ap1* mutant and wild-type inflorescences provided examples of its necessity for the regulation of high-confidence target genes (table S6).

Although AP1 has only minor or no effects on the expression of many of the genes near which it binds, the preferential location of binding sites in close proximity to transcriptional start sites (Fig. 1F and fig. S6) suggests that at least a subset of these sites may mediate transcriptional responses. Whereas weak transcriptional responses might indicate a role of AP1 in fine-tuning gene expression, some of the genes that did not respond in our experiments may do so when additional cofactors are present. In agreement with this idea, a fraction of those genes showed robust changes in

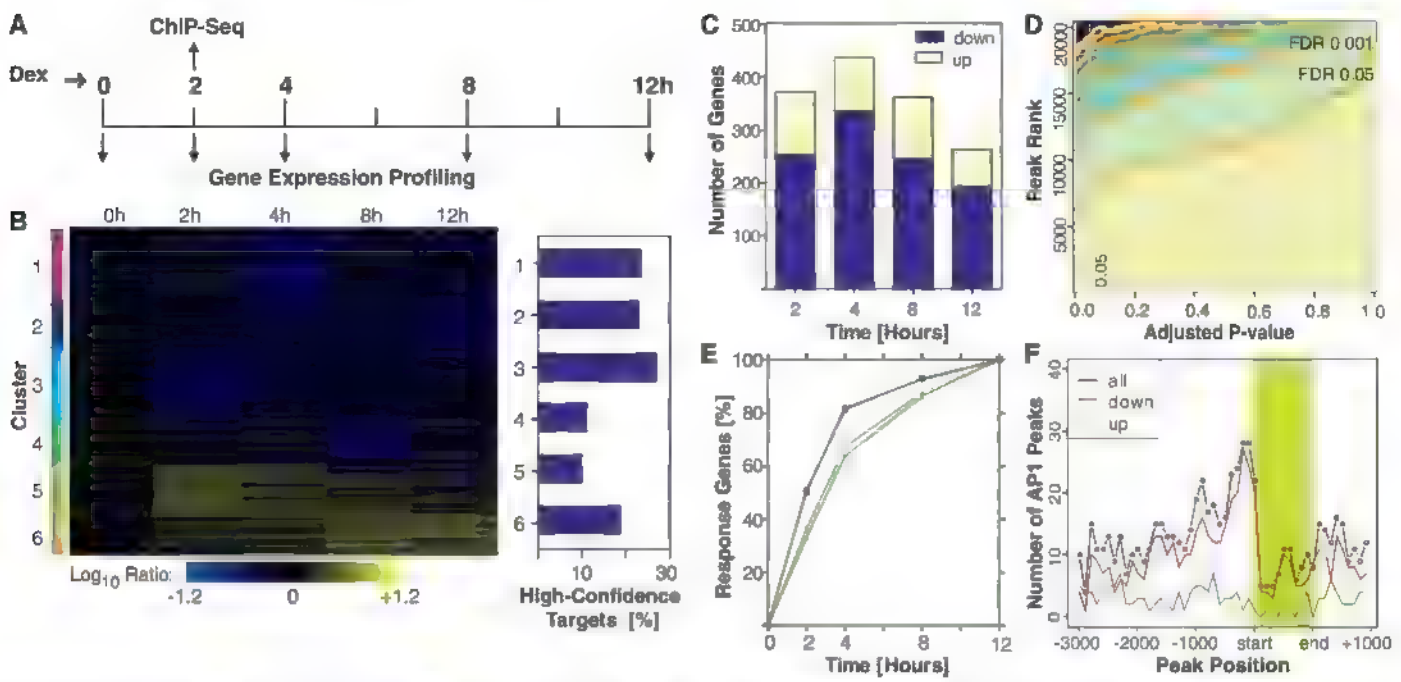

Fig. 1. Overview of results from microarray (Agilent, Santa Clara, California) and ChIP-Seq analyses. **(A)** Experimental setup. **(B)** Gene expression changes after AP1 activation. Cluster analysis was performed by using $\log_{10}$ ratios for 1017 response genes identified by means of microarray analysis. The fraction of high-confidence targets in each cluster is indicated on the right. **(C)** Gene expression changes at different time points after AP1 activation. The numbers of genes that were up- or down-regulated are shown. **(D)** Contour plot showing the relationship between the rank of ChIP-Seq peaks and the adjusted *P* values for differential expression (2-hour time point). Horizontal and vertical white lines indicate FDR and *P* value thresholds, respectively. **(E)** Fraction of response genes identified at different times after AP1 activation. Colored lines indicate results for all response genes (orange), high-confidence targets (black), and response genes excluding high-confidence targets (green). **(F)** Spatial distribution and number of ChIP-Seq peaks in proximity to transcribed regions of differentially expressed genes (identified in the 2-hour time point). To account for different gene sizes, the positions of binding sites within transcribed regions (shaded in green) were calculated relative to their lengths. Colored lines represent results for all differentially expressed genes and genes that were either down- or up-regulated (as indicated).

expression at more advanced stages of flower development (fig. S7) when AP1-GR nuclear accumulation still persisted (fig. S8). Furthermore, members of the family of MADS-domain transcription factors share similar DNA-binding specificities (*15*). Therefore, AP1 might be able to bind to sites that become functional only when they are occupied by other MADS-domain proteins.

Among the high-confidence AP1 targets, we found a strong enrichment of transcription factor–coding genes (25% as compared with ~6% genome-wide) (*17*) (fig. S9 and table S7), indicating that AP1 mediates floral initiation to a large extent by controlling the expression of other transcriptional regulators. Among these genes, several are known to be involved in the control of *AP1* expression. An example is *LFY*, which is directly up-regulated by AP1 (Fig. 2), indicating that the positive feedback loop between AP1 and LFY is mediated by direct interactions. AP1 also represses the flowering time gene *FD*, which is known to be involved in the activation of *AP1* in incipient floral primordia, and its paralog *FDP*. This result is in agreement with the observation that *FD* is repressed at stage 2 of flower development (*5*) and thus shortly after *AP1* expression commences. In a similar fashion, AP1 represses *SPL9*, which encodes another direct activator of *AP1* that is down-regulated in stage 2 flowers (*7*), and its paralog *SPL15* (fig. S10).

We also found that several genes encoding members of the AP2 family of transcription factors, which had been shown previously to act as floral repressors (*18*–*20*), were down-regulated by AP1 (Fig. 2). These include *TARGET OF EAT1* (*TOE1*), *TOE3* and *SCHNARCHZAPFEN* (*SNZ*) but not the closely related *TOE2* or *SCHLAFMÜTZE* (*SMZ*) (fig. S4). It has been suggested that the corresponding factors act redundantly and may prevent flowering in part by directly repressing *AP1* (*20*). Thus, AP1 appears to counteract its own suppression by down-regulating these genes. AP1 also down-regulates *TEMPRANILLO1* (*TEM1*) and *TEM2* (Fig. 2), which code for related transcription factors that contribute to the regulation of flowering through the repression of *FT* expression in leaves (*21*). The finding that these genes are directly repressed by AP1 suggests an additional function for *TEM1*/*TEM2* in the inflorescence meristem. Lastly, we found that AP1 represses the known AP1 antagonist *TFL1* and binds to at least two sites in the 3′ region of the gene (Fig. 2A). The results of genetic analyses confirmed that the region 3′ to *TFL1* is required for proper *TFL1* activity (Fig. 3 and table S8), although we currently do not know whether the AP1-binding sites we identified in it are essential. Taken together, these results indicate that AP1 controls a complex gene regulatory module that ensures and fine-tunes its own expression and that suppresses floral-repressor and shoot-identity genes in emerging floral primordia (Fig. 2 and fig. S10). Furthermore, a global analysis of gene expression changes after AP1 activation revealed that more than 80% of AP1 targets were down-regulated (Fig. 1, B and C, and table S1), indicating that AP1 acts predominantly as a transcriptional repressor during floral initiation.

Shortly after the onset of flower formation, the flowering time genes *AGL24* and *SVP* are down-regulated by AP1 (*9*). Because AGL24 and SVP repress *SEP3*, their down-regulation leads to the induction of *SEP3* expression at stage 2 of flower development (*22*). In addition, AP1 binds to the *SEP3* promoter, and *SEP3* expression is rapidly up-regulated after AP1 activation (fig. S10). Thus, AP1 appears to promote *SEP3* expression through both direct and indirect mechanisms.

It has been proposed that the induction of *SEP3* and the concomitant down-regulation of *AGL24* and *SVP* during early flower development lead to the formation of AP1/SEP3 heterodimers (*11*, *22*, *23*), which are then involved in the activation of floral homeotic genes required for floral organ formation. To test this idea, we compared the ChIP-Seq data for AP1 with those recently obtained for SEP3 in whole inflorescences (*24*). This comparison revealed a large overlap between both their putative target genes (~64% of all genes bound by AP1 also contain SEP3-binding sites) and location of their binding sites (Fig. 4, A and B, and fig. S11), strongly suggesting that they indeed preferentially act together in transcriptional complexes.

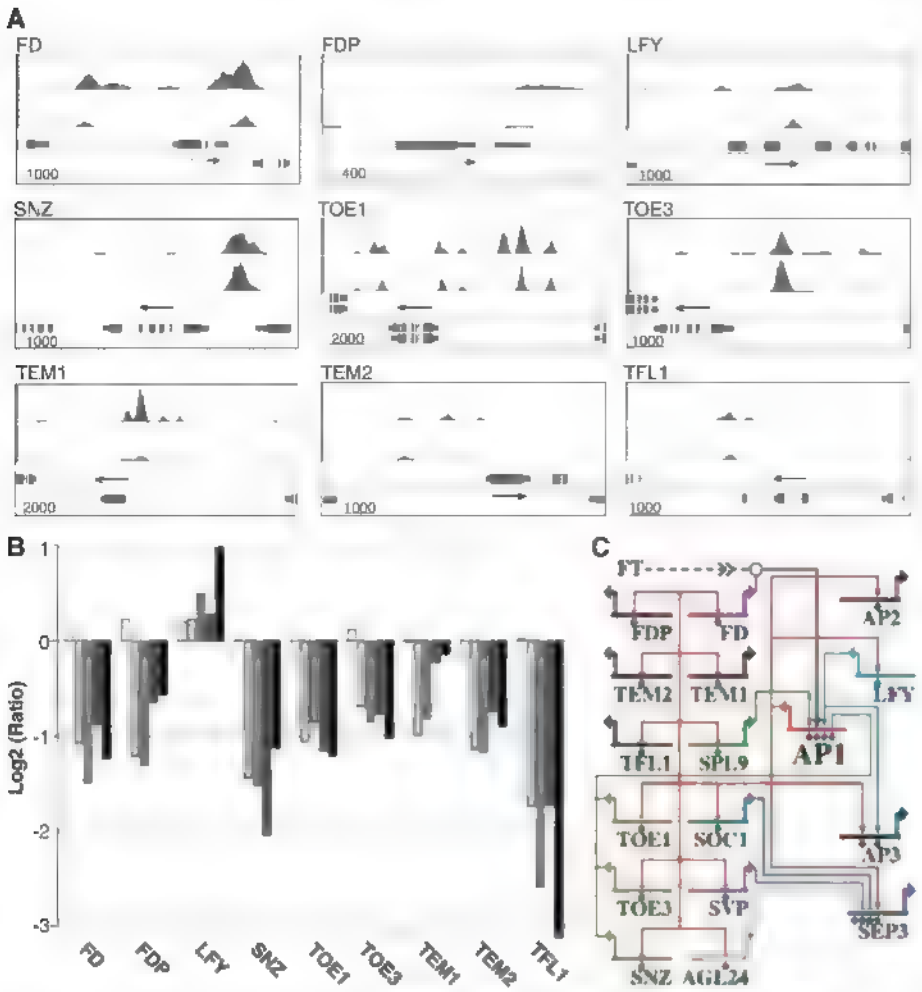

Fig. 2. Selected AP1 target genes. (**A**) ChIP-Seq results for selected targets (as indicated). In each panel, the topmost trace represents AP1 ChIP-Seq data followed by those for SEP3 (*24*), which are shown for comparison. Genes found in the genomic regions analyzed, as well as their exon-intron structure, are indicated in the bottom half of each panel. Scale bars indicate sequence lengths [in base pairs (bp)], and arrows indicate gene orientations. The scale of the *y* axis (peak height) is adjusted for individual traces for visual clarity. (**B**) Transcriptional responses of the genes shown above after AP1 activation. The plot was generated by using $\log_2$ ratios derived from Operon (Huntsville, Alabama) (*TEM2*) and Agilent (all other genes) microarray experiments. Time points are 0 (white bars), 2, 4, 8 (gray scale), and 12 hours (black bars). (**C**) Gene-regulatory network controlled by AP1 during floral initiation. Only selected targets are shown. Arrows indicate gene activation, and blunted lines indicate repression. Blue dots underneath gene symbols indicate direct regulation. The diagram was generated with BioTapestry (*29*).

We further found that common targets of SEP3 and AP1 showed a strong enrichment for genes that are activated during floral organ initiation (Fig. 4C). Thus, AP1/SEP3 heterodimers appear to function predominantly, but not exclusively (*11*, *25*), as transcriptional activators during early flower development.

Floral primordia are initiated at the flanks of the inflorescence meristem. The morphological changes associated with flower primordium formation suggested a possible role of AP1 in regulating cell proliferation. In agreement with this idea, we found that AP1 directly controls the expression of genes with known functions in the control of organ growth. Examples are genes involved in the metabolism of and response to the hormone gibberellin (GA), which affects both cell elongation and proliferation (*26*). AP1 up-regulates *GA3ox1*, which encodes a key enzyme involved in GA biosynthesis. Conversely, AP1 promotes expression of *GA2ox1*, which encodes a GA catabolic enzyme, as well as of *RGA-LIKE2*, which is a known repressor of GA response. Thus, AP1 appears to mediate GA homeostasis in floral primordia through complex interactions. AP1 also directly regulates the expression of genes involved in patterning processes. An example is *ARABIDOPSIS THALIANA HOMEOBOX GENE1*, which is involved in boundary formation (*27*) and has been shown to be also a target of the floral homeotic factor AGAMOUS during the formation of the reproductive floral organs (*28*).

Our results suggest distinct functions of AP1 during the initiation of flower development. AP1 appears to establish floral meristem identity by repressing genes that are part of the shoot developmental program or that control the onset of flowering in part by activating *AP1* itself. It also seems to orchestrate the formation of floral primordia by regulating genes involved in organ growth and patterning. Lastly, at more advanced stages of flower development AP1 initiates downstream pathways required for floral organ specification, most likely in combination with SEP3. Thus, AP1 acts as a true hub in the regulatory network that mediates the switch from floral induction to flower formation.

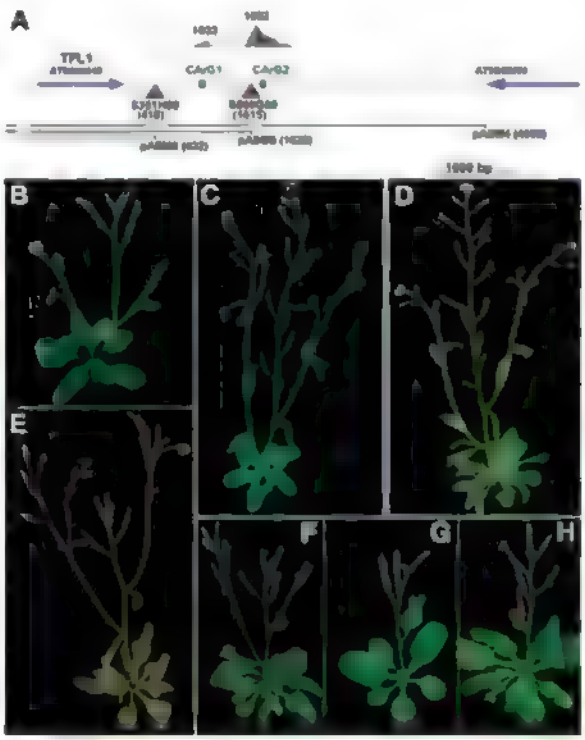

Fig. 3. The genomic region downstream of *TFL1* is required for its function. (**A**) Diagram depicting the *TFL1* genomic region. Coordinates are relative to the last position of the *TFL1* stop codon. Blue arrows indicate gene orientation, green boxes mark two CArG boxes (at positions 1011 and 1756) within AP1 ChIP-Seq peaks, and purple arrowheads indicate the positions of T-DNA insertions. Black lines represent the genomic fragments used for complementation experiments (as indicated). (**B**) *tfl1-1* mutant. The primary inflorescence forms a terminal flower, and secondary inflorescences are replaced by solitary flowers. (**C**) Wild-type plant. Primary and secondary inflorescences show indeterminate growth. (**D**) *tfl1-1* mutant fully rescued by transformation with pASM4. (**E**) *tfl1-1* mutant partially rescued after transformation with pASM8, which lacked one of the AP1-binding sites. (**F**) Plant homozygous for a T-DNA insertion 1615 bp downstream of the *TFL1* stop codon. Although more severe, its phenotype overall resembled that of *tfl1-1* pASM8 plants. (**G**) *tfl1-1* mutant not rescued after transformation with pASM6, which lacked both AP1-binding sites. (**H**) Plant homozygous for a T-DNA insertion 418 bp downstream from the *TFL1* stop codon showing a *tfl1-1* mutant phenotype.

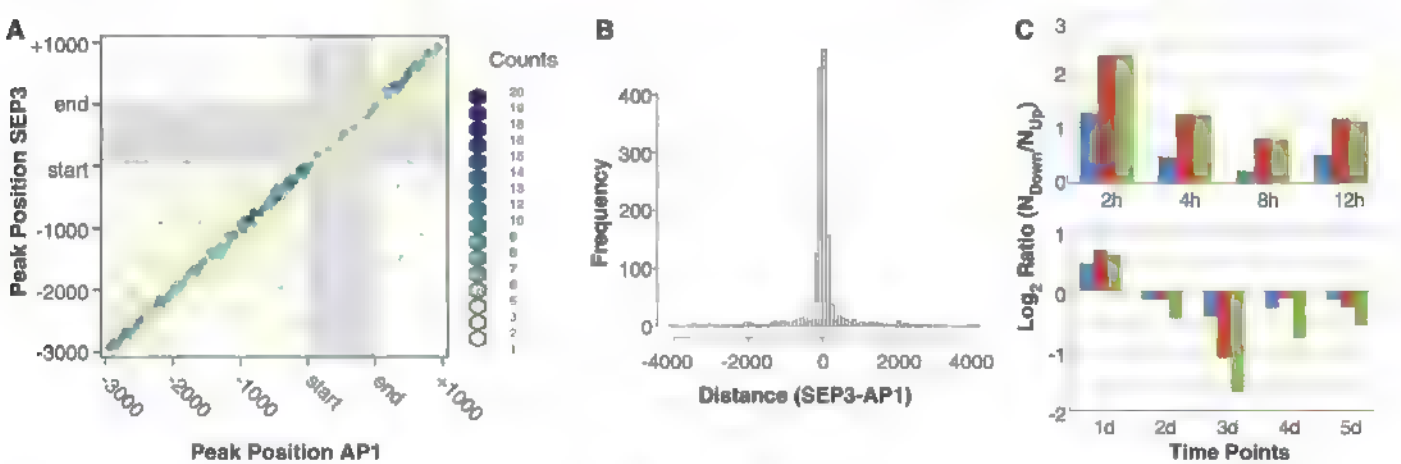

Fig. 4. Spatial distribution of AP1- and SEP3-binding sites. (**A**) Position of SEP3- and AP1-paired ChIP-Seq peaks in common target genes. The paired AP1 peaks depicted in this diagram represent ~87% of all AP1 peaks detected in the set of common target genes (*14*). Binding data for SEP3 were taken from (*24*). Transcribed regions are shaded in gray. Within transcribed regions, peak positions were calculated as a fraction of the gene length (Fig. 1F). The density of peak pairs in the graph is represented with a color scale (counts are the number of peak pairs per area unit). (**B**) Distance distribution of SEP3- and AP1-binding sites in common target genes. Each bar represents a 100-bp window. (**C**) Differential expression of AP1 and SEP3 target genes during early flower development. Log_2 ratios for the number of down- and up-regulated genes were calculated for a given time point after AP1 activation (as indicated). Gene sets analyzed included all differentially expressed genes (blue bars), genes bound by AP1 (red bars), and genes bound by both AP1 and SEP3 (green bars). Expression data analyzed for the bottom panel were taken from (*13*), and the top panel displays data obtained with the same microarray platform (Operon).

References and Notes

1. G. Chuck, S. Hake, *Curr. Opin. Plant Biol.* **8**, 67 (2005)
2. C. Ferrandiz, Q. Gu, R. Martienssen, M. F. Yanofsky, *Development* **127**, 725 (2000)
3. M. A. Mandel, C. Gustafson-Brown, B. Savidge, M. F. Yanofsky, *Nature* **360**, 273 (1992)
4. D. Wagner, R. W. Sablowski, E. M. Meyerowitz, *Science* **285**, 582 (1999)
5. P. A. Wigge *et al.*, *Science* **309**, 1056 (2005)
6. M. Abe *et al.*, *Science* **309**, 1052 (2005)
7. J. W. Wang, B. Czech, D. Weigel, *Cell* **138**, 738 (2009)
8. A. Yamaguchi *et al.*, *Dev. Cell* **17**, 268 (2009)
9. C. Liu *et al.*, *Development* **134**, 1901 (2007).
10. S. J. Liljegren, C. Gustafson-Brown, A. Pinyopich, G. S. Ditta, M. F. Yanofsky, *Plant Cell* **11**, 1007 (1999)
11. V. Gregis, A. Sessa, C. Dorca-Fornell, M. M. Kater, *Plant J.* **60**, 626 (2009)
12. M. Ng, M. F. Yanofsky, *Plant Cell* **13**, 739 (2001)
13. F. Wellmer, M. Alves-Ferreira, A. Dubois, J. L. Riechmann, E. M. Meyerowitz, *PLoS Genet.* **2**, e117 (2006)
14. Materials and methods are available as supporting material on *Science* Online.
15. J. L. Riechmann, M. Wang, E. M. Meyerowitz, *Nucleic Acids Res.* **24**, 3134 (1996)
16. X. Y. Li *et al.*, *PLoS Biol.* **6**, e27 (2008)
17. J. L. Riechmann *et al.*, *Science* **290**, 2105 (2000)
18. M. J. Aukerman, H. Sakai, *Plant Cell* **15**, 2730 (2003)
19. M. Schmid *et al.*, *Development* **130**, 6001 (2003)
20. J. Mathieu *et al.*, *PLoS Biol.* **7**, e1000148 (2009)
21. C. Castillejo, S. Pelaz, *Curr. Biol.* **18**, 1338 (2008)
22. C. Liu, W. Xi, L. Shen, C. Tan, H. Yu, *Dev. Cell* **16**, 711 (2009)
23. V. Gregis, A. Sessa, L. Colombo, M. M. Kater, *Plant J.* **56**, 891 (2008)
24. K. Kaufmann *et al.*, *PLoS Biol.* **7**, e1000090 (2009)
25. V. V. Sridhar, A. Surendrarao, Z. Liu, *Development* **133**, 3159 (2006)
26. P. Achard *et al.*, *Curr. Biol.* **19**, 1188 (2009)
27. C. Gomez-Mena, R. Sablowski, *Plant Cell* **20**, 2059 (2008)
28. C. Gómez-Mena, S. de Folter, M. M. Costa, G. C. Angenent, R. Sablowski, *Development* **132**, 429 (2005)
29. W. J. Longabaugh, E. H. Davidson, H. Bolouri, *Dev. Biol.* **283**, 1 (2005)

30. We are grateful to T. Mastro for help with microarray hybridizations, S. Kushnir for generating AP1 antibodies, Y. Hanzawa and D. Bradley for providing transferred DNA (T-DNA) insertion lines, and E. Graciet for help with AP1-GR detection in nuclear extracts. This work was supported by grants from Science Foundation Ireland (06/IN.1/B851 to F.W.), European Union (EU)–Marie Curie program (Transistor-MRTNCT-2004–512285 to G.C.A. and IRG-224864 to J.L.R.), NSF (2010-0520193 to J.L.R. and E.M.M.), Spanish Ministerio de Ciencia e Innovacion (BFU2008-04251 to J.L.R. and BIO2006-10994 and BIO2009-10876 to F.M.), and by the Millard and Muriel Jacobs Laboratory at Caltech. G.C.A. was also supported by the Netherlands Proteomics Centre and CBSG, which are part of the Netherlands Genomic Initiative. K.K. and J.M.M. were supported by fellowships from the EU–Marie Curie program; J.M.M. was also supported by CBSG and a Horizon grant (#93519020). T.F. was supported by a fellowship from CRAG. Microarray data have been deposited with the National Center for Biotechnology Information Gene Expression Omnibus under accession numbers GSE20184 and GSE20138 and the sequencing data under accession number GSE20176.

Supporting Online Material

www.sciencemag.org/cgi/content/full/328/5974/85/DC1
Materials and Methods
Figs. S1 to S11
Tables S1 to S12
References

26 November 2009; accepted 4 March 2010
10.1126/science.1185244

Maize Tumors Caused by *Ustilago maydis* Require Organ-Specific Genes in Host and Pathogen

David S. Skibbe,[1]* Gunther Doehlemann,[2]* John Fernandes,[1] Virginia Walbot[1]†

Infection of maize by corn smut (*Ustilago maydis*) provides an agronomically important model of biotrophic host-pathogen interactions. After penetration of the maize epidermis, fungal colonization of host tissue induces tumor formation on all aerial maize organs. We hypothesized that transformation of different primordia into plant tumors would require organ-specific gene expression by both host and pathogen and documented these differences by transcriptome profiling. Phenotypic screening of *U. maydis* mutants deleted for genes encoding secreted proteins and maize mutants with organ-specific defects confirmed organ-restricted tumorigenesis. This is the foundation for exploring how individual pathogen effectors, deployed in an organ-specific pattern, interact with host factors to reprogram normal ontogeny into a tumor pathway.

Ustilago maydis, the causal agent of corn smut disease, is a basidiomycete fungus parasitizing only maize and its wild progenitor teosinte (both *Zea mays* L.) (*1*). *U. maydis* elicits large tumors on all aerial organs, where it completes pathogenic development by forming teliospores, its predominant dispersal agent (*1*). Unlike oncogenic agents that reactivate cell division, *U. maydis* is tumorigenic because fungal signals subvert normal programming of proliferating host cells, resulting in an extended period of plant cell division, chromosome endoreduplication, and cell expansion (*2*).

During the arms race with the multilayered plant defense system, plant pathogens such as *U. maydis* evolved a broad molecular repertoire to establish a compatible interaction (*3*). In contrast to necrotrophic pathogens that kill invaded cells and feed on debris, biotrophic pathogens establish an intimate interaction with living hosts (Fig. 1, A and B) by suppressing plant defenses while tapping the nutritional supply of colonized cells. This interaction is maintained by secretion of fungal effector proteins, which either act at the biotrophic interface between pathogen and plant cell or are translocated into the host cytoplasm (*3*). Sequencing of the *U. maydis* genome and transcriptome profiling during seedling infection identified 12 gene clusters encoding primarily uncharacterized, predicted secreted proteins expressed in planta (*4*). Infection assays with maize seedlings identified five of these clusters as functionally involved in tumor formation (*4*).

Extensive analysis of bacterial and oomycete effector proteins has identified several mechanisms for host cell manipulation (*5*); however, to date there is no evidence that the action or expression of any pathogen effector is tailored to individual host tissues. This is surprising because *U. maydis* is tumorigenic in leaves, stems, and flowers, and these organs and constituent maize tissues and cell types express distinctive developmental genes (*6*), as is true in any complex eukaryote. Furthermore, maize mutations that disrupt normal development can enhance or suppress tumor progression (*7*), demonstrating that host developmental status is important in the biotrophic interaction.

To define the genes expressed by maize and *U. maydis* during infections culminating in tumors (Fig. 1, C and D), transcriptomes were assessed on a microarray with probes to ~6700 annotated *U. maydis* genes (*4*), 4941 of which showed only background levels of hybridization with maize RNA in control hybridizations (i.e., high-confidence probes), and 36,800 maize genes, representing most gene models (*8*). Water-injected (mock infection) and fungal-infected organs were evaluated at 1 and 3 dpi (days postinjection) in seedling leaves and at 3 and 9 dpi in adult leaves and tassels (male reproductive inflorescences), as diagrammed in Fig. 1E (*9*).

Confirming previous reports (*10*, *11*), more than 30,000 maize genes were constitutively expressed (from mock 3-dpi samples), plus over 1500 organ-specific genes (table S1). Combined data from all three organs, comparing infected to mock samples, showed that 9207 (25%) unique maize transcripts were up-regulated (Fig. 2A) and 4455 (12%) were expressed only during fungal infection (Fig. 2B). At 3 dpi, *U. maydis* infection altered about one-third of the seedling leaf transcriptome: 4041 types were up-regulated or detected only in the infected sample ("on") (Fig. 2A), and 8111 transcript types were down-regulated or not detected in the infected sample ("off") (Fig. 2C). In adult leaves, more genes were up-regulated or on (6339) (Fig. 2A) than were down-regulated or off (3899) (Fig. 2C). In tassels,

[1]Department of Biology, Stanford University, Stanford, CA 94305-5020, USA. [2]Max Planck Institute for Terrestrial Microbiology, D-35043 Marburg, Germany.

*These authors contributed equally to this work.
†To whom correspondence should be addressed. E-mail: walbot@stanford.edu

only 7% of maize transcripts were altered by *U. maydis*, and the up or on (1118) (Fig. 2A) and down-regulated or off (1436) (Fig. 2C) classes were almost equivalent. Fungal infection alters only one-third as many genes in tassels, showing that formation of floral tumors was accompanied by less reprogramming of development compared to leaves (*12*).

Host responses were primarily organ-specific in both the up- and down-regulated classes. There were only 223 commonly up-regulated (Fig. 2A) and 23 on (Fig. 2B) transcripts. Although many genes were down-regulated or off among organs, only 135 were commonly down-regulated in all infected organs (Fig. 2C). We found differences in expression of defense-related genes in individual organs, e.g., the gene encoding pathogenesis-related protein 10 was strongly induced in seedling leaves but not in adult leaves. Hormone and metabolism genes were also differentially expressed during infection: gibberellic acid-oxidases, auxin transporter *pin1*, and auxin-response *tf-3* were up-regulated in adult but not in seedling leaves. These data establish that maize organs display discrete responses to *U. maydis* infection.

U. maydis expresses many genes during seedling infections, particularly the class encoding secreted proteins, which are not detected during saprophytic fungal growth (*4*). Notably, *U. maydis* exhibits expression patterns specific to infection location (Fig. 2D). Nearly one-third (n =1353) of fungal transcripts were induced in all three organs, with another third (n =1412) present in two organs. Almost 1200 fungal genes were uniquely expressed in adult leaves, with smaller numbers in seedling (n = 296) and tassel (n = 88). That more than 36% of the fungal transcriptome profile is organ-specific at 3 dpi suggests that successful host colonization requires deployment of gene products that can interact with maize proteins characteristic of three distinct developmental states. The specificity of interaction is also true at 9 dpi, when tumors are evident in adult leaves and tassels: In addition to 915 genes in common, *U. maydis* expresses 223 genes specifically in adult leaves and 714 in tassels (table S1).

There are 554 in silico–predicted secretory proteins encoded by *U. maydis*, collectively designated as the secretome (*13*); these are of particular interest for biotrophic fungal development. Most of these proteins were *U. maydis*–specific and lacked similarity to known enzymes (*13*). Of these, 325 were evaluated with high-confidence probes, resulting in the identification of 261 genes that were expressed in at least one infected versus mock sample type at 3 dpi (Fig. 2E). Only 21% (n = 70) of these genes were expressed in all three maize organs at 3 dpi whereas 45% (n = 118) showed organ-specific expression. 28 in seedling leaves, 86 in adult leaves, and 4 in tassels, a trend that continued at 9 dpi (Fig. 2F).

In a complementary approach, phenotypic screening of plant and fungal mutants tested the necessity of organ-specific host and *U. maydis* gene expression to make tumors. Maize mutants with defects in hormone signaling were scored for tumor formation in seedlings, adult leaves, and tassels as summarized in Table 1. *Dwarf8* (*D8*), which is disrupted in gibberellin hormone signaling, has drastically reduced shoot size (*14*). Infected *D8* seedlings support extensive tumor formation but completely lack adult tissue tumors (fig. S1A), indicating that gibberellin signaling is dispensable for tumor formation in seedlings but is indispensable in adult tissues. This observation is also consistent with the transcriptional induction of gibberellic acid-oxidases only in the adult tissue. Furthermore, the auxin hormone response mutant *sparse inflorescence1* (*spi1*) (*15*) shows normal vegetative tumors but essentially no floral tumors. The *Knotted1* (*Kn1*) mutant displays excessive adult leaf growth (*16*) from disrupted gibberellin regulation (*17*); *Kn1* has normal symptom formation in seedlings but displayed more frequent and larger adult leaf tumors and larger tassel tumors (Table 1 and fig. S1, B and C). Three premeiotic male-sterile mutants all produced normal seedling and adult leaf tumors but lacked floral organ tumors (Table 1). These observations demonstrate organ-specific control of tumor progression in maize growth control mutants.

To address the organ-specific role of *U. maydis* secretome proteins, deletion mutants in the SG200 solopathogenic strain for 12 gene clusters encod-

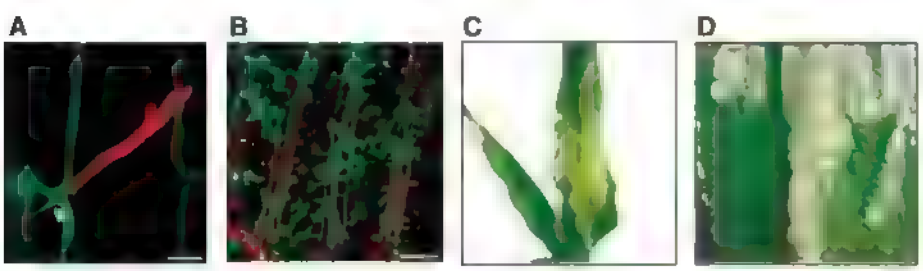

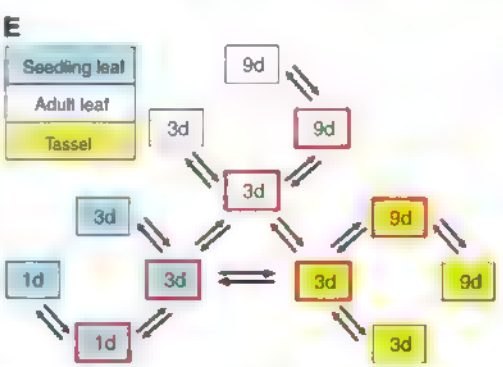

Fig. 1. Analysis of *U. maydis* infection and tumor progression. (**A**) Confocal microscopy at 1 dpi illustrates *U. maydis* hyphae (red) penetrating the seedling leaf epidermis that expresses the plasma-membrane marker PIN1A-YFP (yellow fluorescent protein) 15 (green) (*18*). Arrowhead indicates penetration site. Scale bar, 10 μm. (**B**) At 3 dpi, *U. maydis* hyphae (green, WGA-AF488 stained) proliferate inside seedling leaf tissue (red, plant cell wall autofluorescence). Scale bar, 50 μm. (**C** and **D**) Photographs illustrate the onset of tumor formation at 5 dpi (C) and evident tumors at 9 dpi (D). (**E**) Schema for the RNA profiling experiment. Each arrow represents a paired, two-color hybridization assay; the tail and arrowhead indicating cRNA samples labeled with Cy3 and Cy5 dyes, respectively. Samples were collected from plants injected with either *U. maydis* SG200 (outlined in red) or water at 1, 3, or 9 dpi.

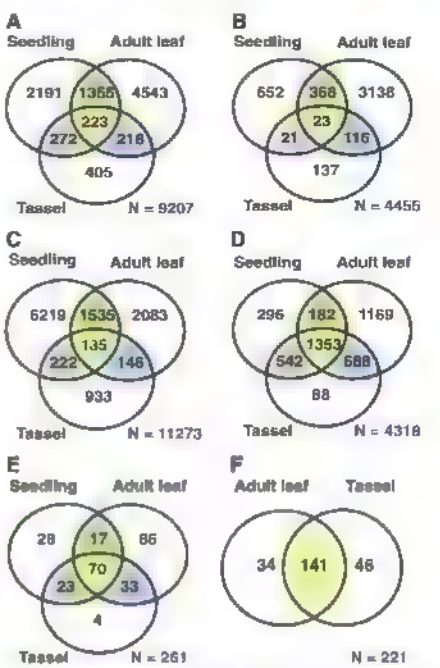

Fig. 2. Analysis of differentially expressed maize and *U. maydis* genes in infected versus mock-infected tissue at 3 dpi. The transcript sets of organ-specific (white), common to all organs (yellow), and shared between organs (green, seedling leaf and adult leaf; blue, adult leaf and tassel; gray, seedling leaf and tassel) are displayed in Venn diagrams. (**A**) Up-regulated plus now detected ("on") maize genes at 3 dpi. (**B**) Maize transcripts "on" at 3 dpi. (**C**) Down-regulated plus not detected ("off") maize genes at 3 dpi. (**D**) *U. maydis* transcripts expressed at 3 dpi. (**E**) *U. maydis* genes encoding secretome proteins at 3 dpi. (**F**) *U. maydis* genes encoding secretome proteins at 9 dpi. Tables S2 to S4 contain additional comparisons.

ing 71 secreted proteins (*4*) were inoculated on adult leaves and tassels of W23 inbred maize. In addition, all 12 mutants were reevaluated in W23 seedlings to confirm previous phenotypes reported on Golden Bantam corn (*4*). Five of the *U. maydis* mutants showed significantly different virulence depending on the organ infected: Δ5B was nonpathogenic (failed to penetrate beyond one cell) on seedlings (*3*) (Table 1); however, in adult leaves at 9 dpi, it caused extensive chlorosis spreading around infection sites indicative of successful fungal penetration (fig. S2C). Δ2A was hypervirulent on seedlings (*4*) but had a lower frequency and smaller tumors in adult leaves and a normal frequency of larger tumors in tassels (Table 1). Δ10A showed reduced frequency and size of seedling and adult leaf tumors but caused developmental arrest of the tassel, which formed no or only a few tiny tumors. The Δ9A mutant showed wild-type frequency of tumors on seedlings but exhibited reduced virulence on adult leaves and, similar to Δ10A, caused developmental arrest in tumor-free tassels (Table 1 and fig. S2, D and E). Most noteworthy are the findings for the Δ19A mutant deleted for 24 secretome proteins. This mutant did not cause any seedling tumors (*4*) but induced formation of tumors at a frequency comparable to that of SG200 in adult leaves and tassel, although the tumors were smaller (Table 1 and fig. S2F).

Consistent with these observations, the genes within the secretome clusters showed quantitative expression differences at 3 dpi in each maize organ (Fig. 3 and table S5). We found 39 organ-specific gene expression differences among the 47 secretome proteins contained in the five clusters with organ-specific phenotypes (Fig. 3). In particular, 15 genes of cluster 19A, which is essential for tumor formation in seedlings but dispensable in adult tissue, showed significantly reduced expression in tassel and adult leaves compared with seedling infections at 3 dpi, whereas only two genes showed increased expression in the tassel relative to seedlings (Fig. 3). In contrast, two genes of cluster 9A, which is more important for symptoms in adult tissue than in seedlings, were expressed at similar levels in all three organs.

Collectively, the gene expression and genetic findings demonstrate organ-specific expression of *U. maydis* effectors, showing essential roles in tumorigenesis. These secretome proteins, which likely constitute the majority of effector molecules eliciting host responses, indicate deployment of different "weapons" tuned to host organ properties. Smut fungi typically infect host seedlings and spread systemically in zones of proliferating cells during plant development; however, they cause symptoms exclusively in inflorescences (*18*). *U. maydis* is unique among smuts in converting leaves and stems into tumors; a larger suite of *U. maydis* genes is involved in tumor formation in vegetative organs than in the tassel. Floral tumors may draw on pathogenic factors that are more highly conserved with other fungi and that could serve general roles during pathogenesis in maize such as the *U. maydis* genes required for fungal penetration of plant cells (*19*).

Individual maize organs express distinctive proteins, and mutations that alter organ development can enhance or repress tumorigenesis by *U. maydis* (*7*) (Table 1). Mirroring the role of host differential gene expression is the unexpected transcriptional plasticity of *U. maydis* during infection of seedlings, adult leaves, and tassels and the observation that some deletion mutants alter tumor formation only in specific organs. We conclude that reprogramming by *U. maydis* may involve dedifferentiation from normal maize cell fates into new pathways, utilizing repression and de novo activation of different developmental programs in each infected proliferative zone.

We propose a model with two phases in this pathogenic interaction. First is establishment of compatibility, which most likely depends on universal pathogenicity factors to suppress plant defenses during fungal penetration (*12*, *20*).

Table 1. Organ-specific susceptibility to *U. maydis* in mutants. The solopathogenic SG200 strain was injected into W23 inbred or mutant maize lines in two greenhouse trials ($n = 16$ or more mutant plants per trial) or in field trials ($n = 20$ male sterile mutants) infected with FB1+FB2 (*7*). Responses in W23 and segregating (1:1) wild-type siblings were used as standards for judging the effect of maize mutants shown in the upper half of the table. Two trials were conducted in the greenhouse and three in the field for the fungal deletion strains in comparison to SG200 in infections of the W23 inbred as shown in the lower half of the table. Symptoms were highly consistent in trials summing to a minimum of $n = 40$ per strain. *U. maydis* symptoms of infection, tumor frequency, and tumor size were scored 10 to 14 dpi (*8*) by two individuals; the mode is reported using a scale of 0 (no tumors), 1 (much fewer or far smaller tumors), 2 (smaller or fewer tumors), 3 (wild type), or 4 (higher frequency or larger than that of the wild type). Scoring integers different from "3" indicates significant differences in symptom formation compared to control experiments. Leaf number and tassel floral area affected (±SD) are reported.

Genetic stock	Adult leaves [ave. no. with tumors (T) or symptoms (S)]	Adult leaf tumors: frequency, size	Tassel tumors (ave. % floral area area affected)	Tassel tumors: frequency, size
Maize				
W23 control	T 4.0 ± 0.4	3, 3	55 ± 5	3, 3
Dwarf8	0*	0, 0	0*	0, 0
spi1	T 4.6 ± 0.8	3, 3	4 ± 2*	1, 1
Kn1	T 4.9 ± 0.8	4, 4	65 ± 11	3, 4
mac1	T 4.0 ± 1.0	3, 3	0*	1, 1 on tassel stem
msca1	T 4.0 ± 0.8	3, 3	0*	1, 1 on tassel stem
ms23	T 4.0 ± 0.8	3, 3	0*	1, 1 on tassel stem
U. maydis				
SG200 control	T 4.7 ± 1.0	3, 3	66 ± 12	3, 3
Δ5B	S 2.0 ± 0.5*	0, 0	0*	0, 0
Δ2A	T 4.6 ± 0.6	2, 2	69 ± 15	3, 4
Δ10A	T 3.0 ± 0.4*	1, 1	4 ± 2*	1, 1
Δ9A	T 4.5 ± 0.3	3, 2	44 ± 10	3, 2
Δ19A	T 4.7 ± 0.6	3, 2	63 ± 13	3, 2

*$P < 0.05$ compared with controls.

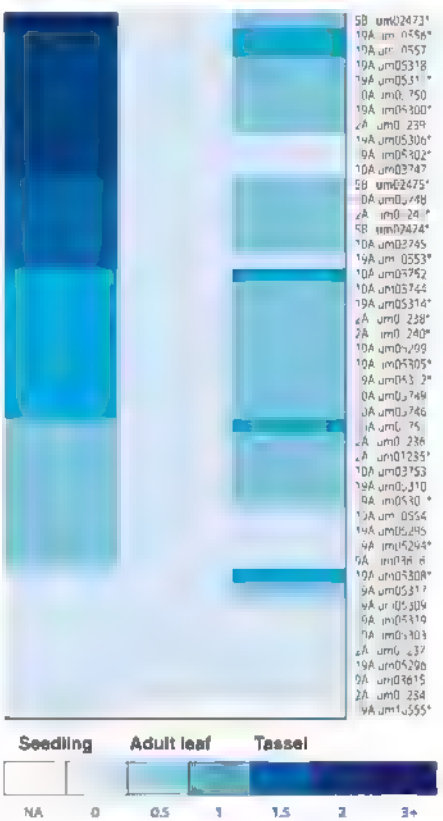

Fig. 3. Organ-specific expression of 47 *U. maydis* secretome genes contained within five gene clusters. The $\log_2$ ratio of normalized intensity divided by minimum normalized intensity for each probe is shown. The relative intensity of each gene among the tissues is displayed by shades of blue. White is used to represent genes without detectable expression. The chromosome and deletion cluster identifier (*4*) followed by the gene name are shown on the right. For the subset of 24 genes chosen for validation, statistically significant differences confirmed by quantitative reverse transcription–polymerase chain reaction are denoted by an asterisk.

Second, disease progression requires response to maize organ-specific properties so that *U. maydis* can tailor effector deployment to redirect physiology and development of a specific organ primordium. Sequential refinement of specificity may be of particular importance in this biotrophic interaction, which lasts 14 days from host penetration to fungal spore release. Within this conceptual framework, the next step is elucidation of distinct fungal and host factors interacting in a tissue-specific and temporal context. This new knowledge will clarify how organ-specific factors modulate biotrophy and, ultimately, tumor formation.

References and Notes

1. F. Banuett, in *Molecular Biology of Fungal Development*, H. D. Osiewacz, Ed. (Dekker, New York, 2002), pp. 349–398.
2. J. A. Callow, *New Phytol.* **75**, 253 (1975).
3. T. Boller, S. Y. He, *Science* **324**, 742 (2009).
4. J. Kämper *et al.*, *Nature* **444**, 97 (2006).
5. P. N. Dodds *et al.*, *New Phytol.* **183**, 993 (2009).
6. J. Ma, D. J. Morrow, J. Fernandes, V. Walbot, *Genome Biol.* **7**, R22 (2006).
7. V. Walbot, D. S. Skibbe, *Sex. Plant Reprod.* **23**, 1 (2010).
8. P. S. Schnable *et al.*, *Science* **326**, 1112 (2009).
9. Materials and methods and supporting materials are available on *Science* Online.
10. D. S. Skibbe, J. F. Fernandes, K. F. Medzihradszky, A. L. Burlingame, V. Walbot, *Plant J.* **59**, 622 (2009).
11. J. Fernandes, D. J. Morrow, P. Casati, V. Walbot, *Plant Biotechnol. J.* **6**, 782 (2008).
12. G. Doehlemann *et al.*, *Plant J.* **56**, 181 (2008).
13. O. Mueller *et al.*, *Fungal Genet. Biol.* **45** (suppl. 1), S63 (2008).
14. J. Peng *et al.*, *Nature* **400**, 256 (1999).
15. S. Barazesh, P. McSteen, *Trends Plant Sci.* **13**, 656 (2008).
16. L. G. Smith, B. Greene, B. Veit, S. Hake, *Development* **116**, 21 (1992).
17. N. Bolduc, S. Hake, *Plant Cell* **21**, 1647 (2009).
18. A. D. Martínez-Espinoza, M. D. García-Pedrajas, S. E. Gold, *Fungal Genet. Biol.* **35**, 1 (2002).
19. G. Doehlemann *et al.*, *PLoS Pathog.* **5**, e1000290 (2009).
20. F. L. W. Takken, W. I. L. Tameling, *Science* **324**, 744 (2009).

21. Research was supported by NSF grant IOS-0852788 (V.W.), the Savitzky Fund (D.S.S.), European Molecular Biology Organization STF program (G.D.), and Deutsche Forschungsgemeinschaft priority program FOR 666. We thank R. Kahmann for *U. maydis* strains. We appreciate critical comments on this manuscript by R. Kahmann, R. Fisher, and M. Barnett. Microarray data have been deposited in Gene Expression Omnibus (GEO) under accession GSE20130.

Supporting Online Material

www.sciencemag.org/cgi/content/full/328/5974/89/DC1
Materials and Methods
References
Figs. S1 and S2
Tables S1 to S6
References

9 December 2009; accepted 2 March 2010
10.1126/science.1185775

Cryptic Sex-Ratio Bias Provides Indirect Genetic Benefits Despite Sexual Conflict

Robert M. Cox* and Ryan Calsbeek

When selection favors sexual dimorphism, high-fitness parents often produce low-fitness progeny of the opposite sex. This sexual conflict is thought to overwhelm the genetic benefits of mate choice because preferred males incur a cost through the production of low-fitness daughters. We provide a counterpoint in a lizard (*Anolis sagrei*) that exhibits sexual conflict over body size. By using mate-choice experiments, we show that female brown anoles produce more sons than daughters via large sires but more daughters than sons via small sires. Measures of progeny fitness in the wild suggest that maximal fitness payoffs can be achieved by shifting offspring production from daughters to sons as sire size increases. These results illustrate how the resolution of sexual conflict can restore the genetic benefits of mate choice.

Because of their divergent reproductive roles, males and females often experience different selection pressures acting on the same phenotypic traits (*1*). However, sharing a common genome constrains the sexes from evolving independently in response to these antagonistic selection pressures (*2*–*4*). This can result in a genomic tug of war referred to as intralocus sexual conflict (*5*–*7*). When such conflict is widespread throughout the genome, high-fitness parents may actually produce low-fitness progeny of the opposite sex (*8*–*14*). This outcome can override the potential genetic benefits of mate choice because preferred males incur a net fitness cost through the production of low-fitness daughters (*8*–*10*). When sire genotypes have differential fitness effects on sons versus daughters, females are predicted to alter progeny sex ratio accordingly (*15*). We tested whether progeny sex-ratio bias can facilitate the sex-specific inheritance of good genes, thereby preserving the genetic benefits of mate choice in the face of sexual conflict.

Department of Biological Sciences, Dartmouth College, Hanover, NH 03755, USA.

*To whom correspondence should be addressed. E-mail: robert.m.cox@dartmouth.edu

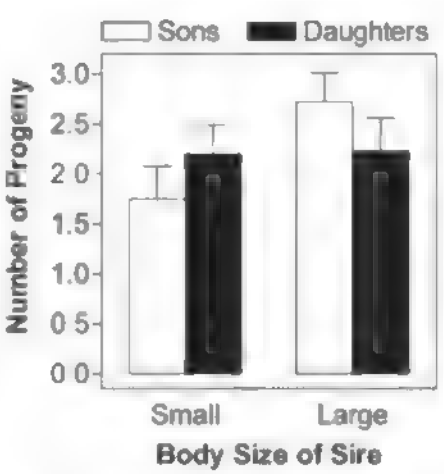

Fig. 1. Female anoles bias progeny sex ratio as a function of sire body size. Data are least-squares means ± 1 SEM from analyses weighted by the total number of progeny produced by each dam-sire pair. Size is dichotomized relative to the population mean.

The brown anole lizard (*Anolis sagrei*) exhibits signatures of intralocus sexual conflict over body size (fig. S1). On average, adult males are 30% longer and 150% heavier than adult females (*16*). Selection creates the potential for sexual conflict by favoring large size in males and intermediate size in females (*17*). However, anoles have also evolved several mechanisms that may resolve this conflict. First, body size and other morphological traits are heritable within each sex but exhibit negative genetic correlations between the sexes (*18*). Second, paternity analyses of wild populations reveal that females produce more sons via large sires but more daughters via small sires (*18*). This suggests a form of cryptic sex-ratio bias that may allow females to adaptively sort genes with sex-specific fitness effects into sons and daughters.

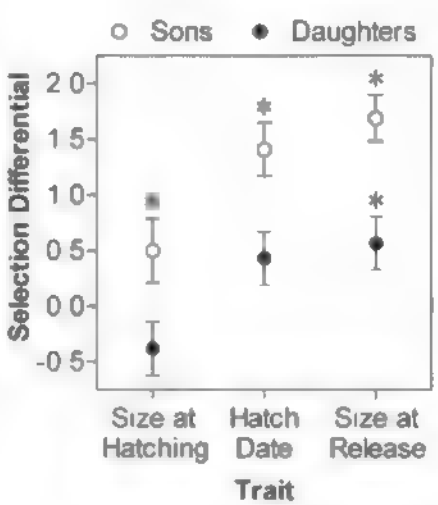

Fig. 2. Natural selection on three phenotypic traits differs between male and female progeny. Data are selection differentials ± 1 SEM derived from regressions of relative survival on trait values standardized to the population mean in unit variance. Asterisks indicate statistical significance ($P < 0.05$) on the basis of logistic regression.

Because it is unknown whether this sex-ratio bias actually increases progeny fitness, we mated females to males of varying sizes, assigned paternity to their progeny, and then measured the fitness of these sons and daughters in the wild (*19*). Because the hypothesized fitness advantage of sex-ratio bias requires indirect genetic benefits, we hatched and raised all sires to adult size in a laboratory common garden to minimize nongenetic variation in body size. We provided each dam with two potential sires, paired such that some dyads consisted of two males of similar size whereas others consisted of two males of disparate sizes. We allowed dams to assess both males together for several days and then permitted each male to mate exclusively with the dam for 1 week to prevent direct male-male interactions from influencing mating success.

Overall, dams produced a balanced sex ratio (111 sons, 101 daughters, $\chi^2 = 0.47$; $P = 0.49$). However, as predicted by sexual conflict theory (*12*, *13*, *18*), dams produced relatively more sons with large sires and more daughters with small sires (sex × sire size: $F_{1,72} = 4.23$; $P = 0.043$) (Fig. 1). This bias became stronger when we increased the dichotomy between small and large sires by excluding males of intermediate size that fell within ±0.25 SD (±1 mm) of the population mean (sex × sire size: $F_{1,47} = 9.07$; $P = 0.004$). This confirms the pattern previously observed in wild populations (*18*) and suggests a refined form of cryptic fertilization bias. Moreover, this bias was driven primarily by the differential production of sons ($F_{1,72} = 4.95$, $P = 0.029$), rather than daughters ($F_{1,72} = 0.01$; $P = 0.945$), with sires of different sizes (Fig. 1). Therefore, we predicted that the fitness of sons in particular should be strongly tied to body size and positively correlated with the size of the sire.

To test these predictions, we released progeny from our breeding experiment into their natural habitat and followed their survival over 8 months to measure natural selection acting on juvenile phenotypes (Fig. 2). In both sexes, viability selection favored early hatch date ($\beta = 0.86 \pm 0.17$; $\chi^2 = 25.15$; $P < 0.001$) and large body size at release ($\beta = 1.06 \pm 0.16$, $\chi^2 = 35.81$; $P < 0.001$). However, this selection was significantly stronger for sons than it was for daughters (sex × hatch date: $\chi^2 = 7.55$, $P = 0.006$, sex × size at release: $\chi^2 = 8.82$, $P = 0.003$). Moreover, selection on size at hatching exhibited sexual antagonism, favoring large sons and small daughters (sex × size at hatching: $\chi^2 = 6.41$; $P = 0.011$) (Fig. 2). Collectively, these patterns of phenotypic selection indicate that large size and early hatch date are particularly important for the survival of sons, as predicted from patterns of cryptic sex-ratio bias.

To directly assess the adaptive value of cryptic sex-ratio bias, we examined the fitness of progeny as a function of sire body size. As predicted, survival of sons increased with sire size ($\chi^2 = 7.21$; $P = 0.007$). By contrast, survival of daughters was unrelated to sire size ($\chi^2 = 1.09$; $P = 0.30$). The resulting fitness functions (Fig. 3) reveal that maximal fitness payoffs are achieved by shifting progeny sex ratio from female-biased to male-biased as sire size increases. This suggests an adaptive function for sex-ratio bias, as previously hypothesized (*17*). However, sex-ratio bias at hatching could also arise as a non-adaptive by-product if small males sire sons with reduced embryonic viability. Given the fitness functions in Fig. 3, we favor an adaptive explanation, although it would be informative to generate analogous fitness functions for embryonic viability.

To date, adaptive interpretations of sex-ratio bias have been based on the assumption that fitness is negatively heritable from sire to daughter (*18*), as typically observed in the face of intralocus sexual conflict (*8*–*14*). By contrast, our data suggest that the fitness of daughters is independent of sire size. This implies that cryptic sex-ratio bias has not evolved to avoid the production of low-quality daughters but as a means of obtaining genetic benefits that are sex-specific to sons. This raises the question of why females mate with small males. In part, this reflects the nature of our experimental design, which constrained many females to mate only with small males (*19*). Those females that were given a choice between small and large males produced nearly twice as many total progeny with large sires (mean of 1.7 progenies) as they did with small sires (0.9 progeny; $F_{1,64} = 2.90$; $P = 0.09$). This suggests that females prefer large sires for all of their progeny, which is expected on the basis of progeny fitness functions (Fig. 3). Field studies of this and other territorial *Anolis* species indicate that females mate almost exclusively (95 to 98% of copulations) with males on whose territories they reside, displaying little precopulatory mate choice with respect to male phenotype (*20*, *21*). Our data suggest that, through post-copulatory control over progeny sex ratio, females can nonetheless minimize the production of low-quality sons when mating with small males.

Unexpectedly, although the survival of progeny was positively related to the size of the sire ($\chi^2 = 12.17$; $P < 0.001$), it was negatively related to the size of the dam ($\chi^2 = 8.09$; $P = 0.005$; Fig. 4). In particular, small dams that mated with large sires produced progeny with higher survival than any other combination of parental phenotypes ($\chi^2 = 14.49$, $P = 0.002$). This illustrates how intralocus sexual conflict can extend beyond sex differences in selection for adult viability and reproductive success and include the antagonistic effects of progeny survival on adult phenotypes. This form of intralocus sexual conflict may have been previously overlooked because of the lack of detailed pedigrees and intergenerational measures of fitness (*1*).

We note several important differences between brown anoles and other species (*8*–*10*) in which the costs of sexual conflict overwhelm the genetic benefits of mate choice. First, brown anoles exhibit strong intergenerational links between

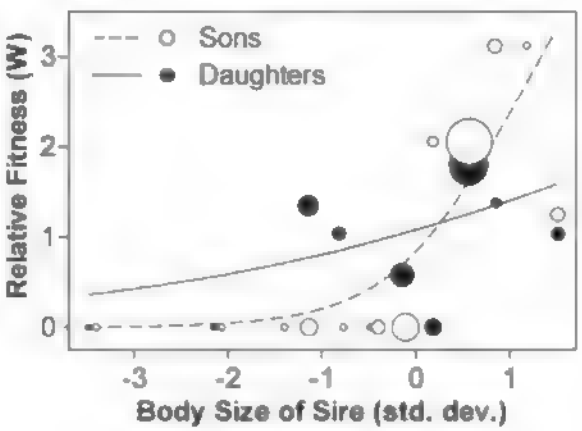

Fig. 3. Sex-specific fitness payoffs favor a transition from production of daughters to sons as sire body size increases. Body size is expressed in unit variance relative to the population mean. Data points report relative fitness for each increment of sire body size, calculated by dividing the mean probability of survival at each size by the overall probability of survival within each sex. The size of each point is proportional to the number of progeny (range from 1 to 15) produced by sires of that size. Fitness functions are best-fit cubic splines with standard errors omitted for clarity.

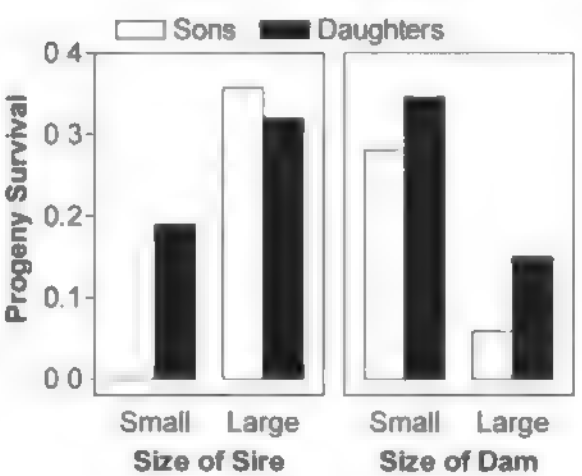

Fig. 4. Large sires had progeny with high survival (**left**), whereas large dams had progeny with low survival (**right**). Size is dichotomized relative to the separate population means for sires and dams.

the fitness of sires and sons. Natural selection favors large size in adult males (*17*), and dams produce more sons via large sires [Fig. 1 and (*8*)]. Body size is heritable from sire to son (*18*), and selection on juvenile viability favors large size and early hatch date in male progeny (Fig. 2). Consequently, large sires have high adult fitness and produce sons with high juvenile fitness (Fig. 3). Given the heritability of adult body size (*18*), large sires presumably also produce sons with high adult fitness. This differs from systems in which fitness is not heritable within males (*9*, *11*) because of the accumulation of sexually antagonistic genes on the X chromosome (*10*, *22*, *23*), which does not pass from sire to son. The mechanism of sex determination is unknown in brown anoles, but related *Anolis* species exhibit XY and XXY male heterogamety or genetic sex determination without heteromorphic sex chromosomes (*24*, *25*).

Second, in other species, males with high fitness often sire daughters with low fitness (*8*, *13*). This negative intersexual heritability of fitness may be common when sexually antagonistic X-linked genes are inherited from sire to daughter (*8*, *10*). However, the outcome of good-genes mate choice is complex and likely varies with patterns of sex linkage (*26*). Moreover, intersexual genetic correlations are often reduced or negative for sexually dimorphic traits (*27*–*29*), and the intersexual genetic correlation for body size is actually negative in brown anoles (*18*). This suggests that potential sexual conflict over body size has been largely resolved. Indeed, we found no evidence that large sires produce low-fitness daughters (Fig. 3). In this situation, any potential genetic benefits of mate choice should be preserved, contrary to the situation when high-fitness sires produce low-fitness daughters (*9*–*11*).

Our study suggests that indirect genetic benefits can be obtained even in the face of intralocus sexual conflict. However, this outcome is likely contingent on the evolution of mechanisms that resolve sexual conflict, thereby facilitating sex-specific inheritance and expression of good genes. In brown anoles, these mechanisms may include cryptic sex-ratio bias, which would allow females to preferentially produce high-fitness sons, and negative intersexual genetic correlations, which would mitigate the potential costs of producing low-fitness daughters. Because the underlying physiological mechanisms that produce cryptic sex-ratio bias are presently unknown, we cannot reject the alternative that this bias reflects differential embryonic mortality of sons and daughters with respect to sire size. Given the emerging perspective that intralocus sexual conflict can maintain genetic variation and constrain evolution via mate choice (*8*–*10*), further investigation of these mechanisms should clarify the implications of sexual conflict for a variety of fundamental evolutionary processes.

References and Notes

1. R. M. Cox, R. Calsbeek, *Am. Nat.* **173**, 176 (2009).
2. R. Lande, *Evolution* **34**, 292 (1980).
3. L. F. Delph, J. L. Gehring, F. M. Frey, A. M. Arntz, M. Levri, *Evolution* **58**, 1936 (2004).
4. D. J. Fairbairn, D. A. Roff, *Heredity* **97**, 319 (2006).
5. S. Bedhomme, A. K. Chippindale, in *Sex, Size and Gender Roles: Evolutionary Studies of Sexual Size Dimorphism*, D. J. Fairbairn, W. U. Blanckenhorn, T. Szekely, Eds. (Oxford Univ. Press, Oxford, 2007), pp. 185–194.
6. T. Chapman, G. Arnqvist, J. Bangham, L. Rowe, *Trends Ecol. Evol.* **18**, 41 (2003).
7. G. Arnqvist, L. Rowe, *Sexual Conflict* (Monographs in Behavior and Ecology, Princeton Univ. Press, Princeton, NJ, 2000).
8. K. Foerster *et al.*, *Nature* **447**, 1107 (2007).
9. A. Pischedda, A. K. Chippindale, *PLoS Biol.* **4**, e356 (2006).
10. T. Connallon, E. Jakubowski, *Evolution* **63**, 2179 (2009).
11. K. M. Fedorka, T. A. Mousseau, *Nature* **429**, 65 (2004).
12. A. K. Chippindale, J. R. Gibson, W. R. Rice, *Proc. Natl. Acad. Sci. U.S.A.* **98**, 1671 (2001).
13. R. Calsbeek, B. Sinervo, *J. Evol. Biol.* **17**, 464 (2004).
14. W. R. Rice, A. K. Chippindale, *J. Evol. Biol.* **14**, 865 (2001).
15. S. R. Pryke, S. C. Griffith, *Science* **323**, 1605 (2009).
16. R. M. Cox, D. S. Stenquist, R. Calsbeek, *J. Evol. Biol.* **22**, 1586 (2009).
17. R. M. Cox, R. Calsbeek, *Evolution* **64**, 798 (2010).
18. R. Calsbeek, C. Bonneaud, *Evolution* **62**, 1137 (2008).
19. Materials and methods are available as supporting material on *Science* Online.
20. R. R. Tokarz, *Herpetologica* **54**, 388 (1998).
21. R. L. Trivers, *Evolution* **30**, 253 (1976).
22. W. F. Rice, *Evolution* **38**, 735 (1984).
23. J. R. Gibson, A. K. Chippindale, W. R. Rice, *Proc. Biol. Sci.* **269**, 499 (2002).
24. G. C. Gorman, L. Atkins, *Am. Nat.* **100**, 579 (1966).
25. F. J. Janzen, P. C. Phillips, *J. Evol. Biol.* **19**, 1775 (2006).
26. M. Kirkpatrick, D. W. Hall, *Evolution* **58**, 683 (2004).
27. R. Bonduriansky, L. Rowe, *Evolution* **59**, 1965 (2005).
28. E. I. Svensson, A. G. McAdam, B. Sinervo, *Evolution* **63**, 3124 (2009).
29. J. Poissant, A. J. Wilson, D. W. Coltman, *Evolution* **64**, 97 (2010).

30. We thank M. C. Duryea and M. Najarro for genotyping samples and conducting paternity analyses and M. Callahan, D. Cheney, and L. Symes for assistance with mating trails and animal care. M. C. Duryea, S. Kuchta, M. Logan, M. Najarro, and D. Urbach provided comments on the manuscript. Research was conducted under permits from the Bahamas Ministry of Agriculture and approval from the Dartmouth College Institutional Animal Care and Use Committee (protocol 07-02-03). An award from NSF (DEB 0816862 to R. Calsbeek) and funding from Dartmouth College provided financial support.

Supporting Online Material

www.sciencemag.org/cgi/content/full/science.1185550/DC1
Materials and Methods
Fig. S1
References

4 December 2009; accepted 23 February 2010
Published online 4 March 2010;
10.1126/science.1185550
Include this information when citing this paper.

Partitioning of Histone H3-H4 Tetramers During DNA Replication–Dependent Chromatin Assembly

Mo Xu,[1,2]* Chengzu Long,[2]* Xiuzhen Chen,[3,2] Chang Huang,[4,2] She Chen,[2]† Bing Zhu[2]†

Semiconservative DNA replication ensures the faithful duplication of genetic information during cell divisions. However, how epigenetic information carried by histone modifications propagates through mitotic divisions remains elusive. To address this question, the DNA replication–dependent nucleosome partition pattern must be clarified. Here, we report significant amounts of H3.3-H4 tetramers split in vivo, whereas most H3.1-H4 tetramers remained intact. Inhibiting DNA replication–dependent deposition greatly reduced the level of splitting events, which suggests that (i) the replication-independent H3.3 deposition pathway proceeds largely by cooperatively incorporating two new H3.3-H4 dimers and (ii) the majority of splitting events occurred during replication-dependent deposition. Our results support the idea that "silent" histone modifications within large heterochromatic regions are maintained by copying modifications from neighboring preexisting histones without the need for H3-H4 splitting events.

Histone and DNA modifications provide key epigenetic information (*1*–*3*). A newly synthesized DNA strand acquires its DNA methylation pattern by copying the preexisting DNA methylation signature from the template strand (*1*, *4*, *5*). However, the mechanism by which patterns of histone modifications are passed on to daughter cells through mitotic divisions remains enigmatic. To understand this, the DNA replication–dependent nucleosome partition pattern must be unveiled first. Initial studies indicated that the nucleosomes do not dissociate (*6*, *7*), which was amended by the discoveries of "hybrid nucleosomes" that contain old H3-H4 tetramers and new H2A-H2B dimers or vice versa (*8*–*11*). Nevertheless, H3-H4 tetramers—the core particles of nucleosomes—do not dissociate during replication-dependent nucleosome assembly (*12*–*15*). Because all six major lysine methylation sites are present on either H3 (Lys4/9/27/36/79) or H4 (Lys20), newly deposited nucleosomes may become methyl-

[1]Graduate Program, Peking Union Medical College and Chinese Academy of Medical Sciences, Beijing 100730, People's Republic of China. [2]National Institute of Biological Sciences, 7 Science Park Road, Zhong Guan Cun Life Science Park, Beijing 102206, People's Republic of China. [3]Life Science College, Beijing Normal University, Beijing 100875, People's Republic of China. [4]Department of Biochemistry, College of Biological Sciences, China Agricultural University, Beijing 100094, People's Republic of China.

*These authors contributed equally to this work.
†To whom correspondence should be addressed. E-mail: zhubing@nibs.ac.cn (B.Z.); chenshe@nibs.ac.cn (S.C.)

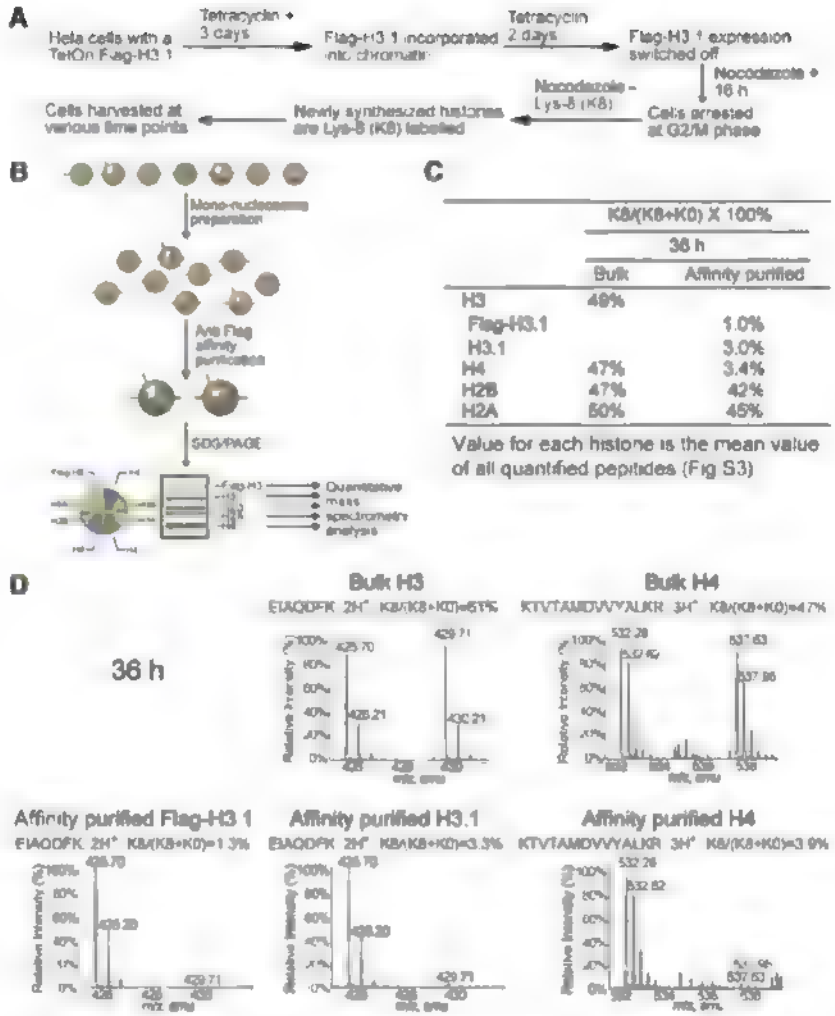

Fig. 1. H3.1-H4 tetramers do not split. (**A** and **B**) Experimental schemes. (**C**) Summary of K8-labeling status of bulk and affinity-purified histones. (**D**) Representative mass spectra for peptides derived from bulk H3, H4, and affinity-purified Flag-H3.1, H3.1, and H4.

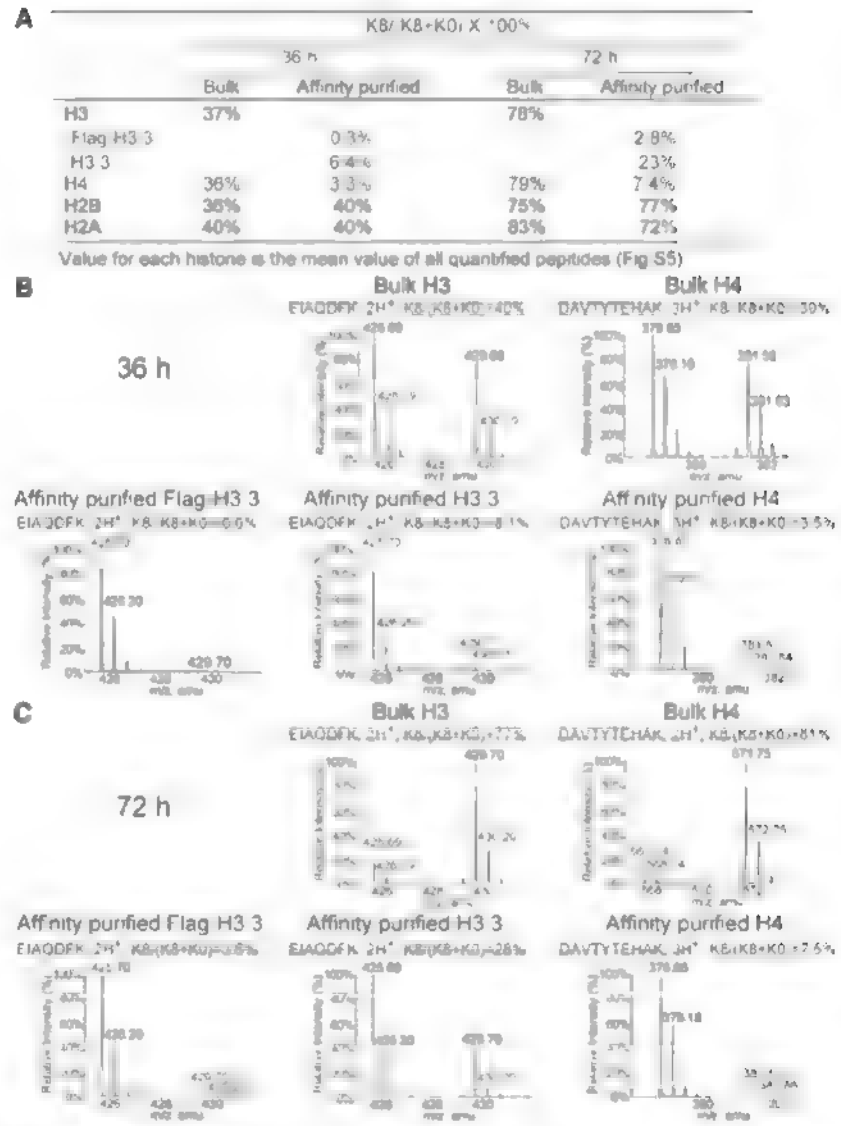

Fig. 2. Significant amounts of H3.3-H4 tetramers split. (**A**) Summary of K8-labeling status of bulk and affinity-purified histones. (**B** and **C**) Representative mass spectra for peptides derived from bulk H3, H4, affinity-purified Flag-H3.3, H3.3, and H4.

ated by "copying" the modification pattern from nearby parental nucleosomes (*1*). However, evidence that the H3-H4 tetramers may split emerged with the discoveries that H3-H4 histones deposit into chromatin as dimers rather than as tetramers (*16*–*18*) and that the histone chaperone Asf1 is capable of disrupting H3-H4 tetramers to form H3-H4/Asf1 heterotrimers (*19*). Thus, the H3-H4 tetramer partitioning pattern needs a definitive reexamination (*1*). In addition, H3.3 variant histones do not form hybrid nucleosomes with canonical H3 histones in vivo (*16*), and they differ from canonical H3 histones for their chromatin localization, chaperon choice, deposition timing, posttranslational modifications, and functions (*16*, *20*–*22*), thus the partitioning pattern of H3.3–containing tetramers is also highly interesting.

We first established stable HeLa cell lines with N-terminally Flag-tagged histone H3.1 or H3.3 under the control of a tetracycline-inducible promoter. To differentiate the "new" histones from the "old" ones and to calculate their ratio, lysine-8 ([$^{13}C_6$, $^{15}N_2$] heavy isotope–labeled L-lysine, abbreviated as K8 for its 8-dalton mass increase from normal lysine) was used in combination with a cell-cycle arrest reagent (nocodazole), thus specifically labeling the "newly synthesized" histones with K8 while leaving the old histones unlabeled (Fig. 1A). By timing the induction with tetracycline, Flag-H3 histones could be designated as old histones or new ones. In addition, we could also study the two major H3 variants, H3.1 and H3.3, individually. Mononucleosomes were prepared from cells with Flag-H3 incorporated into their chromatin (Fig. 1B and fig. S1C) and subjected to affinity purification with antibody to Flag, which selectively purified Flag-H3 -containing mononucleosomes (Fig. 1B and fig. S1D). Flag-H3 histones were associated with native H3 and other core histones, as expected (fig. S1D). Flag-H3, copurified native H3, and other core histones were effectively separated by using 13% SDS–polyacrylamide gel electrophoresis (SDS-PAGE) (fig. S1D). Each histone band was excised individually and subjected to SILAC [stable isotope labeling with amino acids in cell culture (*23*)]–based quantitative mass spectrometry analysis. The percentage of new (K8) and old (K0) histones in each band was subsequently calculated (see the explanatory illustration in fig. S2).

At 36 hours after cell-cycle release, all cells had gone through the first S phase, with a vast majority of the cells at either the first G_2/M phase or the second G_1 phase; at 72 hours, all cells had gone through two complete cell cycles, with some cells advancing through the third S phase. These observations were supported by the percentage of K8-labeled bulk histones (Fig. 1 and fig. S3) and with flow cytometry analysis (fig. S3).

After 36 hours of K8 labeling, bulk core histones were approximately half light (K0) and half heavy (K8) (Fig. 1, C and D, and fig. S3), which corresponds to one round of histone deposition. Affinity-purified Flag-H3.1 histones were only 1.0% K8 labeled (Fig. 1, C and D, and fig. S3), demonstrating that they indeed served as the old histones according to the experimental design. Copurified native H3.1 and H4 histones were 3.0% and 3.4% K8-labeled, respectively (Fig. 1, C and D, and fig. S3). Thus, we conclude that the vast majority of H3.1-H4 tetramers follow the nonsplitting model. In contrast, copurified H2A and H2B were close to 50% K8-labeled, which resembles the overall pattern in the bulk histone preparation (Fig. 1C and fig. S3), indicating the extensive exchange of H2A-H2B dimers among nucleosomes.

At 72 hours, Flag-H3.1 histones were 3.8% K8-labeled (fig. S3), indicating minor leaky expression. Nonetheless, their associated native H3.1 and H4 histones remained in similar K8-labeling ranges (6.3% for H3.1 and 5.9% for H4), whereas copurified H2A and H2B histones were close to their bulk counterparts (fig. S3). Taken together, our data clearly demonstrate old Flag-H3.1 histones stay with old H3.1 and H4 histones at the mononucleosome level.

In a second set of experiments, we generated newly synthesized Flag-H3.1 histones by altering the timing of induction (fig. S4). After one

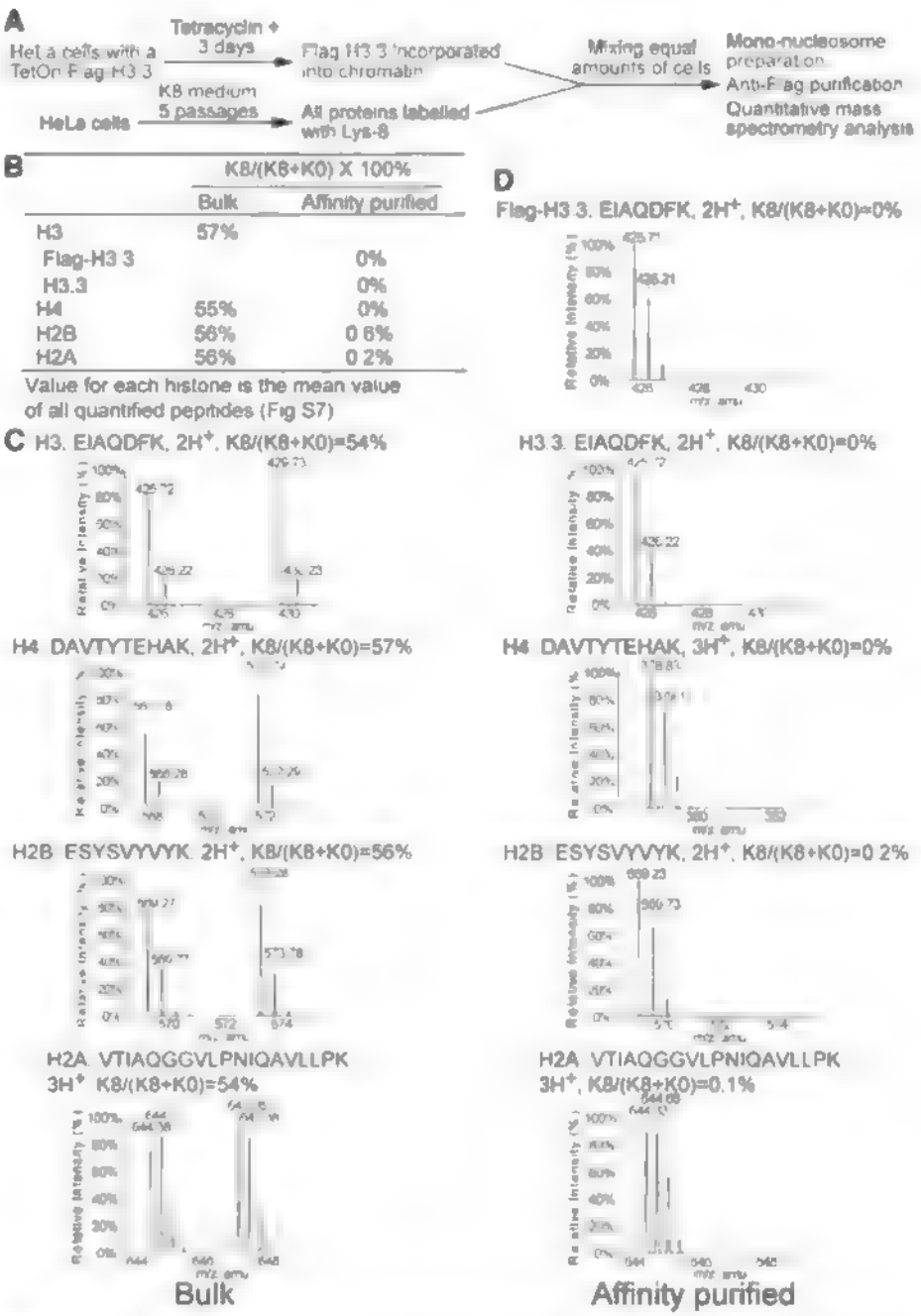

Fig. 3. H3.3-H4 tetramer splitting events occurred in vivo. (**A**) Experimental schemes. (**B**) Summary of K8-labeling status of bulk and affinity-purified histones. (**C** and **D**) Representative mass spectra for peptides derived from bulk core histones and affinity-purified core histones.

round of DNA synthesis, mononucleosomes were affinity-purified and subjected to quantitative mass spectrometry analysis. Flag-H3.1 histones were 93% K8-labeled and native H3.1 and H4 histones copurified with Flag-H3.1 were 90% and 92% K8-labeled, whereas bulk H3 and H4 histones were approximately 50% K8-labeled (fig. S4). In contrast, H2A and H2B histones copurified with newly synthesized Flag-H3.1 were approximately 50% K8-labeled, reflecting the level of labeling in bulk histones (fig. S4). These results indicate that newly synthesized Flag-H3.1 histones associate with newly synthesized native H3.1 and H4 histones, further supporting the H3.1-H4 tetramer nonsplitting model.

The experiments were then extended to the histone variant H3.3, which is known for marking active chromatin (*20*, *21*). We repeated the "on" to "off" experiments for H3.1 (Fig. 1) using the Flag-H3.3 stable cell line. At 36 hours, Flag-H3.3 histones were only 0.3% K8-labeled, indicating almost no leaky expression. However, copurified native H3.3 histones were 6.4% K8-labeled, reflecting a significant level of splitting events (Fig. 2, A and B, and fig. S5). Moreover, at 72 hours Flag-H3.3 was 2.8% K8-labeled, but copurified H3.3 histones were 23% K8-labeled (Fig. 2, A and C, fig. S5). Thus, about one fifth of the Flag-3.3/H4 tetramers had split within roughly two cell cycles. Given that two histone H4 molecules exist in each tetramer, one co-deposited with Flag-H3.3 and the other co-deposited with native H3.3, the density of H4 should lie between Flag-H3.3 and the native H3.3, which is indeed the case at both time points (Fig. 2). The above experiments were repeated in a second Flag-H3.3 stable cell clone that expresses at least fivefold less Flag-H3.3 (fig. S1A) without cell synchronization, and similar results were obtained (fig. S6).

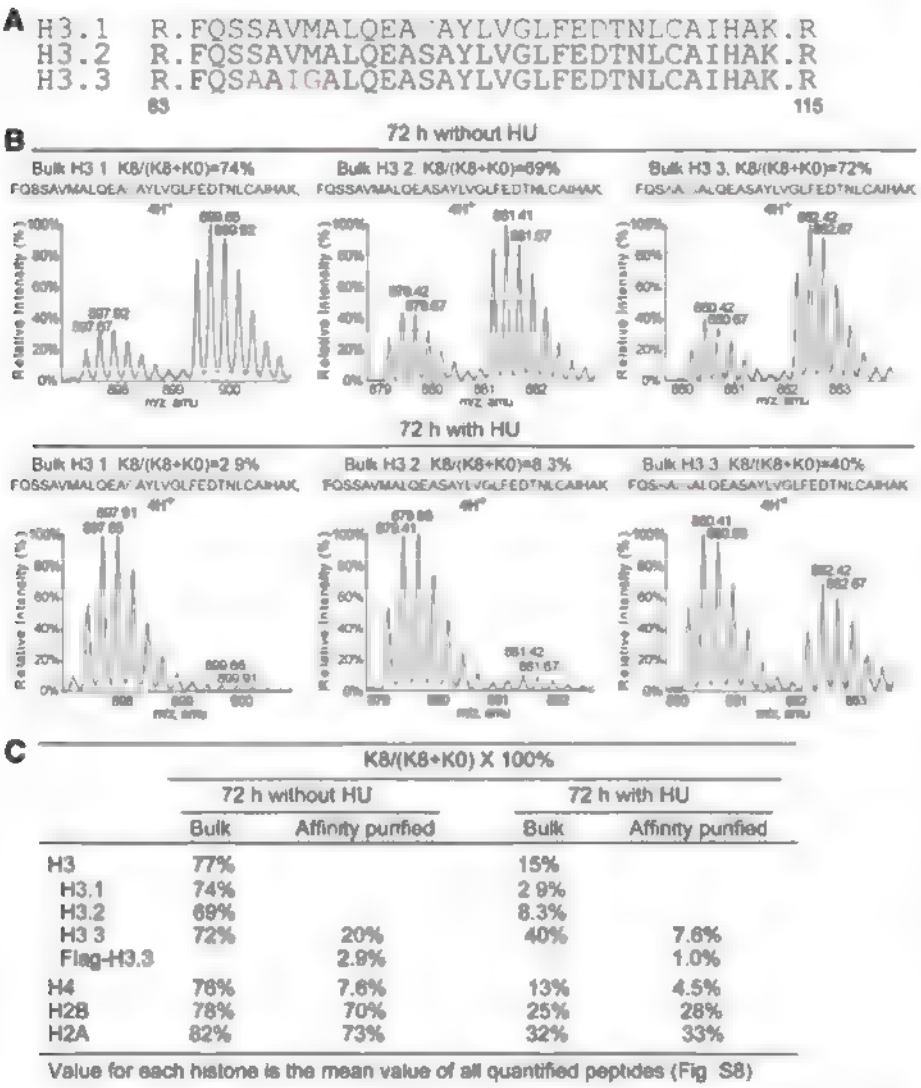

	72 h without HU		72 h with HU	
	Bulk	Affinity purified	Bulk	Affinity purified
H3	77%		15%	
H3.1	74%		2.9%	
H3.2	69%		8.3%	
H3.3	72%	20%	40%	7.6%
Flag-H3.3		2.9%		1.0%
H4	76%	7.6%	13%	4.5%
H2B	78%	70%	25%	28%
H2A	82%	73%	32%	33%

Value for each histone is the mean value of all quantified peptides (Fig. S8)

Fig. 4. Inhibiting DNA replication greatly reduces the number of splitting events for H3.3-H4 tetramers. (**A**) H3 variants can be discriminated by a single tryptic peptide. Variant-specific amino acids are in red. The amino acid positions are indicated. (**B**) HU treatment strongly inhibits new H3.1 deposition while allowing replication-independent H3.3 deposition to occur. (**C**) Summary of K8-labeling status of bulk and affinity-purified histones from cells with or without HU treatment.

To further validate our conclusion, equal amounts of cells expressing Flag-H3.3 in regular medium were mixed with wild-type HeLa cells cultured in K8 medium. Mononucleosomes were then purified from the mixed cells and subjected to affinity purification with antibody to Flag and subsequent quantitative mass spectrometry analysis (Fig. 3A). In this control experiment, affinity-purified Flag-H3.3 histones showed no K8 labeling, and the copurified H3.3 and H4 histones also showed absolutely no K8 labeling. Even the relatively dynamic H2A and H2B histones were less than 1% K8-labeled (Fig. 3, B and D, and fig. S7), despite the existence of roughly 50% K8-labeled bulk histones in the starting material (Fig. 3, B and C, and fig. S7). These data clearly demonstrate the robustness of our assay system, thus ruling out the possibility that core histones might exchange among nucleosomes during the purification processes. Therefore, we conclude that the significant H3.3-H4 tetramer splitting events observed earlier (Fig. 2 and figs. S5 and S6) indeed occur in vivo.

Unlike canonical histones, which are deposited by the DNA replication–dependent pathway during S phase, H3.3 can also be deposited by a DNA replication–independent pathway (*16*, *20*). To test whether a replication-independent pathway is fully responsible for the splitting events, we performed the splitting assay using cells treated with hydroxyurea (HU) or aphidicolin, two reagents that arrest cells at S phase. These experiments allowed us to specifically study the replication-independent deposition pathway. The three H3 variants H3.1, H3.2, and H3.3 can be discriminated by a single peptide after trypsin digestion (Fig. 4A). We took advantage of this property, and successfully achieved individual quantification of H3.1, H3.2, and H3.3 in bulk histone preparations. Seventy-two hours of treatment with 2 mM HU almost fully inhibited the incorporation of new H3.1 (Fig. 4B), demonstrating strong inhibition of DNA replication. In contrast, newly deposited H3.3 accounted for ~40% of the total H3.3 (Fig. 4B), indicating that the replication-independent H3.3 deposition pathway remained effective. In addition, the splitting events in HU-treated cells were significantly reduced from the untreated control cells (7.6% versus 20%) (Fig. 4C and fig. S8). In a separate set of experiments, cells treated with 5 μg/ml aphidicolin displayed full inhibition of new H3.1 deposition while allowing incorporation of 53% new H3.3 in the same cells (fig. S9). Aphidicolin-treated cells also displayed a significantly lower level of splitting events (2.5%) in comparison with that of their parallel untreated control cells (11%) (fig. S9). These results collectively suggest that (i) the replication-independent H3.3 deposition pathway proceeds largely by cooperatively incorporating two new H3.3-H4 dimers and (ii) the majority of splitting events occurred during replication-dependent deposition, although detectable amounts of splitting events were observed during replication-independent deposition.

Our results support the idea that "silent" histone modifications within large heterochromatic regions are maintained by copying modifications from neighboring preexisting histones (*1*, *24*) without the need for H3-H4 splitting events. However, mechanisms underlying the mitotic inheritance of "active" modifications remain debatable. Our observation that significant amounts of H3.3-H4 tetramers split during replication-dependent nucleosome assembly brings up an intriguing question: Do these tetramer splitting events occur at specific regions of chromatin for specific functions, such as mitotic inheritance (*25*, *26*)? Although we observed significant splitting events only for H3.3–containing tetramers, it remains an open question whether such splitting events are variant-specific or rather chromatin region–specific. We did observe ~2% K8-labeling difference between Flag-H3.1 and copurified H3.1 in several experiments (Fig. 1 and figs. S3 and S4), which could be within our detection error but may also suggest splitting events for a small subset of H3.1–containing tetramers. One possible model is that the replication-dependent nucleosome assembly pathway differs at euchromatic and heterochromatic regions, resulting in specific splitting events, predominantly at euchromatic regions. This is particularly tempting because H3.3 is enriched in euchromatin (*20*, *21*, *27*), and H3.1 histones display a similar modification pattern in the vicinity of H3.3 histones (*22*). Detecting the "splitting hot spots" and unveiling their potential role in the mitotic inheritance of active modifications are interesting directions for future investigation.

References and Notes

1. C. D. Allis, T. Jenuwein, D. Reinberg, *Epigenetics* (Cold Spring Harbor Laboratory Press, New York, 2006).
2. T. Kouzarides, *Cell* **128**, 693 (2007).
3. R. Margueron, P. Trojer, D. Reinberg, *Curr. Opin. Genet. Dev.* **15**, 163 (2005).
4. R. Holliday, J. E. Pugh, *Science* **187**, 226 (1975).
5. T. H. Bestor, *EMBO J.* **11**, 2611 (1992).
6. R. L. Seale, *Cell* **9**, 423 (1976).
7. I. M. Leffak, R. Grainger, H. Weintraub, *Cell* **12**, 837 (1977).
8. G. Russev, R. Hancock, *Nucleic Acids Res.* **9**, 4129 (1981).
9. V. Jackson, R. Chalkley, *Cell* **23**, 121 (1981).
10. V. Jackson, R. Chalkley, *J. Biol. Chem.* **256**, 5095 (1981).
11. A. T. Annunziato, R. K. Schindler, M. G. Riggs, R. L. Seale, *J. Biol. Chem.* **257**, 8507 (1982).
12. C. P. Prior, C. R. Cantor, E. M. Johnson, V. G. Allfrey, *Cell* **20**, 597 (1980).
13. V. Jackson, *Biochemistry* **27**, 2109 (1988).
14. V. Jackson, *Biochemistry* **29**, 719 (1990).
15. K. Yamasu, T. Senshu, *J. Biochem.* **107**, 15 (1990).
16. H. Tagami, D. Ray-Gallet, G. Almouzni, Y. Nakatani, *Cell* **116**, 51 (2004).
17. C. M. English, N. K. Maluf, B. Tripet, M. E. Churchill, J. K. Tyler, *Biochemistry* **44**, 13673 (2005).
18. L. J. Benson *et al.*, *J. Biol. Chem.* **281**, 9287 (2006).
19. R. Natsume *et al.*, *Nature* **446**, 338 (2007).
20. K. Ahmad, S. Henikoff, *Mol. Cell* **9**, 1191 (2002).
21. Y. Mito, J. G. Henikoff, S. Henikoff, *Nat. Genet.* **37**, 1090 (2005).
22. A. Loyola, T. Bonaldi, D. Roche, A. Imhof, G. Almouzni, *Mol. Cell* **24**, 309 (2006).
23. J. J. Pesavento, H. Yang, N. L. Kelleher, C. A. Mizzen, *Mol. Cell. Biol.* **28**, 468 (2008).
24. J. Nakayama, J. C. Rice, B. D. Strahl, C. D. Allis, S. I. Grewal, *Science* **292**, 110 (2001).
25. Y. Nakatani, D. Ray-Gallet, J. P. Quivy, H. Tagami, G. Almouzni, *Cold Spring Harb. Symp. Quant. Biol.* **69**, 273 (2004).
26. A. V. Probst, E. Dunleavy, G. Almouzni, *Nat. Rev. Mol. Cell Biol.* **10**, 192 (2009).
27. S. Henikoff, J. G. Henikoff, A. Sakai, G. B. Loeb, K. Ahmad, *Genome Res.* **19**, 460 (2009).

28. We thank X. Wang from the Howard Hughes Medical Institute/University of Texas Southwestern Medical Center for critical comments on the manuscript. We thank N. Yang and J. Ni for color illustration. We thank P. Mortensen from the University of Southern Denmark for developing and supporting the MSQuant software. This work was supported by the Chinese Ministry of Science and Technology 863 projects 2007AA02Z1A6 (to B. Z.) and 2007AA02Z1A3 (to S.C.).

Supporting Online Material

www.sciencemag.org/cgi/content/full/328/5974/94/DC1
Materials and Methods
Figs. S1 to S9

13 July 2009; accepted 27 January 2010
10.1126/science.1178994

Dynamic Regulation of Archaeal Proteasome Gate Opening As Studied by TROSY NMR

Tomasz L. Religa,[1] Remco Sprangers,[2] Lewis E. Kay[1]*

The proteasome catalyzes the majority of protein degradation in the cell and plays an integral role in cellular homeostasis. Control over proteolysis by the 20*S* core-particle (CP) proteasome is achieved by gated access of substrate; thus, an understanding of the molecular mechanism by which these gates regulate substrate entry is critical. We used methyl–transverse relaxation optimized nuclear magnetic resonance spectroscopy to show that the amino-terminal residues that compose the gates of the α subunits of the *Thermoplasma acidophilum* proteasome are highly dynamic over a broad spectrum of time scales and that gating termini are in conformations that extend either well inside (closed gate) or outside (open gate) of the antechamber. Interconversion between these conformers on a time scale of seconds leads to a dynamic regulation of 20*S* CP proteolysis activity.

The 20*S* core-particle (CP) proteasome is a hollow, barrel-like structure that, through protein degradation, plays an important role in cellular homeostasis (*1*, *2*) and is a target for the design of inhibitors (*3*, *4*). The CP is composed of four homo-heptameric rings. In the case of the archaeal version, discussed here, each ring consists of seven identical monomers ($\alpha_7\beta_7\beta_7\alpha_7$), with the active sites sequestered inside the catalytic chamber formed by $\beta_7\beta_7$ (Fig. 1A) (*5*, *6*). Unfolded substrates enter the CP through the α annulus (Fig. 1, A and B), which is occluded by N termini of the α subunits (the gating residues). Although detailed x-ray structures (*6*–*8*) have established the overall architecture of the isolated archaeal CP, density has not been observed for the gating residues, and the molecular mechanism by which they control entry of substrates remains to be elucidated.

We have previously obtained high-quality ^1H-^{15}N transverse relaxation optimized spectroscopy (TROSY) (*9*) and ^1H-$^{13}C'$ methyl-TROSY (*10*) data sets for α_7 (*11*, *12*), a single-ring version of molecular weight = 180 kilodaltons. The N-terminal 35 residues could not be observed in amide spectra of α_7 (fig. S1), reflecting dynamics on the microsecond-millisecond time scale, which also severely attenuated peaks from isoleucine, leucine, and valine methyl groups in this region (fig. S2). We used a labeling scheme in which highly deuterated $^{13}CH_3$-methionine (Met) proteins were produced (*13*), so that Met methyl groups could be used as probes of structure and dynamics. The 20*S* CP α subunit contains only four natural Met residues, providing spectra of low complexity. To augment the two Met residues (M1 and M6) located in the gating termini, an additional Met residue (M-1) was introduced at the N-terminal end of the protein (Fig. 1C).

Methionine side-chains undergo large-amplitude, fast–time scale motions (*14*) that average out much of the conformational exchange broadening that affects other resonances, allowing high-quality Met methyl-TROSY spectra to be recorded. Figure 1D shows the ^1H-^{13}C correlation map of wild-type (WT) α_7. A total of 9 Met correlations were observed in the spectra, subsequently assigned via mutagenesis (fig. S3). Three peaks originate from each M-1 and M1 residue in WT α_7, corresponding to the major state ("A") and a pair of minor states ("B" and "C"). Similar multiple peaks were observed in spectra recorded on the intact WT $\alpha_7\beta_7\beta_7\alpha_7$ CP (Fig. 1D), establishing that they are not an artifact associated with the single-ring structure. Additionally, they do not emerge from the slightly longer-than-normal N terminus (Fig. 1C), as three peaks for M1 are also noted in spectra

[1]Departments of Molecular Genetics, Biochemistry, and Chemistry, University of Toronto, Toronto, Ontario M5S 1A8, Canada. [2]Max Planck Institute for Developmental Biology, Tübingen, Germany.

*To whom correspondence should be addressed. E-mail: kay@pound.med.utoronto.ca

recorded where the α subunit starts at G0 (fig. S4) (*15*). We also noted extra correlations in a construct in which residues Y8 and D9 [which stabilize the open-gate conformation of the proteasome in a complex with the 11*S* activator (*8*)] were mutated to glycine residues (Y8G/D9G α_7). Correlations of states B and C were of higher intensity than in spectra of the wild type, providing more accurate probes of the minor states. Furthermore, in Y8G/D9G α_7, an extra correlation is also observed for M6. Notably, spectra of the monomeric α subunit α_1 contain the "correct" number of peaks (Fig. 1D), indicating that peak duplication is dependent on the formation of ring structures. The fact that similar Met cross peaks are observed in spectra of α_7, $\alpha_7\alpha_7$, and the $\alpha_7\beta_7\beta_7\alpha_7$ 20*S* CP provides strong evidence that the α_7 ring is an excellent model system for the study of proteasome gate structure and dynamics.

We established the identity of these multiple conformations through measurements of paramagnetic relaxation enhancements (PREs) (*16*, *17*), in which nitroxide spin labels are attached to cysteine residues at various positions in the α subunit, and decay rates of either amide or methyl proton magnetization are quantified for the nitroxide label in the oxidized, R_2^{ox}, and reduced, R_2^{red}, states (fig. S5). The PRE effect ($\Gamma_2 = R_2^{ox} - R_2^{red}$) scales as the inverse sixth power of the distance between the unpaired electron of the nitroxide and the nuclear magnetic resonance (NMR) spin, providing a powerful probe of structure. Initially, we quantified amide Γ_2 (Γ_2^{NH}) rates on a sample with a nitroxide attached to position 4 of α_7 (Gly4Cys); Γ_2^{NH} rates were high for residues in helices H1 and H2 (which line the antechamber) with residues on the surface of α_7 being substantially less affected (Fig. 2A). PRE rates of more than 150 s^{-1} for V87 and F91 in H1 indicate a distance between the paramagnetic center and the amide group of less than 17 Å, not consistent with crystal structures (*7*) or a recent cryo–electron microscopy model (*18*). In the latter, the N termini extend outward on the surface of the alpha ring. We were not able to satisfy many of the Γ_2^{NH} rates in structure calculations unless the N terminus of at least one of the seven α subunits in α_7 was allowed to cross the α annulus (Fig. 1B) and extend into the interior of the ring, corresponding to the antechamber in the intact proteasome (Fig. 1B). In this case, all rates could be satisfied. Because Γ_2^{NH} values for residues around positions 80 to 100 were most affected, a spin label was added at position 95 [located >24 Å from the α annulus on the inside of the antechamber (Fig. 1B)], and the effects on the Met correlations quantified by recording methyl-TROSY spectra of both WT (fig. S6) and Y8G/D9G (Fig. 2B) α_7. In the oxidized paramagnetic state, peaks corresponding to sites B and C were completely eliminated, whereas those from the major state (A) showed little change in intensity, with methyl ^{1}H Γ_2 ($\Gamma_2^{CH_3}$) rates of only 3 to 7 s^{-1}. This observation provides strong evidence that states B and C derive from gating residues inside the chamber (the "in" position). Placement of a spin-label at position 20, located above the α annulus and well outside the lumen of the proteasome (Fig. 1B), eliminated peaks from state A (Fig. 2B), establishing that this conformation corresponds to the "out" position for the terminal residues. Once signals from the in and out conformations were assigned, the relative populations of each were quantified from heteronuclear multiple-quantum coherence (HMQC) spectra, as summarized in Fig. 2C. For WT α_7, approximately two termini are inserted into the cavity, on average, very similar to what is quantified for the full 20*S* WT CP. In the case of Y8G/D9G α_7, approximately three termini populate the in state (fig. S7).

We inserted additional spin labels at positions 72, 107, 115, and 143 [located inside the chamber (Fig. 1B, red)], confirming the large differences in ^{1}H $\Gamma_2^{CH_3}$ rates between state A and either of states B and C noted for spin label at position 95 and providing additional distance restraints from which structures of the out and in states could be calculated. The in conformations corresponding to states B and C were not distinguished in structure calculations because a maximum dif-

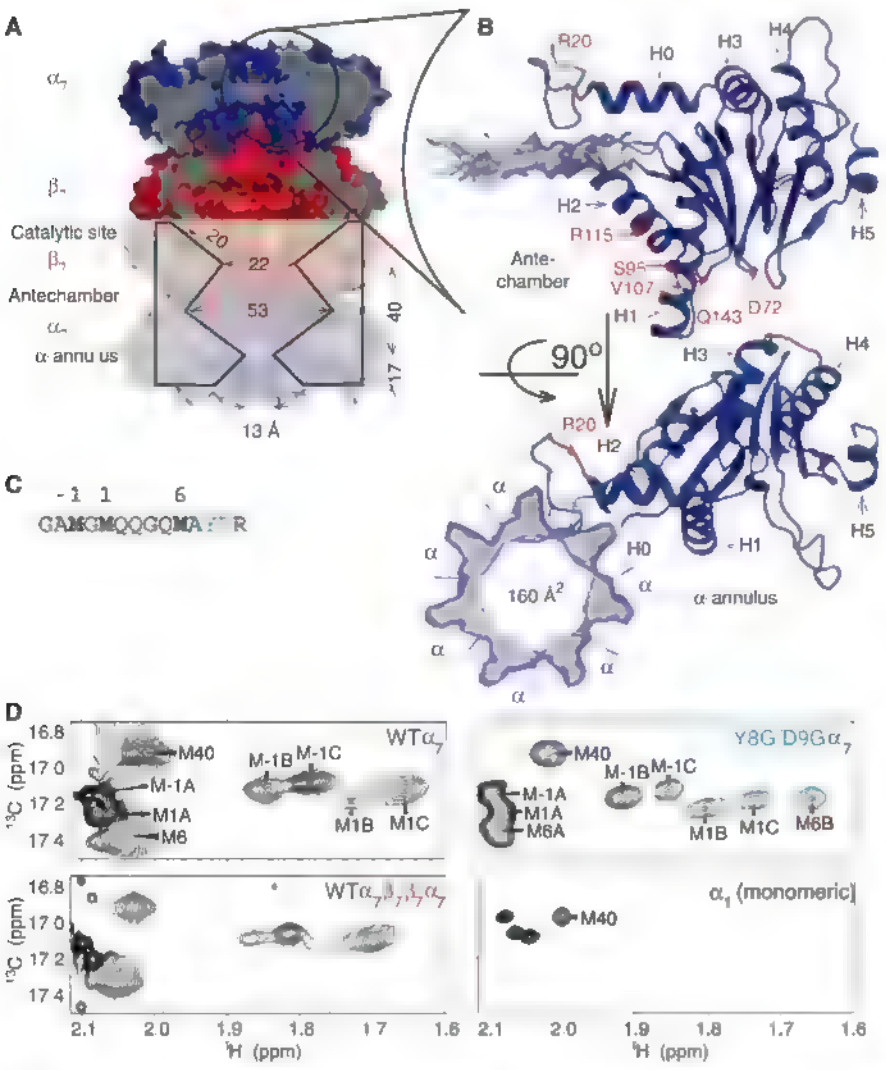

Fig. 1. Multiple conformations for the proteasome gating residues. **(A)** Space-filling, cross-sectional side-view representation of the 20*S* CP proteasome ($\alpha_7\beta_7\beta_7\alpha_7$) from *Thermoplasma acidophilum*, showing the relative positions of the α annulus, the antechambers, and the catalytic chamber, as well as the dimensions of the molecule [PDB accession code 1YA7 (*7*)]. **(B)** Each α ring is composed of seven identical α subunits. A single α subunit is shown in ribbon diagram (two orientations), along with the α annulus that is composed of residues from all seven subunits. The locations of added spin-labels for PRE measurements are indicated in red. **(C)** Primary sequence of the N-terminal α-subunit residues, including GAMG introduced by cloning. The Met residues that we used as probes in this study are shown in bold. When YD residues (in light blue) are mutated to G residues, the out conformation of the gating residues is destabilized. **(D)** ^{1}H-^{13}C Met methyl HMQC spectra of the WT α_7 ring, WT $\alpha_7\beta_7\beta_7\alpha_7$, and the Y8G/D9G α_7 ring showing multiple correlations for M1, M-1 (denoted by A, B, and C), and M6 (Y8G/D9G α_7 ring, denoted by A and B). Multiple correlations are not observed for the isolated α subunit (bottom). In all spectra, the M120 correlation is outside the spectral window shown here. ppm, parts per million.

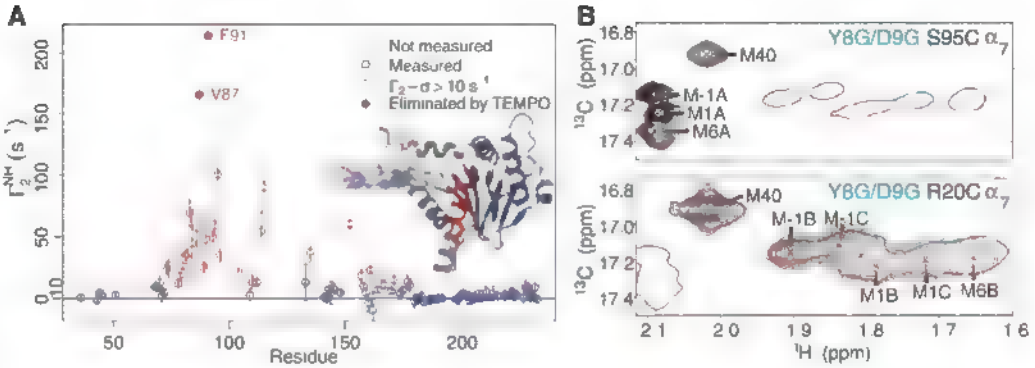

Position	OUT	IN
α_7 M-1	A	B+C
WT	76	24
Y8G/D9G	55	45
E25G	87	13
E25P	100	0
	+ 11S	
WT	91	9
Y8G/D9G	56	44

Fig. 2. Assignment of correlations to in and out conformations and calculation of structural ensembles. **(A)** H^N Γ_2 rates quantified on a sample with a nitroxide attached to position 4 of each α subunit. Red open circles indicate those residues for which rates exceed measurement errors (σ) by at least 10 s^{-1}, whereas peaks for V87 and F91 disappeared in the oxidized state (solid red circles). Rates were high for residues in helices H1 and H2 (indicated in red). Note that amides of residues 1 to 35 are not visible in the spectra due to a microsecond-millisecond exchange process (fig. S1) and are thus not available as probes. TEMPO, 2,2,6,6-tetramethyl-1-piperidinyloxyl. **(B)** Superposition of ^1H-^{13}C Met methyl HMQC spectra recorded from the Y8G/D9G α_7 ring. Attachment of a spin-label at position 95 (see Fig. 1B) eliminates correlations from states B and C for M1, −1, and 6 (top), whereas a nitroxide positioned at residue 20 eliminates peaks from the A conformation (bottom) (see fig. S6). Spectra recorded with nitroxide in the oxidized (black) and reduced states (red, 1 contour) are shown. **(C)** Relative populations of the out (state A) and in (states B and C) conformations obtained from peak volumes in ^1H-^{13}C HMQC spectra. Errors of no more than 2% are estimated based on quantification from multiple spectra. **(D)** Ensembles of 10 structures calculated for WT α_7 showing gating residues in the in (teal) and out (blue) conformations for an α subunit. In WT α_7, approximately two of the seven subunits are in the in state.

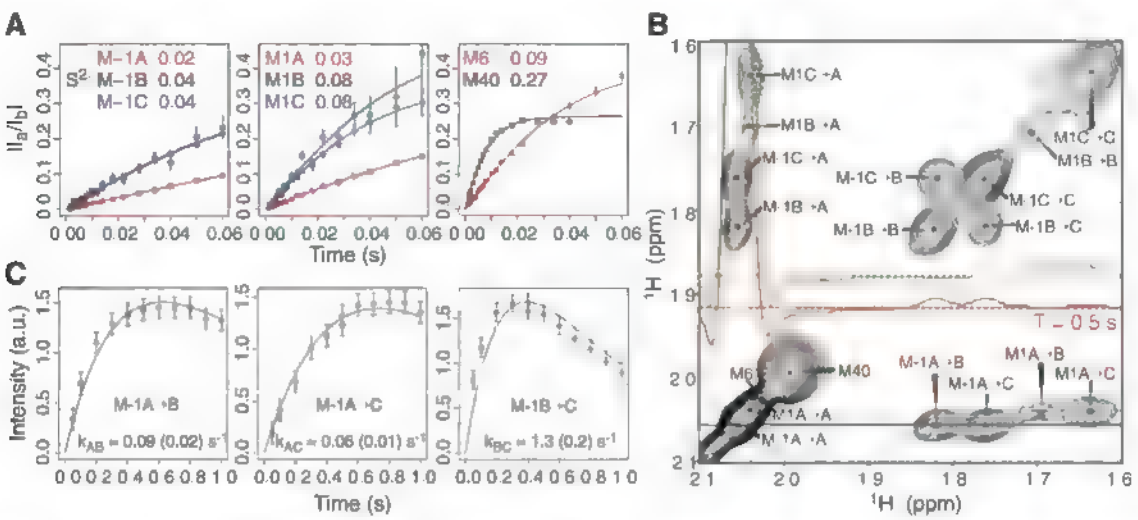

Fig. 3. Proteasome gates are dynamic over a broad spectrum of time scales. **(A)** Ratio of intensities of cross peaks in ^1H-^{13}C spectra that are sensitive to the difference (I_a) and sum (I_b) of methyl ^1H transitions (*21*); this ratio can be fit (solid lines) to extract methyl axis order parameters (S^2), as listed. **(B)** Magnetization exchange spectroscopy (*22*) showing that states A, B, and C [corresponding to out (A) and in (B and C) gate conformations] are in dynamic equilibrium. Exchange cross peaks are not observed when the exchange mixing time is set to 0 (green trace), but they are present for nonzero values (red). **(C)** The build-up of exchange peaks can be used to quantify exchange rates (k_{mn}).

ference of only 3 Å was noted in a comparison of all spin-label/Met methyl distances involving these states (for the most part, within the error bounds of our measurements). Figure 2D shows the 10 lowest-energy structures corresponding to out and in conformations of a given α monomer within the context of a WT α_7 ring, calculated from a restrained molecular dynamics procedure (*19*) and outlined in the supporting online material (SOM) (*20*). Interestingly, the reverse-turn loop (formed by the conserved residues Y8, D9, P17, and Y26) that stabilizes the open conformation of the proteasome-11S activator complex (*8*) is present in most structures of the out state but is always broken in the in state. The in/out configurations deviate considerably around A11, where the backbone starts pointing toward the α annulus for the in state. Termini in the in state

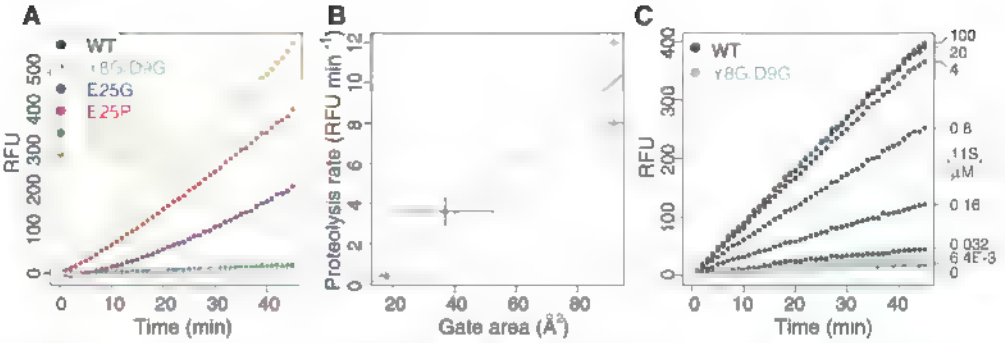

Fig. 4. Proteasome activity correlates with accessible surface area of the α annulus. (**A**) Relative fluorescence units (RFU) versus hydrolysis time of the nine-residue (*31*) Mca-RPPGFSAFK(Dnp)-OH peptide using different 20*S* CP constructs (see SOM), with hydrolysis rates increasing with accessible surface area of the α annulus. (**B**) Correlation of proteasome hydrolysis rates with α annulus–accessible surface area (horizontal error bars are derived from the ensemble of calculated structures, as described in the SOM), color-coded as in (A). (**C**) Binding of the 11*S* activator increases hydrolysis of the nine-residue peptide for the WT (black), but not the Y8G/D9G (light blue), proteasome. Concentrations of 11*S* (per monomer) for each WT CP trace are shown along the right vertical axis. The same range of concentrations was employed for Y8G/D9G, with little effect. The proteasome concentration (in monomer) was 2 nM (A) and 4 nM [(C), 11*S* binding]. The curves in (A) and (C) are representative from at least 4 separate measurements, with errors in estimated rates (slope of the curves) up to 20%.

cross the annulus at residues A7 to R10 (depending on the structure), effectively closing the α annulus to substrate entry. Structures were also obtained for Y8G/D9G α_7 and are very similar to those for the wild type. Notably, each of the ensembles in Fig. 2D shows a major amount of disorder, reflecting to some extent the small numbers of restraints used in structure calculations (table S1). However, the structures also represent what most certainly is a very dynamic gating terminus. For example, measured order parameters squared (S^2) that quantify the amplitudes of methyl-axis picosecond time-scale motion (*21*) are <0.1 for M-1, M1, and M6 (in all states), indicating near isotropic motion characteristic of a high level of dynamics (Fig. 3A).

As a test of our model, we prepared a complex consisting of spin-labeled 11*S* activator with label at position 108 and Met-labeled Y8G/D9G α_7. Because the paramagnet is placed in the lumen of 11*S* at a position accessible only to the out states of the gating residues, it would be expected to substantially attenuate the A-state correlations, whereas those from the B and C states are hardly affected. ^{1}H-^{13}C methyl-TROSY spectra establish that this is indeed the case with A-state peaks eliminated and ^{1}H $\Gamma_2^{(H)}$ rates of only $6 \pm 3\ s^{-1}$ for the minor states (fig. S8). This result provides a strong cross-validation of our proposed model of gating in which α-subunit terminal residues can assume two very distinct states, corresponding to out and in conformations, with activation occurring by shifting the relative populations of each state, leading to an increase in the out conformation.

The in and out states of the gating termini interconvert on the seconds time scale that can be quantified by magnetization exchange spectroscopy (Fig. 3, B and C) (*22*). Figure 3C shows the build-up of peak intensities corresponding to the transfer of magnetization between states j and k ($j \neq k$) during a prescribed time interval that can be fit to extract lifetimes of each state; values on the order of 6.5 s $(k_{AB} + k_{AC})^{-1}$ and 2 s $\frac{1}{2}(k_{BA}^{-1} + k_{CA}^{-1})$ are obtained for the out and in states, respectively, at 45°C (k_{ij} is the rate of interconversion from state i to state j). Whereas, on average, approximately two gating termini lie within the antechamber of the WT proteasome, the experiments reported here indicate a stochastic exchange process that controls the number of in and out termini in any given molecule as a function of time, thereby regulating function.

To establish a correlation between proteasome function and relative population of in versus out gating termini, we performed proteolysis assays on the series of 20*S* CP ($\alpha_7\beta_7\beta_7\alpha_7$) mutants listed in Fig. 4A. Large enhancements of proteolysis rates were observed for the gateless Δ(3 11) mutant (yellow) and for E25P α_7 (red) [only the out states are populated in E25P α_7; no minor states exist in HMQC spectra (Fig. 2C and fig. S9)], clearly indicating that the all-out state corresponds to the completely open form of the gate. As expected, proteolysis was much slower for the E25G mutant, where, on average, slightly less than one of the seven N termini resides in the chamber (Fig. 2C). Slower proteolysis rates were observed for the wild type and the deletion mutant Δ(3 4). As expected, similar rates were quantified because, in both cases, the same number of termini are inside the chamber (approximately two), with the same residues (A7 to R10, see above) blocking the α annulus. We did not observe a major difference in proteolysis rates between WT and Y8G/D9G 20*S* CP, although the population of in termini is considerably higher in the mutant (Fig. 2C). However, a comparison of the accessible surface areas of the α annulus calculated on the basis of the PRE-derived structures shows little difference whether two (WT) or three (Y8G/D9G) termini cross the annulus (18 ± 9 versus 16 ± 10 Å^2), because the bulky residues tyrosine and aspartic acid in the WT have been substituted by glycine in the mutant. Notably, we observed a strong correlation between hydrolysis rates and accessible surface area of the α annulus for the mutants considered in our study (Fig. 4B). Binding of the 11*S* activator to WT 20*S* CP that is known to stabilize the open-gate conformation (*23*) leads to an increase in hydrolysis rates with added activator, whereas no effect is observed for the Y8G/D9G mutant (Fig. 4C). These findings are consistent with the shift in out versus in populations in the case of the wild type [but not for the mutant (Fig. 2C)] and are in agreement with results showing that 11*S* binding to the Y8G/D9G 20*S* CP (fig. S10) cannot open the gate because key interactions are eliminated due to the mutations (*7*, *8*). Finally, very similar results to those for 11*S* binding have been obtained for an 11*S* chimeric construct in which the final 10 C-terminal 11*S* residues are substituted for those from the hexameric proteasome-activating nucleotidase (PAN) (fig. S11) (*24*, *25*). It is worth noting that Archaea contain a hexameric PAN-like activator with the conserved C-terminal hydrophobic-tyrosine-X motif that has been shown to be essential for proteasome binding (*26*).

Thus, gating of the 20*S* CP archaeal proteasome is controlled through highly dynamic N termini that interconvert between conformations that place them either outside or well inside the antechamber, with rates of proteolysis that depend on the relative populations of termini in the in and out states. 20*S* CPs from Archaea and beyond can cleave a variety of different intrinsically disordered proteins (*27*, *28*) in the absence of auxiliary components, and there is growing consensus of the importance of this non-ubiquitin–based degradation pathway (*29*). Additionally, regulation of protein cleavage by the gating termini of the naked 20*S* CP is critical for cell viability (*30*). An understanding of the dynamic mechanism of 20*S* CP gating is therefore important and may open the possibility of regulating proteasome function through the design of drugs that alter the ratio of in versus out conformers or that perhaps change the dynamics of exchange between them.

References and Notes

1. W. Baumeister, J. Walz, F. Zühl, E. Seemüller, *Cell* **92**, 367 (1998).
2. A. L. Goldberg, *Nature* **426**, 895 (2003).
3. A. L. Goldberg, *Biochem. Soc. Trans.* **35**, 12 (2007).
4. G. Nalepa, M. Rolfe, J. W. Harper, *Nat. Rev. Drug Discov.* **5**, 596 (2006).
5. Y. Cheng, *Curr. Opin. Struct. Biol.* **19**, 203 (2009).
6. J. Löwe *et al.*, *Science* **268**, 533 (1995).
7. A. Förster, E. I. Masters, F. G. Whitby, H. Robinson, C. P. Hill, *Mol. Cell* **18**, 589 (2005).

8. A. Förster, F. G. Whitby, C. P. Hill, *EMBO J.* **22**, 4356 (2003)
9. K. Pervushin, R. Riek, G. Wider, K. Wüthrich, *Proc. Natl. Acad. Sci. U.S.A.* **94**, 12366 (1997)
10. V. Tugarinov, L. E. Kay, *J. Am. Chem. Soc.* **125**, 13868 (2003)
11. R. Sprangers, L. E. Kay, *Nature* **445**, 618 (2007)
12. R. Sprangers *et al.*, *Biochemistry* **47**, 6727 (2008)
13. I. Gelis *et al.*, *Cell* **131**, 756 (2007)
14. A. Mittermaier, L. E. Kay, J. D. Forman-Kay, *J. Biomol. NMR* **13**, 181 (1999)
15. Single-letter abbreviations for the amino acid residues are as follows: A, Ala; C, Cys; D, Asp; E, Glu; F, Phe; G, Gly; H, His; I, Ile; K, Lys; L, Leu; M, Met; N, Asn; P, Pro; Q, Gln; R, Arg; S, Ser; T, Thr; V, Val; W, Trp; and Y, Tyr
16. J. L. Battiste, G. Wagner, *Biochemistry* **39**, 5355 (2000)
17. G. M. Clore, *Mol. Biosyst.* **4**, 1058 (2008)
18. J. Rabl *et al.*, *Mol. Cell* **30**, 360 (2008)
19. C. D. Schwieters, J. J. Kuszewski, N. Tjandra, G. M. Clore, *J. Magn. Reson.* **160**, 65 (2003)
20. Materials and methods are available as supporting material on *Science* Online
21. V. Tugarinov, R. Sprangers, L. E. Kay, *J. Am. Chem. Soc.* **129**, 1743 (2007)
22. N. A. Farrow, O. Zhang, J. D. Forman-Kay, L. E. Kay, *J. Biomol. NMR* **4**, 727 (1994)
23. F. G. Whitby *et al.*, *Nature* **408**, 115 (2000)
24. B. M. Stadtmueller *et al.*, *J. Biol. Chem.* **285**, 13 (2010)
25. Y. Yu *et al.*, *EMBO J.* **29**, 692 (2010)
26. A. Ruepp, B. Rockel, I. Gutsche, W. Baumeister, A. N. Lupas, *J. Struct. Biol.* **135**, 126 (2001)
27. A. F. Kisselev, T. N. Akopian, A. L. Goldberg, *J. Biol. Chem.* **273**, 1982 (1998)
28. C.-W. Liu, M. J. Corboy, G. N. DeMartino, P. J. Thomas, *Science* **299**, 408 (2003), published online 12 December 2002 (10.1126/science.1079293)
29. P. Tsvetkov, N. Reuven, C. Prives, Y. Shaul, *J. Biol. Chem.* **284**, 26234 (2009)
30. M. Bajorek, D. Finley, M. H. Glickman, *Curr. Biol.* **13**, 1140 (2003)
31. D. M. Smith *et al.*, *Mol. Cell* **27**, 731 (2007)
32. We thank J. Forman-Kay for providing laboratory space and for valuable discussions, R. Muhandiram for NMR support, X. Li and A. Shimmer for assistance with the plate reader, and F. Hansen and D. Korzhnev for discussions. T.L.R. acknowledges the European Molecular Biology Organization (ALTF 827-2006) and the Canadian Institutes of Health Research (CIHR) for postdoctoral fellowships. L.E.K. holds a Canada Research Chair in Biochemistry. This work was supported by a grant from the CIHR. The structural ensembles of WT α_7 and Y8G/D9G α_7 have been deposited in the Protein Data Bank (PDB) with accession codes 2ku1 and 2ku2, respectively

Supporting Online Material

www.sciencemag.org/cgi/content/full/328/5974/98/DC1
Materials and Methods
Figs. S1 to S11
Table S1
References

23 November 2009; accepted 2 March 2010
10.1126/science.1184991

Evasion of CD8$^+$ T Cells Is Critical for Superinfection by Cytomegalovirus

Scott G. Hansen,[1]* Colin J. Powers,[1]*† Rebecca Richards,[1] Abigail B. Ventura,[1] Julia C. Ford,[1] Don Siess,[2] Michael K. Axthelm,[1,2] Jay A. Nelson,[1,2] Michael A. Jarvis,[1] Louis J. Picker,[1,2]‡ Klaus Früh[1,2]‡

Cytomegalovirus (CMV) can superinfect persistently infected hosts despite CMV-specific humoral and cellular immunity; however, how it does so remains undefined. We have demonstrated that superinfection of rhesus CMV–infected rhesus macaques (RM) requires evasion of CD8$^+$ T cell immunity by virally encoded inhibitors of major histocompatibility complex class I (MHC-I) antigen presentation, particularly the homologs of human CMV US2, 3, 6, and 11. In contrast, MHC-I interference was dispensable for primary infection of RM, or for the establishment of a persistent secondary infection in CMV-infected RM transiently depleted of CD8$^+$ lymphocytes. These findings demonstrate that US2-11 glycoproteins promote evasion of CD8$^+$ T cells in vivo, thus supporting viral replication and dissemination during superinfection, a process that complicates the development of preventive CMV vaccines but that can be exploited for CMV-based vector development.

A general characteristic of the adaptive immune response to viruses is its ability to prevent or rapidly extinguish secondary infections by identical or closely related viruses. A notable exception is the herpesvirus family member cytomegalovirus (CMV), which can repeatedly establish persistent infection in immunocompetent hosts (*1*–*3*). Sequential infections are likely the reason for the presence of multiple human CMV (HCMV) genotypes in the human host (*4*). This ability to establish secondary persistent infections despite the preexistence of persistent virus (referred to as "superinfection") is particularly notable because healthy CMV-infected individuals develop higher neutralizing antibody responses and manifest very-high-frequency CD4$^+$ and CD8$^+$ CMV-specific T cell responses (>10% of circulating memory T cells can be CMV-specific) (*5*). This evasion of pre-existing immunity has frustrated attempts to develop preventive CMV vaccines (*6*, *7*) but can be exploited for the development of CMV vectors capable of repeatedly initiating de novo T cell responses to heterologous pathogens in CMV-positive hosts (*3*).

The biologic importance of this superinfection capability has prompted our investigation of its extent and mechanism. We previously showed that inoculation of RhCMV$^+$ rhesus macaques (RM) with 10^7 plaque-forming units (PFU) of genetically modified RhCMV (strain 68-1) expressing simian immunodeficiency virus (SIV) antigens resulted in superinfection manifested by the persistent shedding of the genetically modified CMV in the urine and saliva and by the induction and long-term maintenance of de novo CD4$^+$ and CD8$^+$ T cell responses specific for the SIV insert (*3*). To determine whether RhCMV would be able to overcome immunity at lower, more physiologic doses of infection, as reported for HCMV (*7*), a recombinant RhCMV containing a loxP-flanked expression cassette for SIVgag [RhCMV(gagL)] (fig. S1) was inoculated subcutaneously at doses of 10^4 or 10^2 PFU into four RM naturally infected by RhCMV, as manifested by the presence of robust RhCMV-specific T cell responses (table S1A). The SIVgag-specific T cell responses in peripheral blood mononuclear cells (PBMC) or in broncho-alveolar lavage lymphocytes (BAL) were monitored by flow cytometric analysis of intracellular cytokine staining (ICCS) (figs. S2 and S3) after stimulation with consecutive overlapping 15–amino acid peptides corresponding to SIVgag (*8*). Reduction of the inoculating dose had minimal impact on superinfection dynamics: All animals developed SIVgag-specific T cell responses within 2 weeks (Fig. 1A), and secretion of SIVgag-expressing virus in urine or buccal swabs was observed within 4 to 10 weeks of infection in both cohorts (Fig. 1B). The time to first detection of secreted virus in these low-dose-challenged RM was not maternally different from that of eight RhCMV$^+$ animals infected with 10^7 PFU of RhCMV(gagL) (Fig. 1B). Moreover, the SIVgag-specific T cell responses and RhCMV(gagL) secretion were stable for more than 3 years regardless of initial dose (Fig. 1, A and C). These data indicate that, consistent with HCMV in humans, RhCMV is able to overcome high levels of CMV-specific immunity and to establish secondary persistent infections, even with low doses of challenge virus.

We hypothesized that an essential step during CMV superinfection is the ability of the virus to clear an initial immunological checkpoint. A likely candidate for such an immunological barrier is CD8$^+$ cytotoxic T cells (CTL), because they are crucial for controlling CMV-associated diseases (*9*). The importance of CTL control for CMV is also suggested by viral expression of multiple proteins that inhibit presentation of viral peptide antigens to CD8$^+$ T cells via major histocompatibility complex class I (MHC-I) molecules (*10*). HCMV encodes at least four related glycoproteins, each with a unique mechanism to

[1]Vaccine and Gene Therapy Institute, Oregon Health and Science University, 505 Northwest 185th Avenue, Beaverton, OR 97006, USA. [2]Oregon National Primate Research Center, Oregon Health and Science University, 505 Northwest 185th Avenue, Beaverton, OR 97006, USA.

*These authors contributed equally to this work.
†Present address: Salk Institute for Biological Studies, 10010 North Torrey Pines Road, La Jolla, CA 92037, USA.
‡To whom correspondence should be addressed. E-mail pickerl@ohsu.edu (L.J.P.); fruehk@ohsu.edu (K.F.)

prevent antigen presentation. US2 and US11 mediate the retrograde translocation of MHC-I into the cytosol for proteasomal destruction (*11*), US3 retains MHC-I in the endoplasmic reticulum by interfering with chaperone-controlled peptide loading (*12*), and US6 inhibits the translocation of viral and host peptides across the endoplasmic reticulum membrane by the dedicated peptide transporter TAP (transporter associated with antigen processing) (*13*). RhCMV encodes sequence and functional homologs of these genes in a genomic region spanning Rh182 (US2) to Rh189 (US11) (fig. S1) (*14*). Furthermore, the Rh178 gene encodes the RhCMV-specific viral inhibitor of heavy chain expression (VIHCE), which prevents signal-sequence-dependent translation/translocation of MHC-I (*15*).

To determine whether MHC-I interference and CTL evasion played a role in the ability of CMV to superinfect CMV$^+$ animals, we replaced the entire RhUS2-11 region with a SIVgag expression cassette using bacterial artificial chromosome (BAC) mutagenesis, resulting in virus ΔUS2-11(gag) (*8*). We also deleted Rh178 to generate ΔVIHCEΔUS2-11(gag) (fig. S1). We previously showed that MHC-I expression is partially restored upon US2-11 deletion, whereas additional deletion of Rh178 fully restores MHC-I expression in RhCMV-infected fibroblasts (*15*). In vitro analysis showed that all viruses were deleted for the targeted RhCMV open reading frames (ORFs), did not contain any unwanted mutations, and replicated comparably to wild-type RhCMV (figs. S4 and S5). First, we examined whether these viruses were able to infect animals that were CMV-naïve as shown by a lack of CMV-specific T cell responses (table S1B). Three groups of animals were challenged with 10^7 PFU of ΔUS2-11(gag) (n = 2), ΔVIHCEΔUS2-11(gag) (n = 2), or BAC-derived (wild-type) RhCMV(gag) (n = 2). T cell responses against both CMV and SIVgag in PBMC and against SIVgag in BAL were comparable between animals infected with the deletion mutants and the wild-type RhCMV(gag) control (Fig. 2A). Moreover, all animals secreted SIVgag-expressing virus from day 56 onward for the duration of the experiment (>700 days) (Fig. 2B). Polymerase chain reaction (PCR) analysis of DNA isolated from urine cocultured virus at day 428 confirmed that the secreted viruses lacked the respective gene regions and were able to persist in the host (Fig. 2C). Together these results show that viral MHC-I interference is dispensable for primary infection and the establishment and maintenance of persistent infection, despite the development of a substantial CMV-specific T cell response.

To examine whether viral MHC-I interference was required for superinfection of RhCMV$^+$ RM, we challenged two cohorts of four naturally infected RM each with 10^7 PFU of ΔVIHCEΔUS2-11(gag) or RhCMV(gag). All animals displayed immediate early gene (IE)-specific CD4$^+$ and CD8$^+$ T cell responses before challenge (Fig. 3A and table S1C). In keeping with previous results (*3*), RM inoculated with wild-type RhCMV(gag) displayed boosting of the RhCMV-specific T cell response and developed a SIVgag-specific immune response (Fig. 3, A and B, insets). They also secreted SIVgag-expressing virus (Fig. 3C). In contrast, we did not detect SIVgag-specific T cell responses in PBMC or BAL in RM inoculated with ΔVIHCEΔUS2-11(gag), even after repeated inoculation (Fig. 3, A and B), and SIVgag-expressing virus was not detected in secretions (Fig. 3C). These results suggested that MHC-I interference was essential for superinfection. Inoculation of the same animals with ΔUS2-11(gag) and, later, ΔVIHCE(gag) demonstrated that superinfection required the conserved US2-11 region but not the VIHCE region. The development of SIVgag-specific CD4$^+$ and CD8$^+$ T cell responses in blood and BAL (Fig. 3, A and B), as well as the boosting of preexisting RhCMV-specific CD4$^+$ and CD8$^+$ T cell responses in blood (Fig. 3A), or shedding of SIVgag-expressing RhCMV (Fig. 3D) were only detectable after challenge with ΔVIHCE(gag) but not with ΔUS2-11(gag).

Our results show that genes within the US2-11 region are essential for superinfection, which

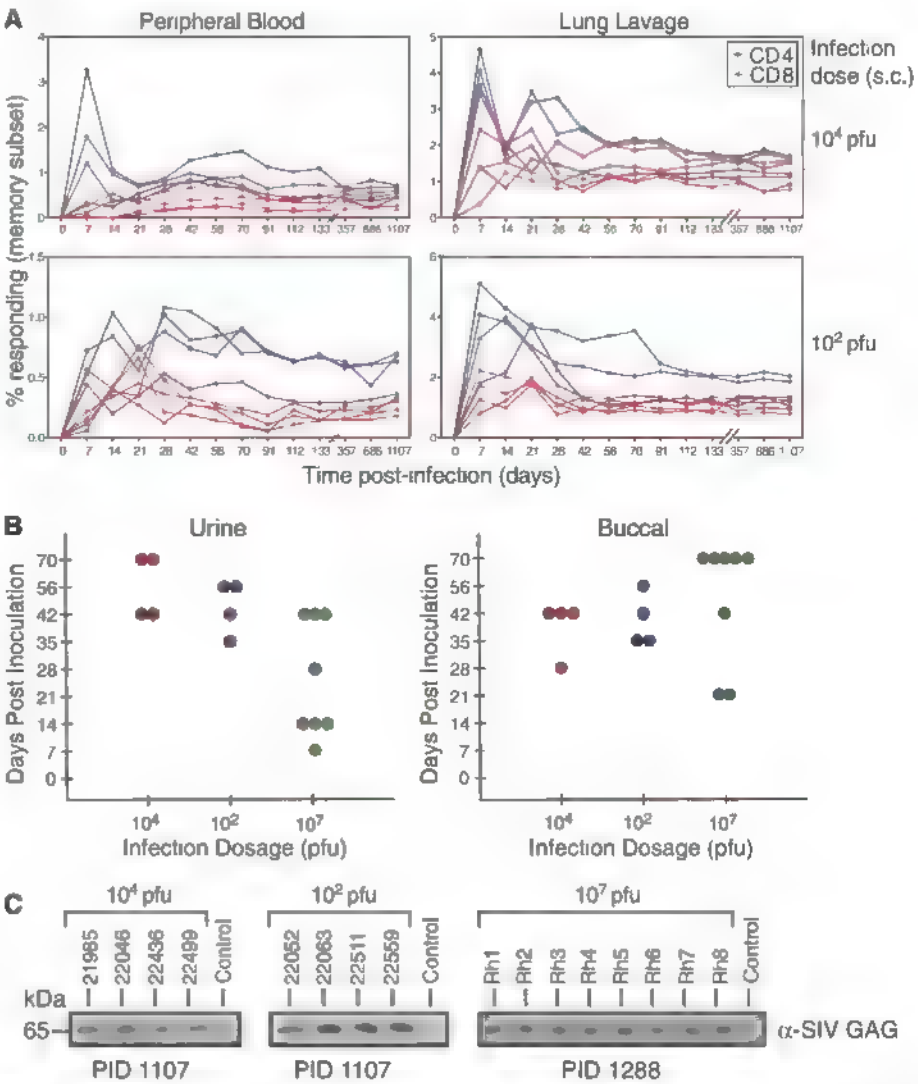

Fig. 1. Superinfection of RhCMV-positive animals is independent of viral dose. (**A**) At day 0, two cohorts of four RhCMV$^+$ animals each were infected subcutaneously with 10^2 or 10^4 PFU of RhCMV(gagL). The SIVgag-specific T cell responses in PBMC or in BAL were monitored by flow cytometric analysis of ICCS for CD69 and tumor necrosis factor–α (TNF-α) (*8*) (figs. S2 and S3). (**B**) Day of first detection of SIVgag-expressing virus in the urine or buccal swabs collected at the indicated intervals from each animal in the two cohorts shown in (A). Also included are results from a third cohort of eight RhCMV$^+$ animals inoculated with 10^7 PFU of RhCMV(gagL). Expression of SIVgag was determined by immunoblot using antibody to SIVgag from viral cocultures (*8*). Each circle represents an individual animal. (**C**) Long-term secretion of SIVgag-expressing virus. Urine was isolated at the indicated days post-infection (PID) from each of the RhCMV(gagL)-infected RM, and SIVgag expression was detected from cocultured virus by immunoblot. For control, a RhCMV-positive animal that did not receive RhCMV(gagL) was included.

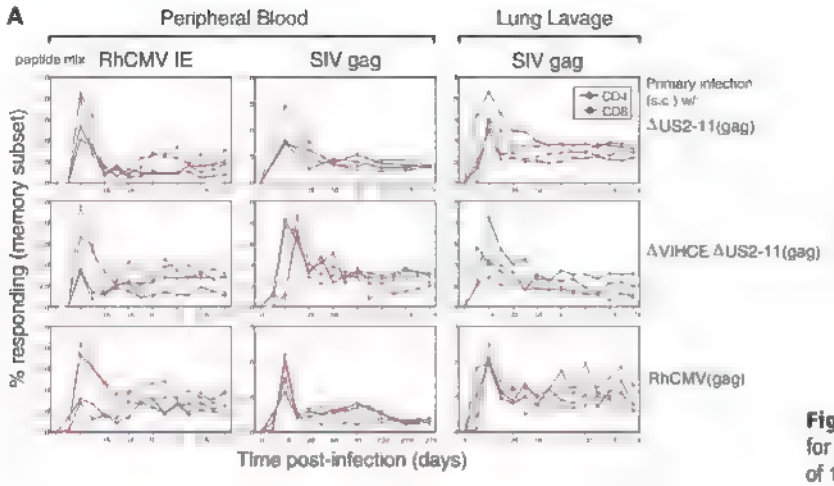

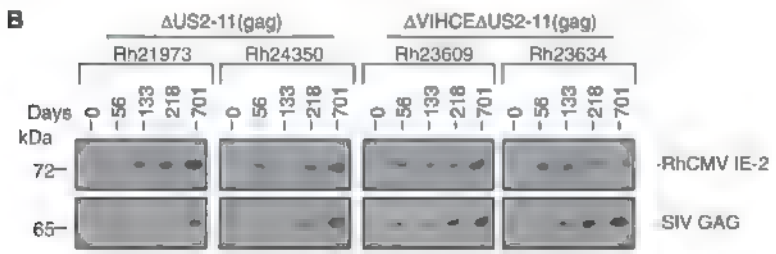

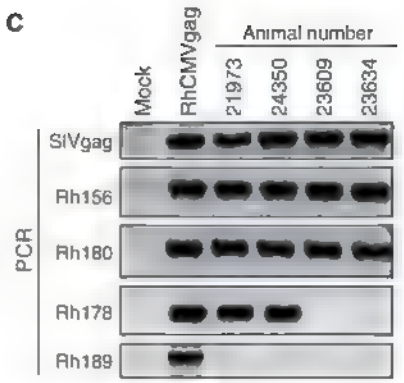

Fig. 2. Interference with MHC-I assembly is not required for primary infection of CMV-naïve animals. Three cohorts of two RM each were inoculated subcutaneously with 10^7 PFU of recombinant ΔUS2-11(gag), ΔVIHCEΔUS2-11(gag), or RhCMV(gag). (**A**) The RhCMV-specific T cell response in PBMC and the SIVgag-specific T cell response in PBMC and BAL were determined at the indicated days post-infection using overlapping peptides to RhCMV immediate early genes IE1 and IE2 or SIVgag by flow cytometric analysis of ICCS for CD69, TNF-α, and interferon-γ (IFN-γ) (*8*) (figs. S2 and S3). (**B**) Immunoblot of RhCMV-IE2 or SIVgag expressed in cocultures of urine samples obtained from animals infected with ΔUS2-11(gag) or ΔVIHCEΔUS2-11(gag). The IE2 blot confirms that the animals were negative for RhCMV before infection, consistent with results from T cell assays (table S1B). (**C**) PCR analysis of viral genomic DNA isolated from viral cocultures at 428 days post-infection. The presence or absence of indicated ORFs was determined by PCR using specific primers (*8*). One of the animals infected with RhCMV(gag) served as a control.

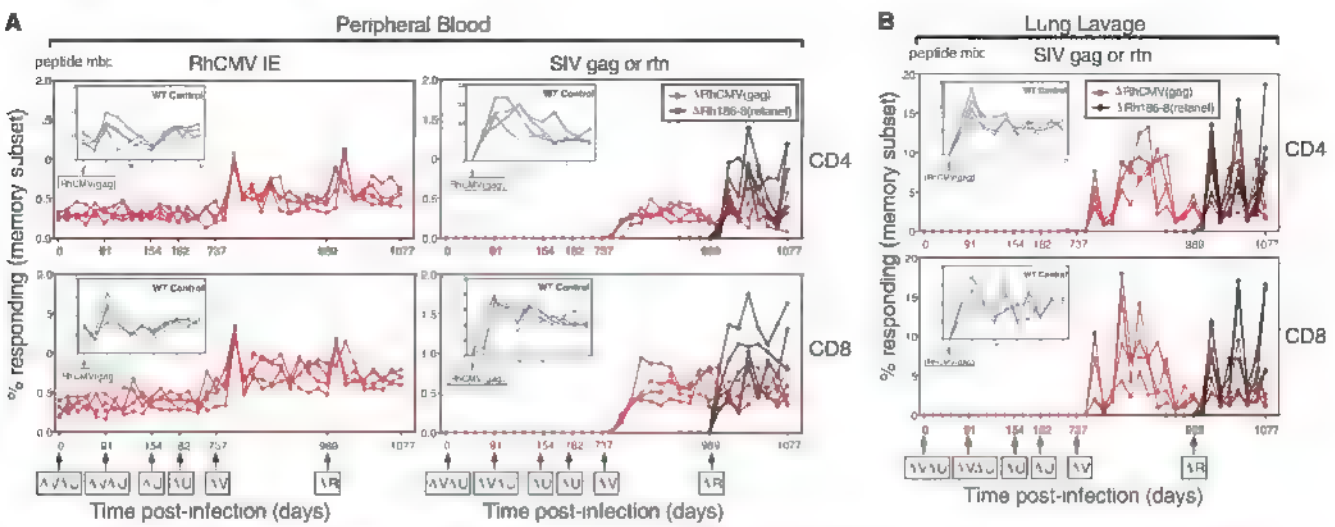

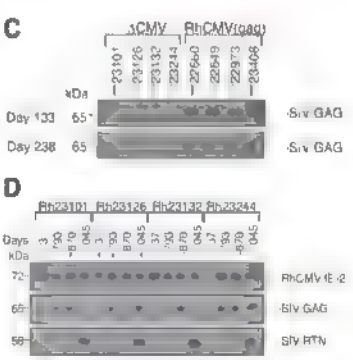

Fig. 3. US2-11-deleted RhCMV is unable to superinfect RhCMV$^+$ rhesus macaques. (**A**) A cohort of four RhCMV$^+$ RM was inoculated subcutaneously with 10^7 PFU of ΔVIHCEΔUS2-11(gag) (ΔVΔU) at days 0 and 91. The CD4$^+$ and CD8$^+$ T cell response to SIVgag or RhCMV-IE was monitored by flow cytometric analysis of ICCS for CD69, TNF-α, and IFN-γ in PBMC. The percentage of the responding, specific T cells within the overall memory subset is shown for each time point. At day 154 and again on day 224, the same cohort was inoculated with 10^7 PFU of ΔUS2-11(gag) (ΔU), and RhCMV-IE and SIVgag-specific T cell responses were monitored bi-weekly. At day 737, the cohort was inoculated with ΔVIHCE(gag) (ΔV), and the T cell response was monitored as before. At day 989, the cohort was inoculated with ΔRh186-8(retanef) (ΔR). Besides SIVgag, a T cell response to SIVrev/nef/tat was detected by ICCS in all four animals (black lines) using corresponding overlapping peptides. (Inset) A separate cohort of four animals was infected with wild-type RhCMV(gag), and the RhCMV-IE and SIVgag-specific CD4$^+$ and CD8$^+$ T cell response was monitored as described above at the indicated time points for 133 days. (**B**) The CD4$^+$ and CD8$^+$ T cell response to SIVgag in BAL was measured in parallel to the PBMC T cell responses shown in (A). (**C**) RhCMV secreted in the urine collected from the cohort infected with RhCMV(gag), or deletion viruses ΔVIHCEΔUS2-11(gag) or ΔUS2-11(gag), labeled ΔCMV. Virus was isolated at the indicated days by coculture with telomerized rhesus fibroblasts (TRFs), and cell lysates were probed for expression of SIVgag by immunoblot. (**D**) Expression of RhCMV IE2, SIVgag, and SIVretanef by virus secreted in urine collected at the indicated days. Note that all animals were IE2-positive at the onset of the experiment, confirming their RhCMV-positive T cell status (table S1D).

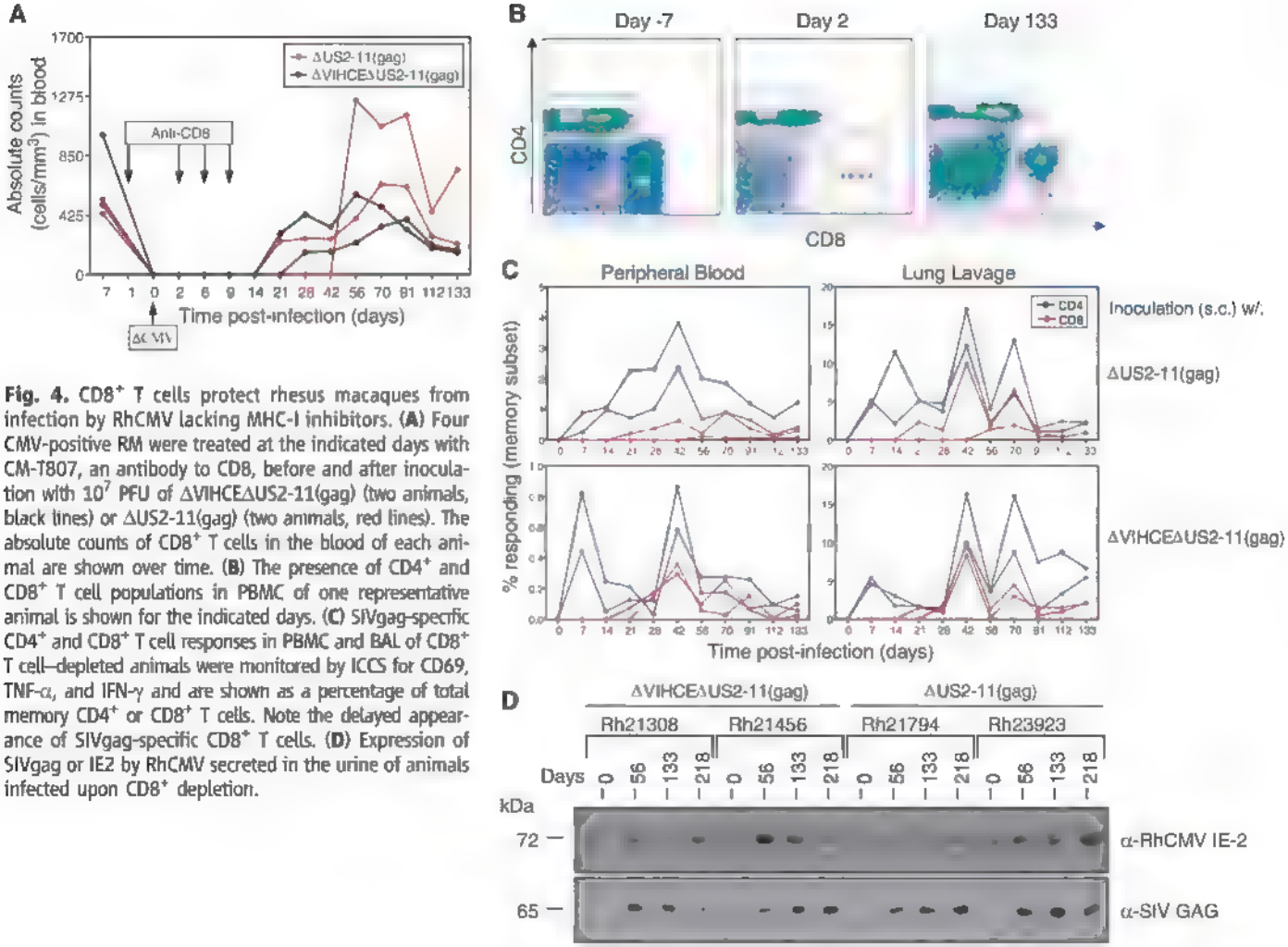

Fig. 4. $CD8^+$ T cells protect rhesus macaques from infection by RhCMV lacking MHC-I inhibitors. **(A)** Four CMV-positive RM were treated at the indicated days with CM-T807, an antibody to CD8, before and after inoculation with 10^7 PFU of ΔVIHCEΔUS2-11(gag) (two animals, black lines) or ΔUS2-11(gag) (two animals, red lines). The absolute counts of $CD8^+$ T cells in the blood of each animal are shown over time. **(B)** The presence of $CD4^+$ and $CD8^+$ T cell populations in PBMC of one representative animal is shown for the indicated days. **(C)** SIVgag-specific $CD4^+$ and $CD8^+$ T cell responses in PBMC and BAL of $CD8^+$ T cell–depleted animals were monitored by ICCS for CD69, TNF-α, and IFN-γ and are shown as a percentage of total memory $CD4^+$ or $CD8^+$ T cells. Note the delayed appearance of SIVgag-specific $CD8^+$ T cells. **(D)** Expression of SIVgag or IE2 by RhCMV secreted in the urine of animals infected upon $CD8^+$ depletion.

is consistent with the known function of US2, US3, US6, and US11 as inhibitors of MHC-I antigen presentation. There are, however, three genes of unknown function (Rh186 to Rh188) encoded between US6 and US11. Rh186 and Rh187 are most closely related to the HCMV glycoproteins US8 and US10, respectively (*14*), whereas Rh188 is an uncharacterized RhCMV-specific ORF. Although binding of HCMV-US8 and US10 to MHC-I has been reported, it is unclear whether this affects antigen presentation because MHC-I surface expression is not reduced by US8 or US10 from either HCMV or RhCMV (*14*, *16*, *17*). To determine whether Rh186, Rh187, or Rh188 are required for superinfection, we generated deletion virus ΔRh186-8. To enable us to monitor superinfection by this recombinant in the same cohort of animals that had already been reinfected with ΔVIHCE(gag), we applied a distinct immunological marker, SIVretanef, a fusion-protein consisting of SIV proteins rev, tat, and nef (*3*). ΔRh186-8(retanef) is deleted for Rh186-188 and contains the Retanef expression cassette between the ORFs Rh213 and Rh214 (fig. S1). We inoculated the same cohort with ΔRh186-8(retanef) and monitored the T cell response to this fusion protein as well as to RhCMV-IE and SIVgag using corresponding peptides. As shown in Fig. 3, A and B, all four RM developed a SIVretanef-specific T cell response within 2 weeks post-challenge, indicating successful superinfection. Moreover, virus expressing SIVretanef was shed in the secretions of infected animals together with SIVgag-expressing ΔVIHCE(gag) (Fig. 3D). We thus conclude that the Rh186-8 region is dispensable for superinfection.

Together, our results suggested that RhCMV was unable to superinfect in the absence of the homologs of US2, US3, US6, and US11 because the virus was no longer able to avoid elimination by CTL. To further examine this hypothesis, a new group of $RhCMV^-$ RM (table S1D) was depleted for $CD8^+$ lymphocytes by treatment with cM-T807, a humanized monoclonal antibody to CD8, before superinfection with ΔUS2-11(gag) or ΔVIHCEΔUS2-11(gag). Flow cytometric analysis of total $CD8^+$ T cells revealed that depletion was extensive, but transient, with detectable $CD8^+$ T cell recovery beginning on day 21 after challenge (Fig. 4, A and B). Upon inoculation with ΔUS2-11(gag) or ΔVIHCEΔUS2-11(gag), SIVgag-specific $CD4^+$ T cell responses were recorded as early as day 7 post-challenge, showing the ability of the deletion viruses to superinfect these animals (Fig. 4C). Moreover, SIVgag-specific $CD8^+$ T cells were observed within the rebounding $CD8^+$ T cells in blood and BAL at day 21 in two RM and at day 28 in a third; in the fourth RM, such responses were only observed in BAL after day 56. From these data, we conclude that $CD8^+$ lymphocytes, most likely $CD8^+$ T cells, were essential for preventing superinfection by ΔUS2-11 virus, strongly indicating that the MHC-I inhibitory function of these molecules is necessary for superinfection of the CMV-positive host. Notably, CMV-specific $CD8^+$ T cells were unable to eliminate RhCMV lacking MHC-I inhibitors once persistent infection had been established (Fig. 4D), providing additional evidence that persistent infection is insensitive to $CD8^+$ T cell immunity, even when the ability of the virus to prevent MHC-I presentation is compromised.

Our data imply that T cell evasion is not required for establishment of primary CMV infection or once the sites of persistence (e.g., kidney and salivary gland epithelial cells) have been occupied, but rather it is essential to enable CMV to reach these sites of persistence from the peripheral site of inoculation in the CMV-immune host. One possible scenario is

that viral infection of circulating cells, for example, monocytes, can succeed only if the virus prevents elimination of these cells by virus-specific CTLs. More work, however, will be required to identify the cell type supporting superinfection

Although the biochemical and cell biological functions of US2, US3, US6, and US11 have been studied extensively (*18*), their role in viral pathogenesis had remained enigmatic. Analogous gene functions in murine CMV (MCMV) had been similarly found to be dispensable for both primary and persistent infection (*10*), although reduced viral titers have been reported for MCMV deleted for these genes (*19*). Thus, the reason all known CMVs dedicate multiple gene products to MHC-I down-regulation had remained elusive. Our current results now identify a critical role for these immunomodulators to enable superinfection of the CMV-positive host. Furthermore, these results suggest that the ability to superinfect is an evolutionary conserved function among CMVs and therefore might play an important role in the biology of these viruses. Superinfection could promote the maintenance of genetic diversity of CMV strains in a highly infected host population, which could provide an evolutionary advantage. However, there is another possibility. CMV is a large virus with thousands of potential T cell epitopes and therefore a high potential for $CD8^+$ T cell cross-reactivity (*20*). Indeed, in a study of pan-proteome HCMV T cell responses, 40% of HCMV seronegative subsets manifested one or more cross-reactive $CD8^+$ T cell responses to HCMV-encoded epitopes (5). As CMV recognition by cytotoxic T cells appears to effectively block primary CMV infection, individuals with cross-reactive $CD8^+$ T cell immunity might be resistant to CMV. Thus, US2-11 function may be necessary to evade such responses and establish infection in this large population of individuals that might otherwise be CMV-resistant.

Our results also may explain why, so far, it has not been possible to develop a vaccine that efficiently protects humans from HCMV infection. Although antibody-mediated mucosal immunity might reduce the rate of superinfection (*7*, *21*), once this layer of defense is breached, CMV-specific CTLs seem to be unable to prevent viral dissemination, due to MHC-I down-regulation by US2-11. Thus, although CMV-vaccines might be able to limit CMV viremia and associated morbidity, this MHC-I interference renders it unlikely that sterilizing protection against CMV infection is an achievable goal

References and Notes

1. S. B. Boppana, L. B. Rivera, K. B. Fowler, M. Mach, W. J. Britt, *N. Engl. J. Med.* **344**, 1366 (2001).
2. S. Gorman *et al.*, *J. Gen. Virol.* **87**, 1123 (2006)
3. S. G. Hansen *et al.*, *Nat. Med.* **15**, 293 (2009)
4. U. Meyer-Konig, K. Ebert, B. Schrage, S. Pollak, F. T. Hufert, *Lancet* **352**, 1280 (1998)
5. A. W. Sylwester *et al.*, *J. Exp. Med.* **202**, 673 (2005).
6. S. P. Adler *et al.*, *J. Infect. Dis.* **171**, 26 (1995)
7. S. A. Plotkin, S. E. Starr, H. M. Friedman, E. Gönczöl, R. E. Weibel, *J. Infect. Dis.* **159**, 860 (1989)
8. Materials and methods are available as supporting material on *Science* Online
9. E. A. Walter *et al.*, *N. Engl. J. Med.* **333**, 1038 (1995)
10. A. K. Pinto, A. B. Hill, *Viral Immunol.* **18**, 434 (2005).
11. F. J. van der Wal, M. Kikkert, E. Wiertz, *Curr. Top. Microbiol. Immunol.* **269**, 37 (2002)
12. Z. Lu, M. Winkler, B. Biegalke, *Int. J. Biochem. Cell Biol.* **41**, 503 (2009)
13. E. W. Hewitt, S. S. Gupta, P. J. Lehner, *EMBO J.* **20**, 387 (2001).
14. N. T. Pande, C. Powers, K. Ahn, K. Früh, *J. Virol.* **79**, 5786 (2005)
15. C. J. Powers, K. Früh, *PLoS Pathog.* **4**, e1000150 (2008)
16. R. S. Tirabassi, H. L. Ploegh, *J. Virol.* **76**, 6832 (2002)
17. M. H. Furman, N. Dey, D. Tortorella, H. L. Ploegh, *J. Virol.* **76**, 11753 (2002)
18. C. Powers, V. DeFilippis, D. Malouli, K. Früh *Curr. Top. Microbiol. Immunol.* **325**, 333 (2008)
19. A. Krmpotic *et al.*, *J. Exp. Med.* **190**, 1285 (1999)
20. L. K. Selin *et al.*, *Immunol. Rev.* **211**, 164 (2006)
21. R. F. Pass *et al.*, *N. Engl. J. Med.* **360**, 1191 (2009)

22. We are grateful to P. Barry for providing the RhCMV-GFP and RhCMV BAC and M. Messerle for plasmid ori6k-F5. The N. H. Nonhuman Primate Reagent Resource Program provided the CD8α-specific antibody cM-T807 used in this work (contracts AI040101 and RR016001), which was originally obtained from Centocor, Inc. We thank A. Townsend for help with the graphics. We thank D. Drummond, L. Coyne-Johnson, M. Spooner Lewis, C. Hughes, N. Whizin, M. Giday, J. Clock, J. Cook, J. Edgar, J. Dewane, and A. Legasse for technical assistance. This research was supported by the National Institutes of Health (RO1 AI059457 to K.F. and RO1 A.060392 to L.J.P.), the International AIDS Vaccine Initiative (to L.J.P.), the National Center for Research Resources (RR016025 and RR18107 to M.K.A., RR00163 supporting the Oregon National Primate Research Center), the Ruth L. Kirschstein National Research Service Awards T32 AI007472 (to C.J.P.) and T32 HL007781 (to R.R.), the OHSU Tartar Trust fellowship (to C.J.P.), and the Achievement Reward for College Scientists (to R.R.). The CMV vector technology has been patented by Oregon Health and Science University (US2008/0199493A1) with L.J.P., J.A.N., and M.A.J. as conventors. This patent has been licensed to the International AIDS Vaccine Initiative. The comparative genome sequencing data shown in fig. S5 were deposited in the Gene Expression Omnibus database (accession number GSE20308)

Supporting Online Material

www.sciencemag.org/cgi/content/full/328/5974/102/DC1
Materials and Methods
Figs. S1 to S5
Table S1
References

1 December 2009; accepted 5 February 2010
10.1126/science.1185350

Synchrony of Thalamocortical Inputs Maximizes Cortical Reliability

Hsi-Ping Wang,[1,2]* Donald Spencer,[1] Jean-Marc Fellous,[3] Terrence J. Sejnowski[1,2]

Thalamic inputs strongly drive neurons in the primary visual cortex, even though these neurons constitute only ~5% of the synapses on layer 4 spiny stellate simple cells. We modeled the feedforward excitatory and inhibitory inputs to these cells based on in vivo recordings in cats, and we found that the reliability of spike transmission increased steeply between 20 and 40 synchronous thalamic inputs in a time window of 5 milliseconds, when the reliability per spike was most energetically efficient. The optimal range of synchronous inputs was influenced by the balance of background excitation and inhibition in the cortex, which could gate the flow of information into the cortex. Ensuring reliable transmission by spike synchrony in small populations of neurons may be a general principle of cortical function.

Neurons can perform coincidence detection of synaptic inputs with a temporal integration window that depends on the time courses of the synaptic conductances and the intrinsic properties of the postsynaptic neuron (*1*). Synchronous cortical inputs occur when there is a salient event in the sensory environment, such as the entrance of a moving object into a receptive field (*2*) or the deflection of a whisker in rodent (*3*). The precise timing of action potentials has been shown to potentially provide information in addition to the spike rate (*2*, *4*–*7*). For a population of presynaptic neurons to fire nearly simultaneously, however, requires resources to time spike initiation precisely, parallel anatomical pathways to carry the spikes, and energy costs for redundant spikes, which may outweigh the benefits of increased information rate (*8*, *9*). We explored these issues in the projections from the lateral geniculate nucleus (LGN) to the primary visual cortex.

The question of efficient information transfer is particularly important for thalamocortical connections, because thalamic synaptic inputs,

[1]Howard Hughes Medical Institute, Computational Neurobiology Laboratory, Salk Institute, La Jolla, CA 92037, USA. [2]Division of Biological Sciences, University of California San Diego, La Jolla, CA 92093, USA. [3]Department of Psychology and Applied Mathematics Program, University of Arizona, Tucson, AZ 85721, USA.

*To whom correspondence should be addressed. E-mail: ping@salk.edu

which are comparable in strength to cortical inputs, constitute only ~5% of the total synaptic input to cortical simple cells (*10*–*12*), but are nonetheless capable of reliably driving cortical neurons. To examine the relationship between synchrony and reliability, we performed computer simulations of a detailed biophysical model of a spiny stellate cell in layer 4 of area V1 (*13*) of the cat primary visual cortex (Fig. 1A). This cell received 300 synaptic inputs from the LGN, competing with 5500 other excitatory and inhibitory intracortical synapses, including feedforward inhibition. All synapses were stochastic, and the excitatory synapses included short-term history-dependent modulation of release probability. We used this model to quantify the number of synchronous synaptic inputs that maximizes the efficient transfer of information to the cortical cell, and we compared these predictions to experimental data obtained in vivo from anesthetized cats (*14*).

The pairwise correlation strength between two neurons is often used to estimate their degree of synchrony (*15*, *16*). In the visual thalamocortical pathway, correlated spikes from two presynaptic LGN neurons strongly increase the probability of firing in a postsynaptic primary visual cortex (V1) simple cell (*17*–*19*) and ensure the transfer of information from the thalamus to the cortex, despite a low probability of synaptic transmission (*3*, *20*). Our simulations support these results by showing that spike output reliability can be predicted by synchrony magnitude (SM), which is the number of thalamocortical synapses that are simultaneously driven by the same presynaptic thalamic spike train. Simultaneous recordings from more than two LGN neurons would be needed to measure the SM directly.

We compared the output of our model with in vivo recordings from Kara *et al.* (*21*), who simultaneously recorded spike trains from retinal ganglion cells, LGN relay cells, and cortical cells in the primary visual pathway of anesthetized cats. The visual stimulus was a drifting grating, which produced patterns of spikes without highly synchronous events, as occurs with flickering visual stimuli (*2*). The presynaptic spike times from the in vivo recordings of LGN cells were distributed across a varying number of input synapses in the model (Fig. 1, B to D), as well as across an inhibitory feedforward pathway leading to the spiny stellate cell. This pattern was transformed by the synapses into a sequence of neurotransmitter releases (Fig. 1, E to G) and integrated with the cortical background inputs to produce a fluctuating membrane potential (Fig. 1, H to J, and figs. S1 and S2). The average firing rate and the reliability (*22*) of the cortical cell spike pattern was then computed across 30 repeated 250-ms trials (Fig. 1, K to N), each using a different LGN cell spike pattern from the in vivo recordings (*14*).

Output reliability was a highly nonlinear function of SM, rising steeply from 20 to a maximum at 40 synapses (Fig. 2A), more rapidly than the output firing rate (Fig. 2C). The reliability-per-SM (RPSM) function, defined by dividing the reliability by the SM, reached an optimal synchrony magnitude (OSM) at approximately 30 synapses (Fig. 2B, dashed line). The reliability-per-spike (RPS) ratio, a measure of the reliability increase for each additional output spike computed by dividing each reliability output by its corresponding firing rate, also peaked at approximately 30 synchronous synapses (Fig. 2D). Similar results were obtained when the synaptic inputs were generated from groups of five synchronous inputs corresponding to single LGN afferents with each group from a different recorded LGN input (fig. S2).

In experimental recordings from thalamic and cortical cells, the trial-to-trial spike-count variability was low (*21*, *23*), indicating that the spike rates of these cells conveyed important information about the input stimulus. Using spike trains from LGN recordings as inputs to the model cell (*21*), we also found low spike-count variability. The Fano factor (FF), defined as the sample variance divided by sample mean, achieved a minimum of 0.2 to 0.4 in the range of 20 to 80 synchronous synapses (fig. S4).

The quantitative analysis of output reliability can be used to predict the number of synchronous inputs that drive cortical cell responses during in vivo behavioral experiments (Fig. 3). We plotted data from in vivo recordings of V1 cells supplied by Kara *et al.* (*21*) against the transfer function of input synchrony as a function of output reliability, as determined by our model, to infer synchrony magnitude of the cells in vivo. Each of the four neurons (from different animals) predicted input synchrony in the range of 20 to 60 synchronous synapses (Fig. 3). The reliability and

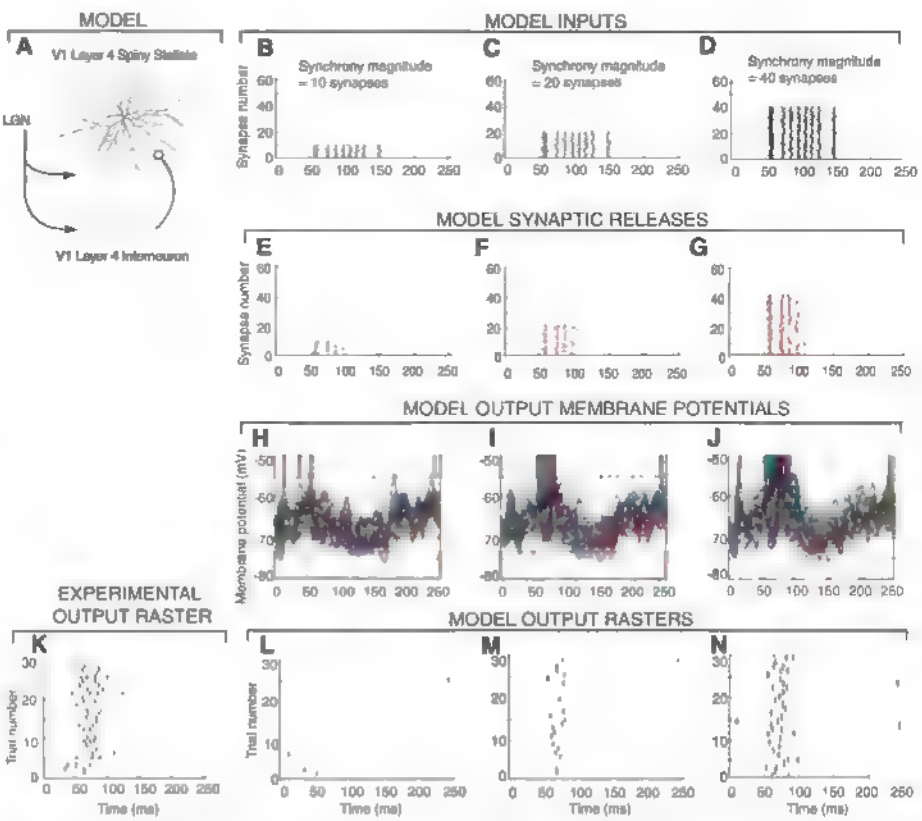

Fig. 1. Varying the synchrony of input synapses affects output reliability and firing rates. (**A**) Morphology of a reconstructed V1 layer 4 spiny stellate cell that was modeled with 748 compartments, thalamocortical (TC) synapses with a release probability of $P = 0.2$ and short-term plasticity (*13*, *14*), and a feedforward inhibitory interneuron that receives input from LGN and projects to the spiny stellate cell. (**B** to **D**) Rastergrams of 60 thalamocortical synaptic inputs into the model cell for one trial. An input spike train obtained from in vivo LGN recordings (*21*) (referred to as event times) was repeated on a number of input synapses (SM). The input events were time jittered on average by 1 ms and had 1 out of 10 spikes randomly deleted. (**E** to **G**) Synaptic release rastergram for inputs (B to D). (**H** to **J**) Superimposed spiny stellate membrane potentials from 30 trials. (**K**) Cortical cell output spike trains from experimental in vivo recordings (*21*). (**L** to **N**) Rastergrams of outputs from 30 trials of inputs based on different LGN spike trains from the in vivo data

firing rate at the OSM from our model (Fig. 2, stars), using recorded thalamic input spike trains, fall within the observed ranges of the experimental values (Fig. 3E).

These results were robust to increasing the jitter and varying the strengths of thalamic inputs and feedforward inhibitory synapses (Fig. 4, A and B, and fig. S4). However, the OSM depended on the balance between background excitatory (E) and inhibitory (I) inputs to the 5500 intracortical synapses. When the integrated inputs were balanced (total average excitatory input equal to the total average inhibitory input), the neuron became highly sensitive to correlated fluctuations of the membrane potential, which affected the reliability (*23*) as well as the gain of the input spike rate to output spike rate curve (*24*). We varied the cortical background rate and the ratio of inhibitory to excitatory input rates, $\beta = I/E$, to assess their influence on the reliability of the synchronous inputs to LGN synapses (Fig. 4C and fig. S3). Background excitatory inputs above 1 spikes depressed the reliability response by directly competing with the LGN excitatory inputs and introducing high levels of spurious output firing. Increasing the background inhibition also increased the OSM and was therefore a potential mechanism for setting the threshold for synchrony detection. The sensitivity of the cortex to synchronous inputs can be varied over a wide range by regulating β.

Spiking due to input synchrony may be a way to ensure that important events are registered by the spiny stellate neurons in the cortex, regardless of asynchronously arriving spikes from ongoing cortical computation. This prediction could be tested with intracellular recordings in vivo by using a dynamic clamp (*25*) to inject somatic conductances reflecting events in the presence of in vivo background noise.

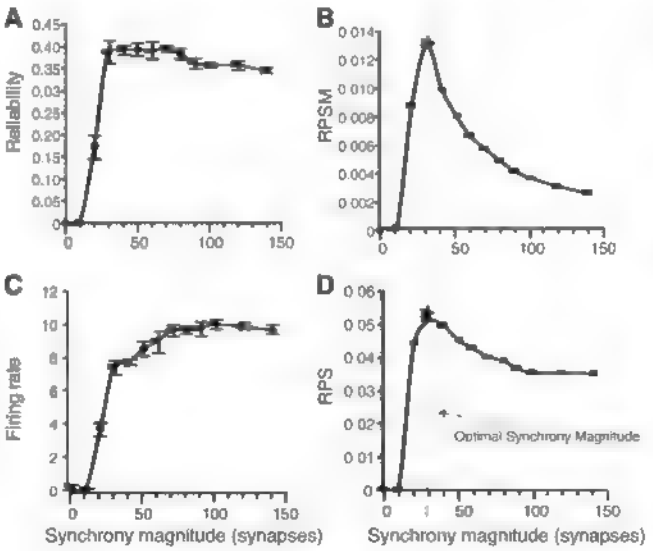

Fig. 2. Average spike-time reliability, firing rate, and efficiency measures as a function of synchrony magnitude for inputs as described in Fig. 1. Standard deviation bars plotted using data from 10 sets of simulations with 30 independent trials each. **(A)** Output spike reliability. **(B)** RPSM has a peak at a synapse synchrony magnitude of 30 (vertical dashed line). **(C)** Firing rate responses. **(D)** RPS efficiency (reliability/firing rate) also peaked at 30 synchronous synapses.

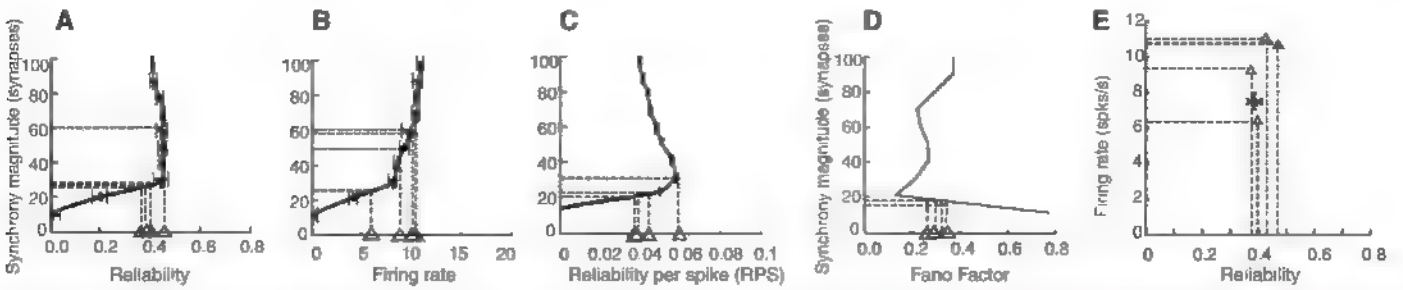

Fig. 3. Predicted input synchrony ranges for in vivo recordings. Graphs from Fig. 2 were inverted to make synchrony magnitude the dependent variable. In each plot, four triangles are positioned along the x axis (input value), corresponding to in vivo experimentally measured values from four separate animals (*21*), and the inferred output synchrony magnitude is shown as a horizontal dashed line from the first intersection on each curve. Predictions were made based on **(A)** reliability, **(B)** firing rates, **(C)** RPS, and **(D)** FF (taken from fig. S4C). **(E)** The predicted firing rate and reliability at SM = 30 (solid circle with error bars indicating SD) is plotted along with the measured values from the four sets of recordings (triangles). Despite the small sample of cells with enough trials, the estimated reliabilities cluster around 0.4.

Fig. 4. Effect of input jitter, inhibitory interneuron strength, and the balance of inhibitory and excitatory background inputs on the predicted OSM. **(A)** The jitter of the input event signals was varied from 0 to 30 ms. The default used in Figs. 1 to 3 used jitter = 1 ms. **(B)** The number of synapses from the feedforward inhibitory interneurons was varied from 0 to 1000 synapses. The default used in Figs. 1 to 3 was 200 synapses. **(C)** The Poisson-distributed presynaptic spike trains for the 4500 excitatory (glutamate) and 1000 inhibitory (γ-aminobutyric acid) intracortical synapses were covaried from 1 to 3 spikes/s excitatory background inputs and 1 to 15 spikes/s inhibitory background inputs. The default in Figs. 1 to 3 was 1 excitatory spike/s and 5 inhibitory spikes/s.

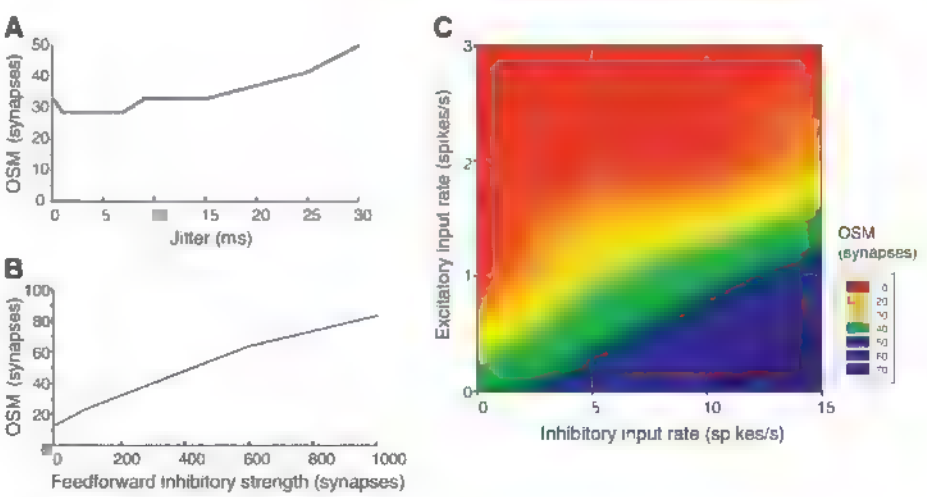

Moving visual inputs give rise to synchronous spikes in retinal ganglion cells (*26*). A single retinal ganglion cell can drive four or more LGN cells (*27*), which can make one to eight synapses each (*28*), with a spiny stellate cell in V1 with overlapping receptive fields (*17*). Thus, assuming an average of four synapses for each LGN axon and an OSM of 20 to 40, as few as 5 to 10 LGN cells could effectively drive a cortical neuron. This prediction could be tested by studying the effects of modulating the contrast of visual stimuli on the firing rates and reliability of spike timing in cortical cells (*21*, *29*). Cortical feedback to the thalamus could also regulate the degree of synchrony among thalamocortical cells.

We have quantified the number of synchronous thalamic spikes needed to reliably report a major sensory event to cortical neurons (*19*), which is consistent with previous physiological experiments that found correlated firing with 1-ms precision in visual cortex (*4*, *17*) and mouse barrel cortex (*3*). Spike synchrony, through converging anatomical pathways, enhances the information transfer rate and speeds up processing (*30*, *31*)

The output spike pattern of a layer 4 neuron is thus determined by the temporal pattern, as well as the rate, of the synchronous thalamic inputs according to the history-dependent dynamics of its synapses acting coherently within 6 to 8 ms. The same analytical methods used here could be applied to study reliability and connectivity in other types of neurons. Spike synchrony, observed throughout the cortex, may also have a more general function in ensuring information transmission between cortical areas (*32*).

References and Notes

1. E. Salinas, T. J. Sejnowski, *Nat. Rev. Neurosci.* **2**, 539 (2001)
2. P. Reinagel, R. C. Reid, *J. Neurosci.* **20**, 5392 (2000)
3. R. M. Bruno, B. Sakmann, *Science* **312**, 1622 (2006)
4. Y. Dan, J. M. Alonso, W. M. Usrey, R. C. Reid, *Nat. Neurosci.* **1**, 501 (1998)
5. D. S. Reich, F. Mechler, K. P. Purpura, J. D. Victor, *J. Neurosci.* **20**, 1964 (2000)
6. W. M. Usrey, *Curr. Opin. Neurobiol.* **12**, 411 (2002)
7. R. D. Kumbhani, M. J. Nolt, L. A. Palmer, *J. Neurophysiol.* **98**, 2647 (2007)
8. D. R. Humphrey, E. M. Schmidt, W. D. Thompson, *Science* **170**, 758 (1970)
9. E. Salinas, L. F. Abbott, *J. Comput. Neurosci.* **1**, 89 (1994)
10. E. L. White, *Cortical Circuits. Synaptic Organization of the Cerebral Cortex—Structure, Function and Theory* (Birkhauser, Boston, 1989)
11. A. Peters, B. R. Payne, *Cereb. Cortex* **3**, 69 (1993)
12. B. Ahmed, J. C. Anderson, R. J. Douglas, K. A. Martin, J. C. Nelson, *J. Comp. Neurol.* **341**, 39 (1994)
13. Z. F. Mainen, T. J. Sejnowski, *Nature* **382**, 363 (1996)
14. Methods are available as supporting material on *Science* Online
15. W. M. Usrey, *Philos. Trans. R. Soc. London Ser. B* **357**, 1729 (2002)
16. W. M. Usrey, R. C. Reid, *Annu. Rev. Physiol.* **61**, 435 (1999)
17. J. M. Alonso, W. M. Usrey, R. C. Reid, *Nature* **383**, 815 (1996)
18. P. Kara, R. C. Reid, *J. Neurosci.* **23**, 8547 (2003)
19. W. M. Usrey, J. M. Alonso, R. C. Reid, *J. Neurosci.* **20**, 5461 (2000)
20. J. de la Rocha, B. Doiron, E. Shea-Brown, K. Josic, A. Reyes, *Nature* **448**, 802 (2007)
21. P. Kara, P. Reinagel, R. C. Reid, *Neuron* **27**, 635 (2000)
22. S. Schreiber, D. Whitmer, J. M. Fellous, P. Tiesinga, T. J. Sejnowski, *Neurocomputing* **52–54**, 925 (2003)
23. Z. F. Mainen, T. J. Sejnowski, *Science* **268**, 1503 (1995)
24. E. Salinas, T. J. Sejnowski, *J. Neurosci.* **20**, 6193 (2000)
25. A. A. Sharp, M. B. O'Neil, L. F. Abbott, E. Marder, *J. Neurophysiol.* **69**, 992 (1993)
26. S. Chatterjee, D. K. Merwine, F. R. Amthor, N. M. Grzywacz, *Vis. Neurosci.* **24**, 827 (2007).
27. J. E. Hamos, S. C. Van Horn, D. Raczkowski, S. M. Sherman, *J. Comp. Neurol.* **259**, 165 (1987).
28. T. F. Freund, K. A. C. Martin, D. J. Whitteridge, *Comp. Neurol.* **242**, 263 (1985)
29. E. Schneidman, M. J. Berry 2nd, R. Segev, W. Bialek, *Nature* **440**, 1007 (2006)
30. D. A. Butts *et al.*, *Nature* **449**, 92 (2007)
31. N. A. Lesica *et al.*, *Neuron* **55**, 479 (2007)
32. P. Tiesinga, J. M. Fellous, T. J. Sejnowski, *Nat. Rev. Neurosci.* **9**, 97 (2008)

33. We thank P. Kara, P. Reinagel, and R. C. Reid for sharing in vivo recordings of simultaneously recorded retinal, thalamic, and cortical neurons. K. Martin provided invaluable anatomical data on thalamocortical connectivity. This research was supported by the Howard Hughes Medical Institute and the NSF Science of Learning Center SBE-0542013

Supporting Online Material

www.sciencemag.org/cgi/content/full/328/5974/106/DC1
Materials and Methods
References

9 October 2009; accepted 5 March 2010
10.1126/science.1183108

NEW PRODUCTS FOCUS: ESSENTIAL LAB EQUIPMENT

VIBRATION ISOLATION

The Ergonomic Low-Profile-Format platform is a lightweight benchtop vibration isolation system designed for portability. It can be easily repositioned on the benchtop, even with a load and in float. An economical alternative to heavyweight models, it features a load capacity of 100 or 300 pounds. The platform has a low profile, uses a small tabletop, and weighs only 40 pounds. Ergonomic features include gauges tilted upward for easy viewing and recessed handles for easy carrying. Designed for use in laboratories and Class 100 cleanrooms, it is suitable for supporting atomic force microscopes, microhardness testers, analytical balances, profilometers, audio equipment, and more.

Kinetic Systems

For info: 617-522-8700 | www.kineticsystems.com

THERMAL CYCLERS

The TC-Plus thermal cyclers can be combined with satellite units to give the flexibility to configure any multiblock format. These thermal cyclers have one of the fastest aluminum blocks on the market, delivering greater uniformity than a silver block, and therefore more reproducible polymerase chain reaction results. The 5.7-inch VGA color touchscreen with graphical display is intuitive and easy to use. The TC-Plus features a patent-pending CD-drive-type sample drawer. The force used to push the drawer in also lowers the heated lid into position, applying the correct pressure onto the samples to prevent evaporation. The TC-Plus can accommodate all consumable types from 0.5-ml tubes to 384-well plates, sealed with either heat or adhesive seals.

Bibby Scientific

For info: +44-(0)-1785-812121 | www.bibby-scientific.com

NANOPOSITIONING STAGE

The SCR 100 stage is an ultrahigh-pressure, compact, single-axis stage that integrates a slide guide, encoder, and linear shaft motor. The stage features a moving magnet design, with all cables and connectors in the stationary base. With no moving cable, there are no motion errors due to cable forces. The precision-ground, cross-roller way provides high stiffness and smooth motion. The noncontact linear shaft motor and optical linear encoders are self-contained inside the stage. The optical linear encoder is available with resolutions from 1 micron to 10 nanometers with digital output. The linear shaft motor has no cogging, which gives it a higher resolution, speed, and continuous force than standard stepper motors and piezo servomotors.

Nippon Pulse America

For info: 540-633-1677 | www.nipponpulse.com

BENCHTOP COLD PLATES

The AHP1200CPV Cold Plate is a versatile instrument that can be enhanced by a wide range of accessories. These benchtop cold plates feature a design based on thermoelectric technology to cool or heat a surface plate. They are intended for laboratory, quality control and electrical component tests, and research applications. Biomedical applications include pain research, tissue dissection, histology, cold/hot dry wells, and sample cooling. The precision-machined, aluminum cold plate surface measures 5.8 inches by 13.3 inches, with a footprint of just 11.2 inches by 15.1 inches. In a 25°C environment, the cold plate surface is controllable from –15°C to +90°C. Options can extend that range to below –45°C and above +90°C. The cold plate includes an integral temperature control with remote sensing, precise adjustment of surface temperature within ±0.1°C, temperature cycling, ramping and soaking programs, and RS-232 communication.

Thermoelectric Cooling America Corporation

For info: 888-832-2872 | www.thermoelectric.com

UV-VISIBLE SPECTROPHOTOMETER

The Evolution 60S spectrophotometer is a powerful ultraviolet–visible light instrument with the flexibility to perform quality assurance, life science methods, and general research methods. It features a 1.0 nm spectral bandwidth, bringing a new level of clarity to measurements in an affordable, compact design. Its enhanced scanning technology can acquire high-quality spectral data at speeds greater than 4,200 nm per minute. It meets the stringent requirements of international pharmacopoeias and offers validation tools and protocols for users operating in regulated environments. The instrument's long-life xenon lamp requires no warm-up time, providing instant measurements and excellent performance over the wavelength range of 190–1,100 nm. The instrument includes a wide array of preprogrammed biological assays for analyzing protein and nucleic acid samples and performing cell growth measurements.

Thermo Fisher Scientific

For info: 800-532-4752 | www.thermo.com/uv-vis

Electronically submit your new product description or product literature information? Go to www.sciencemag.org/products/newproducts.dtl for more information. Newly offered instrumentation, apparatus, and laboratory materials of interest to researchers in all disciplines in academic, industrial, and governmental organizations are featured in this space. Emphasis is given to purpose, chief characteristics, and availability of products and materials. Endorsement by *Science* or AAAS of any products or materials mentioned is not implied. Additional information may be obtained from the manufacturer or supplier.

POSITIONS OPEN

USDA ARS Agricultural Research Service
www.ars.usda.gov

The U.S. Department of Agriculture, Agricultural Research Service, Vegetable Crops Research Unit, located at the University of Wisconsin in Madison is accepting applications for two permanent, full-time positions. (1) Interdisciplinary: **RESEARCH MOLECULAR BIOLOGIST (PLANTS)/RESEARCH GENETICIST PLANTS** GS-440/401-12/14. To lead research in cranberry germplasm enhancement, genetics, and genomics on a project developing germplasm enhanced for use by growers, consumers, and researchers, identifying traits useful for cranberry breeders, determining their inheritance, and developing tools for evaluating and broadening the knowledge base of cranberry. (2) **RESEARCH ENTOMOLOGIST,** GS-414-12/14. To lead research developing integrated approaches using new and especially reduced-risk technologies to manage cranberry insect pests. Both positions present rich opportunities to work in an interdisciplinary environment and to collaborate with faculty, staff, and industry. Salary is commensurate with experience ($68,809 to $125,695 per annum), plus benefits. *Candidates must be U.S. citizens.* For information on application procedures, visit full **vacancy announcement ARS-X10W-0095 and ARS-X10W-0098** at **website: http://www.afm.ars.usda.gov/divisions/hrd/vacancy/VAC2.HTM** or by contacting **Jean Weinbrenner, telephone: 608-890-0044, or e-mail: jean.weinbrenner@ars.usda.gov**. Candidates must submit specific information as outlined in the vacancy announcement. Applications must be received by the closing date of June 1, 2010. For information on the research program, contact **Philipp Simon, telephone: 608-262-1248, or e-mail: philipp.simon@ars.usda.gov.** *USDA is an Equal Opportunity Provider and Employer. Women and minorities are encouraged to apply.*

USDA ARS Agricultural Research Service
www.ars.usda.gov

RESEARCH ENTOMOLOGIST/ GENETICIST/BIOLOGIST
Pacific Basin Agriculture Research Center
Hilo, Hawaii
Salary Range $63,119.00 to $115,301 Per Year

The Pacific West Area is seeking highly qualified candidates for a permanent, full-time scientific position. This position affords the opportunity to conduct research that will lead to the development of efficacious, cost-effective and environmentally acceptable and sustainable methods to control, suppress, and eradicate tropical arthropod pests that impact U.S. agriculture. Research includes developing improvements to sterile insect techniques (SIT) through improved strains, production systems, and release methodologies to control tephritid fruit flies and other tropical insect pests. To apply, print a copy of **vacancy announcement ARS-X10W-0115** from the ARS Careers **website: http://www.ars.usda.gov/careers**, and follow the application directions provided. To have a printed copy mailed, call **telephone: 808-932-2103**. *U.S. citizenship is required.* Applications must be received by April 30, 2010. For more detailed information on this listing, please contact **Dr. Eric Jang, e-mail: eric.jang@ars.usda.gov.**

USDA/ARS is an Equal Opportunity Employer and Provider.

SENIOR RESEARCH ASSOCIATE wanted to conceptualize, lead, and plan epidemiological clinical research projects on chronic diseases such as cancer and cardiovascular diseases. Must have M.D. or Ph.D. in epidemiology, biostatistics, or a related field, or foreign equivalents and have three years of experience in job offered or three years of research experience in epidemiology, including experience with statistical analysis system, data management, and quality control measures. Send resume to: **Lynn L. Moore, Associate Professor of Medicine, Boston University School of Medicine, 715 Albany Street, Boston, MA 02118.**

POSITIONS OPEN

School of Pharmacy
TEMPLE UNIVERSITY

FACULTY POSITION
ASSOCIATE/FULL PROFESSOR
in Pharmacokinetics

Temple University School of Pharmacy, located in the heart of the Philadelphia academic and pharmaceutical technology area, seeks candidates for a tenure track academic year appointment at the rank of Associate or Full Professor, whose research focus is pharmacokinetics and pharmacokinetic/pharmacodynamic modeling/simulation. We are seeking an experienced investigator with demonstrated research excellence (sustained track record of publications and/or research funding) and quality teaching commitment and ability. The position is in the Department of Pharmaceutical Sciences, which has core strengths and NIH funded faculty, a current good manufacturing practices manufacturing facility, the Moulder Center for Drug Discovery Research, and the Jayne Haines Center for Pharmacogenomics and Drug Safety. The successful candidate will be expected to develop a vigorous, externally funded research program, have a commitment to professional and graduate education, develop collaborative research programs.

Applicants should submit a cover letter indicating their area of interest and desired appointment rank, complete curriculum vitae, statement of research expertise, teaching philosophy, and contact information for three professional references to:

Evgeny Krynetskiy, Ph.D.
Search Committee Chair
Department of Pharmaceutical Sciences
Temple University School of Pharmacy
3307 North Broad Street
Philadelphia, PA 19140
Telephone: 215-707-4972 Fax: 215-707-5620
E-mail: ckrynets@temple.edu

Review of applicants will continue until position is filled. *Temple University is an Affirmative Action/Equal Opportunity Employer.*

STEM CELL FACULTY POSITIONS
The Johns Hopkins University
School of Medicine

Applications are invited for full-time, tenure track Faculty Positions in stem cell and vascular programs within the Institute for Cell Engineering. Preference will be given to applicants with broad interests in the cellular and molecular aspects of stem cells including vascular biology, reprogramming, cell fate specification, development, and metabolomics. Applicants should have a Ph.D. or M.D. and appropriate postdoctoral training. Faculty members are expected to establish or to have active independent research programs and participate in teaching graduate and medical students. Deadline for application is May 1, 2010.

Please send curriculum vitae, a brief description of current and future research interests, and arrange to have three letters of recommendation sent to:

Search Committee
Institute for Cell Engineering
The Johns Hopkins University
School of Medicine
E-mail: icesearch@jhmi.edu

An Equal Employment Opportunity/Affirmative Action Employer

CAREER OPPORTUNITY. Doctor of Optometry (O.D.) degree in 27 months for Ph.D.s in science and M.D.s. Excellent career opportunities for O.D. Ph.D.s and O.D. M.D.s in research, education, industry, and clinical practice. This unique program starts in March of each year, features small classes, and has 12 months devoted to clinical care.

Contact the **Admissions Office, telephone: 800-824-5526** at **The New England College of Optometry, 424 Beacon Street, Boston, MA 02115.** Additional information at **website: http://www.neco.edu. E-mail: admissions@neco.edu.**

Department of Health and Human Services
National Institutes of Health
National Center on Minority Health and Health Disparities

The National Center on Minority Health and Health Disparities (NCMHD), a component of the National Institutes of Health (NIH), Department of Health and Human Services (DHHS), is seeking exceptional candidates for the position of Director, Division of Intramural Research (DIR). The incumbent serves as the principal advisor to the NCMHD Director on biomedical and scientific affairs involving the intramural research programs conducted by basic and clinical research investigators in the field of minority health and health disparities research. This position offers a unique and exciting opportunity for an extremely capable individual to evaluate research efforts and establish program priorities, direct training of pre- and post doctoral fellows, collaborate with other NIH programs, and advise the NCMHD Director and senior staff of the DIR in areas of science of interest to the Center. The Division of Intramural Research will have staff of approximately 10 employees and a current annual budget of $4.3 million dollars. In addition to the managerial/administrative responsibilities outlined above, the Scientific Director is expected to carry out his/her own research program. Resources commensurate with the proposed program will be provided. The NCMHD seeks candidates who have a commitment to scientific excellence and the energy, enthusiasm, and innovative thinking necessary to lead and direct the DIR's research efforts at the forefront of science.

QUALIFICATIONS: Applicants must possess an M.D., Ph.D., or equivalent degree, and have demonstrated scientific leadership and research experience in either a basic or clinical research program of national and international standing in one or more of the areas of research that has or will contribute new knowledge in biomedical and behavioral issues recognized as part of the NCMHD mandate.

SALARY/BENEFITS: Salary is very competitive and will be commensurate with the experience of the candidate. A full package of Civil Service benefits is available including retirement, health and life insurance, long term care insurance, annual and sick leave and the thrift savings plan (401K equivalent). The position is subject to a background investigation.

HOW TO APPLY: Interested candidates should send a letter of interest, including a brief description of research and administrative experience, curriculum vitae and bibliography and full contact information for three to five individuals who may be contacted to provide letters of reference. Application packages should be sent to the **National Institutes of Health (NIH), National Center on Minority Health and Health Disparities, c/o Dr. John O'Shea, Chair, Search Committee, 6707 Democracy Blvd., Suite 800, Bethesda, Maryland 20892**, or electronically: Victoria Purcell, purcellv@mail.nih.gov. **Subject Line: NCMHD Scientific Director Search**. For further information about the position please contact Dr. John O'Shea on (301) 496-7613 or e-mail at osheaj@arb.niams.nih.gov. All information provided by the candidates will remain confidential and will not be released outside the NCMHD search process without a signed release from candidate. Persons who previously applied need not reapply.

Applications should be received by April 30, 2010

NIDDK | NATIONAL INSTITUTE OF DIABETES AND DIGESTIVE AND KIDNEY DISEASES

DEPARTMENT OF HEALTH AND HUMAN SERVICES
NATIONAL INSTITUTES OF HEALTH
NATIONAL INSTITUTE OF DIABETES DIGESTIVE AND KIDNEY DISEASES
INTRAMURAL RESEARCH PROGRAM

Postdoctoral Fellowship

POSTDOCTORAL FELLOWSHIP in Molecular Genetics at the Department of Health and Human Services (DHHS), National Institutes of Health (NIH), National Institute of Diabetes and Digestive and Kidney Diseases (NIDDK), in Phoenix, AZ. We are working to identify and characterize novel genes that cause type 2 diabetes and obesity in humans. Applicants must have a Ph.D. or M.D. degree obtained within the past 5 years, with research experience in molecular biology. Please send curriculum vitae to Leslie Baier, Ph.D. 445 North 5th Street, Suite 210, National Institutes of Health, Phoenix, AZ 85004. email: lbaier@phx.niddk.nih.gov

DHHS and NIH are Equal Opportunity Employers.

The National Institute of Neurological Disorders and Stroke (NINDS) is seeking a Biologist for its Laboratory of Molecular Medicine and Neuroscience (LMMN) at the National Institutes of Health (NIH), Bethesda, MD. The position is for a biologist and laboratory technical person with experience in nervous system cell cultures including primary cells derived from brain tissue. The LMMN focuses its work on questions of viral pathogenesis on two human neurotropic agents, JCV that causes the demyelinating disease progressive multifocal leukoencephalopathy and HIV-1 that causes an encephalitis in AIDS patients. Along with the LMMN CLIA certified assays for viral diagnostics, this work contributes to the translation of the fundamental understanding of brain infections to the discovery of interventional treatment drugs that specifically block infection. This position is part of a team in the LMMN whose responsibility would include but are not limited to the management of a cell model, further characterization of the phenotypes of the cells, and contribution to the many collaborators that are maintained by the LMMN. The laboratory maintains state of the art facilities along with BSL2/3 and clean room cell culture suites. A strong background in methods involving nucleic acids would also be welcome.

The qualified candidate should have a degree in a biological science, agriculture, natural resource management, chemistry, or related disciplines appropriate to this position. Applicants must be U.S. citizens to qualify for federal government GS positions. The salary ranges from $62,467 to $97,333 per annum and is commensurate with experience and qualifications. Full Federal benefits are available including leave, health and life insurance, long-term care insurance, retirement, and retirement savings plan (401k equivalent). Qualified individuals should apply to Vacancy Announcement #HHS/NIH-2010-0152 via www.usajobs.gov, and are encouraged to contact Ms. Brittany Broussard (broussardb@mail.nih.gov) for additional information. Candidates who are not citizens but have 'green card' status as permanent residents would be considered under a contract mechanism and should contact K. Augustine, AugustinK@ninds.nih.gov. DHHS and NIH are Equal Opportunity Employers. All positions are subject to a background investigation.

WWW.NIH.GOV

NIAID needs you because the world needs us!

Director, Therapeutics Research Program, Division of AIDS, NIAID, NIH, HHS

The National Institute of Allergy and Infectious Diseases (NIAID) is seeking an exceptional and visionary leader to be the director of the Therapeutics Research Program (TRP) in the Division of AIDS (DAIDS). The TRP director is responsible for planning, implementing, and directing a global research program for the preclinical development and clinical testing of therapies for HIV/AIDS and its associated co-morbidities. This includes oversight of the largest collection of global HIV/AIDS clinical trials networks.

The TRP director serves as a key scientific advisor to the directors of DAIDS and NIAID and is responsible for ensuring that the therapeutics research supported by DAIDS is integrated and complementary with the other programs within NIAID and NIH.

The TRP director is responsible for formulating an overall scientific agenda for the development and clinical testing of therapeutic interventions; recommending resource allocation across competing activities; and continually assessing program priorities and activities, anticipating and responding to emerging scientific opportunities, changing research needs, or revised policies or guidelines.

Qualifications: Applicants must possess an M.D. and demonstrate experience in 1) working independently and collaboratively in planning, organizing, conducting, and/or overseeing clinical research in infectious diseases; 2) serving effectively in research program administration; and 3) communicating effectively.

Application Process: Provide your curriculum vitae, your bibliography, and a three-page statement explaining your vision for a global clinical research program in infectious diseases, reasons for being interested in the position, and specific leadership skills and experience relevant to this position.

Submit your application package and any inquiries to Mr. Robert Gulakowski via email at rgulakow@niaid.nih.gov or call 301-496-0545. The deadline for receipt of applications is **May 21, 2010**. Additional information can be found at www.niaid.nih.gov/careers/trp2/ite.

NIAID

National Institute of Allergy and Infectious Diseases

All information provided by applicants will remain confidential and will only be reviewed by authorized NIAID officials. The successful candidate will be appointed under the Title 42(f) authority, which has a salary limit of $200,000 per year. A full package of benefits is also available, including retirement; health, life, and long-term care insurance; annual and sick leave; and a thrift savings plan (401K equivalent). This position is subject to confidential financial disclosure requirements.

Help Us Help Millions

U.S. DEPARTMENT OF HEALTH AND HUMAN SERVICES
National Institutes of Health

THE UNIVERSITY OF ARIZONA.

DEPARTMENT OF IMMUNOBIOLOGY

Applicants are invited for Tenured/Tenure Track positions at the assistant, associate, and full professor rank, depending upon qualifications, at the Department of Immunobiology, University of Arizona College of Medicine. Qualified applicants will develop strong, extramurally funded programs. Preference will be given to those candidates investigating initiation and regulation of innate and inflammatory responses, however, applicants with outstanding programs in other areas of immunobiology will be considered as well. Successful applicants are expected to not only develop independent research programs and contribute to graduate (Ph.D.) and medical (M.D.) education, but also to invest a fraction of their effort to help build interactive and collaborative programs within and outside the Department to tackle larger biomedical problems relevant to human health.

The University of Arizona is amongst the top 20 public research and education universities, boasting excellent core facilities, strong departments and centers, as well as lively campus culture and life, and a blossoming recreations center. It is located in sunny Tucson, a city with a vibrant multicultural population of approximately 900,000, strong economy, and business. Tucson is surrounded by a majestic desert and mountains rising to more than 9,000 feet.

Please complete an on-line application for Job #44945 at **www.hr.arizona.edu**. Be prepared to attach your curriculum vitae.

The University of Arizona is an EEO/AA Employer – M/W/D/V

St. Jude Children's Research Hospital

PEDIATRIC CANCER GENOME PROJECT LABORATORY DIRECTOR POSITION

In an unprecedented effort to identify the genetic changes that give rise to some of the world's deadliest childhood cancers, St. Jude Children's Research Hospital, in collaboration with Washington University, has launched the Pediatric Cancer Genome Project (PCGP). The goal of this project is to sequence the entire genome of paired tumor and normal samples from 600 pediatric tumors, and to determine the frequency of the identified mutations across a large panel of pediatric cancers.

We invite applications for the position of Director of the St. Jude Children's Research Hospital PCGP DNA Sequencing Laboratory. The Director of this laboratory will be responsible for all aspects of sample handling and DNA sequencing acquisition required for mutation validation, mutation recurrency determination, and transcriptome sequencing. The Director will be responsible for the supervision of a staff of four full-time FTEs, and will interact closely with the PCGP bioinformatics group and report to the Scientific Director.

The successful candidate should have a PhD in a relevant scientific field of biomedical research, four years of post-degree training, and direct supervisory experience including staff supervision and management of laboratory quality control issues and budgets. Experience in DNA sequencing methodologies including Next Generation approaches is highly desirable.

St. Jude Children's Research Hospital focuses on the fundamental causes and treatment of catastrophic childhood diseases including cancer, infectious diseases and genetic disorders. Founded by Danny Thomas in 1962, the hospital includes over 200 basic and clinical investigators. Our interactive research environment is optimal for interdisciplinary translational research. In addition, SJCRH is a National Cancer Institute Comprehensive Cancer Center.

Applicants should send curriculum vitae and three letters of recommendation to: James R. Downing, M.D., Scientific Director, St. Jude Children's Research Hospital, 262 Danny Thomas Place, Memphis, TN 38105. St. Jude Children's Research Hospital is an Equal Opportunity Affirmative Action Employer.

www.stjude.org

University of Glasgow

Faculty of Medicine
Beatson Institute

Lecturer/Senior Lecturer/Reader

The Glasgow Centre for Cancer Research, comprising the Beatson Institute for Cancer Research and the University of Glasgow, is engaged in a programme of world-class science directed towards understanding aspects of cancer growth, motility and survival. As part of an ongoing expansion we are seeking applications from successful and highly motivated scientists to join us as a Junior Group Leader. We particularly welcome applicants using mouse models of cancer to develop an independent research programme in one of our key research areas. You should have a minimum of three years postdoctoral training and an excellent publication record.

The GCCR is housed in a complex of new buildings that provide an outstanding environment for our scientists. We offer generous support that includes a competitive personal salary, a start up package that will allow recruitment of up to 5 additional positions, running costs, high quality lab space with room for expansion and access to state-of-the-art facilities and core services. In total this package of support is worth approximately £1 million. Further information on the Beatson's research activities, infrastructure and facilities is available on our website www.beatson.gla.ac.uk

Informal Enquiries can be directed to Professor Karen Vousden, Director, the Glasgow Centre for Cancer Research and the Beatson Institute for Cancer Research. (Email: k.vousden@beatson.gla.ac.uk)

Apply online at www.glasgow.ac.uk/jobs

If you are unable to apply online please contact us on 0141 330 3898 for an application pack, quoting Ref 00326-1

Closing date 31st May 2010

The University is committed to equality of opportunity in employment. The University of Glasgow is a registered Scottish charity, number SC004401.

www.glasgow.ac.uk

Call for applications for FY2011 Foreign Postdoctoral Researcher (FPR) RIKEN, Japan

RIKEN is one of Japan's largest research organizations with institutes and centers in various locations in Japan and overseas. RIKEN carries out advanced basic and applied research in a wide range of fields, including physics, chemistry, medical science, biology, and engineering.

RIKEN is now accepting applications for the position of Foreign Postdoctoral Researcher (FPR) for FY2011. This position is for young foreign scientists who have demonstrated creative and innovative ideas and who can be expected to achieve broad international recognition in the future.

The FPR program will provide an opportunity for young foreign scientists to apply their creative and innovative ideas, under the direction of RIKEN's laboratory heads, to research currently being conducted at RIKEN.

Job Description Summary

1. Number of openings: Around 18
2. Qualifications
   (1) Applicants should be non-Japanese citizens.
   (2) Applicants must have a PhD in the natural sciences awarded in or after 2005, or expect to be awarded a PhD by the date of hire.
   (3) Applicants must be able to start working at RIKEN within fiscal year 2011 (April 1, 2011 to March 31, 2012).
3. Contract duration
   (1) From date of hire to March 31, 2012
   (2) This contract may be renewed for up to a maximum of 3 years.
4. Remuneration
   Salary is 487,000 yen per month. Commuting and housing allowances are also available. An annual research budget of 1 million yen will be allocated to the host laboratory.

Send an e-mail indicating your desire to apply for the position of FPR to RIKEN by **Friday, May 21, 2010**. Reference material will be sent to those with an interest in applying.

Application Deadline: 5pm on Friday, May 28, 2010 (Japan Standard Time)

Additional information on the program and application procedures is available at **http://www.riken.jp/fpr/**

FPR Desk, Global Relations Office, RIKEN, 2-1 Hirosawa, Wako, Saitama 351-0198 Japan, Fax +81-48-463-3687, Email **fpr@riken.jp**

Science
AAAS

Associate Editor

Science and AAAS seek a talented scientist to serve as an Associate Editor for our new interdisciplinary journal, *Science Translational Medicine*

This position is designed for an individual with broad interests, a lively curiosity, and experience with cutting-edge research in at least one, but preferably more than one, biomedical or clinical research field. To round out our editorial team, we would like our new Associate Editor to have expertise in immunology (vaccines and autoimmune disease especially welcome) or bioengineering (devices, tissue engineering and stem cells are areas of preference)

Responsibilities include, but are not limited to

- Judge the scientific value of research,
- Foster relationships and communication with the scientific community through literature reviews, meetings and professional contacts.
- Manage the review, selection, and editing of submitted manuscripts.
- Select reviewers for submitted manuscripts.
- Discuss and make recommendations regarding manuscripts and reviews with other staff, advisers, authors.
- Write summaries of research results for publication.
- Guide authors on manuscript revisions.
- Edit the manuscripts for scientific content and style before and after revisions,
- Follow the manuscript through production process to ensure material is published in a timely manner; and
- Travel to scientific meetings

The minimum qualifications to be competitive and considered for the position are

- Mastery of a professional field typically acquired through completion of a doctoral degree in at least one biomedical or clinical research field.
- 3-5 years experience, including post-doctoral research experience and multiple publications,
- Ability to work constructively as a member of a team,
- Experience with cutting-edge research in one of the fields mentioned above;
- Comprehensive knowledge of scientific research methods in order to discuss technical issues with authors, and
- Exceptional written, communication, and listening skills in order to communicate with authors and reviewers in evaluating, editing and modifying manuscripts

Previous editorial experience is not required

If you would like to be a member of the AAAS team, please visit our Job Information website at **http://www.aaas.org/careercenter/employmentatAAAS/** to get more information and to apply online today

AAAS is an Equal Opportunity Employer

University of Reading

www.reading.ac.uk/jobs

International Project Office Co-ordinator: GHRSST (Global High Resolution Sea Surface Temperature)

National Centre for Earth Observation (NCEO)

This appointment is full-time, fixed-term for 3 years
Grade 7 - £36,715 to £45,155 per annum

NCEO requires a capable scientist with project management experience to run the International GHRSST Project Office. The project aims to produce a scientifically definitive record of sea-surface temperatures.

The post holder will support the activities of the GHRSST international partnership, and will develop detailed scientific and technical plans to deliver its objectives. The post holder will work closely with the NCEO and its partners, and will report regularly to the European Space Agency

Experience in international co-ordination would be an advantage

Informal enquiries, contact the Director, NCEO, Professor Alan O'Neill on +44(0)118 378 8317 or email alan.oneill@nceo.ac.uk

Closing date: 6 May 2010

To formally apply please visit www.reading.ac.uk/jobs or contact Human Resources, University of Reading, Whiteknights, PO Box 217, Reading RG6 6AH. Telephone +44(0)118 378 6771 (voicemail)

Please quote reference number PM10012

We value a diverse workforce and welcome applications from all sections of the community

ARC Centre of Excellence

Coral Reef Studies

Research Fellowships

The ARC Centre of Excellence for Coral Reef Studies seeks applicants for two Research Fellowships to be affiliated with Program 2: Understanding and Managing Coral Reef Biodiversity. The Centre is an internationally renowned research hub encompassing >200 researchers and graduate students (www.coralcoe.org.au)

Coral Reef Biodiversity – Ref. No. 1060
This fellowship is open to candidates interested in research in any area of coral reef biodiversity

Modelling Coral Reef Biodiversity – Ref. No. 1061
This fellowship is for those with interest and expertise in the formulation and analysis, or empirical evaluation, of ecological models.

Enquiries: Professor Sean Connolly, Email: Sean.Connolly@jcu.edu.au

Employment Type: Appointments will be full-time for a fixed-term of 3 years subject to a probationary period, based at the Townsville campus of James Cook University, Queensland, Australia

Salary: Academic Level A - A$61,856 through to Academic Level C - A$85,013 per annum. Level of appointment and commencing salary will be in accordance with qualifications and experience

Further information: http://www.coralcoe.org.au/employment.html
Applications should be made online through: http://www.jcu.edu.au/jobs/

Applications close on 23 April 2010

Equal Opportunity in Employment is University Policy
The University reserves the right to invite applications or not to make an appointment

TMP 0091025

Science Careers is the ke
that opens doors.

ENHANCED WEBSITE!

Opening doors is what we do. We're the key to connecting with the industry's top employers. We're the experts and source for accessing the latest and most relevant career information across the globe.

Our newly designed website offers a set of tools that help you unlock career opportunities and your personal potential. Whether you're seeking a new job, career advancement in your chosen field, or ways to stay current on industry trends, *Science* Careers is your key to a brighter future.

Your Future Awaits.

Improved Website Features:

- Relevant Job E-mail Alerts
- Improved Resume Uploading
- Content Specific Multimedia Section
- Facebook Profile

Job Search Functionality:

- Save and Sort Jobs
- Track Your Activity
- Search by Geography
- Enhanced Job Sorting

Science Careers
From the Journal *Science* AAAS

ScienceCareers.org

UNIVERSITY AT ALBANY
State University of New York

Vice President for Research

The University at Albany/SUNY invites nominations and applications for the position of Vice President for Research (VPR) The Vice President for Research serves as a member of the University's senior leadership reporting directly to the President, and works closely with the Provost and Executive Vice President for Academic Affairs. As the senior research officer of the University, the Vice President for Research is responsible for developing and implementing the vision, plan and policies to guide the University's growing research agenda, and for leading the University at Albany's research infrastructure and operations.

Located in New York's state capital in the Hudson Valley, the University at Albany/SUNY is one of four university centers in the state university system with a broad mission of excellence in undergraduate and graduate education, research and public service The University at Albany/SUNY is classified as Doctoral/Research University-Extensive. The faculty generate over $340 million in external funding yearly

Please the following site for position requirements and online application

http://albany.interviewexchange.com/joboffer details.jsp?JOBID=17929

A review of applications will start on April 20, 2010 and the search will remain open until the position is filled

The University at Albany, State University of New York is an Equal Opportunity/Affirmative Action/IRCA/ADA employer.

UNIVERSITY OF MARYLAND
SCHOOL OF MEDICINE

Neurobiology Faculty Position

University of Maryland School of Medicine
Baltimore, Maryland

The Department of Anatomy and Neurobiology (**http://neurobiology.umaryland.edu**) is recruiting for tenured/tenure-track faculty positions in Neuroscience. We are particularly interested in candidates who will strongly complement existing strengths in the Department, chemical senses, peptidergic circuits, sensorimotor functions, and neural circuits subserving higher order cortical functions. Candidates should have a strong history of scholarly activity and preference will be given to those with an independent funded research program and whose presence will catalyze multi-PI initiatives within the department

We offer an outstanding intellectual and collaborative environment with highly competitive salary and recruitment packages. All department faculty are members of the Graduate Program in Life Sciences and the interdisciplinary Program in Neuroscience (**http://neuroscience.umaryland.edu**).

Candidates should submit the following as one single PDF file to **facsearch@umaryland.edu** detailed curriculum vitae, a brief statement of research interests and goals, and names/contact information for three references. For best consideration candidates should submit their application by **June 1, 2010** and should be addressed to the attention of **Professor Geoffrey Schoenbaum, Chair of Faculty Search Committee**

University of Maryland, Baltimore is an Equal Opportunity, Affirmative Action Employer. Minorities, women, veterans, and individuals with disabilities are encouraged to apply.

International Agency for Research on Cancer
World Health Organization

Scientist, P4, Head of Genetic Cancer Susceptibility Group

The overall objective of the Genetic Cancer Susceptibility Group is the evaluation of inherited genetic factors in the etiology and outcome of cancer and the interaction between environmental factors and susceptibility genes Reporting to the Head of the Genetics Section (GEN), the successful incumbent is expected to lead a research Group focusing on genetic susceptibility to cancer Based on agreed guidelines, he/she is responsible to undertake projects aimed at evaluating the role of inherited and somatic genetic factors in combination with environmental factors in cancer development and outcome This programme of research will build on large scale international molecular epidemiological studies conducted within IARC and with external partners He/she interacts and collaborates with other IARC scientists and outside collaborators in the implementation and execution of molecular epidemiological studies and presents findings at scientific meetings. The incumbent has to keep abreast with the methodological development in this field and to train/supervise the appropriate staff

Requirements: Candidates must have a Master's degree or Ph D in cancer genetics or related field The successful candidate will have advanced knowledge in human genetics and genetic epidemiology of cancer He/She also have excellent publication record in Mendelian cancer genetics and/or multigenic traits and strong record in obtaining external funding.
Demonstration of strong laboratory skills and very good knowledge of English with a working knowledge of French is also required. Basic knowledge in molecular genetics and strong computing and bio-informatics skills would be desirable

Experience: Minimum of seven years' experience in molecular genetic or genetic epidemiology studies of cancer including documented international experience in the planning/development and coordination of collaborative projects.

For complete details and to apply please visit **www.iarc.fr**
Position Number IARC/10/FT128
Closing date for applications. **5 May 2010**

Edward E. Whitacre Jr. College of Engineering

The Maddox Chairs *in Energy* at Texas Tech University

The Edward E. Whitacre Jr. College of Engineering at Texas Tech University is committed to leveraging those **two exceptionally large endowed chairs at over $7 million each**, to become one of the nation's leaders in finding solutions to the world's energy challenges. The college is seeking world-class researchers in solar and sustainable energy as candidates for the Maddox Chairs.

Donovan Maddox Distinguished Engineering Chair *in Solar Energy*

Candidates are expected to have national and international reputation in solar energy based on research publications. In addition, a record of acquiring external resources to support research, team building, and mentoring of associates and graduate and undergraduate students is necessary. The holder of the Donovan Maddox Chair will be expected to not only bring his or her own research activities to the Whitacre College of Engineering, but also to build collaborative community of scholars at Texas Tech dedicated to solar energy research thereby, building a world-class research program. The appointment will be as a full professor in the Whitacre College of Engineering

Jack Maddox Distinguished Engineering Chair *in Sustainable Energy*

Candidates with exceptional and diverse backgrounds in energy sciences and engineering are sought for this endowed position. The successful candidate will demonstrate a national and international reputation for contributions to the solution or advancement of the state of the art on a variety of research issues in the sustainable energy fields including energy efficiency, biofuels, wind power, tidal power, geothermal, and energy storage. The successful candidate, along with the Donavan Maddox Chair in Solar Energy, will set the tone, vision, and the path in order to build a nationally and internationally recognized program at Texas Tech University in sustainable energy research. The appointment will be as a full professor in the Whitacre College of Engineering.

Screening will begin upon the receipt of applications and will continue until the position is filled. Candidates names will not be made public until the final stages of the search.
Curriculum vitae and the names and contact information of at least four references should be submitted at www.coe.ttu.edu/maddox. To nominate a colleague for these chairs, visit www.coe.ttu.edu/maddox. Nominations can be made anonymously.

Questions about the Jack Maddox or Donovan Maddox Chairs should be directed to:
Jack Maddox and Donovan Maddox Search Committees
Texas Tech University | Whitacre College of Engineering
Box 43103 Lubbock, Texas 79409-3013 engineeringdean.coe@ttu.edu | 1.800.528.5583

Texas Tech University | Whitacre College of Engineering
1.800.528.5583 | www.coe.ttu.edu/maddox

CONFERENCE

10th Annual Conference of Science & Technology in Society

A venue for all graduate students from Science & Technology Policy (STP), Science & Technology Studies (STS), and related fields

April 9-11, 2010
Washington, DC

Keynote Speakers:

Dr. Vint Cerf:
Google Vice President & Chief Internet Evangelist

Dr. John P. Holdren:
Director OSTP

Dr. Margaret Hamburg:
Commissioner FDA

4th speaker TBA

For more information and to register go to http://www.stglobal.org

Science & Technology in Society: An Interdisciplinary Graduate Student Conference

POSITIONS OPEN

Smithsonian Tropical Research Institute

POSTDOCTORAL FELLOWSHIP

in the Physiology of Trees in a Changing Climate Center for Tropical Forest Science, Smithsonian Institution Global Earth Observatory

The Smithsonian Institution seeks a Postdoctoral Fellow in tree physiology within the Center for Tropical Forest Science (CTFS), Smithsonian Institution Global Earth Observatory (SIGEO) program. CTFS-SIGEO coordinates a network of long-term forest research plots in 16 tropical and four temperate countries. A core goal of this program is to understand the impacts of changing environmental conditions on the world's forests. This two-year position is based at the Smithsonian Tropical Research Institute (STRI) in Panama. Research is on growth, photosynthetic, water, and nutrient relationships of tropical tree species in response to light, CO2 enrichment, and increased temperature. Research is conducted in conjunction with STRI's Plant Physiology Program and is expected to provide mechanistic information for interpreting plant characteristics and dynamics in forest plots. Candidates should have a strong background in experimental plant ecophysiology and a record of scholarly publication.

Electronically send curriculum vitae, a statement of research interests, and names of three references to **William Tootle, CTFS Program Manager, e-mail: wtootle@oeb.harvard.edu**. For further information about the research, contact **Klaus Winter, e-mail: winterk@si.edu**.

To learn more about CTFS and SIGEO, visit our **websites: http://www.ctfs.si.edu/** and **http://www.sigeo.si.edu/** and our news blog at **website: http://ctfsnews.blogspot.com/**.

POSTDOCTORAL RESEARCHER
The Ohio State University
Division of Cardiothoracic Surgery

The Division of Cardiothoracic Surgery in the Department of Surgery at The Ohio State University College of Medicine seeks a qualified candidate for a Postdoctoral Research position to study atherosclerosis. Salary will be based on experience and qualifications. The candidate must have a Ph.D degree with experience in the quantitation of atherosclerosis and in lipid metabolism. Expertise in molecular biological techniques is needed. Familiarity with liquid chromatography–mass spectrometry, image analysis, LCM, and chromatographic methods desired. Candidates may apply electronically with a copy of resume and date of availability to **Sampath Parthasarathy, Ph.D., M.B.A., Klassen Chair and Professor of Cardiothoracic Surgery, e-mail: spartha@osumc.edu**.

The Ohio State University is an Equal Opportunity/Affirmative Action Employer. Qualified women, minorities, Vietnam-era veterans, disabled veterans, and individuals with disabilities are encouraged to apply.

A **POSTDOCTORAL POSITION** is available at the University of Maryland School of Medicine to model inherited lipid storage diseases using induced pluripotent stem (iPS) cell technology. Patient-derived iPS cells will be differentiated and used to study the molecular mechanisms leading to abnormal cell function, and to develop stem cell–based therapy. The candidate should have a Ph.D., experience in molecular and cell biology, excellent oral and written communication skills, and be able to work independently. Our laboratory is part of the Center for Stem Cell Biology and Regenerative Medicine at University of Maryland Baltimore. Preference will be given to candidates with experience in human embryonic stem/iPS cell technology and hematopoietic development. Salary is commensurate with experience. To apply, electronically send curriculum vitae and contact information for three references to **Dr. Ricardo A. Feldman, e-mail: rfeldman@umaryland.edu**.

POSITIONS OPEN

ASSOCIATE/FULL PROFESSOR
Oral Biology Vacancy Announcement
Position Number 00025506

The Department of Oral Biology is seeking applications for a full-time, tenure-track **CELL BIOLOGIST** at the rank of Associate or Full Professor. Applicants must have demonstrated ability to sustain a highly productive and interactive research program in the area of cell/developmental biology, cancer biology, autoimmunity, host response/innate immunity, epigenetics, and/or microRNA-dependent regulation of gene expression. The incumbent will work closely with College of Dentistry faculty in the departments of Oral Biology, Periodontology, and Oral Diagnostic Sciences. She/he will also work to establish collaborations with other Health Science Center units and cross-cutting initiatives at University of Florida, such as the Genetics Institute, Emerging Pathogens Institute, Biomedical Engineering, and/or the Cancer Center. This position will provide valuable resources to enhance and expand current initiatives in areas such as oral cancer, autoimmune disease, gene regulation, microbial pathogenesis, or host cell responses to pathogens. Minimum requirements include a Ph.D. or equivalent and at least five years of related experience. Preference will be given to candidates who have a history of external funding. Salary and academic rank are commensurate with credentials and experience. Anticipated start date is September 2010.

Review of applications is currently under way and will continue until an applicant pool is identified. Applicants should send curriculum vitae, a cover letter describing their interest in the position, referencing **requisition #0804202,** and a list of three references to:

Prof. Edward K.L. Chan, Search Committee Chair
c/o Ms. Mary Bennett
P.O. Box 100405
Gainesville, FL 32610-0405

Or the information can be sent electronically to **e-mail: mbennett@dental.ufl.edu**.

Any questions regarding the position may be directed to **Dr. Chan at e-mail: echan@dental.ufl.edu**.

The University of Florida is an Equal Opportunity Institution dedicated to building a culturally diverse and inclusive faculty and staff. The selection process will be conducted in accord with the provisions of Florida's "Government in the Sunshine" and Public Records laws. Search committee meetings and interviews will be open to the public, and all applications, resumes, and other documents related to the search will be available for public inspection.

UT SOUTHWESTERN MEDICAL CENTER

MOLECULAR IMMUNOLOGY AND CHROMATIN (T26)

A **POSTDOCTORAL POSITION** is available in molecular immunology and chromatin to elucidate the nuclear organization of the mouse kappa immunoglobulin gene locus using D3 FISH/3C/4C. To apply, Ph.D. required; send curriculum vitae and two letters of reference to:

William T. Garrard
Department of Molecular Biology
UT Southwestern Medical Center
5323 Harry Hines Boulevard
Dallas, TX 75390-9148
E-mail: william.garrard@utsouthwestern.edu

UT Southwestern is an Equal Opportunity, Affirmative Action Employer.

POSITIONS OPEN

UT SOUTHWESTERN MEDICAL CENTER

POSTDOCTORAL POSITION, Tularemia. A Postdoctoral position is available to study *Francisella tularensis* outer membrane proteins (OMPs), with emphasis on understanding their roles in the pathogenesis of tularemia and their potentials as acellular/subunit vaccines (**J.F. Huntley et al.,** *Infect. Immun.* **76:3664, 2008**). Talented, dedicated, Ph.D. level individuals with interests in molecular pathogenesis, vaccinology, and/or BSL-3 work are encouraged to apply. A background in assessing the correlates of protective immunity is a plus. The appointment will be contingent on achieving CDC/FBI clearance for work on a Category A select agent. Please send curriculum vitae and three letters of reference to: **Dr. Michael V. Norgard, Chair, Department of Microbiology, U.T. Southwestern Medical Center, 6000 Harry Hines Boulevard, Dallas, TX 75390-9048. E-mail: michael.norgard@utsouthwestern.edu.** *U.T. Southwestern Medical Center is an Equal Opportunity University.*

MARKETPLACE

Call for Symposium Proposals

AAAS Annual Meeting + You = Global Visibility

17-21 February ▸ 2011 Washington, D.C.

Science Without Borders

Science and teaching that cross conventional borders, or break out from silos, will be highlighted at the 2011 Annual Meeting. Sessions are encouraged that have strong scientific content, particularly at the interface of different disciplines, or exemplify a multidisciplinary approach to problem solving.

Symposium proposals are due 27 April 2010. For details, go to www.aaas.org/meetings and sign up for updates throughout the year.

Call for Poster Submissions

Student Poster Competition

Open to college undergraduate and graduate students only

The competition recognizes the individual efforts of students who are actively working toward a college-level degree. Posters are judged at the meeting. Winners in each category receive a cash award and framed certificate, and are listed in *Science*. Postdoctoral scholars who hold a doctoral degree are not eligible to enter.

General Poster Session

Open to postdocs and professionals

This session provides an opportunity for participants to present their research to the broad community of scientists attending the AAAS Annual Meeting.

The submission site for poster submissions for the 2011 Annual Meeting in Washington, DC, 17-21 February, will open on 12 May 2010 at www.aaas.org/meetings.

AAAS
ADVANCING SCIENCE, SERVING SOCIETY

R&D Systems Bioactive Proteins

High quality proteins aren't a luxury, they are a necessity.

WHAT'S THE RISK? ✓ Missed opportunities ✓ Non-specific results
✓ Experiments that can't be repeated ✓ Weeks or months of wasted time

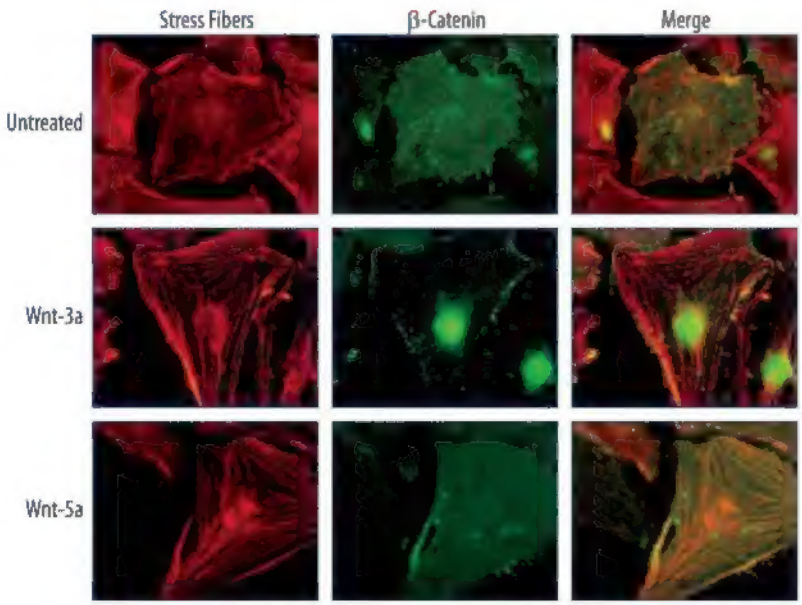

R&D Systems recombinant mouse Wnt-3a (Catalog # 1324-WN) and Wnt-5a (Catalog # 645-WN) promote stress fiber formation in NIH-3T3 cells, while only Wnt-3a promotes nuclear β-Catenin accumulation. Please visit our website for information about our new high purity human Wnt-3a (Catalog # 5036-WNP). *Images Courtesy of Dr. Raymond Habas, Robert Wood Johnson School of Medicine.*

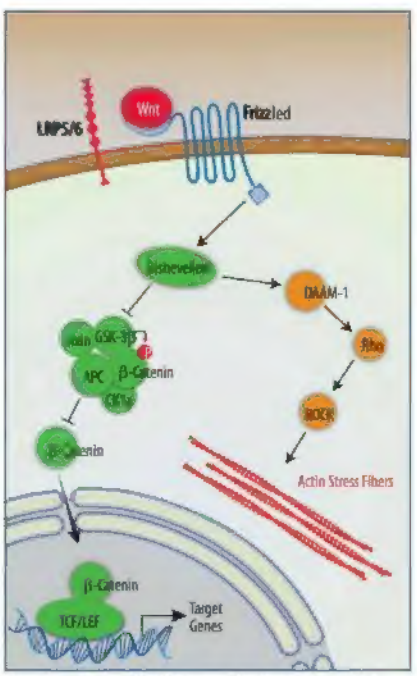

For research use only. Not for use in diagnostic procedures.

R&D Systems has spent almost 25 years building its reputation as a source for high quality proteins.

Every stage of protein development takes place in R&D Systems' laboratories, from cloning of the gene, to protein purification and testing for bioactivity. Because we control all aspects of protein manufacturing, R&D Systems can better control the quality of our products and the technical assistance we offer. Please visit our website at **www.RnDSystems.com/go/Proteins** for more information.

Cancer Development Endocrinology Glycobiology Immunology Neuroscience Proteases Signal Transduction Stem Cells

R&D Systems Tools for Cell Biology Research™

USA & Canada **R&D Systems, Inc.** Tel: (800) 343-7475 info@RnDSystems.com
Europe **R&D Systems Europe, Ltd.** Tel: +44 (0)1235 529449 info@RnDSystems.co.uk
China **R&D Systems China Co., Ltd.** Tel: (800) 988-1270 info@RnDSystemsChina.com.cn

Selection expanding weekly—visit **www.RnDSystems.com/go/request** to sign up for weekly new product updates.

R&D SYSTEMS®